Kinetic Theory of Magnon Bose-Einstein Condensation

by

JULIAN HÜSER

2016

Theoretische Physik | *Theoretical physics*

Kinetic Theory of Magnon Bose-Einstein Condensation

Inaugural-Dissertation zur Erlangung des Doktorgrades der
Naturwissenschaften im Fachbereich Physik der
Mathematisch-Naturwissenschaftlichen Fakultät der Westfälischen
Wilhelms-Universität Münster

Dissertation in partial fulfillment of the requirements for a doctoral
degree presented to the Department of Physics of the Faculty of
Mathematics and Natural Sciences at the University of Muenster

vorgelegt von | *submitted by*

Julian Hüser

aus | *from*

Emden

-2016-

Dekan | *Dean*	Prof. Dr. Christian Weinheimer
Erster Gutachter | *First Referee*	Prof. Dr. Tilmann Kuhn
Zweiter Gutachter | *Second Referee*	Prof. Dr. Peter Krüger
Tag der mündlichen Prüfung | *Date of Defense*	08.07.2016
Tag der Promotion | *Date of Graduation*	08.07.2016

Abstract

The present thesis provides a systematic theoretical study of the magnon dynamics and the room temperature Bose-Einstein condensation (BEC) of magnons in yttrium iron garnet (YIG). A kinetic model for the simulation of the time evolution of the magnetic system is established which includes the main interactions between magnons themselves and between magnons and phonons. The model is furthermore capable of describing the challenging phenomenon of magnon Bose-Einstein condensation which has been observed in several experiments to date.

The beginning of this thesis is devoted to a detailed introduction of the model which is based on an effective spin Hamiltonian in YIG. Subsequently, the kinetic equations resulting from the three-magnon process, the four-magnon process as well as from the magnon-phonon Cherenkov process are derived which jointly determine the time evolution of the magnetic system. The formal properties of the kinetic equations are analyzed which yield the individual equilibrium states for the different interaction processes. Furthermore, the fulfillment of Boltzmann's H-theorem is verified which constitutes the irreversibility of the time evolution towards the equilibrium.

In the subsequent part, the relaxation rates of the various interaction processes are discussed individually and are compared with the well known parallel pump experiments. A modified strong four-magnon process is introduced which is compatible with both the relaxation rates following from the experiment and with current theoretical estimates of the relaxation rate of the uniform mode in YIG. As it will be shown, this modified process is indispensable for explaining the fast thermalization of magnons observed in various experiments in the field of magnon BEC. In addition, the individual equilibration processes of non-equilibrium initial conditions, caused by the respective magnon interactions, are investigated and reveal the basic mechanisms of magnon damping and magnon thermalization.

The final part deals with the full model containing all interactions and focusses on magnon Bose-Einstein condensation in different cases. At first, the dynamics of the magnon system is studied which is brought out of equilibrium by means of short intense pumping. It turns out that the scattering amplitude of the modified four-magnon process has the correct order of magnitude in order to reproduce the experiments of pumped magnons reasonably. The case of continuous pumping is discussed subsequently revealing that the characteristic overshoot of pumped magnons, as observed in the experiments, is well reproduced by the model. Furthermore, it is shown that the recently observed upward jump of the condensate population, caused by switching off the pumping at high pumping powers, can also be well described by the kinetic model augmented by a hypothetic strong condensate damping. Finally, the possibility of magnon BEC induced by an abrupt temperature decrease of the underlying lattice, which affects the magnetic system via the magnon-phonon Cherenkov process, is discussed.

Zusammenfassung

Die vorliegende Arbeit stellt eine systematische theoretische Studie über die Dynamik und die Bose-Einstein Kondensation von Magnonen in Yttrium-Eisen-Granat (YIG) bei Raumtemperatur dar. Es wird ein kinetisches Modell zur Simulation der zeitlichen Entwicklung des magnetischen Systems vorgestellt, das die wesentlichen Wechselwirkungen zwischen Magnonen untereinander und zwischen Magnonen und Phononen berücksichtigt. Ferner ist das Modell in der Lage, das Phänomen der Bose-Einstein Kondensation von Magnonen zu beschreiben, das bereits in zahlreichen Experimenten nachgewiesen wurde.

Zu Beginn der Arbeit wird das Modell detailliert vorgestellt, das auf einem effektiven Spin Hamiltonoperator in YIG beruht. Darauffolgend werden die kinetischen Gleichungen hergeleitet, die aus dem Drei-Magnonen-, Vier-Magnonen- und dem Magnon-Phonon-Cherenkov-Prozess hervorgehen, welche zusammen die zeitliche Entwicklung des magnetischen Systems bestimmen. Es werden die formalen Eigenschaften der kinetischen Gleichungen erörtert, welche die individuellen Gleichgewichtszustände der verschiedenen Wechselwirkungsprozesse offenbaren. Ferner wird die Erfüllung des Boltzmannschen H-Theorems validiert, welches die Irreversibilität der zeitlichen Entwicklung hin zum Gleichgewicht begründet.

Im darauffolgenden Teil der Arbeit werden die Relaxationsraten der einzelnen Wechselwirkungsprozesse untersucht und mit wohlbekannten Experimenten parallel gepumpter Magnonen verglichen. Es wird ein modifizierter starker Vier-Magnonen-Prozess vorgestellt, der sowohl mit den im Experiment gemessenen Relaxationsraten sowie mit aktuellen theoretischen Abschätzungen der Relaxationsrate der uniformen Mode in YIG vereinbar ist. Es wird gezeigt, dass dieser modifizierte Prozess essenziell ist um die schnelle Thermalisierung der Magnonen, wie sie in zahlreichen Experimenten beobachtet wurde, zu erklären. Ferner werden die individuellen Relaxationsprozesse von anfänglichen Nichtgleichgewichtszuständen untersucht, die durch die jeweiligen Wechselwirkungen von Magnonen hervorgerufen werden und die die wesentlichen Dämpfungs- und Thermalisierungsmechanismen zum Vorschein bringen.

Der letzte Teil der Arbeit behandelt das komplette Modell mit allen Wechselwirkungen und thematisiert im Speziellen die Bose-Einstein Kondensation von Magnonen in unterschiedlichen Situationen. Als erstes wird die Dynamik des magnetischen Systems untersucht, das durch kurzes intensives Pumpen aus dem Gleichgewicht gebracht wird. Es stellt sich heraus, dass die Streuamplitude des modifizierten Vier-Magnonen-Prozesses die richtige Größenordnung besitzt um die Experimente von gepumpten Magnonen angemessen reproduzieren zu können. Darauffolgend wird der Fall von kontinuierlich gepumpten Systemen behandelt, der zeigt, dass das in Experimenten beobachtete charakteristische Überschwingen der gepumpten Magnonen durch das Modell gut reproduziert wird. Darüber hinaus kann

der kürzlich beobachtete Sprung in der Population des Kondensats, der durch das plötzliche Abschalten des Pumpens bei hohen Pumpleistungen verursacht wird, auf Basis einer hypothetischen starken Dämpfung des Kondensats sehr gut durch das Modell beschrieben werden. Schließlich wird die Möglichkeit der Bose-Einstein Kondensation von Magnonen diskutiert, die durch einen abrupten Temperatursturz des zugrundeliegenden Kristallgitters induziert wird, der ferner durch den Magnon-Phonon-Cherenkov-Prozess das magnetische System beeinflusst.

Table of Contents

1

Introduction

Bose-Einstein condensation (BEC) is one of the most fascinating phenomena predicted by quantum mechanics which has ultimately been confirmed experimentally. Based on the preceding work by Bose [1] who rederived Planck's law by means of a statistical description of the quanta of light, Einstein extended this approach to ideal gases in 1925 and furthermore predicted a phase transition to occur at high densities of the gas which is associated with the condensation of atoms in the lowest energy state [2,3]. Nowadays known as the *Bose-Einstein distribution*,

$$\bar{n}(E) = \frac{1}{\exp\left(\frac{E-\mu}{k_\mathrm{B}T}\right) - 1}, \tag{1.1}$$

$\bar{n}$ describes the average occupation of the quantum state with energy E at a given temperature T and chemical potential μ of the gas, where k_B is the Boltzmann constant. Einstein soon realized that this distribution only permits the accommodation of a limited amount of atoms in a three-dimensional ideal gas, which is reached if the chemical potential is equal to the ground state of the system, given by the famous relation

$$\rho_\mathrm{crit} = \zeta(3/2)\,\frac{(2\pi m k_\mathrm{B} T_\mathrm{crit})^{3/2}}{h^3}, \tag{1.2}$$

where ρ_crit is the critical density of the gas and m is the mass of a single atom, whereas h is the Planck constant and $\zeta(x)$ is the Riemann zeta function with $\zeta(3/2) \approx 2.612$. Since the right-hand side of Eq. (1.2), except for the Riemann zeta function, is just the inverse thermal de Broglie wavelength cubed, BEC sets in, in a simplified picture, as soon as the mean distance between the particles gets close to the thermal wavelength, where the indistinguishability of the particles becomes crucial, thus revealing the quantum nature of this phenomenon. Besides the macroscopic population of the ground state, BEC manifests itself also in the coherence of condensed particles which are described by a single wave function thus allowing for the observation of quantum effects on the macroscopic scale [4]. However, as stated by the spin-statistics theorem, firstly formulated in 1939 by Fierz [5], only particles or composite particles with integral spin obey the Bose-Einstein statistics (1.1), now known as *bosons*, whereas the other class of particles with half-integral spin obey the Fermi-Dirac statistics, now known as *fermions*.

The critical condition (1.2) basically permits for BEC to be observable at any temperature, providing the critical density is reached. However, in order to observe BEC in an atomic gas, the temperature has to be decreased significantly in order to ensure the stability of the gas, preventing the phase transition into a solid. And indeed, benefiting from both the recent developments in atomic physics of magnetic and optical trapping and also from advanced cooling techniques, such as laser cooling and evaporation, the experimental teams of Cornell and Wieman in Boulder and Ketterle at MIT eventually succeeded in 1995, 70 years after its prediction, in reaching the critical conditions for BEC in vapors of rubidium [6] and sodium [7] at temperatures in the nanokelvin to microkelvin range, which was appreciated with the Nobel Prize in Physics in 2001. However, the first signatures of BEC have already been observed long before the first realizations of atomic BECs in the appearance of superfluidity in liquid helium which is closely related to Bose-Einstein condensation [4].

Apart from BEC of gases which consist of massive particles, BEC has also been reported in various systems of quasiparticles, including excitons [8–10], exciton-polaritons [11–13], and photons [14]. Also the appearance of magnon BEC in spin dimer compounds has been discussed in the past [15, 16]. In general, the BEC of quasiparticles is only possible at non-equilibrium since quasiparticles, in contrast to massive particles, obey no particle number conservation and thus exhibit a vanishing chemical potential in thermal equilibrium. Therefore, it is always a matter of timescales if BEC can be observed in the various systems since the thermalization of quasiparticles has to be much faster than their respective decay.

A gas of magnons in yttrium iron garnet (YIG) provides a very attractive system for BEC due to the small magnetic losses in this material and short thermalization times of magnons. Magnons are the elementary collective excitations of a ferromagnet, as depicted in Fig. 1.1, which have been introduced by Bloch in 1930 in order to determine the temperature dependence of the spontaneous magnetization in ferromagnets at low temperatures [17], which is now known as the *Bloch's* $T^{3/2}$*-law* [18]. Carrying spin 1, magnons are bosonic quasiparticles which consequently obey the Bose-Einstein statistics and hence are principally allowed to undergo the BEC transition under certain conditions. And indeed, in 2006, Demokritov *et al.* obtained the first unambiguous experimental evidence for magnon BEC in YIG [19]. In contrast to the experiments in the field of excitonic BEC, which are commonly carried out at cryogenic temperatures, the magnon BEC has been achieved at room temperature owing to the very small effective mass of magnons in YIG, which is roughly six times the mass of an electron. Therefore, the critical condition for BEC can be reached at magnon densities which lie only slightly above the room temperature magnon density. At thermal equilibrium, the magnon gas has a zero chemical potential. However, in this experiment, the critical density has been achieved by excitation of additional magnons with a fixed frequency by means of the parallel pumping technique [20, 21]. The time evolution of the magnon gas, being out of equilibrium, was then measured by means of time-resolved inelastic Brillouin light scattering (BLS) [22]. The interpretation of the experiment is as follows. The pumped non-equilibrium magnons redistribute over the spectrum due to inherent scattering processes which conserve the total magnon number. By sufficiently strong pumping, the thermalization of the magnons is faster than their respective decay resulting in a Bose-Einstein distribution of the magnon gas with nonzero chemical potential. By further pumping, the chemical potential eventually approaches the minimal energy state and the magnon system undergoes the BEC transition, which is manifested in a very narrow magnon distribution at the bottom of the magnon spectrum, observed in the experiment.

Since this observation, a lot of experimental work has been performed in order to confirm the concept of magnon BEC [23–31]. In recent publications, particular insight into the thermalization process of magnons has been obtained [32, 33]. However, from the theoretical point of view, it is not quite clear if the inherent magnon interaction processes are indeed strong enough to redistribute the pumped magnons on a short timescale, constituting a quantitative problem which has not yet been addressed in the literature so far. In contrast,

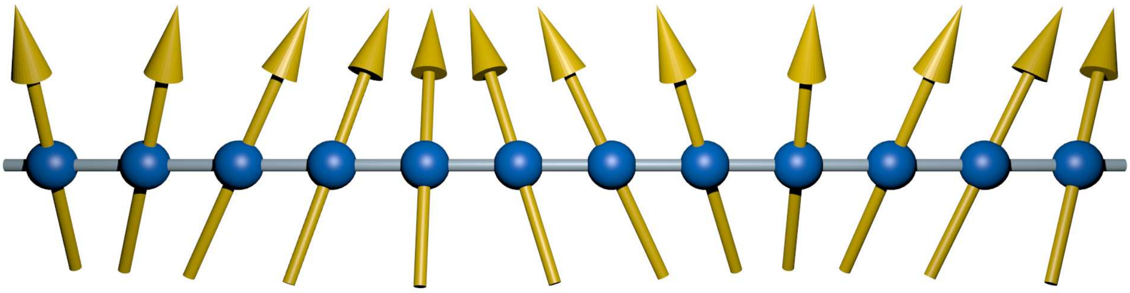

Figure 1.1: Semiclassical illustration of a magnon. The spin difference of $1\hbar$ between the ferromagnetic ground state and the one-magnon state is distributed homogeneously over each spin in the lattice, resulting in a bosonic collective excitation.

there are a lot of phenomenological models which, however, do not describe the important stage of the magnon thermalization [34–42]. In a first attempt to describe the thermalization process, only the interaction of magnons with phonons has been considered [43], its coupling constant, nevertheless, has been adjusted in order to get agreement with the experiment. Later, it was shown that this type of coupling is negligible at small wave vectors, where the magnon thermalization takes place [44]. In a recent work [45], a stochastic approach has been employed in order to explain the thermalization process based on the magnon-phonon interaction, which, unfortunately, does not give insight into the microscopic interactions governing the magnon dynamics. Therefore, it is not quite clear which processes are really responsible for the thermalization and the damping of the magnons.

In conclusion, there is still missing a quantitative theoretical description of the magnon thermalization process which provides the motivation of this work. The present thesis is organized as follows.

In Chap. 2, we introduce the microscopic model which we employ in order to describe the magnon dynamics as well as the BEC of magnons. We derive the main interactions between magnons based on an effective magnon Hamiltonian in YIG and we furthermore introduce the kinetic theory which we employ in order to describe the time evolution of the magnetic system.

In Chap. 3, we individually discuss the properties of the various magnon interactions in order to give an overview and better understanding of the mechanisms and special attributes which are characteristic for the respective interaction processes. We first discuss the linear properties of the interactions which are given by the respective relaxation rates and we subsequently focus on the equilibration processes caused by the individual magnon interactions.

In Chap. 4, we consider the full model combining all the interaction processes and we investigate in particular the BEC of magnons under distinct conditions. First, we discuss the dynamics of the magnon system, brought out of equilibrium by means of short intense pumping, which then freely evolves and we compare our results with the experiment. The second section is dedicated to the case of continuous pumping, a technique also applied in the seminal work of Demokritov *et al.* [19]. We further address a recent experiment of Serga *et al.* [32], who found unexpected behavior of the condensate at high pumping powers. Finally, we consider the BEC of magnons by cooling the magnetic system which is induced by a quick temperature decrease in the phonon system.

2

Theoretical Model

This chapter thoroughly describes the theoretical model which we have developed in order to calculate the magnon dynamics and the Bose-Einstein condensation of magnons. In the first section we start with the Hamiltonian of the magnetic system, which describes the main interactions between the localized spins in the material yttrium iron garnet (YIG). We further illustrate the transformation into the magnon basis and we discuss the resulting spectrum of non-interacting magnons. Subsequently, we derive the main interactions between the magnons themselves and we introduce the coupling between magnons and phonons. Finally, we derive the parallel pumping Hamiltonian, resulting from a time-dependent magnetic field, which is important to describe the creation of non-equilibrium magnons. The second section is dedicated to the Boltzmann equation which we employ in order to describe the time evolution of the magnon system. We first consider the classical Boltzmann equation, which already reveals the basic concepts of a kinetic theory, in order to extend the considerations to the case of a Bose gas. We continue with the derivation of the kinetic equations resulting from the magnon interactions determined in the first section and we introduce the isotropic approximation which is essential for the numerical treatment of the kinetic equations. Afterwards, we discuss the challenging phenomenon of Bose-Einstein condensation described by the Boltzmann equation and we finally reveal an important peculiarity of the four-magnon scattering process, which is responsible for the phase transition to occur.

2.1 Hamiltonian of the Magnetic System

In this section, we present the effective Hamiltonian of the magnetic system in YIG. YIG is a complex ferrimagnetic insulator, exhibiting a cubic lattice structure with eighty atoms in the primitive unit cell of which twenty atoms have a net magnetic moment which accordingly results in twenty magnon branches [46]. Fortunately, at room temperature, only the lowest (acoustic) magnon branch is excited considerably, which in the low energy region exhibits frequencies in the gigahertz-range thus being accessible in experiments [19,23–33,47,48]. For these reasons, it is sufficient to consider only the lowest magnon branch and to describe the physical properties of YIG by means of an effective ferromagnet on a simple cubic lattice, based on the microscopic Heisenberg model [49,50]. The lattice constant amounts to $a_0 = 12.376$ Å [51], and the effective spin follows from the measured saturation magnetization at room temperature $\mu_0 M_\mathrm{S} = 175$ mT [52], which corresponds to an effective total spin [49,50]

$$S = \frac{M_\mathrm{S}\, a_0^3}{g\mu_\mathrm{B}} \approx 14.2, \tag{2.1}$$

where g is the electron g-factor, μ_0 is the permeability of the vacuum and μ_B is the Bohr magneton. The main interactions between the localized spins are the exchange and the magnetic dipole-dipole interactions, whereas the Zeeman energy additionally arises due to the coupling of the spins to an external magnetic field. The resulting Hamiltonian is widely used in the literature [49, 50, 53–61] and reads

$$\hat{\mathcal{H}} = -\frac{1}{\hbar^2}\sum_{ij} J_{ij}\, \hat{\boldsymbol{S}}_i \cdot \hat{\boldsymbol{S}}_j - g\frac{\mu_{\mathrm{B}}}{\hbar}\mu_0 H_0 \sum_i \hat{S}_i^z + \frac{\mu_0\, g^2 \mu_{\mathrm{B}}^2}{8\pi\hbar^2}\sum_{ij}\sum_{\alpha\beta} D_{ij}^{\alpha\beta}\hat{S}_i^{\alpha}\hat{S}_j^{\beta}, \tag{2.2}$$

$$\text{with}\quad D_{ij}^{\alpha\beta} = \frac{\delta_{\alpha\beta} - 3\hat{R}_{ij}^{\alpha}\hat{R}_{ij}^{\beta}}{|\boldsymbol{R}_{ij}|^3}, \quad \{\alpha,\beta\} = \{x,y,z\}$$

$$\text{and}\quad \hat{\boldsymbol{R}}_{ij} = \boldsymbol{R}_{ij}/|\boldsymbol{R}_{ij}| = (\hat{x}_{ij}, \hat{y}_{ij}, \hat{z}_{ij}),$$

where H_0 is the external magnetic field, conventionally oriented in the z-direction, and $\boldsymbol{R}_{ij}$ denotes the position vector connecting two spins which are located at lattice sites i and j, respectively. The sums are running over all sites N of the simple cubic lattice. We exclude the self-energies by setting $J_{ii} = D_{ii}^{\alpha\beta} = 0$. Due to the short range exchange interaction a nearest neighbor approximation is justified, so we set $J_{ij} = J$ for nearest neighbors and $J_{ij} = 0$ otherwise, where $J \approx 33.2$ GHz is the exchange constant, which follows from the exchange stiffness $2JSa_0^2/g\mu_{\mathrm{B}}\mu_0 = 5.17 \times 10^{-9}\,\mathrm{Oe\,cm^2}$ [20].

In the following, we show how the spin Hamiltonian (2.2) is transformed into the corresponding magnon Hamiltonian. This approach is well known in the literature and we refer to Refs. [18, 20, 62–64]. Since the spins are ferromagnetically ordered ($J > 0$), the classical ground state is the state where all the spins are aligned parallel to each other. We therefore apply the Holstein-Primakoff transformation [53]

$$\hat{S}_i^z = \hbar\left(S - \hat{a}_i^{\dagger}\hat{a}_i\right), \tag{2.3a}$$

$$\hat{S}_i^+ = \hbar\sqrt{2S}\sqrt{1 - \frac{\hat{a}_i^{\dagger}\hat{a}_i}{2S}}\;\hat{a}_i, \tag{2.3b}$$

$$\hat{S}_i^- = \hbar\sqrt{2S}\,\hat{a}_i^{\dagger}\sqrt{1 - \frac{\hat{a}_i^{\dagger}\hat{a}_i}{2S}}, \tag{2.3c}$$

which maps the spin operators to Bose operators, where $\hat{a}_i^{\dagger}$ creates and $\hat{a}_i$ annihilates a local spin deviation from the classical ground state. The operators $\hat{a}_i^{\dagger}$ and $\hat{a}_i$ indeed fulfill the fundamental Bose commutation rules

$$\left[\hat{a}_i, \hat{a}_j^{\dagger}\right] = \delta_{ij}, \tag{2.4a}$$

$$\left[\hat{a}_i, \hat{a}_j\right] = \left[\hat{a}_i^{\dagger}, \hat{a}_j^{\dagger}\right] = 0, \tag{2.4b}$$

showing that the spin representation of the Hamiltonian is equivalent to a corresponding Bose representation. In order to take advantage of this transformation, we have to expand the square root of the operators appearing in Eqs. (2.3b) and (2.3c) into a power series

$$\sqrt{1 - \frac{\hat{n}_i}{2S}} = 1 - \frac{\hat{n}_i}{4S} - \frac{\hat{n}_i^2}{32S^2} - \frac{\hat{n}_i^3}{128S^3} - \cdots, \tag{2.5}$$

where $\hat{n}_i = \hat{a}_i^{\dagger}\hat{a}_i$. Since $\hat{n}_i$ and all powers of $\hat{n}_i$ are operators rather than complex scalars as in classical theories [21, 65], it is necessary to bring the series (2.5) into a normal ordered form. Essential for the further derivation is the fact that all powers of $\hat{n}_i$ additionally contribute to the bilinear order. Subsequently applying the relation $\hat{n}_i^2 = \hat{n}_i + (\hat{a}_i^\dagger)^2 \hat{a}_i^2$ yields

$$\sqrt{1 - \frac{\hat{n}_i}{2S}} = 1 - \left(1 - \sqrt{1 - \frac{1}{2S}}\right) \hat{n}_i + \text{h.o.t.} = 1 - \frac{1}{S}\left(\frac{1}{4} + S_0\right) \hat{n}_i + \text{h.o.t.}, \tag{2.6}$$

where we have introduced the quantity

$$S_0 = S\left(1 - \sqrt{1 - \frac{1}{2S}}\right) - \frac{1}{4}, \tag{2.7}$$

which is similar to the corresponding expression defined in chapter 7 of Ref. [18]. Since S_0 only exists because of the consecutive application of the Bose commutator rules of the operators $\hat{a}_i$ and $\hat{a}_i^\dagger$, this term has a purely quantum mechanical origin and hence is missing in every classical spin wave theory. Despite its smallness ($S_0 \approx 0.002$) compared with 1/4 in Eq. (2.6), this term plays an important role in the case of the four-magnon interaction Hamiltonian, as we will show soon. In addition to the Holstein-Primakoff transformation (2.3a)-(2.3c), we further perform a Fourier transformation

$$\hat{a}_i = \frac{1}{\sqrt{N}} \sum_{\boldsymbol{q}} \exp\left(i\boldsymbol{q} \cdot \boldsymbol{R}_i\right) \hat{a}_{\boldsymbol{q}}, \tag{2.8a}$$

$$\hat{a}_i^\dagger = \frac{1}{\sqrt{N}} \sum_{\boldsymbol{q}} \exp\left(-i\boldsymbol{q} \cdot \boldsymbol{R}_i\right) \hat{a}_{\boldsymbol{q}}^\dagger, \tag{2.8b}$$

in order to exploit the translational invariance of the system. Thus, we finally obtain the transformed Hamiltonian

$$\hat{\mathcal{H}} = \hat{\mathcal{H}}_0 + \hat{\mathcal{H}}_2 + \hat{\mathcal{H}}_3 + \hat{\mathcal{H}}_4 + \text{h.o.t.}, \tag{2.9}$$

where the index denotes the number of operators. The zero-order part $\hat{\mathcal{H}}_0$ describes the energy of the classical ground state (if the spins are treated as classical quantities), whereas the bilinear part $\hat{\mathcal{H}}_2$ determines the spectrum of non-interacting magnons, which we discuss subsequently. The higher-order parts including three and four operators yield the most important mutual interactions between the magnons, since the series (2.9) quickly converges at low temperatures, far below the Curie temperature of the material, which for YIG amounts to $T_\mathrm{C} \approx 559$ K [51].

2.1.1 Spectrum of Non-Interacting Magnons

As already mentioned, the bilinear order in the bosonized Hamiltonian determines the spectrum of non-interacting magnons. By neglecting all higher-order parts, this treatment is also known as *harmonic approximation* or *linear spin wave approximation* [18] and the bilinear part explicitly reads

$$\hat{\mathcal{H}}_2 = \sum_{\boldsymbol{q}} \left(A(\boldsymbol{q})\, \hat{a}_{\boldsymbol{q}}^\dagger \hat{a}_{\boldsymbol{q}} + B(\boldsymbol{q})\, \hat{a}_{\boldsymbol{q}} \hat{a}_{-\boldsymbol{q}} + B^*(\boldsymbol{q})\, \hat{a}_{\boldsymbol{q}}^\dagger \hat{a}_{-\boldsymbol{q}}^\dagger\right), \tag{2.10}$$

where the coefficients A and B are given in Appendix A.1.1. As can be seen, the harmonic Hamiltonian is not yet diagonal in the operators $\hat{a}_{\boldsymbol{q}}^\dagger$ and $\hat{a}_{\boldsymbol{q}}$. In order to diagonalize this part, we have to perform the third Holstein-Primakoff transformation [20, 53, 63], also known as *Bogoliubov transformation* [18, 62, 63], which reads

$$\hat{c}_{\boldsymbol{q}} = u(\boldsymbol{q})\, \hat{a}_{\boldsymbol{q}} + v(\boldsymbol{q})\, \hat{a}_{-\boldsymbol{q}}^\dagger, \tag{2.11a}$$

$$\hat{c}_{\boldsymbol{q}}^\dagger = u^*(\boldsymbol{q})\, \hat{a}_{\boldsymbol{q}}^\dagger + v^*(\boldsymbol{q})\, \hat{a}_{-\boldsymbol{q}}, \tag{2.11b}$$

with the Bogoliubov coefficients u and v. These coefficients have to fulfill the conditions

$$|u(\boldsymbol{q})|^2 - |v(\boldsymbol{q})|^2 = 1, \tag{2.12a}$$

$$u(\boldsymbol{q})\, v(-\boldsymbol{q}) = u(-\boldsymbol{q})\, v(\boldsymbol{q}), \tag{2.12b}$$

in order to preserve the Bose commutation rules [18]. In Appendix A.3.1, we show that by means of the coefficients

$$u(\boldsymbol{q}) = \sqrt{\frac{1}{2}\left(\frac{A(\boldsymbol{q})}{\sqrt{A^2(\boldsymbol{q}) - 4|B(\boldsymbol{q})|^2}} + 1\right)} \exp(i\phi_B), \tag{2.13a}$$

$$v(\boldsymbol{q}) = \sqrt{\frac{1}{2}\left(\frac{A(\boldsymbol{q})}{\sqrt{A^2(\boldsymbol{q}) - 4|B(\boldsymbol{q})|^2}} - 1\right)}, \tag{2.13b}$$

where ϕ_B is the phase of the coefficient $B = |B| \exp(i\phi_B)$, the harmonic Hamiltonian becomes diagonal and reads

$$\hat{\mathcal{H}}_2 = G_\mathrm{B} + \sum_{\boldsymbol{q}} \hbar\omega(\boldsymbol{q})\, \hat{c}^\dagger_{\boldsymbol{q}} \hat{c}_{\boldsymbol{q}}, \tag{2.14}$$

where $\hat{c}^\dagger_{\boldsymbol{q}}$ ($\hat{c}_{\boldsymbol{q}}$) creates (annihilates) a magnon with wave vector $\boldsymbol{q}$. G_B is a constant arising from the Bose commutation rules of the magnon operators, which leads to a modification of the classical ground state energy, described by the zero-order part $\hat{\mathcal{H}}_0$. Therefore, the quantum mechanical ground state exhibits zero-point fluctuations being not the state of a fully ordered ferromagnet any more [18]. The magnon bulk dispersion finally reads [64]

$$\hbar\omega(\boldsymbol{q}) = \sqrt{A^2(\boldsymbol{q}) - 4|B(\boldsymbol{q})|^2} \tag{2.15}$$

$$= \begin{cases} \sqrt{(zH_i + zD_x M_\mathrm{S})\,(zH_i + zD_y M_\mathrm{S})} & \text{if } \boldsymbol{q} = 0 \\ \sqrt{(zH_i + 2S\,[\,J(0) - J(\boldsymbol{q})\,])\,(zH_i + 2S\,[\,J(0) - J(\boldsymbol{q})\,] + zM_\mathrm{S}\sin^2(\theta_{\boldsymbol{q}}))} & \text{if } \boldsymbol{q} \neq 0, \end{cases} \tag{2.16}$$

where $z = g\mu_\mathrm{B}\mu_0$, D_x, D_y and D_z are the demagnetization factors of the sample as defined in Eq. (A.5) of Appendix A.2.1, $H_i = H_0 - D_z M_\mathrm{S}$ is the internal field and $\theta_{\boldsymbol{q}}$ is the angle between the wave vector and the applied magnetic field. In the exchange part, we have defined the function

$$J(\boldsymbol{q}) = \frac{1}{N}\sum_{ij} J_{ij}\, \exp\left(i\boldsymbol{q}\cdot\boldsymbol{R}_{ij}\right) = 2J\, \left[\cos(q_x\, a_0) + \cos(q_y\, a_0) + \cos(q_z\, a_0)\right], \tag{2.17}$$

which is valid for the simple cubic lattice. The upper term in the bracket in Eq. (2.16) applies to the uniform mode ($\boldsymbol{q} = 0$), whereas the lower term applies to the $\boldsymbol{q} \neq 0$ modes. Kittel was the first to observe the dependence of the ferromagnetic resonance frequency (FMR) on the shape of the sample [66], therefore the upper relation in the magnon dispersion is also called *Kittel formula*.

We now discuss the magnon dispersion in detail. Without the dipolar contribution, the magnon dispersion reduces to

$$\hbar\omega(\boldsymbol{q}) = g\mu_\mathrm{B}\mu_0 H_0 + 2S\,[J(0) - J(\boldsymbol{q})] \tag{2.18a}$$

$$\approx g\mu_\mathrm{B}\mu_0 H_0 + 2JS(qa_0)^2, \tag{2.18b}$$

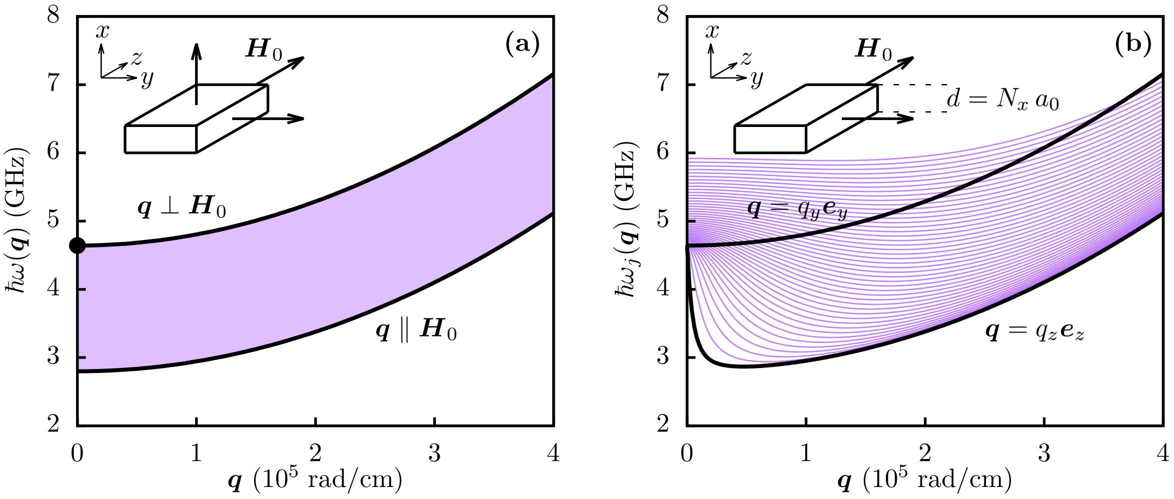

Figure 2.1: Magnon dispersion relations in YIG in the case of the film-geometry for an in-plane magnetic field of $H_0 = 1000\,\mathrm{Oe}$. The arrows in the sketches of both figures illustrate the directions in which the sample is infinitely extended. (a) Bulk dispersion (2.16). The black lines denote the magnon dispersion parallel and perpendicular to the direction of the external magnetic field, respectively, whereas the purple shaded area indicates the continuum of magnon frequencies at intermediate angles $\theta_{\boldsymbol{q}}$ at fixed modulus of the wave vector $\boldsymbol{q}$. The black dot marks the FMR, given by Eq. (2.19). (b) Magnon dispersion for a thin film with the thickness $d = 5$ µm calculated by means of Eq. (2.24). The black lines show the lowest mode ($j = 0$) with the wave vector $\boldsymbol{q}$ oriented in the y- and z-direction, respectively. The purple lines show the subsequent 45 modes ($j = 1 \ldots 45$) with the wave vector $\boldsymbol{q}$ oriented in the z-direction.

where the last relation is valid for small wave vectors, even by considering an arbitrary cubic lattice [18]. As can be seen from Eq. (2.16), the dipolar interaction causes an anisotropy of the form $zM_\mathrm{S}\sin^2(\theta_{\boldsymbol{q}})$ for magnons propagating with an angle $\theta_{\boldsymbol{q}}$ with respect to the direction of the external field. Figure 2.1(a) shows the magnon dispersion for an in-plane magnetized YIG film of infinite extensions with an external magnetic field of $H_0 = 1000\,\mathrm{Oe}$. The demagnetization factors for the given film-geometry are $D_x = 1, D_y = D_z = 0$, so that the dispersion in the direction of the applied magnetic field ($\theta_{\boldsymbol{q}} = 0$) coincides with the exchange dispersion (2.18a). Due to the dipolar anisotropy, the magnon frequency increases with increasing angle $\theta_{\boldsymbol{q}}$ resulting in a continuum of possible frequencies for a given modulus of the wave vector $\boldsymbol{q}$, as indicated by the purple shaded area. It is also apparent that there is a discontinuity in the magnon frequency in the limit $\boldsymbol{q} \to 0$, whereas the FMR depends on the shape of the sample and is determined by the upper term of Eq. (2.16) to be

$$\hbar\omega(\boldsymbol{q} = 0) = g\mu_\mathrm{B}\mu_0 \sqrt{H_0\,(H_0 + M_\mathrm{S})}, \tag{2.19}$$

in the case of an in-plane magnetized film. In order to emphasize this point, we mark the FMR by means of the black dot in Fig. 2.1(a), which shows that the dispersion is steady only for magnons propagating perpendicular to the direction of the applied magnetic field.

By now, we have only discussed the magnon dispersion of samples with infinite extensions. Real samples are of course not infinitely extended, which results in some specific modifications of the bulk dispersion relation (2.16) as we will show now. In experiments in the field of magnon BEC, thin films are commonly used with lateral dimensions in the millimetre and centimetre range but with a thickness of only several micrometres [19, 23–33]. Let us therefore consider a film, which is only infinite in the plane, but which has a finite thickness

$d = N_x\, a_0$, where N_x is the number of layers of which the film is composed. Calculations of the resulting magnon dispersion have already been made in the literature [50, 54–59], for the sake of completeness we yet show how to derive the magnon dispersion in this case. For this purpose, we repeat all the steps beginning with the original spin Hamiltonian (2.2) but we modify the Fourier transformation (2.8a) and (2.8b) due to the absence of translational invariance in the x-direction. We thus perform a partial Fourier transformation in the y- and z-direction and keep the x-direction in real space

$$\hat{a}_i = \frac{1}{\sqrt{N_y N_z}} \sum_{\boldsymbol{q}} \exp\left(i\boldsymbol{q}\cdot\boldsymbol{r}_i\right) \hat{a}_{x_i}(\boldsymbol{q}), \tag{2.20a}$$

$$\hat{a}_i^\dagger = \frac{1}{\sqrt{N_y N_z}} \sum_{\boldsymbol{q}} \exp\left(-i\boldsymbol{q}\cdot\boldsymbol{r}_i\right) \hat{a}_{x_i}^\dagger(\boldsymbol{q}), \tag{2.20b}$$

with the in-plane wave vector $\boldsymbol{q} = (q_y, q_z)$ and $\boldsymbol{r}_i = (y_i, z_i)$, where N_y and N_z are the number of lattice sites in the y- and z-direction, respectively. By keeping only the bilinear order in the operators $\hat{a}_{x_i}^\dagger$ and $\hat{a}_{x_i}$, the transformed Hamiltonian reads

$$\hat{\mathcal{H}}_2 = \sum_{x_i x_j} \sum_{\boldsymbol{q}} \Big(A_{x_i,x_j}(\boldsymbol{q})\, \hat{a}_{x_i}^\dagger(\boldsymbol{q}) \hat{a}_{x_j}(\boldsymbol{q}) + B_{x_i,x_j}(\boldsymbol{q})\, \hat{a}_{x_i}(\boldsymbol{q}) \hat{a}_{x_j}(-\boldsymbol{q}) + B_{x_i,x_j}^*(\boldsymbol{q})\, \hat{a}_{x_i}^\dagger(\boldsymbol{q}) \hat{a}_{x_j}^\dagger(-\boldsymbol{q}) \Big), \tag{2.21}$$

where the coefficients A_{x_i,x_j} and B_{x_i,x_j} are given in Appendix A.1.2. For the sake of simplicity, let the indices i and j now label the layers. We then diagonalize the harmonic Hamiltonian similarly to the bulk case by means of a generalized Bogoliubov transformation

$$\hat{c}_j(\boldsymbol{q}) = \frac{1}{\sqrt{N_x}} \sum_i \Big(u_{j,i}(\boldsymbol{q})\, \hat{a}_i(\boldsymbol{q}) + v_{j,i}(\boldsymbol{q})\, \hat{a}_i^\dagger(-\boldsymbol{q}) \Big), \tag{2.22a}$$

$$\hat{c}_j^\dagger(\boldsymbol{q}) = \frac{1}{\sqrt{N_x}} \sum_i \Big(u_{j,i}^*(\boldsymbol{q})\, \hat{a}_i^\dagger(\boldsymbol{q}) + v_{j,i}^*(\boldsymbol{q})\, \hat{a}_i(-\boldsymbol{q}) \Big), \tag{2.22b}$$

which for one layer ($N_x = 1$) reduces to the ordinary Bogoliubov transformation (2.11a) and (2.11b). Thus, the harmonic Hamiltonian finally takes the form

$$\hat{\mathcal{H}}_2 = G_{\mathrm{B}}^{\mathrm{film}} + \sum_j \sum_{\boldsymbol{q}} \hbar\omega_j(\boldsymbol{q})\, \hat{c}_j^\dagger(\boldsymbol{q}) \hat{c}_j(\boldsymbol{q}), \tag{2.23}$$

where $G_{\mathrm{B}}^{\mathrm{film}}$ again arises due to the Bose commutation rules and modifies the classical ground state energy similarly as in the bulk case. As shown in Appendix A.3.2, the magnon energies $\hbar\omega_j$ follow from the condition

$$\det \begin{pmatrix} \hbar\omega_j(\boldsymbol{q})\, \mathbb{1} - A(\boldsymbol{q}) & -2B(\boldsymbol{q}) \\ 2B(-\boldsymbol{q}) & \hbar\omega_j(\boldsymbol{q})\, \mathbb{1} + A(\boldsymbol{q}) \end{pmatrix} = 0, \tag{2.24}$$

with $\mathbb{1}$ being the $N_x \times N_x$ identity matrix. We solve this eigenvalue problem numerically for $N_x = 4040$, which corresponds to a film-thickness of $d = 5$ µm. The finiteness of the sample has two important consequences. First of all, as also following from the ansatz (2.20a) and (2.20b), it leads to a quantization of the modes in the direction of the film normal. Figure 2.1(b) shows the calculated magnon spectrum with an applied magnetic field of $H_0 = 1000\,\mathrm{Oe}$, where the black lines show the lowest mode in the y- and z-direction, respectively, and the purple lines show the subsequent 45 modes in the z-direction. As it is visible, the dispersion in the y-direction as well as the FMR coincide with the bulk case, whereas the discontinuity in the limit $\boldsymbol{q} \to 0$ vanishes and the magnon spectrum consequently exhibits two degenerate characteristic minima in the direction parallel to the applied magnetic field at nonzero wave vectors, depending on the film-thickness (cf. Ref. [50]). This is a remarkable result regarding Bose-Einstein condensation, which takes place at the minimal energy state of the system, being not the state of zero wave vector in the case of magnons. As can be seen in Fig. 2.1(b), for a film with a thickness of $d = 5$ µm, the minimum is located at about $q_{\mathrm{min}} \approx 0.5 \times 10^5$ rad/cm, thus lying in the wave vector interval accessible for Brillouin light scattering [19]. Noteworthy, Kalinikos and Slavin derived an approximate analytic expression of the dipole-exchange dispersion in the thin film geometry [67].

2.1.2 Magnon-Magnon Interactions

In this subsection, we go beyond the harmonic spin wave approximation treated in the preceding subsection and discuss the inherent interactions between magnons which result from the higher-order parts of the bosonized Hamiltonian (2.9). The most important processes are the three-magnon and four-magnon interactions since processes involving more particles are less probable. In contrast to the thin film-geometry considered for obtaining the correct magnon spectrum, we derive the interaction parts in turn for the simple cubic lattice which is infinitely extended in all three directions for convenience. We start with the three-magnon interaction and subsequently discuss the four-magnon interaction.

Three-Magnon Interaction

The three-magnon interaction Hamiltonian is solely induced by the dipole-dipole interaction of the original Hamiltonian and reads

$$\hat{\mathcal{H}}_3 = \frac{1}{\sqrt{N}} \sum_{\boldsymbol{q}\boldsymbol{q}'} \Big(V_3(\boldsymbol{q}')\, \hat{c}^\dagger_{\boldsymbol{q}} \hat{c}_{\boldsymbol{q}'} \hat{c}_{\boldsymbol{q}-\boldsymbol{q}'} + V_3^*(\boldsymbol{q}')\, \hat{c}^\dagger_{\boldsymbol{q}} \hat{c}^\dagger_{\boldsymbol{q}'} \hat{c}_{\boldsymbol{q}+\boldsymbol{q}'} \Big) \,, \tag{2.25}$$

which generates the elementary processes of splitting of a magnon into two magnons and the reverse process of the confluence of two magnons. Since this interaction obviously does not conserve the total magnon number, it leads to a damping of the magnetic system as we will further illustrate in the subsequent section as well as in Sec. 3.2. The corresponding three-magnon interaction potential reads

$$V_3(\boldsymbol{q}) = -\sqrt{2S}\, \frac{\mu_0\, g^2 \mu_{\mathrm{B}}^2}{4a_0^3}\, \sin(2\theta_{\boldsymbol{q}}) \exp\left(-i\phi_{\boldsymbol{q}}\right) , \tag{2.26}$$

which is derived in Appendix A.1.1, where $\theta_{\boldsymbol{q}}$ and $\phi_{\boldsymbol{q}}$ are the polar and azimuthal angles between the wave vector $\boldsymbol{q}$ and the direction of the applied magnetic field, respectively. As can be seen from Eq. (2.26), the three-magnon interaction is strongly anisotropic and the interaction potential even vanishes for magnons propagating with the polar angles $\theta_{\boldsymbol{q}} \in \{0, \pi/2, \pi\}$. Noteworthy, the same result for the interaction potential has already been obtained by means of a macroscopic treatment of the demagnetizing energy [63, 68, 69], in contrast to our approach based on the microscopic dipole-dipole energy. In the derivation of Eq. (2.26), we have neglected the third Holstein-Primakoff transformation (2.11a) and (2.11b), which in the first instance diagonalizes the bilinear part of the Hamiltonian but which as an ancillary effect also modifies the three-magnon interaction potential. However, this modification is negligible for magnons exhibiting frequencies $\omega \gtrsim g\mu_{\mathrm{B}}\mu_0 M_{\mathrm{S}}/2\hbar$ [70], which can be satisfied by applying sufficiently high magnetic fields. Performing the third Holstein-Primakoff transformation would also result in the appearance of another type of three-magnon interaction having the form $\hat{c}^\dagger_{\boldsymbol{q}}\hat{c}^\dagger_{\boldsymbol{q}'}\hat{c}^\dagger_{\boldsymbol{q}''}$ and $\hat{c}_{\boldsymbol{q}}\hat{c}_{\boldsymbol{q}'}\hat{c}_{\boldsymbol{q}''}$, respectively. However, due to the violation of the energy conservation, these terms do not contribute to the kinetic processes in the first Born approximation, which we employ in order to calculate the magnon dynamics (cf. Sec. 2.2). For these reasons, we keep the three-magnon interaction described by Eqs. (2.25) and (2.26).

Four-Magnon Interaction

In contrast to the three-magnon interaction, the four-magnon interaction is induced by both the dipole-dipole interaction as well as the exchange interaction

$$\hat{\mathcal{H}}_4 = \hat{\mathcal{H}}_4^{\mathrm{ex}} + \hat{\mathcal{H}}_4^{\mathrm{dip}}. \tag{2.27}$$

Since the series (2.9) quickly converges at low temperatures, meaning that processes involving more particles are less important, the three-magnon interaction should be stronger than the four-magnon interaction. However, the three-magnon interaction is induced only by the dipole-dipole interaction, which naturally is much weaker than the exchange interaction. Therefore, the four-magnon interaction induced by the exchange interaction even prevails over the three-magnon interaction in certain situations.

We start with the four-magnon interaction Hamiltonian induced by the exchange interaction

$$\hat{\mathcal{H}}_4^{\mathrm{ex}} = \frac{1}{N}\sum_{\boldsymbol{q}\boldsymbol{q}'\boldsymbol{q}''} V_4^{\mathrm{ex}}(\boldsymbol{q},\boldsymbol{q}'')\; \hat{c}^\dagger_{\boldsymbol{q}}\hat{c}^\dagger_{\boldsymbol{q}'}\hat{c}_{\boldsymbol{q}-\boldsymbol{q}''}\hat{c}_{\boldsymbol{q}'+\boldsymbol{q}''}, \tag{2.28}$$

which generates the elementary process of the scattering of four magnons (2 in, 2 out). In contrast to the three-magnon process, this process apparently conserves the total magnon number and yields the most important mechanism for the internal magnon thermalization which we will illustrate in Sec. 3.2. The four-magnon exchange interaction potential reads

$$V_4^{\mathrm{ex}}(\boldsymbol{q},\boldsymbol{q}'') = -J(\boldsymbol{q}'') + \frac{1}{2}\,(1+4\,S_0)\,\left[\,J(\boldsymbol{q}-\boldsymbol{q}'') + J(\boldsymbol{q})\,\right], \tag{2.29}$$

with the correction term S_0 defined in Eq. (2.7) and $J(\boldsymbol{q})$ defined in Eq. (2.17). For small wave vectors, the interaction potential simplifies to

$$V_4^{\mathrm{ex}}(\boldsymbol{q},\boldsymbol{q}'') \approx J\,a_0^2\left(-\,\boldsymbol{q}^2 + \frac{1}{2}\boldsymbol{q}''^2 + \,\boldsymbol{q}\cdot\boldsymbol{q}''\right) + 4\,S_0\,J\left[6 - a_0^2\left(\boldsymbol{q}^2 + \frac{1}{2}\boldsymbol{q}''^2 -\, \boldsymbol{q}\cdot\boldsymbol{q}''\right)\right]. \tag{2.30}$$

As already mentioned, the quantity S_0 is of purely quantum mechanical origin and in the exchange case even qualitatively modifies the classical four-magnon interaction potential (which follows by setting $S_0 = 0$) by leading to a non-vanishing contribution in the limit of zero wave vectors. It should be noted that this correction term is widely ignored in the literature, despite the fact that quantum descriptions of spin waves are employed. We postpone the discussion of this peculiarity to the next section.

Next, we consider the contribution of the dipole-dipole interaction to the four-magnon interaction Hamiltonian

$$\begin{aligned}\hat{\mathcal{H}}_4^{\mathrm{dip}} = {}& \frac{1}{N}\sum_{\boldsymbol{q}\boldsymbol{q}'\boldsymbol{q}''} V_4^{\mathrm{dip}}(\boldsymbol{q},\boldsymbol{q}'')\; \hat{c}^\dagger_{\boldsymbol{q}}\hat{c}^\dagger_{\boldsymbol{q}'}\hat{c}_{\boldsymbol{q}-\boldsymbol{q}''}\hat{c}_{\boldsymbol{q}'+\boldsymbol{q}''} \\ & + \frac{1}{N}\sum_{\boldsymbol{q}\boldsymbol{q}'\boldsymbol{q}''}\Big(V_{31}(\boldsymbol{q}'')\;\hat{c}^\dagger_{\boldsymbol{q}}\hat{c}_{\boldsymbol{q}'}\hat{c}_{\boldsymbol{q}''}\hat{c}_{\boldsymbol{q}-\boldsymbol{q}'-\boldsymbol{q}''} + V_{31}^*(\boldsymbol{q}'')\;\hat{c}^\dagger_{\boldsymbol{q}}\hat{c}^\dagger_{\boldsymbol{q}'}\hat{c}^\dagger_{\boldsymbol{q}''}\hat{c}_{\boldsymbol{q}+\boldsymbol{q}'+\boldsymbol{q}''}\Big),\end{aligned} \tag{2.31}$$

which in addition to the four-magnon interaction conserving the total magnon number also generates the elementary processes of the splitting of a magnon into three magnons and the reverse process of the confluence of three magnons, respectively. The corresponding dipolar four-magnon interaction potentials read

$$V_4^{\mathrm{dip}}(\boldsymbol{q},\boldsymbol{q}'') = \left(\frac{1}{4}+S_0\right) D(\boldsymbol{q}) + \left(\frac{1}{4}+S_0\right) D(\boldsymbol{q}-\boldsymbol{q}'') + D(\boldsymbol{q}''), \tag{2.32a}$$

$$V_{31}(\boldsymbol{q}) = -\left(\frac{1}{4}+S_0\right) \frac{\mu_0\, g^2 \mu_{\mathrm{B}}^2}{2a_0^3}\, \sin^2(\theta_{\boldsymbol{q}}) \exp\left(-2i\phi_{\boldsymbol{q}}\right), \tag{2.32b}$$

where

$$D(\boldsymbol{q}) = \frac{\mu_0\, g^2 \mu_{\mathrm{B}}^2}{a_0^3} \left(\frac{1}{3} - \frac{1}{2}\sin^2(\theta_{\boldsymbol{q}})\right), \tag{2.33}$$

which are derived in Appendix A.1.1 and where $\theta_{\boldsymbol{q}}$ and $\phi_{\boldsymbol{q}}$ are again the polar and azimuthal angles between the wave vector $\boldsymbol{q}$ and the direction of the applied magnetic field, respectively. The interaction potential in the first interaction in Eq. (2.31) is identical to the symmetrized coefficient given in Refs. [21,46] except for the correction term S_0. In contrast to the exchange case, the dipolar four-magnon interaction naturally exhibits a contribution in the limit of zero wave vectors, so that the quantum mechanical term S_0 only slightly modifies the classical interaction potentials. As already mentioned, the probability of scattering decreases with increasing number of magnons. For this reason, we neglect the second interaction in Eq. (2.31) for describing the magnon dynamics, which would also lead to a damping of the magnetic system as in the case of the three-magnon interaction, but being considerably weaker in most situations. Furthermore, it should also be justified to neglect the first interaction in Eq. (2.31) since this interaction is also induced by the significantly stronger exchange interaction. However, without the correction term S_0, the four-magnon exchange interaction vanishes at small wave vectors in contrast to the dipolar four-magnon interaction. Therefore, we keep this interaction at the moment and discuss its role in the thermalization of the magnetic system in Sec. 4.1. As in the derivation of the three-magnon interaction, we again neglected the third Holstein-Primakoff transformation (2.11a) and (2.11b) in deriving the four-magnon interaction, which again is well justified at sufficiently high magnetic fields. The consideration of the third Holstein-Primakoff transformation would also result in the appearance of another type of four-magnon interaction having the form $\hat{c}^\dagger_{\boldsymbol{q}}\hat{c}^\dagger_{\boldsymbol{q}'}\hat{c}^\dagger_{\boldsymbol{q}''}\hat{c}^\dagger_{\boldsymbol{q}'''}$ and $\hat{c}_{\boldsymbol{q}}\hat{c}_{\boldsymbol{q}'}\hat{c}_{\boldsymbol{q}''}\hat{c}_{\boldsymbol{q}'''}$, respectively. However, these terms also violate the energy conservation and therefore do not contribute to the kinetic processes in the first Born approximation.

2.1.3 Magnon-Phonon Interactions

Until now, we have consistently assumed that the atomic lattice, on which the spins are stacked, is static, so that the distance between two spins is fixed. At room temperature however, where most of the experiments are carried out, lattice vibrations are not negligible anymore and indeed influence the magnetic system. Microscopically, there exist a coupling between the elementary excitations of the magnetic system and the lattice, which gives rise to a magnon-phonon interaction. On the one hand, this interaction can be induced by the spin-orbit interaction [20], which leads to an effective potential of a spin in the presence of phonons, which change the distance between two atoms on the lattice. Due to the associated variation of the Coulomb interaction, the electron clouds consequently change their positions which eventually results in a change of orientation of the electron spin mediated by the spin-orbit interaction. Noteworthy, the magnon-phonon interactions induced by the spin-orbit interaction have recently been studied by means of a phenomenological expression for the magnetoelastic energy [44]. On the other hand, the change of distance between two atoms necessarily results in a modification of the magnetic interaction strength, which is clearly evident in the case of the dipole-dipole energy, which scales as $1/r_{ij}^3$ with the distance r_{ij} between two spins i and j. However, magnon-phonon interactions induced by the weak dipole-dipole interaction are negligible in most cases. Nevertheless, also the exchange coupling constant J depends on the distance between two spins, since the exchange interaction requires a finite overlap of the corresponding electronic wave functions. As a model, we assume an exponential dependence of the exchange constant on the distance between two spins

$$J(r_{ij}) = J\,\exp\left(-\kappa\,\frac{r_{ij}-R_{ij}}{R_{ij}}\right), \tag{2.34}$$

where r_{ij} denotes the actual distance, R_{ij} denotes the distance in equilibrium and κ is a dimensionless constant (see also Ref. [71]). The following derivation is well known in the literature and we refer to Refs. [20, 62, 72, 73]. By considering only small deviations from the equilibrium position, it is convenient to expand the exchange constant with respect to the distance

$$J(r_{ij}) = \sum_{k=0}^{\infty} \frac{1}{k!} \left(\boldsymbol{u}_{ij}\cdot\boldsymbol{\nabla}\right)^k J(r)|_{r=R_{ij}} = J - \frac{\kappa J}{R_{ij}}\,\hat{\boldsymbol{x}}_{ij}\cdot\boldsymbol{u}_{ij} + \ldots, \tag{2.35}$$

where $\hat{\boldsymbol{x}}_{ij}$ is the unit vector connecting two sides of the cubic lattice. $\boldsymbol{u}_{ij}$ denotes the lattice displacement which in turn can be expressed in terms of phonon operators

$$\boldsymbol{u}_i = \frac{1}{\sqrt{N}} \sum_{\boldsymbol{q}\sigma} \sqrt{\frac{\hbar}{2m\omega_\sigma(\boldsymbol{q})}}\,\hat{\boldsymbol{e}}_\sigma(\boldsymbol{q})\,\exp\left(i\boldsymbol{q}\cdot\boldsymbol{R}_i\right)\left(\hat{b}^\dagger_{-\boldsymbol{q}\sigma} + \hat{b}_{\boldsymbol{q}\sigma}\right), \tag{2.36}$$

where $\hat{b}^\dagger_{\boldsymbol{q}\sigma}$ creates and $\hat{b}_{\boldsymbol{q}\sigma}$ annihilates a phonon with wave vector $\boldsymbol{q}$ and polarization σ, respectively, which can be either longitudinal ($\sigma = \|$) or transverse ($\sigma = \perp_1, \perp_2$). $\hat{\boldsymbol{e}}_\sigma$ denotes the polarization vector, $m = \rho a_0^3$ is the mass of the YIG unit cell which follows from the density $\rho = 5.17\ \mathrm{g/cm^3}$ [20] and

$$\omega_\sigma(\boldsymbol{q}) = v_\sigma q, \tag{2.37}$$

is the dispersion relation of acoustic phonons, where v_σ is the velocity of sound in YIG depending on the polarization [20]

$$v_\| = 7.209\ \times 10^5\mathrm{cm/s}, \tag{2.38a}$$

$$v_\perp = 3.843\ \times 10^5\mathrm{cm/s}. \tag{2.38b}$$

By replacing the exchange constant J with $J(r_{ij})$ in the original exchange part of the magnon Hamiltonian (2.2) and by keeping only the bilinear order in the magnon operators and the linear order in the lattice displacement, the magnon-phonon interaction Hamiltonian finally reads

$$\hat{\mathcal{H}}_{\text{m-ph}} = \frac{1}{\sqrt{N}} \sum_{\boldsymbol{q}\boldsymbol{q}'\sigma} V_\sigma(\boldsymbol{q},\boldsymbol{q}')\,\hat{c}^\dagger_{\boldsymbol{q}+\boldsymbol{q}'}\hat{c}_{\boldsymbol{q}}\left(\hat{b}^\dagger_{-\boldsymbol{q}'\sigma} + \hat{b}_{\boldsymbol{q}'\sigma}\right), \tag{2.39}$$

whose elementary processes of phonon absorption or emission by a magnon are also known as *Cherenkov processes* [20], for reasons illustrated in Sec. 3.1. As we will show in the next section and further illustrate in Sec. 3.2, the Cherenkov process leads to an energy transfer between the magnetic system and the lattice. The interaction potential reads

$$V_\sigma(\boldsymbol{q},\boldsymbol{q}') = i\kappa \frac{JS}{a_0}\sqrt{\frac{2\hbar}{m v_\sigma q'}}\hat{\boldsymbol{e}}_\sigma(\boldsymbol{q}')\cdot\frac{1}{N}\sum_{ij}\hat{\boldsymbol{x}}_{ij}\Big[\sin\left((\boldsymbol{q}+\boldsymbol{q}')\cdot\boldsymbol{R}_{ij}\right)-\sin\left(\boldsymbol{q}\cdot\boldsymbol{R}_{ij}\right)-\sin\left(\boldsymbol{q}'\cdot\boldsymbol{R}_{ij}\right)\Big], \tag{2.40}$$

where the summation is over nearest neighbors. For small wave vectors, the interaction potential can be simplified and reads

$$V_\sigma(\boldsymbol{q},\boldsymbol{q}') \approx JSa_0^2\sqrt{\frac{2\hbar}{m v_\sigma}}\, q\, k\sqrt{q'}\,\phi_\sigma(\boldsymbol{q},\boldsymbol{q}'), \tag{2.41}$$

with

$$\phi_\sigma(\boldsymbol{q},\boldsymbol{q}') = -i\kappa\hat{\boldsymbol{e}}_\sigma(\boldsymbol{q}')\cdot\sum_{i=1}^{3}\hat{\boldsymbol{x}}_i\left(\hat{\boldsymbol{q}}\cdot\hat{\boldsymbol{x}}_i\right)\left(\hat{\boldsymbol{q}}'\cdot\hat{\boldsymbol{x}}_i\right)\left(\hat{\boldsymbol{k}}\cdot\hat{\boldsymbol{x}}_i\right), \tag{2.42}$$

where $\boldsymbol{k} = \boldsymbol{q}+\boldsymbol{q}'$ and quantities with a hat are unit vectors. The $\hat{\boldsymbol{x}}_i$ denote the three unit vectors of the lattice coordinate system. By now, we have not yet quantified the constant κ which is indeed difficult to access in experiments. However, as following from Ref. [62], the function ϕ_σ is of the order of unity for small wave vectors which we thus neglect in the following. The interaction potential (2.41) reveals that the magnon-phonon interaction induced by the exchange interaction vanishes at small wave vectors but dominates over the spin-orbit induced process at larger wave vectors $q \gtrsim 10^6$ rad/cm in YIG [20]. Since the inherent magnon-magnon interactions yield the most important contributions in the low energy part of the spectrum, we neglect the spin-orbit induced processes. As in the cases of the magnon-magnon interactions, we yet again did not take into account the third Holstein-Primakoff transformation in the derivation of the magnon-phonon interaction. Apart from energy conservation violating terms, the third Holstein-Primakoff transformation would also result in another type of magnon-phonon interaction having the form $\hat{c}^\dagger_{\boldsymbol{q}}\hat{c}^\dagger_{\boldsymbol{q}'}\hat{b}_{\boldsymbol{q}''\sigma}$ and $\hat{c}_{\boldsymbol{q}}\hat{c}_{\boldsymbol{q}'}\hat{b}^\dagger_{\boldsymbol{q}''\sigma}$, respectively, which indeed conserves the energy. Since the transformation is only relevant at small wave vectors, where the dipolar energy has a large influence, the interaction potential would nevertheless be negligibly small because the original magnon-phonon interaction vanishes at small wave vectors. However, this type of magnon-phonon interaction is relevant in the case of spin-orbit induced interactions [20, 44]. Noteworthy, the dipole-dipole interaction as well as the spin-orbit interaction lead to the appearance of bilinear terms such as $\hat{c}_{\boldsymbol{q}}\hat{b}_{-\boldsymbol{q}\sigma}$ and $\hat{c}^\dagger_{\boldsymbol{q}}\hat{b}_{\boldsymbol{q}\sigma}$ and the corresponding Hermitian conjugates, respectively, which result in a hybridization of magnon and phonon modes to so-called *magnetoelastic modes* in the vicinity of the nominal crossings of the dispersion relations [20, 44, 72].

2.1.4 Parallel Pumping of Magnons

In the foregoing subsections, we have discussed interaction processes between magnons themselves and between magnons and phonons which lead to dynamical processes if the magnetic system is out of equilibrium. Here, we introduce a technique of creating non-equilibrium magnons which is commonly used in experiments in the field of magnon BEC [19, 23–25, 27–30, 32, 33]. An intuitive way of creating magnons is to apply a time-dependent magnetic field either perpendicular or parallel to the static magnetic field [20, 21]. In the perpendicular pump geometry, the time-dependent microwave field with frequency ω_{pump} excites magnons with wave vector $\boldsymbol{q}$ if the resonance condition $\omega(\boldsymbol{q}) = \omega_{\text{pump}}$ is fulfilled. In experiments, this configuration can be achieved by means of a microstrip resonator which is attached to the magnetized sample and which is fed with microwave currents [26]. This technique is also often used to directly excite the uniform mode in ferromagnetic resonance experiments, in which the samples are placed in transmission cavities [47]. In contrast, in the parallel pump geometry which we are considering, the time-dependent microwave field with frequency ω_{pump} is oriented parallel to the static magnetic field resulting in the appearance of an additional contribution in the Zeeman energy

$$\hat{\mathcal{H}}_{\text{pump}}(t) = g\mu_{\text{B}}\mu_0\, h_{\text{pump}}\, \frac{\exp(i\omega_{\text{pump}}t) + \exp(-i\omega_{\text{pump}}t)}{2} \sum_{\boldsymbol{q}} \hat{a}^{\dagger}_{\boldsymbol{q}}\hat{a}_{\boldsymbol{q}}, \tag{2.43}$$

where h_{pump} denotes the amplitude of the pumping field. By applying the Bogoliubov transformation and by keeping only those terms which conserve the energy, the parallel pumping Hamiltonian finally reads

$$\hat{\mathcal{H}}_{\text{pump}}(t) = \sum_{\boldsymbol{q}} \Big(V_{\text{pump}}(\boldsymbol{q})\, \exp(i\omega_{\text{pump}}t)\, \hat{c}_{\boldsymbol{q}}\hat{c}_{-\boldsymbol{q}} + V^{*}_{\text{pump}}(\boldsymbol{q})\, \exp(-i\omega_{\text{pump}}t)\, \hat{c}^{\dagger}_{\boldsymbol{q}}\hat{c}^{\dagger}_{-\boldsymbol{q}} \Big), \tag{2.44}$$

with the interaction potential

$$V_{\text{pump}}(\boldsymbol{q}) = \frac{1}{2}\, g\mu_{\text{B}}\mu_0 h_{\text{pump}}\, u^{*}(\boldsymbol{q}) v^{*}(\boldsymbol{q}) = \frac{(g\mu_{\text{B}}\mu_0)^2}{8}\, h_{\text{pump}}\, M_{\text{S}}\, \frac{\sin^2(\theta_{\boldsymbol{q}}) \exp\left(2i\phi_{\boldsymbol{q}}\right)}{\hbar\omega(\boldsymbol{q})}, \tag{2.45}$$

where we have used the relation $u(\boldsymbol{q})\, v(\boldsymbol{q}) = B(\boldsymbol{q})/\hbar\omega(\boldsymbol{q})$. The discrepancy of a factor of two from the interaction potential given in Ref. [21] results from the different definition of the time-dependent magnetic field. As following from the parallel pumping Hamiltonian (2.44), the microwave field excites pairs of magnons with opposite wave vectors $\boldsymbol{q}$ and $-\boldsymbol{q}$ but with equal frequencies which in resonance obey $\omega(\pm\boldsymbol{q}) = \omega_{\text{pump}}/2$, that is half the pump frequency. This is directly evident in a semiclassical picture, in which the spins precess about the applied magnetic field. As can be seen from Eq. (2.45), the interaction potential is proportional to $B(\boldsymbol{q})$, which only emerges due to the dipole-dipole interaction. The dipolar interaction, as a necessary precondition for the parallel pumping Hamiltonian to exist, also leads to an elliptical precession of the spins rather than a circular precession as in the case of pure exchange interaction [20]. Since the length of the spin vector remains constant during the precession, the longitudinal component of the spin vector is not fixed and varies with twice the precession frequency. Therefore, the parallel pumping field having twice the precession frequency just excites this longitudinal mode. The ellipticity of the precession is strongest for magnons propagating perpendicular to the applied magnetic field, which is also reflected by the interaction potential (2.45). Thus, in a parallel pumping experiment, these so-called $\pi/2$-*magnons* [69] are the first to become unstable which is indeed the case in the famous Kasuya-LeCraw experiment [48] which we discuss in Sec. 3.1 of the subsequent chapter.

2.2 Time Evolution of the Magnon Gas: Boltzmann Equation

In the preceding section, we have derived the harmonic magnon Hamiltonian, as well as the various interaction Hamiltonian, which describe a weakly interacting gas of magnons. In this section, we further introduce the kinetic theory we employ in order to determine the time evolution of the magnetic system. The following remarks are based on the textbooks of Balescu [74] and Van Vliet [75]. According to Balescu, a kinetic equation is "*a closed, nonlinear equation describing the time evolution and the approach to equilibrium of the one-particle reduced distribution function*". Before we turn to the case of a Bose gas, we briefly consider the case of an interacting classical gas, for which Boltzmann in 1872 derived his famous equation, thus called the *Boltzmann equation*, revealing the basic concepts of a kinetic theory and, by the way, being the first kinetic equation in the history of statistical mechanics. Let $f(\boldsymbol{r},\boldsymbol{v},t)$ be the particle density at position $\boldsymbol{r}$ and velocity $\boldsymbol{v}$, then the time evolution of the distribution function in the absence of forces is given by

$$\begin{aligned}\frac{\partial}{\partial t}f(\boldsymbol{r},\boldsymbol{v},t)+\boldsymbol{v}\cdot\boldsymbol{\nabla}_{\boldsymbol{r}}f(\boldsymbol{r},\boldsymbol{v},t)=\iint \mathrm{d}^3v_2\,\mathrm{d}\Omega_{\boldsymbol{u}'}\,\sigma(\Omega_{\boldsymbol{u}'})\,u'\Big[&f(\boldsymbol{r},\boldsymbol{v}',t)f(\boldsymbol{r},\boldsymbol{v}_2',t)\\ &-f(\boldsymbol{r},\boldsymbol{v},t)f(\boldsymbol{r},\boldsymbol{v}_2,t)\Big],\end{aligned}\tag{2.46}$$

where the second term on the left-hand side describes the streaming of particles in the $(\boldsymbol{v},\boldsymbol{r})$-space and the right-hand side describes collisions between two particles, where $\sigma(\Omega_{\boldsymbol{u}'})$ is the differential cross section and $\boldsymbol{u}'=\boldsymbol{v}'-\boldsymbol{v}_2'$ is the relative velocity in the center-of-mass system of the two colliding particles after the collision. Note that the respective velocities $\boldsymbol{v}'$ and $\boldsymbol{v}_2'$ are uniquely determined with the aid of the energy and momentum conservation laws of the scattering. The collision term thus describes a balance of particles entering the velocity space at $\boldsymbol{v}$, that is $(\boldsymbol{v}',\boldsymbol{v}_2')\to(\boldsymbol{v},\boldsymbol{v}_2)$, and the reversed process of leaving it $(\boldsymbol{v},\boldsymbol{v}_2)\to(\boldsymbol{v}',\boldsymbol{v}_2')$, whose probabilities are multiplied by the respective densities of colliding particles.

Considering the properties of the Boltzmann equation, we recognize that for a spatially homogenous gas the equilibrium state is the Maxwell distribution

$$f(\boldsymbol{v})=\frac{N}{V}\left(\frac{m}{2\pi k_{\mathrm{B}}T}\right)^{3/2}\exp\left(-\frac{m}{2k_{\mathrm{B}}T}v^2\right),\tag{2.47}$$

where N is the total amount of particles and V is the volume of the gas. The merit of Boltzmann was to show that the collisions between the particles lead to an irreversible approach to equilibrium. For this purpose, he defined the function

$$\mathrm{H}(t)=\iint \mathrm{d}^3r\mathrm{d}^3v f(\boldsymbol{r},\boldsymbol{v},t)\log f(\boldsymbol{r},\boldsymbol{v},t),\tag{2.48}$$

which he showed to decrease monotonically during the time evolution, induced by the kinetic equation (2.46). The result

$$\frac{\mathrm{d}}{\mathrm{d}t}\mathrm{H}(t)\leq 0\tag{2.49}$$

is the celebrated *Boltzmann's* H-*theorem*, which indicates that the Boltzmann equation violates the time-reversal invariance of the basic microscopic equations and leads to an irreversible evolution to equilibrium (equal sign in Eq. (2.49)). As a consequence of Boltzmann's H-theorem, the equilibrium state is achieved when the function H(t) reaches its minimal value, which thus follows by inserting the Maxwell distribution (2.47) into the definition (2.48). H then becomes

$$-k_{\mathrm{B}}\mathrm{H}=S+k_{\mathrm{B}}N\log\left(\frac{h^3}{em^3}\right),\tag{2.50}$$

where

$$S=k_{\mathrm{B}}N\log\left(\frac{V}{N}\left(\frac{2\pi mk_{\mathrm{B}}T}{h^2}\right)^{3/2}\exp\left(5/2\right)\right)\tag{2.51}$$

is the entropy of a mono-atomic ideal gas, also known as the *Sackur-Tetrode equation.* So except for the constant in Eq. (2.50) ensuring the correct dimensionality of $\mathrm{H}(t)$, $-k_\mathrm{B}\mathrm{H}$ is for the equilibrium distribution just the entropy of the ideal gas. In accordance with the second law of thermodynamics, the function $-k_\mathrm{B}\mathrm{H}(t)$ has the correct behavior out of equilibrium and reduces to the equilibrium entropy deduced from the canonical ensemble. Therefore, Boltzmann's H-theorem generalizes the entropy to non-equilibrium situations and permits for the definition of a *non-equilibrium entropy.*

The problem of how irreversibility enters the kinetic equation (2.46) though its original derivation is based on reversible Newtonian mechanics is a fundamental one and has been the basis for a lot of controversies about the validity of the H-theorem. The solution to this paradox is the fact that a probabilistic argument enters the equation (2.46), which deviates from the laws of mechanics. Formally, the time evolution of the many-body system is given by the Liouville equation, which in the absence of interactions between the particles yields Eq. (2.46) without the collision term on the right-hand side. However, assuming that the particles interact via a two-body interaction, the equation for the the single-particle distribution is not closed anymore and depends on the two-particle distribution, which in turn depends on the three-particle distribution and so forth. Therefore, one obtains an infinite hierarchy of equations, also known as the *BBGKY-hierarchy* which is named for its respective developers (Bogoliubov, Born, Green, Kirkwood and Yvon). This hierarchy is only manageable if truncated at a certain level which can be achieved by factorizing the n-particle distribution which results, as a consequence, in the neglect of n-particle correlations. In order to consider collisions between the particles, the hierarchy has to be truncated at least at the equation for the two-particle distribution so that three-particle correlations are neglected. However, in his original derivation, Boltzmann heuristically set up the right-hand side of Eq. (2.46), which thus has been called *Boltzmann's Stoßzahlansatz.* In conclusion, the neglect of correlations apparently breaks the time-reversal symmetry and leads to an irreversible evolution of the system. A deeper analysis to this problem can be found in Ref. [74].

2.2.1 Kinetic Equations for Magnons

In the case of magnons, however, we are dealing with a weakly interacting Bose gas rather than a gas of classical particles. We now show that it is possible to derive a quantum analog to the classical Boltzmann equation, which exhibits similar (kinetic) properties and furthermore even captures the challenging phenomenon of Bose-Einstein condensation. The dynamical variable in this case is the single-particle density matrix [76]

$$f(\boldsymbol{q}) = \mathrm{Tr}\,\hat{\rho}\,\hat{n}(\boldsymbol{q}) = \sum_i p_i \, \langle\phi_i|\hat{c}^\dagger_{\boldsymbol{q}}\hat{c}_{\boldsymbol{q}}|\phi_i\rangle = \sum_i p_i n_i(\boldsymbol{q}), \tag{2.52}$$

which is determined by the density operator $\hat{\rho}$ of the system. In this case, the function $f(\boldsymbol{q})$ is a number rather than a density in the classical case. From now on, we refer to the function $f(\boldsymbol{q})$ as the *single-particle distribution* or simply the *distribution.* Since we are considering bosons, we are working in the Fock space and in the spatially homogenous case, which we are considering, the Fock states are solely characterized by the crystal momentum $\boldsymbol{q}$. The set of Fock states $\{|\phi_i\rangle\}$ build an eigenbasis of the harmonic magnon Hamiltonian

$$\hat{\mathcal{H}}_2 = \sum_{\boldsymbol{q}} \hbar\omega(\boldsymbol{q})\, \hat{c}^\dagger_{\boldsymbol{q}}\hat{c}_{\boldsymbol{q}}, \tag{2.53}$$

which describes the ideal magnon gas, discussed in the preceding section. The various interaction terms $\hat{\mathcal{H}}_{\text{int}}$ now lead to transitions between an initial state $|i\rangle$ to a final state $|f\rangle$, and the transition rates are following from Fermi's golden rule [77]

$$W_{i\to f} = \frac{2\pi}{\hbar}\delta(E_f - E_i)\,|\,\langle f|\hat{\mathcal{H}}_{\text{int}}|i\rangle\,|^2, \tag{2.54}$$

where the delta distribution ensures the energy conservation. We first consider the four-magnon interaction, which reads

$$\hat{\mathcal{H}}_4 = \frac{1}{N}\sum_{\boldsymbol{q}\boldsymbol{q}'\boldsymbol{q}''} V_4(\boldsymbol{q},\boldsymbol{q}'')\;\hat{c}^\dagger_{\boldsymbol{q}}\hat{c}^\dagger_{\boldsymbol{q}'}\hat{c}_{\boldsymbol{q}-\boldsymbol{q}''}\hat{c}_{\boldsymbol{q}'+\boldsymbol{q}''}. \tag{2.55}$$

The time evolution of the distribution function $f(\boldsymbol{q}_0)$ follows by the balance of all possible scattering processes increasing the occupation of the state with wave vector $\boldsymbol{q}_0$ and the scattering processes which decrease it [75]. We therefore obtain

$$\frac{\mathrm{d}}{\mathrm{d}t}f(\boldsymbol{q}_0) = \frac{2\pi}{\hbar}\frac{1}{2}\sum_{\boldsymbol{q}_1\boldsymbol{q}_2\boldsymbol{q}_3}\Big(S^+_{\boldsymbol{q}_0}(\boldsymbol{q}_1,\boldsymbol{q}_2,\boldsymbol{q}_3) - S^-_{\boldsymbol{q}_0}(\boldsymbol{q}_1,\boldsymbol{q}_2,\boldsymbol{q}_3)\Big)\,\delta(\hbar\omega(\boldsymbol{q}_0)+\hbar\omega(\boldsymbol{q}_1)-\hbar\omega(\boldsymbol{q}_2)-\hbar\omega(\boldsymbol{q}_3)), \tag{2.56}$$

where the prefactor 1/2 avoids double counting. The respective gain (+) and loss (−) terms read

$$\begin{aligned} S^\pm_{\boldsymbol{q}_0}(\boldsymbol{q}_1,\boldsymbol{q}_2,\boldsymbol{q}_3) &= \sum_i p_i\,|\,\langle f_i^\pm|\hat{\mathcal{H}}_4|\phi_i\rangle\,|^2 \\ &= \frac{1}{N^2}\,\delta_{\boldsymbol{q}_0+\boldsymbol{q}_1,\boldsymbol{q}_2+\boldsymbol{q}_3}|A_4(\boldsymbol{q}_0,\boldsymbol{q}_1,\boldsymbol{q}_2,\boldsymbol{q}_3)|^2 \\ &\times\sum_i p_i\begin{cases} n_i(\boldsymbol{q}_2)n_i(\boldsymbol{q}_3)\,(1+n_i(\boldsymbol{q}_0))\,(1+n_i(\boldsymbol{q}_1)) \\ n_i(\boldsymbol{q}_0)n_i(\boldsymbol{q}_1)\,(1+n_i(\boldsymbol{q}_2))\,(1+n_i(\boldsymbol{q}_3)) \end{cases} \\ &= \frac{1}{N^2}\,\delta_{\boldsymbol{q}_0+\boldsymbol{q}_1,\boldsymbol{q}_2+\boldsymbol{q}_3}|A_4(\boldsymbol{q}_0,\boldsymbol{q}_1,\boldsymbol{q}_2,\boldsymbol{q}_3)|^2 \\ &\times\begin{cases} f_2(\boldsymbol{q}_2,\boldsymbol{q}_3)+f_3(\boldsymbol{q}_2,\boldsymbol{q}_3,\boldsymbol{q}_0)+f_3(\boldsymbol{q}_2,\boldsymbol{q}_3,\boldsymbol{q}_1)+f_4(\boldsymbol{q}_2,\boldsymbol{q}_3,\boldsymbol{q}_0,\boldsymbol{q}_1) \\ f_2(\boldsymbol{q}_0,\boldsymbol{q}_1)+f_3(\boldsymbol{q}_0,\boldsymbol{q}_1,\boldsymbol{q}_2)+f_3(\boldsymbol{q}_0,\boldsymbol{q}_1,\boldsymbol{q}_3)+f_4(\boldsymbol{q}_0,\boldsymbol{q}_1,\boldsymbol{q}_2,\boldsymbol{q}_3), \end{cases} \end{aligned} \tag{2.57}$$

where $|f_i^+\rangle$ ($|f_i^-\rangle$) exhibits one magnon more (less) in the respective states with wave vector $\boldsymbol{q}_0$ and $\boldsymbol{q}_1$ than the state $|\phi_i\rangle$. The f_n are higher-order distribution functions where the index n denotes the number of magnons. Note that the Kronecker delta in Eq. (2.57) leads to the conservation of momentum. Since the quantity A_4 is proportional to the ordinary scattering amplitude in scattering theory [78], we call A_4 the *scattering amplitude* which in the first Born approximation reads

$$A_4(\boldsymbol{q}_0,\boldsymbol{q}_1,\boldsymbol{q}_2,\boldsymbol{q}_3) = V_4(\boldsymbol{q}_3,\boldsymbol{q}_0-\boldsymbol{q}_2)+V_4(\boldsymbol{q}_2,\boldsymbol{q}_0-\boldsymbol{q}_3)+V_4(\boldsymbol{q}_3,\boldsymbol{q}_1-\boldsymbol{q}_2)+V_4(\boldsymbol{q}_2,\boldsymbol{q}_1-\boldsymbol{q}_3). \tag{2.58}$$

In deriving Eq. (2.57), we have already exploited the micro-reversibility property of the scattering amplitude

$$A_4(\boldsymbol{q}_0,\boldsymbol{q}_1,\boldsymbol{q}_2,\boldsymbol{q}_3) = A_4(\boldsymbol{q}_2,\boldsymbol{q}_3,\boldsymbol{q}_0,\boldsymbol{q}_1), \tag{2.59}$$

which implies that each microscopic scattering process is reversible [75]. The problem remains obtaining a closed equation for the single-particle distribution function since the gain and loss terms in Eq. (2.57) involve higher-order distribution functions. We therefore neglect higher-order correlations between the particles, in analogy to the derivation of the classical Boltzmann equation (2.46), and we thus factorize the distribution functions according to the truncation rule

$$f_2(\boldsymbol{q}_0, \boldsymbol{q}_1) \to f(\boldsymbol{q}_0) f(\boldsymbol{q}_1). \tag{2.60}$$

The three- and four-magnon distribution functions are factorized analogously. By taking the thermodynamic limit, we can replace the sums by integrals

$$\frac{1}{N}\sum_{\boldsymbol{q}} \to \frac{a_0^3}{2\pi}\int \mathrm{d}^3 q, \tag{2.61}$$

and we finally obtain a closed equation for the single-particle distribution function

$$\begin{aligned} \frac{\mathrm{d}}{\mathrm{d}t} f(\boldsymbol{q}_0) = \frac{2\pi}{\hbar}\frac{a_0^6}{(2\,\pi)^6}\frac{1}{2}\iiint \mathrm{d}^3q_1 \mathrm{d}^3q_2 \mathrm{d}^3q_3 \Big[&\delta(\hbar\omega(\boldsymbol{q}_0) + \hbar\omega(\boldsymbol{q}_1) - \hbar\omega(\boldsymbol{q}_2) - \hbar\omega(\boldsymbol{q}_3)) \\ &\times \delta(\boldsymbol{q}_0 + \boldsymbol{q}_1 - \boldsymbol{q}_2 - \boldsymbol{q}_3)\, |A_4(\boldsymbol{q}_0, \boldsymbol{q}_1, \boldsymbol{q}_2, \boldsymbol{q}_3)|^2 \\ \times \Big(f(\boldsymbol{q}_2) f(\boldsymbol{q}_3)\,(1 + f(\boldsymbol{q}_0))\,(1 + f(\boldsymbol{q}_1)) - f(\boldsymbol{q}_0) f(\boldsymbol{q}_1)\,&(1 + f(\boldsymbol{q}_2))\,(1 + f(\boldsymbol{q}_3)) \Big) \Big]. \end{aligned} \tag{2.62}$$

Equation (2.62) is the Boltzmann kinetic equation for a gas of bosons which is also known as the *Uehling-Uhlenbeck equation* [74, 76] and which by some authors is variously called a *quantum Boltzmann equation* [79]. Figure 2.2(a) illustrates the corresponding scattering processes. In contrast to the Boltzmann equation for a classical gas, in which the scattering rate is proportional only to the density of colliding particles, the scattering probability in the case of the Boltzmann equation for a Bose gas is also enhanced if the final states are occupied. This is a quantum statistical effect which ensures the equilibrium state to be a Bose-Einstein distribution, as we will show soon. Besides, due to the cubic terms in the distribution function (the quartic terms cancel each other), the kinetic equation for the Bose gas is more highly nonlinear than its classical counterpart. Noteworthy, the Boltzmann equation for a gas of fermions simply follows by replacing the plus signs in the distribution factors by minus signs, which ensures the scattering to be prohibited if the final states are already occupied, which is clearly a manifestation of the Pauli exclusion principle [74]. Since the wave vector of a magnon is only unique up to a reciprocal lattice vector, the integrations in Eq. (2.62) are done over the first Brillouin zone, respectively.

Analogously, it is possible to obtain a kinetic equation resulting from the three-magnon interaction (2.25) which reads

$$\begin{aligned} \frac{\mathrm{d}}{\mathrm{d}t} f(\boldsymbol{q}_0) = \frac{2\pi}{\hbar}\frac{a_0^3}{(2\pi)^3}\frac{1}{2}\iint \mathrm{d}^3q_1 \mathrm{d}^3q_2 \Big[&|V_3(\boldsymbol{q}_1) + V_3(\boldsymbol{q}_2)|^2\, \delta(\hbar\omega(\boldsymbol{q}_0) - \hbar\omega(\boldsymbol{q}_1) - \hbar\omega(\boldsymbol{q}_2)) \\ \times \delta(\boldsymbol{q}_0 - \boldsymbol{q}_1 - \boldsymbol{q}_2) \Big(f(\boldsymbol{q}_1) f(\boldsymbol{q}_2)\,&(1 + f(\boldsymbol{q}_0)) - f(\boldsymbol{q}_0)\,(1 + f(\boldsymbol{q}_1))\,(1 + f(\boldsymbol{q}_2)) \Big) \Big] \\ + \frac{2\pi}{\hbar}\frac{a_0^3}{(2\pi)^3}\iint \mathrm{d}^3q_1 \mathrm{d}^3q_2 \Big[&|V_3(\boldsymbol{q}_0) + V_3(\boldsymbol{q}_1)|^2\, \delta(\hbar\omega(\boldsymbol{q}_0) + \hbar\omega(\boldsymbol{q}_1) - \hbar\omega(\boldsymbol{q}_2)) \\ \times \delta(\boldsymbol{q}_0 + \boldsymbol{q}_1 - \boldsymbol{q}_2) \Big(f(\boldsymbol{q}_2)\,(1 + f(\boldsymbol{q}_0))\,&(1 + f(\boldsymbol{q}_1)) - f(\boldsymbol{q}_0) f(\boldsymbol{q}_1)\,(1 + f(\boldsymbol{q}_2)) \Big) \Big], \end{aligned} \tag{2.63}$$

where the first term is the three-magnon splitting process and the second term is the three-magnon confluence process [20, 62]. The corresponding scattering processes are illustrated in

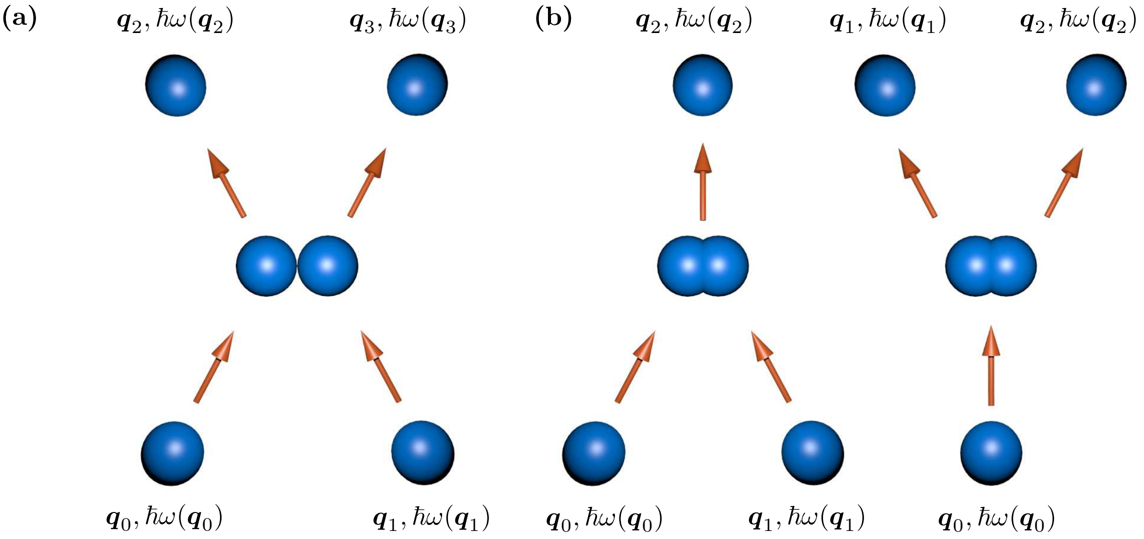

Figure 2.2: Schematic illustration of the scattering processes. The blue spheres represent the colliding magnons with the respective momenta and energies, as indicated. The reversed processes follow by considering the diagrams from the top to the bottom. (a) Four-magnon scattering (2.62). (b) Three-magnon scattering (2.63). The left diagram shows the confluence process whereas the right diagram shows the splitting process.

Fig. 2.2(b). The three-magnon kinetic equation has no classical counterpart since it violates the particle number conservation, which is an inherent property of magnons being quasiparticles. The three-magnon process is therefore the main cause of magnon damping, which we particularly address in the subsequent chapter.

In the case of the parallel pumping of magnons (2.44), which is a technique for the creation of non-equilibrium magnons, we employ Fermi's golden rule for harmonic perturbations [77] in order to obtain the time evolution of the distribution function, which thus reads

$$\frac{\mathrm{d}}{\mathrm{d}t} f(\boldsymbol{q}_0) = \frac{8\pi}{\hbar} \left|V_{\text{pump}}(\boldsymbol{q}_0)\right|^2 \delta(2\hbar\omega(\boldsymbol{q}_0) - \hbar\omega_{\text{pump}}) \left(1 + f(\boldsymbol{q}_0) + f(-\boldsymbol{q}_0)\right). \tag{2.64}$$

This equation just reflects the fact that the microwave photon of energy $\hbar\omega_{\text{pump}}$ splits into two magnons having opposite wave vectors and half the energy of the photon. As it is apparent from Eq. (2.64), the pumping leads to an exponential increase of the magnon number, revealing that the parallel pumping process indeed leads to a spin wave instability [20]. However, as we show in Sec. 4.2, the exponential increase does not remain unlimited since nonlinear magnon-magnon interactions provide an inherent damping mechanism of the pumped magnons. In addition, the instability only occurs above a certain pumping threshold determined by the linear relaxation rates of the magnon interactions which we discuss in Sec. 3.1.

System-Bath Approach

In the case of the magnon-phonon interaction, the magnetic system is coupled to the lattice and the global Hamiltonian takes the form

$$\hat{\mathcal{H}} = \sum_{\boldsymbol{q}} \hbar\omega(\boldsymbol{q})\, \hat{c}^\dagger_{\boldsymbol{q}} \hat{c}_{\boldsymbol{q}} + \sum_{\boldsymbol{q}\sigma} \hbar\omega_\sigma(\boldsymbol{q})\, \hat{b}^\dagger_{\boldsymbol{q}\sigma} \hat{b}_{\boldsymbol{q}\sigma} + \frac{1}{\sqrt{N}} \sum_{\boldsymbol{q}\boldsymbol{q}'\sigma} V_\sigma(\boldsymbol{q}, \boldsymbol{q}')\, \hat{c}^\dagger_{\boldsymbol{q}+\boldsymbol{q}'} \hat{c}_{\boldsymbol{q}} \left(\hat{b}^\dagger_{-\boldsymbol{q}'\sigma} + \hat{b}_{\boldsymbol{q}'\sigma}\right), \tag{2.65}$$

where the first term describes the evolution of free magnons, the second term describes the phonon system and the third term describes the interaction between the two subsystems,

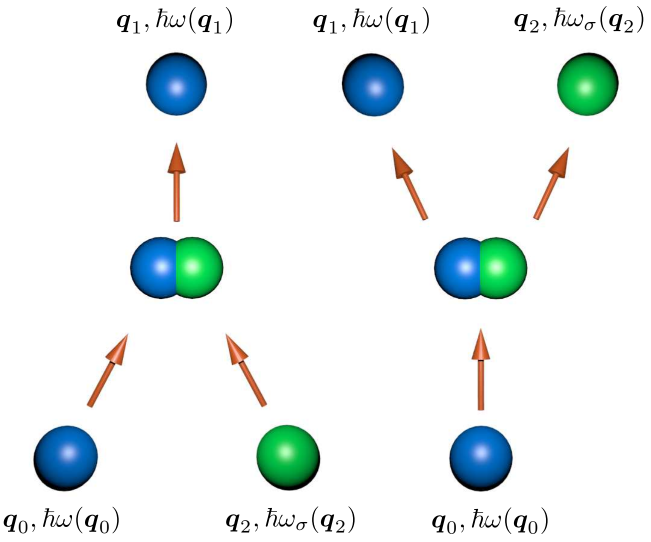

Figure 2.3: Schematic illustration of the magnon-phonon Cherenkov processes (2.66). The blue spheres represent the magnons whereas the green spheres represent the phonons with the respective momenta and energies, as indicated. The left diagram shows the Cherenkov confluence process whereas the right diagram shows the Cherenkov splitting process. The reversed processes follow by considering the diagrams from the top to the bottom.

derived in the previous section. The Hamiltonian (2.65) thus describes the dynamics of the magnetic system under the influence of the phonon system which is also known as *system-bath approach* in quantum dissipative systems [80]. We additionally derive a kinetic equation for the magnon distribution where in this case also the phonon distributions f_σ, depending on the polarization σ, enter the kinetic equation which reads

$$\begin{aligned}\frac{\mathrm{d}}{\mathrm{d}t} f(\boldsymbol{q}_0) = {} & \frac{2\pi}{\hbar}\frac{a_0^3}{(2\pi)^3}\sum_\sigma \iint \mathrm{d}^3 q_1 \mathrm{d}^3 q_2 \Big[|V_\sigma(\boldsymbol{q}_1, \boldsymbol{q}_2)|^2 \, \delta(\hbar\omega(\boldsymbol{q}_0) - \hbar\omega(\boldsymbol{q}_1) - \hbar\omega_\sigma(\boldsymbol{q}_2)) \\ & \times \delta(\boldsymbol{q}_0 - \boldsymbol{q}_1 - \boldsymbol{q}_2) \Big(f(\boldsymbol{q}_1) f_\sigma(\boldsymbol{q}_2) \left(1 + f(\boldsymbol{q}_0)\right) - f(\boldsymbol{q}_0) \left(1 + f(\boldsymbol{q}_1)\right) \left(1 + f_\sigma(\boldsymbol{q}_2)\right) \Big) \Big] \\ & + \frac{2\pi}{\hbar}\frac{a_0^3}{(2\pi)^3}\sum_\sigma \iint \mathrm{d}^3 q_1 \mathrm{d}^3 q_2 \Big[|V_\sigma(\boldsymbol{q}_0, \boldsymbol{q}_2)|^2 \, \delta(\hbar\omega(\boldsymbol{q}_0) + \hbar\omega_\sigma(\boldsymbol{q}_2) - \hbar\omega(\boldsymbol{q}_1)) \\ & \times \delta(\boldsymbol{q}_0 + \boldsymbol{q}_2 - \boldsymbol{q}_1) \Big(f(\boldsymbol{q}_1) \left(1 + f(\boldsymbol{q}_0)\right) \left(1 + f_\sigma(\boldsymbol{q}_2)\right) - f(\boldsymbol{q}_0) f_\sigma(\boldsymbol{q}_2) \left(1 + f(\boldsymbol{q}_1)\right) \Big) \Big],\end{aligned} \tag{2.66}$$

where the first term is the Cherenkov splitting process and the second term is the Cherenkov confluence process [20, 62]. Figure 2.3 illustrates the corresponding scattering processes. In principle, one could also derive kinetic equations describing the time evolution of the phonon distribution, however, we assume the phonons to be in thermal equilibrium for all time, which is the Planck distribution

$$f_\sigma(\boldsymbol{q}) = \frac{1}{\exp\left(\frac{\hbar\omega_\sigma(\boldsymbol{q})}{k_\mathrm{B} T_\mathrm{ph}}\right) - 1}, \tag{2.67}$$

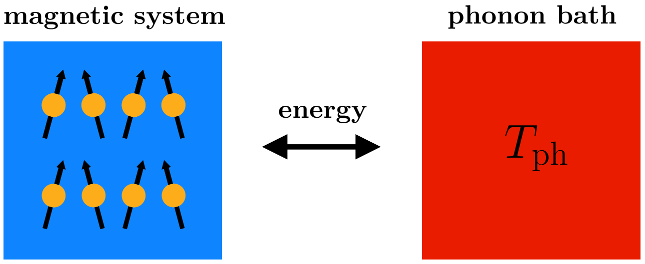

Figure 2.4: Schematic illustration of the system-bath coupling. The arrow indicates the capability of energy transfer between the magnetic system and the lattice which exhibits the fixed temperature T_ph.

where T_{ph} is the fixed lattice temperature. As we have already mentioned in the preceding section, the Cherenkov process allows for an energy transfer between the magnetic system and the lattice, as depicted in Fig. 2.4, which follows from the subsequent discussion.

2.2.2 Physical Properties

In this subsection, we discuss the physical properties of the three kinetic equations (2.62), (2.63) and (2.66), which are in particular the conserved quantities, which in the case of the Boltzmann equation are also called *collisional invariants* [74], as well as the individual equilibrium states. In order to derive the latter, we employ modified versions of the original H-theorem and define the non-equilibrium entropy in the closed magnon system as well as the non-equilibrium free energy in the open magnon system, which are introduced subsequently.

Collisional Invariants

At first, we define the total magnon number N_{tot} and the internal energy of the magnetic system U, which read

$$N_{\mathrm{tot}} = \frac{a_0^3}{(2\,\pi)^3} \int \mathrm{d}^3q\, f(\boldsymbol{q}), \tag{2.68a}$$

$$U = \frac{a_0^3}{(2\,\pi)^3} \int \mathrm{d}^3q\, f(\boldsymbol{q})\, \hbar\omega(\boldsymbol{q}), \tag{2.68b}$$

and which are generally time-dependent due to the dynamic magnon distribution $f(\boldsymbol{q})$. As already noted, the four-magnon Hamiltonian (2.55) describes processes, in which two magnons are annihilated and two magnons are created. By exploiting the micro-reversibility property of the scattering amplitude (2.59), it is easy to show [81, 82] that the corresponding kinetic equation (2.62) conserves both, the total magnon number as well as the internal energy

$$\frac{\mathrm{d}}{\mathrm{d}t} N_{\mathrm{tot}} = 0, \tag{2.69a}$$

$$\frac{\mathrm{d}}{\mathrm{d}t} U = 0, \tag{2.69b}$$

which are thus collisional invariants in the four-magnon process. For the sake of completeness, we have to mention that also the total momentum is a collisional invariant in the four-magnon process. However, since we are solely dealing with distributions exhibiting the symmetry property $f(\boldsymbol{q}) = f(-\boldsymbol{q})$, the total momentum vanishes and does not need to be considered further. In addition, as we have seen, the three-magnon interaction Hamiltonian (2.25) describes processes, in which two magnons either coalesce or one magnon splits into two magnons, respectively. The corresponding kinetic equation (2.63) consequently does not conserve the total magnon number, however, the internal energy is still a collisional invariant, which is reasonable since the three-magnon process is a process in the closed magnetic system. Turning to the magnon-phonon interaction Hamiltonian (2.39), which describes processes of phonon emission or absorption by a magnon, respectively, the associated kinetic equation (2.66) conserves the total magnon number which is thus a collisional invariant in the Cherenkov process. Since this coupling leads to an interaction of the magnetic system with the phonon heat bath, the Cherenkov process allows for an energy transfer between the two systems and hence the conservation of the internal energy is lost, in agreement with Eq. (2.66). In table 2.1, we summarize the collisional invariants of each interaction process.

	four-magnon process	**three-magnon process**	**Cherenkov process**
N_{tot}	conserved	not conserved	conserved
U	conserved	conserved	not conserved

Table 2.1: Collisional invariants of the individual interaction processes.

Equilibrium States

Before we turn to the calculation of the equilibrium state, we first introduce the modified H-theorem for the closed magnetic system in the form

$$\frac{\mathrm{d}}{\mathrm{d}t} S \geq 0, \tag{2.70}$$

where the equal sign is valid in equilibrium. For bosons, it follows that this quantity takes the form

$$S = k_{\mathrm{B}} \frac{a_0^3}{(2\,\pi)^3} \int \mathrm{d}^3 q \,\Big[(1 + f(\boldsymbol{q})) \log(1 + f(\boldsymbol{q})) - f(\boldsymbol{q}) \log(f(\boldsymbol{q}))\Big], \tag{2.71}$$

which for an equilibrium distribution is just the entropy of a Bose gas [75]. As a consequence, also the kinetic equations (2.62) and (2.63) for bosons describe an irreversible time evolution towards the equilibrium state and in accordance with the classical case, we call Eq. (2.71) the *non-equilibrium entropy*. Since S monotonically increases and saturates in equilibrium, we conveniently derive the equilibrium state by maximizing this quantity under moment constraints [81]. These constraints depend on the conservation properties of the actual scattering process, which we summarized in table 2.1. In the case of the four-magnon scattering, both the total magnon number and the internal energy are conserved, we thus introduce two Lagrange multipliers λ_1 and λ_2, so that the condition of maximal entropy under moment constraints reads

$$\frac{\delta}{\delta f(\boldsymbol{q})} \left[S[f] + \frac{a_0^3}{(2\,\pi)^3} \int \mathrm{d}^3 q \,\left[\lambda_1 f(\boldsymbol{q})\, \hbar\omega(\boldsymbol{q}) + \lambda_2 f(\boldsymbol{q})\right] \right] = 0, \tag{2.72}$$

where $\delta/\delta f(\boldsymbol{q})$ denotes the variational derivative. Solving this equation yields

$$f(\boldsymbol{q}) = \frac{1}{\exp\left(\frac{-\lambda_1 \hbar\omega(\boldsymbol{q}) - \lambda_2}{k_{\mathrm{B}}}\right) - 1}, \tag{2.73}$$

which is just a Bose-Einstein distribution if we identify $\lambda_1 = -1/T_{\mathrm{m}}$ and $\lambda_2 = \mu_{\mathrm{m}}/T_{\mathrm{m}}$. The magnon temperature T_{m} and the chemical potential of the magnons μ_{m} are therefore determined uniquely by the total magnon number and the internal energy, which are fixed by the initial conditions. In the case of the three-magnon process, which only conserves the internal energy, the second Lagrange multiplier becomes redundant and the equilibrium state therefore reduces to a Planck distribution. Noteworthy, the equilibrium state of the four-magnon coupling violating the conservation of the total magnon number (second term in Eq. (2.31)), which is solely induced by the dipole-dipole interaction, is also a Planck distribution. However, as already mentioned in the preceding section, we neglect this process being much weaker than the three-magnon process.

In the case of the Cherenkov process, we are dealing with an open magnetic system which is coupled to a phonon heat bath at fixed temperature T_{ph}. In analogy to thermodynamics,

	four-magnon process	**three-magnon process**	**Cherenkov process**
BE	no constraints	$\mu_{\mathrm{m}} = 0$	$T_{\mathrm{m}} = T_{\mathrm{ph}}$

Table 2.2: Equilibrium states of the individual interaction processes. “BE” is an abbreviation for Bose-Einstein distribution.

we consider the free energy of the magnetic system

$$\begin{aligned} F &= U - T_{\mathrm{ph}} S \\ &= \frac{a_0^3}{(2\,\pi)^3} \int \mathrm{d}^3 q \Big[f(\boldsymbol{q})\, \hbar\omega(\boldsymbol{q}) - k_{\mathrm{B}} T_{\mathrm{ph}} \left[(1 + f(\boldsymbol{q})) \log(1 + f(\boldsymbol{q})) - f(\boldsymbol{q}) \log(f(\boldsymbol{q})) \right] \Big], \end{aligned} \tag{2.74}$$

which indeed turns out to decrease monotonically during the time evolution

$$\frac{\mathrm{d}}{\mathrm{d}t} F \leq 0, \tag{2.75}$$

where the equal sign is again valid in equilibrium. The H-theorem in the case of an open magnon system therefore generalizes the free energy to non-equilibrium situations and we thus call Eq. (2.74) the *non-equilibrium free energy*. Noteworthy, the case of a Bose gas coupled to a phonon heat bath has also been treated by means of kinetic equations in Ref. [83] revealing a similar expression for the H-theorem. We thus derive the equilibrium state of the Cherenkov process by minimizing the free energy under moment constraints. Since the Cherenkov process only conserves the total magnon number, we only need a single Lagrange multiplier so that the condition of minimal free energy under this constraint reads

$$\frac{\delta}{\delta f(\boldsymbol{q})} \left[F[f] + \lambda \frac{a_0^3}{(2\,\pi)^3} \int \mathrm{d}^3 q\, f(\boldsymbol{q}) \right] = 0. \tag{2.76}$$

Solving this equation yields

$$f(\boldsymbol{q}) = \frac{1}{\exp\left(\frac{\hbar\omega(\boldsymbol{q}) + \lambda}{k_{\mathrm{B}} T_{\mathrm{ph}}}\right) - 1}, \tag{2.77}$$

which is again a Bose-Einstein distribution with $T_{\mathrm{m}} = T_{\mathrm{ph}}$ if we identify $\lambda = -\mu_{\mathrm{m}}$. This is an intuitive result, which implies that the energy transfer between the magnetic system and the lattice is finished as soon as the magnon temperature approaches the fixed temperature of the phonon heat bath. Noteworthy, magnon-phonon couplings of the respective form $\hat{c}^\dagger_{\boldsymbol{q}} \hat{c}^\dagger_{\boldsymbol{q}'} \hat{b}_{\boldsymbol{q}''\sigma}$ and $\hat{c}_{\boldsymbol{q}} \hat{c}_{\boldsymbol{q}'} \hat{b}^\dagger_{\boldsymbol{q}''\sigma}$, which are relevant in the case of spin-orbit induced interactions [20,44], additionally violate the conservation of the total magnon number and hence directly lead to the thermal equilibrium state with $T_{\mathrm{m}} = T_{\mathrm{ph}}$ and $\mu_{\mathrm{m}} = 0$, being characteristic for quasiparticles.

In table 2.2, we summarize the equilibrium states of each interaction process. As it is apparent, the three-magnon process in addition with the Cherenkov process also leads to the thermal equilibrium state of quasiparticles.

2.2.3 Isotropic Approximation

Numerically solving the quantum Boltzmann equation in the original form (2.62) is beyond the limits of present-day computer technology for being high-dimensional. We therefore have to make some simplifications in order to reduce the dimensionality of this equation. As we have shown in the preceding section, the dispersion of both magnons and phonons read

$$\hbar\omega(q) = g\mu_{\mathrm{B}}\mu_0 H_0 + 2JS(qa_0)^2, \tag{2.78a}$$

$$\hbar\omega_\sigma(q) = \hbar v_\sigma q, \tag{2.78b}$$

where the magnon dispersion follows by neglecting the dipolar contribution as well as finite size effects. By means of this simplification, the quantum Boltzmann equation can be simplified significantly as we will show. However, before we start deriving the corresponding equations, we discuss the validity of this simplification. The characteristic property of the magnon dispersion in in-plane magnetized thin films is the degenerate minimum lying at nonzero wave vectors $\boldsymbol{q} = \pm q_{\mathrm{min}}\boldsymbol{e}_z$ (cf. Fig. 2.1(b)), which is apparently lost in this approximation (2.78a). Since the Bose-Einstein condensation takes place at the minimal energy state of the system, we certainly cannot describe the formation of the condensate at nonzero wave vector or moreover the interaction between the two condensates within the framework of this simplification. However, there are a lot of reasons, why this approximation is not so crude as it seems at first sight. At higher energies, the exchange interaction dominates over the dipolar interaction and thus the dispersion can indeed be approximated by the exchange interaction only. Even for a 5 μm-thick film as we have seen in Fig. 2.1(b), the thickness modes lie very densely and are thermally occupied, so that it is by no means sufficient to retain only the lowest magnon mode in the simulation. Quite the contrary, even the thin film has to be treated three-dimensionally and a transition to a continuum in the direction parallel to the film normal is well justified due to the densely lying thickness modes. So except for the minimum region, the isotropic dispersion (2.78a) does not differ significantly from the dipole-exchange dispersion shown in Fig. 2.1(b). In particular, these high energy magnons, located beyond the minimum region, play an important role in the three-magnon scattering process as well as in the Cherenkov process, as we show in the subsequent chapter. Furthermore, the four-magnon process, which is responsible for the redistribution of the magnons as we show, is almost independent of the actual dispersion owing to the corresponding conservation laws, which are always satisfiable by this process. Since in this thesis, we are mainly interested in the thermalization process, which is solely determined by the different timescales of the individual processes, the simplification of assuming isotropy should be valid for this purpose.

Since the dispersions of both magnons and phonons (2.78a) and (2.78b) are isotropic and if the initial distributions as well as the pumping of magnons are also isotropic, the distribution functions of the magnons $f(\boldsymbol{q}) = f(q)$ and of the phonons $f_\sigma(\boldsymbol{q}) = f_\sigma(q)$ only depend on the modulus of the wave vector throughout the time evolution. The following derivations are mainly based on Refs. [81,82,84–86] and we subsequently present only the steps of transforming the four-magnon kinetic equation (2.62), since the kinetic equations resulting from the three-magnon interaction and the magnon-phonon interaction follow analogously and are given in Appendix A.4. Due to the isotropy, it is reasonable to go over to spherical coordinates

$$\mathrm{d}^3 q_i = q_i^2\,\mathrm{d}q_i\,\mathrm{d}\Omega_i, \tag{2.79}$$

and we separate the integration over the angle-dependent part in the four-magnon kinetic equation (2.62), which reads

$$F_4(q_0, q_1, q_2, q_3) = q_1 q_2 q_3 \iiint \mathrm{d}\Omega_1 \mathrm{d}\Omega_2 \mathrm{d}\Omega_3\, |A_4(\boldsymbol{q}_0, \boldsymbol{q}_1, \boldsymbol{q}_2, \boldsymbol{q}_3)|^2\, \delta(\boldsymbol{q}_0 + \boldsymbol{q}_1 - \boldsymbol{q}_2 - \boldsymbol{q}_3), \tag{2.80}$$

and which is evaluated in Appendix A.5. We now change from momentum space to energy space by means of the substitutions

$$E_i = g\mu_{\mathrm{B}}\mu_0 H_0 + 2JS\,(q_i a_0)^2\,, \tag{2.81a}$$

$$\tilde{f}(E_i) = f(q_i), \tag{2.81b}$$

$$\tilde{F}_4(E_0, E_1, E_2, E_3) = F_4(q_0, q_1, q_2, q_3). \tag{2.81c}$$

Since the original domain of integration in the kinetic equations (2.62), (2.63) and (2.66) is the first Brillouin zone of the simple cubic lattice, we replace the first Brillouin zone with a sphere of the same volume in reciprocal space just as in the *Debye model*, which was originally invented for calculating the phonon contribution to the specific heat of a solid [87]. The Debye wave vector reads

$$q_{\mathrm{D}} = \frac{1}{a_0}\left(6\pi^2\right)^{1/3} \approx 315 \times 10^5 \text{ rad/cm}, \tag{2.82a}$$

which results in specific cut-off energies for the magnons and for the phonons, respectively, which read

$$E_{\mathrm{cut}} = g\mu_{\mathrm{B}}\mu_0 H_0 + 2JS\left(6\pi^2\right)^{2/3} \approx 14.4 \text{ THz}, \tag{2.82b}$$

$$E_{\mathrm{cut}}^{\sigma} = \frac{\hbar v_\sigma}{a_0}\left(6\pi^2\right)^{1/3} \approx \begin{cases} 1.9 \text{ THz} & \text{if } \sigma = \perp \\ 3.6 \text{ THz} & \text{if } \sigma = \parallel\,. \end{cases} \tag{2.82c}$$

Performing the aforementioned steps, the kinetic equation resulting from the four-magnon scattering process finally reads

$$\begin{aligned} \frac{\mathrm{d}}{\mathrm{d}t}\tilde{f}(E_0) = \frac{1}{4096\pi^5\hbar\,(JS)^3} \int\limits_{E_{\mathrm{min}}}^{E_{\mathrm{cut}}} \mathrm{d}E_2 \Bigg[\int\limits_{\max(E_{\mathrm{min}},E_0-E_2+E_{\mathrm{min}})}^{\min(E_{\mathrm{cut}},E_0-E_2+E_{\mathrm{cut}})} \mathrm{d}E_3 \Big[\tilde{F}_4(E_0, E_1, E_2, E_3) \\ \times \Big(\tilde{f}(E_2)\tilde{f}(E_3)\left(1+\tilde{f}(E_0)\right)\left(1+\tilde{f}(E_1)\right) - \tilde{f}(E_0)\tilde{f}(E_1)\left(1+\tilde{f}(E_2)\right)\left(1+\tilde{f}(E_3)\right)\Big)\Big]\Bigg], \end{aligned} \tag{2.83}$$

where $E_1 = E_2 + E_3 - E_0$. With the assumption of isotropy we have reduced the original fivefold-integral (by evaluation of the delta distributions) in Eq. (2.62) to a double integral in Eq. (2.83) which can numerically be computed in $\mathcal{O}(N^3)$ operations, where N is the number of grid points. Particularly in the case of four-particle scattering, there exist fast conservative algorithms which allow computation of the corresponding equations in $\mathcal{O}(N^2 \log(N))$ operations requiring a uniform discretization [82]. However, in order to maintain a high resolution in the gigahertz-range, where the magnons are pumped, and to resolve the terahertz-region up to the cut-off frequency, simultaneously, we define a grid of equally spaced points in the logarithm of energy and employ the cubic spline interpolation for evaluating the magnon distribution function $\tilde{f}(E)$ at intermediate points [85, 86]. Furthermore, we use the classical Runge–Kutta method for the time integration and we employ Riemann sums for approximating the respective integrals.

The transformation to energy space of the kinetic equations resulting from the three-magnon interaction (2.63) and from the magnon-phonon interaction (2.66) follows analogously, however, due to the anisotropy of the respective interaction potentials entering the kinetic equations, we average the square of the respective scattering amplitudes over the remaining solid angle. The same holds true for the parallel pumping process (2.64) where the averaging results in the creation of magnons across a surface of a sphere in momentum space. Details are given in Appendix A.4.

2.2.4 Bose-Einstein Condensation

Until now, we have solely discussed the equilibrium solution of the four-magnon kinetic equation without considering the special case of Bose-Einstein condensation. In this case, the chemical potential of the magnons reaches the minimal energy state of the system

$$\mu_{\mathrm{m}} = E_{\mathrm{min}} = g\mu_{\mathrm{B}}\mu_0 H_0, \tag{2.84}$$

which thus limits the maximal number of magnons which can be accommodated by the thermal spectrum. However, if the actual magnon number exceeds this critical value, the magnon system undergoes Bose-Einstein condensation since magnons which can not be accommodated by the spectrum overpopulate the lowest energy state. Therefore, we have to conclude that the regular Bose-Einstein distributions are not sufficient to describe all possible equilibrium states of the magnon system. We thus have to consider the so-called *generalized Bose-Einstein distribution* [81,82], which reads

$$f(\boldsymbol{q}) = \frac{1}{\exp\left(\frac{\hbar\omega(\boldsymbol{q})-\mu_{\mathrm{m}}}{k_{\mathrm{B}}T_{\mathrm{m}}}\right) - 1} + n_c \, \frac{(2\pi)^3}{a_0^3} \, \delta(\boldsymbol{q}), \tag{2.85}$$

where n_c is the occupation of the condensate, and where the chemical potential has to satisfy the condition $n_c > 0 \to \mu_{\mathrm{m}} = E_{\mathrm{min}}$. By means of this distribution, it is possible to describe the equilibrium state of the system for all possible values of the total magnon number and internal magnon energy.

However, the case of Bose-Einstein condensation is not considered in the kinetic equation (2.62), since the magnon distribution function diverges in the limit $E \to E_{\mathrm{min}}$ when the chemical potential reaches the minimal energy state, resulting in a so-called *blow-up solution* of the kinetic equation [88]. An example of a blow-up solution is illustrated in Fig. 2.5, where the magnon distribution function is displayed at proceeding times, following from the four-magnon kinetic equation (2.83) in the case of supercritical initial conditions. By considering the magnon density of states, which is given by

$$D(E) = \frac{2\pi}{(8\pi^2 JS)^{3/2}} \sqrt{E - E_{\mathrm{min}}}, \tag{2.86}$$

and which vanishes in the limit $E \to E_{\mathrm{min}}$, we realize that the magnon number remains zero in the lowest energy state, despite of the diverging distribution function. Therefore, the equilibrium state (2.85) exhibiting a condensate can never be reached. In order to consider the possibility of Bose-Einstein condensation, we separate from the beginning the lowest energy state from the distribution function [85,86]

$$f_{\mathrm{tot}}(\boldsymbol{q}) = f(\boldsymbol{q}) + n_c \, \frac{(2\pi)^3}{a_0^3} \, \delta(\boldsymbol{q}). \tag{2.87}$$

Inserting this ansatz into the original kinetic equation (2.62) and again making the aforementioned transition to energy space, we obtain an additional kinetic equation describing the

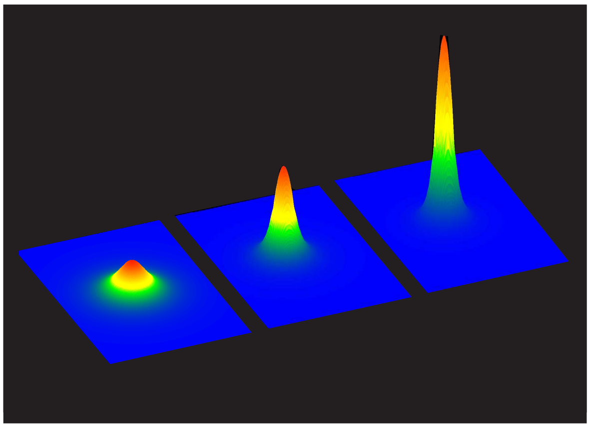

Figure 2.5: Blow-up solution of the four-magnon kinetic equation (2.83) in the case of supercritical initial conditions. The diagram shows the color-coded magnon distribution function in momentum space $f(|\boldsymbol{q}|)$ at proceeding times from left to right.

time evolution of the condensate

$$\begin{aligned}\frac{\mathrm{d}}{\mathrm{d}t} n_c &= \lim_{V_0^* \to 0}\left(\frac{a_0^3}{(2\pi)^3}\int_{V_0^*} \mathrm{d}^3 q_0 \, \frac{\mathrm{d}}{\mathrm{d}t} f_{\mathrm{tot}}(\boldsymbol{q}_0)\right) \\ &= \frac{\pi}{\hbar}\frac{1}{(16\pi^2 JS)^3}\, n_c \int\limits_{E_{\mathrm{min}}}^{E_{\mathrm{cut}}} \mathrm{d}E_2 \left[\int\limits_{E_{\mathrm{min}}}^{E_{\mathrm{min}}-E_2+E_{\mathrm{cut}}} \mathrm{d}E_3 \left[\tilde{F}_4(E_{\mathrm{min}}, E_1, E_2, E_3)\right.\right. \\ &\left.\left.\times \left(\tilde{f}(E_2)\tilde{f}(E_3)\left(1+\tilde{f}(E_1)\right) - \tilde{f}(E_1)\left(1+\tilde{f}(E_2)\right)\left(1+\tilde{f}(E_3)\right)\right)\right]\right], \end{aligned} \tag{2.88}$$

where $E_1 = E_2 + E_3 - E_{\mathrm{min}}$ and V_0^* being a volume in the reciprocal space enclosing $\boldsymbol{q}_0 = 0$. This equation reveals a peculiar property of the condensation process. Since n_c enters the right-hand side of Eq. (2.88) as a factor, the condensate remains zero for all time if the initial value is zero. In order to avoid this problem, we have to give a seed for n_c which then can grow in the numerical calculations. Since there is a non-vanishing condensate already at the beginning of the calculations, we cannot describe the stage where the phase transition sets in, but the model should still be valid briefly before and after the condensate emerges [85,86]. The actual value of the seed is arbitrary, it should however satisfy the condition $n_c(t=0) \ll N_{\mathrm{tot}}$ in order to prevent a distortion of the physical solution, as we will show in Sec. 3.2. The condensate also interacts with the thermal magnons and we obtain an additional kinetic equation for the magnon distribution function by inserting the condensate ansatz (2.87) into the original kinetic equation (2.62) in the case $\boldsymbol{q}_0 \neq 0$, which reads

$$\begin{aligned}\frac{\mathrm{d}}{\mathrm{d}t}\tilde{f}(E_0) = \frac{\pi}{2\hbar}\frac{\sqrt{2JS}}{(16\pi^2 JS)^2}\, n_c &\left[\int\limits_{E_{\mathrm{min}}}^{E_0} \mathrm{d}E_3 \left[\lim_{E_1 \to E_{\mathrm{min}}}\left(\frac{\tilde{F}_4(E_0, E_1, E_2, E_3)}{\sqrt{E_1 - E_{\mathrm{min}}}}\right)\right.\right. \\ &\left.\times \left(\tilde{f}(E_2)\tilde{f}(E_3)\left(1+\tilde{f}(E_0)\right) - \tilde{f}(E_0)\left(1+\tilde{f}(E_2)\right)\left(1+\tilde{f}(E_3)\right)\right)\right] \\ &+ 2\int\limits_{E_0}^{E_{\mathrm{cut}}} \mathrm{d}E_3 \left[\lim_{E_2 \to E_{\mathrm{min}}}\left(\frac{\tilde{F}_4(E_0, E_1, E_2, E_3)}{\sqrt{E_2 - E_{\mathrm{min}}}}\right)\right. \\ &\left.\left.\times \left(\tilde{f}(E_3)\left(1+\tilde{f}(E_0)\right)\left(1+\tilde{f}(E_1)\right) - \tilde{f}(E_0)\tilde{f}(E_1)\left(1+\tilde{f}(E_3)\right)\right)\right]\right], \end{aligned} \tag{2.89}$$

where $E_2 = E_0 + E_{\text{min}} - E_3$ in the first integral and $E_1 = E_{\text{min}} + E_3 - E_0$ in the second integral.

Once more, we study the equilibrium states of the magnon system, now described by the additional kinetic equations (2.88) and (2.89). We realize that these equations also conserve the total magnon number as well as the internal magnon energy, which are in this case given by

$$N_{\text{tot}} = n_c + \frac{a_0^3}{(2\,\pi)^3} \int \mathrm{d}^3q\, f(\boldsymbol{q}), \tag{2.90a}$$

$$U = n_c E_{\text{min}} + \frac{a_0^3}{(2\,\pi)^3} \int \mathrm{d}^3q\, f(\boldsymbol{q})\, \hbar\omega(\boldsymbol{q}), \tag{2.90b}$$

and we notice that the H-theorem (2.70) in the case of the closed magnon system still holds. Since the entropy of the condensate vanishes, which follows by considering the non-equilibrium entropy (2.71) in the limit $f \to \infty$, the equilibrium state follows by maximizing the entropy of the thermal magnons under moment constraints

$$\left(\frac{\delta}{\delta f(\boldsymbol{q})}, \frac{\mathrm{d}}{\mathrm{d}n_c}\right) \left[S[f] + \frac{a_0^3}{(2\,\pi)^3} \int \mathrm{d}^3q\, \left[\lambda_1 f(\boldsymbol{q})\, \hbar\omega(\boldsymbol{q}) + \lambda_2 f(\boldsymbol{q})\right] + \lambda_1 n_c E_{\text{min}} + \lambda_2 n_c\right] = 0, \tag{2.91}$$

where the variation with respect to $f(\boldsymbol{q})$ yields again the original result (2.73) and the derivative with respect to n_c gives the additional condition $\lambda_1 E_{\text{min}} + \lambda_2 = 0$, which thus fixes the chemical potential to be $\mu_{\text{m}} = E_{\text{min}}$. In agreement with the generalized Bose-Einstein distribution (2.85), the equilibrium states of the kinetic equations (2.88) and (2.89) are indeed the trivial solution, that is a regular Bose-Einstein distribution without any condensate $n_c = 0$, and the nontrivial solution, that is the critical Bose-Einstein distribution with $\mu_{\text{m}} = E_{\text{min}}$ augmented by a condensate $n_c \neq 0$.

In conclusion, by means of the additional kinetic equations (2.88) and (2.89), we are able to treat the irreversible time evolution of the magnon system allowing for the phenomenon of Bose-Einstein condensation to take place. We thoroughly discuss this property of the kinetic equations in Sec. 3.2. It is worth noting that only the four-magnon process contributes to the time evolution of the condensate in our isotropic model. However, in Sec. 4.2, we discuss the time evolution of the condensate which would follow in the anisotropic spectrum, shown in Fig. 2.1(b). In this case, the condensate is affected additionally by the three-magnon confluence process, which leads to a linear damping, as we show.

2.2.5 Four-Magnon Scattering at Small Wave Vectors

In the case of the exchange interaction potential (2.30), the four-magnon scattering amplitude (2.58) in the first Born approximation reads

$$A_4^{\text{ex}}(\boldsymbol{q}_0, \boldsymbol{q}_1, \boldsymbol{q}_2, \boldsymbol{q}_3) = -2\,J\,a_0^2\,(\boldsymbol{q}_0 \cdot \boldsymbol{q}_1 + \boldsymbol{q}_2 \cdot \boldsymbol{q}_3) + 4\,S_0\,J\left(24 - a_0^2\left(\boldsymbol{q}_0^2 + \boldsymbol{q}_1^2 + \boldsymbol{q}_2^2 + \boldsymbol{q}_3^2\right)\right), \tag{2.92}$$

where the first addend is the well known classical four-magnon exchange scattering amplitude [20, 46, 62] and the second addend is a quantum mechanical correction term, where S_0 is defined in Eq. (2.7). Unlike the first addend, the second addend does not vanish in the limit of zero wave vector and leads to a contribution

$$A_4^{\text{ex}} = 96\,S_0\,J \approx 7\text{ GHz}. \tag{2.93}$$

However, this term is not small compared with the harmonic magnon energies at small wave vectors and therefore the validity of the first Born approximation and furthermore the applicability of perturbation theory in general is questionable. In order to get a reliable result for the scattering amplitude, we thus have to consider the whole Born series, which in scattering theory is equivalent to the determination of the so-called *transition matrix* or *t-matrix* [78]. Since scattering theory takes as a basis the one-particle Schrödinger equation, the t-matrix approach is exact only at zero temperature. However, for a low density interacting Bose gas at low temperatures, the t-matrix yields the first approximation to the scattering amplitude of the many-body system [89].

In the following, we restrict ourselves to exchange magnons in the simple cubic lattice exhibiting the dispersion (2.18a). First of all, we rewrite the four-magnon interaction (2.28) in a symmetric form according to the two-particle interaction Hamiltonian used in the diagram technique

$$\hat{\mathcal{H}}_{\text{m-m}} = \frac{1}{2N} \sum_{\boldsymbol{q}_0\boldsymbol{q}_1\boldsymbol{q}_2\boldsymbol{q}_3} V_4^{\text{ex}}(\boldsymbol{q}_0, \boldsymbol{q}_1, \boldsymbol{q}_2, \boldsymbol{q}_3)\; \hat{c}^{\dagger}_{\boldsymbol{q}_0} \hat{c}^{\dagger}_{\boldsymbol{q}_1} \hat{c}_{\boldsymbol{q}_2} \hat{c}_{\boldsymbol{q}_3}\, \delta_{\boldsymbol{q}_0+\boldsymbol{q}_1, \boldsymbol{q}_2+\boldsymbol{q}_3}, \tag{2.94}$$

where

$$\begin{aligned} V_4^{\text{ex}}(\boldsymbol{q}_0, \boldsymbol{q}_1, \boldsymbol{q}_2, \boldsymbol{q}_3) = & -\left[\, J(\boldsymbol{q}_0 - \boldsymbol{q}_2) + J(\boldsymbol{q}_1 - \boldsymbol{q}_2) \,\right] + \frac{1}{2}\,(1 + 4S_0) \\ & \times \left[\, J(\boldsymbol{q}_0) + J(\boldsymbol{q}_1) + J(\boldsymbol{q}_2) + J(\boldsymbol{q}_3) \,\right], \end{aligned} \tag{2.95}$$

and with $J(\boldsymbol{q})$ defined in Eq. (2.17). In the case of two-particle scattering, the t-matrix follows by summing the infinite series of ladder graphs shown in Fig. 2.6 [89, 90], where we can deduce an integral equation for the t-matrix from the lower diagrams

$$\begin{aligned} t(\vec{\boldsymbol{q}}_0, \vec{\boldsymbol{q}}_1, \vec{\boldsymbol{q}}_2, \vec{\boldsymbol{q}}_3) = V_4^{\text{ex}}(\boldsymbol{q}_0, \boldsymbol{q}_1, \boldsymbol{q}_2, \boldsymbol{q}_3) + i\frac{\hbar a_0^3}{(2\pi)^4} \int \mathrm{d}^4 k \, \Big[& V_4^{\text{ex}}(\boldsymbol{q}_0, \boldsymbol{q}_1, \boldsymbol{k}, \boldsymbol{q}_0 + \boldsymbol{q}_1 - \boldsymbol{k}) \\ & \times G^{(0)}(\vec{\boldsymbol{k}})\, G^{(0)}(\vec{\boldsymbol{q}}_0 + \vec{\boldsymbol{q}}_1 - \vec{\boldsymbol{k}})\, t(\vec{\boldsymbol{k}}, \vec{\boldsymbol{q}}_0 + \vec{\boldsymbol{q}}_1 - \vec{\boldsymbol{k}}, \vec{\boldsymbol{q}}_2, \vec{\boldsymbol{q}}_3) \Big], \end{aligned} \tag{2.96}$$

where $\vec{\boldsymbol{q}}_i = (\boldsymbol{q}_i, \omega_i)$, $\vec{\boldsymbol{k}} = (\boldsymbol{k}, \omega_k)$, $\mathrm{d}^4 k = \mathrm{d}^3 k \,\mathrm{d}\omega_k$ and $G^{(0)}$ is the free magnon Green's function. In Appendix A.6, we show that the t-matrix is independent of the quantity S_0 and that

$$t(\vec{\boldsymbol{q}}_0, \vec{\boldsymbol{q}}_1, \vec{\boldsymbol{q}}_2, \vec{\boldsymbol{q}}_3) = 0, \tag{2.97}$$

if only one of the ingoing or one of the outgoing wave vectors is zero. Indeed, the original correction term in the scattering amplitude (2.93) appearing in the first Born approximation vanishes in the t-matrix approach. We therefore have to conclude that the series (2.9) of the magnon Hamiltonian resulting from the Holstein-Primakoff transformation (2.3a)-(2.3c) does not converge as quickly as assumed, which significantly becomes apparent in the four-magnon exchange scattering.

Indeed, this problem is known for a long time and was first addressed by Dyson [91, 92] who found a correction term arising due to magnon interactions of the leading order T^4 to the famous Bloch's $T^{3/2}$-law for the temperature dependence of the spontaneous magnetization of a ferromagnet [18]. Motivated by the fact that previous results of other authors were in severe disagreement with each other, Dyson established a spin wave theory, now regarded as being rigorous, revealing that "*the interaction between low-frequency spin waves is quite weak and is grossly overestimated by the Holstein-Primakoff Hamiltonian*" [91]. Maleev then

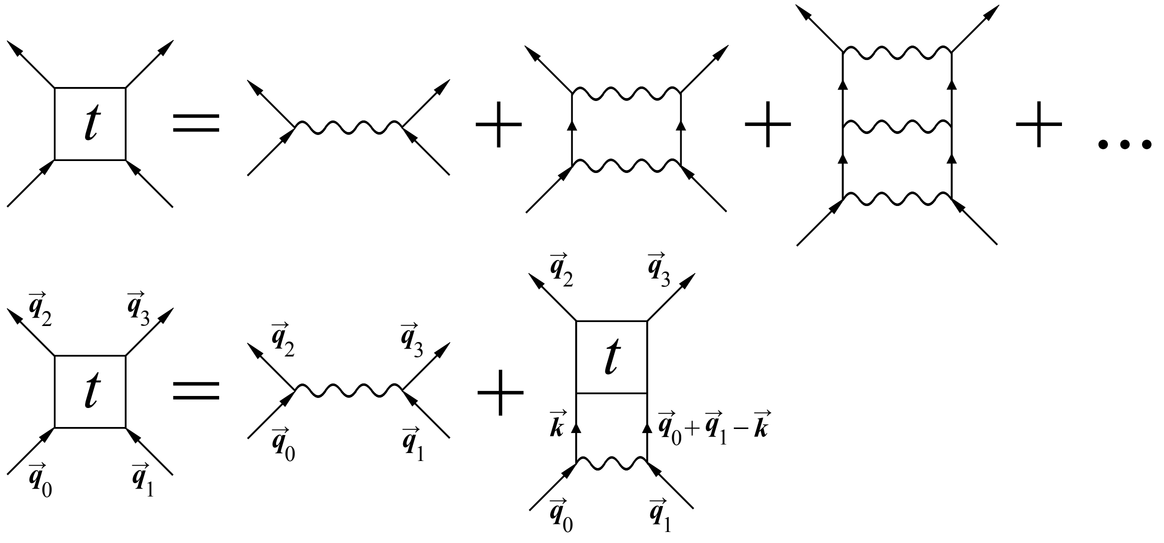

Figure 2.6: Diagrammatic representation of the t-matrix. The determination of the t-matrix requires the calculation of an infinite series of ladder graphs as shown in the upper equation, where the square corresponds to the t-matrix and each wavy line corresponds to the interaction potential V_4^{ex} as defined in Eq. (2.95). Adding an additional wavy line and two solid lines to each diagram of both sides of the upper equation leads to an integral equation for the t-matrix as shown in the lower equation.

showed that Dyson's approach is equal to a corresponding boson mapping [93], now known as the *Dyson-Maleev transformation* [18], which reads

$$\hat{S}_i^z = \hbar\left(S - \hat{a}_i^\dagger \hat{a}_i\right), \tag{2.98a}$$

$$\hat{S}_i^+ = \hbar\sqrt{2S}\,\hat{a}_i, \tag{2.98b}$$

$$\hat{S}_i^- = \hbar\sqrt{2S}\,\hat{a}_i^\dagger\left(1 - \frac{\hat{a}_i^\dagger \hat{a}_i}{2S}\right), \tag{2.98c}$$

where the operators $\hat{a}_i^\dagger$ and $\hat{a}_i$ again fulfill the fundamental Bose commutation rules (2.4a) and (2.4b). In contrast to the Holstein-Primakoff transformation, the Dyson-Maleev transformation is finite since the original square root of operators is circumvented by choosing an asymmetry between the operators $\hat{S}_i^+$ and $\hat{S}_i^-$ still preserving the commutation relations of angular momentum operators. However, as apparent, the transformation is not unitary anymore. Nevertheless, this does not lead to severe problems in determining the thermodynamic properties of the ideal Heisenberg ferromagnet following from the partition function, since the Holstein-Primakoff and Dyson-Maleev mappings are connected via a similarity transformation [94] and thus principally yield equal eigenvalues. However, this is not quite correct since the mapping of the unphysical subspace ($n_i > 2S$) results in the appearance of unphysical eigenvalues which Dyson nevertheless showed to be negligible in the calculation of the partition function at low temperatures [92]. As a result of the Dyson-Maleev transformation, the bilinear part of the Hamiltonian coincides with $\hat{\mathcal{H}}_2$ in Eq. (2.9) revealing the same magnon spectrum as in the Holstein-Primakoff mapping, however, the four-magnon interaction in this case reads

$$\hat{\mathcal{H}}_4^{\text{ex}} = \frac{1}{N}\sum_{\boldsymbol{q}\boldsymbol{q}'\boldsymbol{q}''}\left[J(\boldsymbol{q}-\boldsymbol{q}'') - J(\boldsymbol{q}'')\right]\,\hat{c}_{\boldsymbol{q}}^\dagger \hat{c}_{\boldsymbol{q}'}^\dagger \hat{c}_{\boldsymbol{q}-\boldsymbol{q}''}\hat{c}_{\boldsymbol{q}'+\boldsymbol{q}''}, \tag{2.99}$$

which does not contain the correction term S_0 and which vanishes in the limit of zero wave vectors in accordance with the t-matrix approach.

Basically, as it would be the consequence of the above considerations, we have to determine a closed-form expression for the t-matrix by means of Eq. (2.96) in order to obtain reliable results within the Holstein-Primakoff transformation, since a kinetic theory based on a non-Hermitian representation is doubtful due to the violation of the micro-reversibility property (2.59). Fortunately, it is possible to obtain identical results for the partition function to at least first order in the small parameter $1/S$ within a Hermitian representation of the spin Hamiltonian by using the Holstein-Primakoff approach and expanding the square root to first order in $1/S$ (cf. Eq. (2.5)) rather than to first order in products of normal ordered operators (cf. Eq. (2.6)) [95,96]. Therefore, the $1/S$-expansion provides a unitary approximation of the Dyson-Maleev transformation and furthermore ensures the nonharmonic part in the magnon Hamiltonian to be small so that perturbation theory is again applicable. Noteworthy, this approach leads to the same interaction potentials as in the classical description of spin wave amplitudes, in which the operators are replaced by complex scalars [21, 65].

As a concluding remark, our approach using the Holstein-Primakoff transformation in Sec. 2.1 still yields accurate results, even in the first Born approximation, if we drop the correction term S_0, in accordance with the $1/S$-expansion, mentioned above. However, as it becomes apparent in Chap. 4, the correction term (2.93), curiously enough, exhibits the rough order of magnitude in order to explain the experimentally observed thermalization and Bose-Einstein condensation of magnons within our model. Therefore, for the moment, we keep the term S_0 in the kinetic equation resulting from the four-magnon interaction and discuss the associated consequences in the subsequent chapter.

3

Properties of Magnon Interactions

This chapter individually discusses the four-magnon process, the three-magnon process as well as the Cherenkov process, which provide the basis of our model, before we turn to the full system in Chap. 4 with all interaction processes combined. By this means, we intend to give an overview and better understanding of the mechanisms and special attributes which are characteristic for the individual interaction processes. In the first section, we start with the linear properties of the interactions and study the magnon relaxation rates of each process which give a first insight into the strengths of the interactions. In the previous chapter, we have already determined the equilibrium states of the three interaction processes. The second section moreover describes the paths into the equilibrium and is therefore dedicated to the equilibration dynamics of initially non-equilibrium magnon distributions.

3.1 Magnon Relaxation Rates

In this section, we consider the relaxation rates of the three interaction processes which describe the linear response of the system to a small perturbation from the equilibrium state [20]. A small perturbation means that except for magnon states located at a very narrow region about a certain wave vector $\boldsymbol{q}$, all other magnon states can be described by their equilibrium occupations. By separating the occupation of the magnon state with wave vector $\boldsymbol{q}$ into a perturbation $f_{\mathrm{pert}}(\boldsymbol{q})$ and the equilibrium value $f_{\mathrm{eq}}(\boldsymbol{q})$

$$f(\boldsymbol{q}) = f_{\mathrm{pert}}(\boldsymbol{q}) + f_{\mathrm{eq}}(\boldsymbol{q}), \tag{3.1}$$

it is always possible to cast any of the kinetic equations (2.62), (2.63) and (2.66) into the form

$$\frac{\mathrm{d}}{\mathrm{d}t} f_{\mathrm{pert}}(\boldsymbol{q}) = -\Gamma(\boldsymbol{q})\, f_{\mathrm{pert}}(\boldsymbol{q}), \tag{3.2}$$

where we have defined the magnon relaxation rate Γ. Therefore, a small perturbation will be damped exponentially with the rate Γ into the equilibrium. Prerequisite for this treatment, as mentioned above, is the smallness of the perturbation which should not affect magnon states other than the state with wave vector $\boldsymbol{q}$. We will see in the second section of this chapter that this condition is not so strict for the three-magnon process but that it is essential for the four-magnon process. The knowledge of the relaxation rates reveals the strength of the interaction and also some special attributes of the energy and momentum conservation laws.

First, we start by considering a parallel pump experiment by Kasuya and LeCraw [48] which was performed in order to determine the intrinsic ferromagnetic resonance line width of YIG by measuring the relaxation rates at small wave vectors. We then discuss the relaxation rates of the three interaction processes resulting from our isotropic model and compare them with the experiment.

3.1.1 Kasuya-LeCraw Experiment

The research of ferromagnetic relaxation has a long history. Shortly after the discovery of yttrium iron garnet (YIG) in 1956 [97, 98], a lot of investigations have been performed on this unique magnetic material which to the present has the smallest known ferromagnetic resonance line width. In order to determine the intrinsic line width, which is characteristic for each material and which does not depend on the geometry, impurity level or surface roughness of the samples, Kasuya and LeCraw performed parallel pump experiments with very pure and highly polished spheres of bulk YIG [48]. The advantage of parallel pump experiments in determining the line width is that these experiments do not see the surface pits of the sample since the uniform mode is not excited directly [63]. However, in ferromagnetic resonance experiments, the surface pits strongly influence the relaxation rate of the uniform mode and hence significantly increase the ferromagnetic resonance line width [47]. In parallel pump experiments, a microwave generator creates an rf field with a fixed frequency ω_{pump}, which is applied parallel to the static magnetic field. By means of this technique, as we have already pointed out in Sec. 2.1, two spin waves with half frequency $\omega_{\text{sw}} = \omega_{\text{pump}}/2$ and opposite wave vectors are excited perpendicular to the applied magnetic field [21], which are also known as $\pi/2$-*spin waves* [69]. By determining the threshold field at which the amplitude of these spin waves begins to grow exponentially, it is possible to determine the relaxation rate which is proportional to the threshold field [69]. This procedure is repeated at different static magnetic fields in order to obtain the relaxation rates as a function of the wave vector by using the familiar dispersion relation for spin waves in a sphere (2.16) with the demagnetization factors $D_x = D_y = D_z = 1/3$. The room temperature results of Kasuya and LeCraw at a fixed pump frequency of $f_{\text{pump}} = \omega_{\text{pump}}/2\pi = 11.4$ GHz are shown as the green dots in Fig. 3.1. It follows that the relaxation rates at small wave vectors obey a linear law

$$\Gamma(q_\perp) = \Gamma_0 + \alpha\, q_\perp, \tag{3.3}$$

where the relaxation rate of the uniform mode was extrapolated to be $\Gamma_0 \approx 2.4$ MHz. The linear increase with the slope α and the deviation from the straight line at higher wave vectors is well understood and has been successfully explained as a result of the three-magnon confluence process [68, 99], which we will also discuss in this section. The experiment also revealed the following dependencies of the relaxation rate of the uniform mode on the saturation

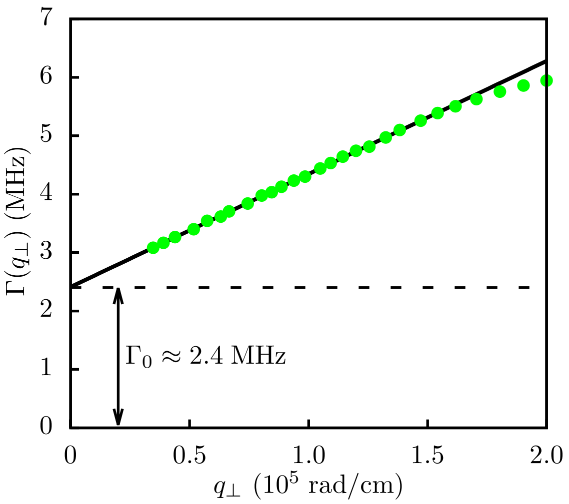

Figure 3.1: Relaxation rates Γ as a function of the wave vector $q_\perp$ oriented perpendicular to the applied magnetic field. The green dots represent the experimental data by Kasuya and LeCraw [48] at room temperature and at a fixed pump frequency $f_{\text{pump}} = \omega_{\text{pump}}/2\pi = 11.4$ GHz, whereas the straight black line is an extrapolation to the relaxation rate of the uniform mode Γ_0. The dashed black line indicates the constant upshift Γ_0 of the relaxation rates at small wave vectors.

magnetization M_S, the ferromagnetic resonance frequency (FMR) ω_0 and the temperature T

$$\Gamma_0 \propto \frac{\omega_0 T^n}{M_\mathrm{S}}, \tag{3.4}$$

with $1 < n < 2$ in the temperature range $140\,\mathrm{K} < T < 400\,\mathrm{K}$ with the higher values of n corresponding to higher temperatures. Attempts to find the origin of Γ_0 have also been made by Kasuya and LeCraw, who made use of the ferrimagnetic nature of YIG and proposed two scattering processes involving magnons or a phonon in the optical branch of the spectrum, now called the *Kasuya-LeCraw processes* [48, 63]. According to their calculations, these processes play the major role in relaxing the uniform mode in the high temperature limit. Later, Cherepanov *et al.* [46] calculated the relaxation rate of the uniform mode for the process involving two optical magnons having a gap in their spectrum and obtained $\Gamma_0 = 0.9$ MHz, in rough agreement with the experiment. Nevertheless, the authors had to estimate the width of the gap which sensitively depends on the temperature.

So from the theoretical point of view, it is not strictly precluded that there are other inherent relaxation mechanisms which contribute to the relaxation rate of the uniform mode. We will account on this possibility subsequently.

3.1.2 Four-Magnon Process

We begin the theoretical investigation of the linear relaxation with the four-magnon process. The relaxation rates, as defined in Eq. (3.2), are given by

$$\begin{aligned}\Gamma(\boldsymbol{q}_0) = \frac{2\pi}{\hbar}\frac{a_0^6}{(2\,\pi)^6}\frac{1}{2}\iiint \mathrm{d}^3q_1\mathrm{d}^3q_2\mathrm{d}^3q_3 \Big[\, &\delta(\hbar\omega(\boldsymbol{q}_0) + \hbar\omega(\boldsymbol{q}_1) - \hbar\omega(\boldsymbol{q}_2) - \hbar\omega(\boldsymbol{q}_3)) \\ &\times \delta(\boldsymbol{q}_0 + \boldsymbol{q}_1 - \boldsymbol{q}_2 - \boldsymbol{q}_3)\,|A_4(\boldsymbol{q}_0, \boldsymbol{q}_1, \boldsymbol{q}_2, \boldsymbol{q}_3)|^2 \\ \times \Big(f(\boldsymbol{q}_1)\,(1 + f(\boldsymbol{q}_2))\,(1 + f(\boldsymbol{q}_3)) &- f(\boldsymbol{q}_2) f(\boldsymbol{q}_3)\,(1 + f(\boldsymbol{q}_1))\Big)\Big],\end{aligned} \tag{3.5}$$

where A_4 is the four-magnon scattering amplitude and the magnon distribution functions $f(\boldsymbol{q})$ are Bose-Einstein distributions at room temperature equilibrium ($T_\mathrm{m} = 300\,\mathrm{K}$ and $\mu_\mathrm{m} = 0$). In order to calculate the relaxation rates (3.5), we again make use of the isotropic approximation, introduced in Sec. 2.2 of the previous chapter, which takes as a basis the isotropic magnon dispersion (2.78a). The resulting deviations in the low wave vector regime in comparison with the results following from the exact bulk dispersion (2.16) are nevertheless smaller than ten percent, which we have ensured by means of numerical integration of the dipole-exchange dispersion (2.16), not presented here. At this point, we distinguish between two different cases $S_0 \neq 0$ and $S_0 = 0$. In the first case $S_0 \neq 0$, which we refer to as the *modified process*, we use the four-magnon scattering amplitude (A.46), which is augmented by the quantum mechanical correction term S_0, and in the second case $S_0 = 0$, which we refer to as the *common process*, we omit the correction term but instead include the dipolar contribution to the four-magnon scattering amplitude (A.49). The resulting relaxation rates of the four-magnon process, being almost independent of the external magnetic field due to the cancellation of the Zeeman contribution in the energy conservative delta function in Eq. (3.5), are shown in Figs. 3.2(a) and 3.2(b) at a fixed magnetic field of $H_0 = 1000\,\mathrm{Oe}$. We see in Fig. 3.2(a) that the relaxation rates in both cases increase with increasing wave vector and coincide at wave vectors larger than approximately $q \approx 50 \times 10^5$ rad/cm. In the

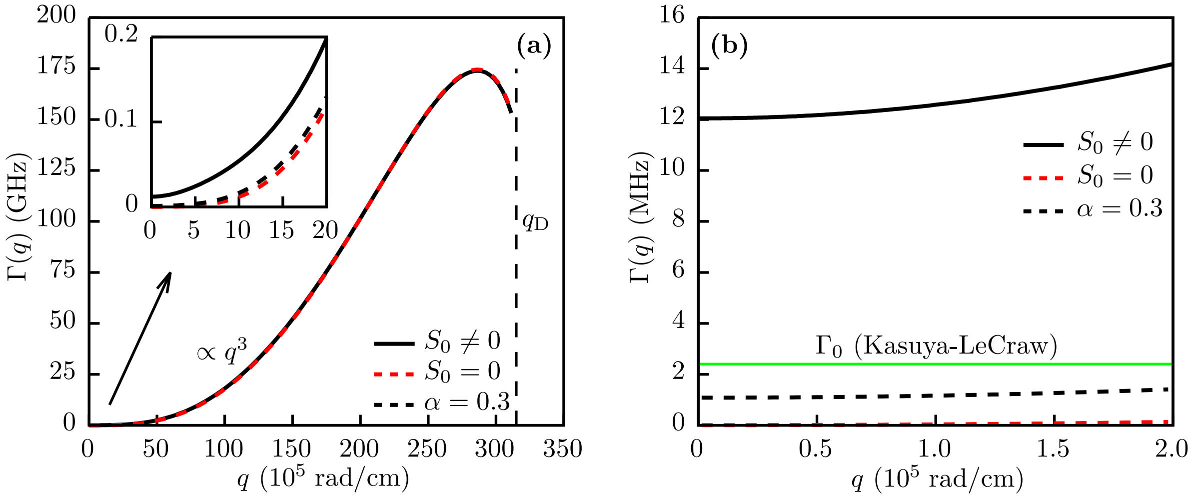

Figure 3.2: Four-magnon relaxation rates as a function of the wave vector of the modified process with $S_0 \neq 0$, denoted by the solid black lines, and of the common process with $S_0 = 0$, denoted by the dashed red lines, at a fixed magnetic field of $H_0 = 1000\,\mathrm{Oe}$. The dashed black lines show the modified process in which the quantum mechanical correction term S_0 is replaced by αS_0 with $\alpha = 0.3$. q_{D} is the Debye wave vector (2.82a). The inset in Fig. (a) shows a zoom into the region with smaller wave vectors. The solid green line in Fig. (b) shows the constant upshift Γ_0 of the relaxation rates as measured in the Kasuya-LeCraw experiment [48] (cf. Fig. 3.1).

pure exchange case, that is the common process without the dipolar contribution, Dyson already showed that the relaxation rates exhibit a cubic dependence on the wave vector [69], which is rigorously confirmed by our numerical results. At large wave vectors, the four-magnon exchange process is the strongest among all other relaxation mechanisms and leads to relaxation rates in the elevated gigahertz range. As can be seen in the inset of Fig. 3.2(a), the correction term S_0 has a strong influence only at small wave vectors where the relaxation rates are clearly larger than those of the common process with $S_0 = 0$. Figure 3.2(b) shows the relaxation rates in the limit of zero wave vectors. The common process, denoted by the dashed red line, is strongly suppressed in this wave vector range but nevertheless does not vanish at zero wave vector due to a very small contribution from the dipolar interaction. The relaxation rate of the uniform mode in the four-magnon process can be estimated via

$$\Gamma_0 = \frac{|A_4|^2 (k_{\mathrm{B}} T_{\mathrm{m}})^2}{3072\,\pi \hbar J^3 S^3}, \tag{3.6}$$

which is derived in Appendix A.7, and which indeed does not depend on the magnetic field (at least in this approximation), as mentioned above. We first set

$$A_4 = \frac{1}{\sqrt{5}} \frac{\mu_0 g^2 \mu_{\mathrm{B}}^2}{a_0^3}, \tag{3.7}$$

which is the scattering amplitude of the common process at zero wave vector, following from Eq. (A.50). Using the physical parameters given in Sec. 2.1, Eq. (3.6) yields $\Gamma_0 \approx 5.7 \times 10^{-6}$ MHz which is indeed several orders of magnitude below the measured relaxation rate in the Kasuya-LeCraw experiment, as denoted by the solid green line in Fig. 3.2(b). Turning to the modified process, as denoted by the solid black line, we see that the correction term S_0 also leads to an almost constant upshift of the relaxation rates at small wave vectors, similar as in the Kasuya-LeCraw experiment, which nevertheless overestimates the measured value Γ_0. In this case, the relaxation rate of the uniform mode can be estimated with Eq. (3.6) by setting

$$A_4 = 96 S_0 J, \tag{3.8}$$

which is the scattering amplitude of the modified process at zero wave vector (2.93), which gives $\Gamma_0 \approx 12.2$ MHz in good agreement with the numerical result. However, by inserting Eq. (3.8) into Eq. (3.6), and using $S_0 \approx 1/32S$, which follows from the definition of S_0 in Eq. (2.7), we realize that the resulting relaxation rate is inversely proportional to the fifth power of the total spin S by keeping unchanged the exchange constant J. This result severely deviates from the dependence on the total spin $\Gamma_0 \propto S^{-1}$, found in the experiment (3.4). As we have already pointed out in Sec. 2.2 of the preceding chapter, the correction term S_0 vanishes in the t-matrix approach and is thus an artifact of the first Born approximation. Anyhow, in order to be compatible at least in strength with both the Kasuya-LeCraw experiment [48] and the estimates by Cherepanov *et al.* [46] of the uniform mode relaxation rate of $\Gamma_0 = 0.9$ MHz via optical magnons, we introduce a correction factor α and replace S_0 by αS_0 in the modified process. We choose $\alpha = 0.3$ which results in a contribution from the four-magnon process to the uniform mode relaxation rate of $\Gamma_0 \approx 1.1$ MHz by using Eq. (3.6) and we show the resulting relaxation rates by the dashed black lines in Figs. 3.2(a) and 3.2(b). Indeed, we see in Fig. 3.2(b) that the correction factor α shifts the relaxation rates below the rates measured in the Kasuya-LeCraw experiment. Augmented by the estimated contribution of optical magnons, the total relaxation rate would be $\Gamma_0 \approx 2$ MHz, not exceeding the experimental value.

If not stated otherwise, we use the modified four-magnon process with the correction factor $\alpha = 0.3$ throughout this thesis in our numerical calculations for two reasons. For the one hand, we can only demonstrate reasonably the condensation process in this chapter with a four-magnon process which is strong enough in the low wave vector regime. On the other hand, as we will see in Sec. 4.1 of the subsequent chapter, this modified four-magnon process exhibits just the correct order of magnitude which is necessary to explain the experimental results of pumped magnons leading to Bose-Einstein condensation.

3.1.3 Three-Magnon Process

We continue the discussion of the relaxation rates with the three-magnon process which can be separated into a splitting process and a confluence process. The relaxation rates of the splitting process are given by

$$\begin{aligned}\Gamma(\boldsymbol{q}_0) = \frac{2\pi}{\hbar}\frac{a_0^3}{(2\,\pi)^3}\frac{1}{2}\iint \mathrm{d}^3 q_1 \mathrm{d}^3 q_2 \Big[&|V_3(\boldsymbol{q}_1) + V_3(\boldsymbol{q}_2)|^2\, \delta(\hbar\omega(\boldsymbol{q}_0) - \hbar\omega(\boldsymbol{q}_1) - \hbar\omega(\boldsymbol{q}_2)) \\ &\times \delta(\boldsymbol{q}_0 - \boldsymbol{q}_1 - \boldsymbol{q}_2)\left((1 + f(\boldsymbol{q}_1))\,(1 + f(\boldsymbol{q}_2)) - f(\boldsymbol{q}_1) f(\boldsymbol{q}_2)\right)\Big], \end{aligned} \tag{3.9a}$$

and the relaxation rates of the confluence process are given by

$$\begin{aligned}\Gamma(\boldsymbol{q}_0) = \frac{2\pi}{\hbar}\frac{a_0^3}{(2\,\pi)^3}\iint \mathrm{d}^3 q_1 \mathrm{d}^3 q_2 \Big[&|V_3(\boldsymbol{q}_0) + V_3(\boldsymbol{q}_1)|^2\, \delta(\hbar\omega(\boldsymbol{q}_0) + \hbar\omega(\boldsymbol{q}_1) - \hbar\omega(\boldsymbol{q}_2)) \\ &\times \delta(\boldsymbol{q}_0 + \boldsymbol{q}_1 - \boldsymbol{q}_2)\left(f(\boldsymbol{q}_1)\,(1 + f(\boldsymbol{q}_2)) - f(\boldsymbol{q}_2)\,(1 + f(\boldsymbol{q}_1))\right)\Big], \end{aligned} \tag{3.9b}$$

where again the magnon distribution functions $f(\boldsymbol{q})$ are Bose-Einstein distributions at room temperature equilibrium. As opposed to the four-magnon process, the relaxation rates of

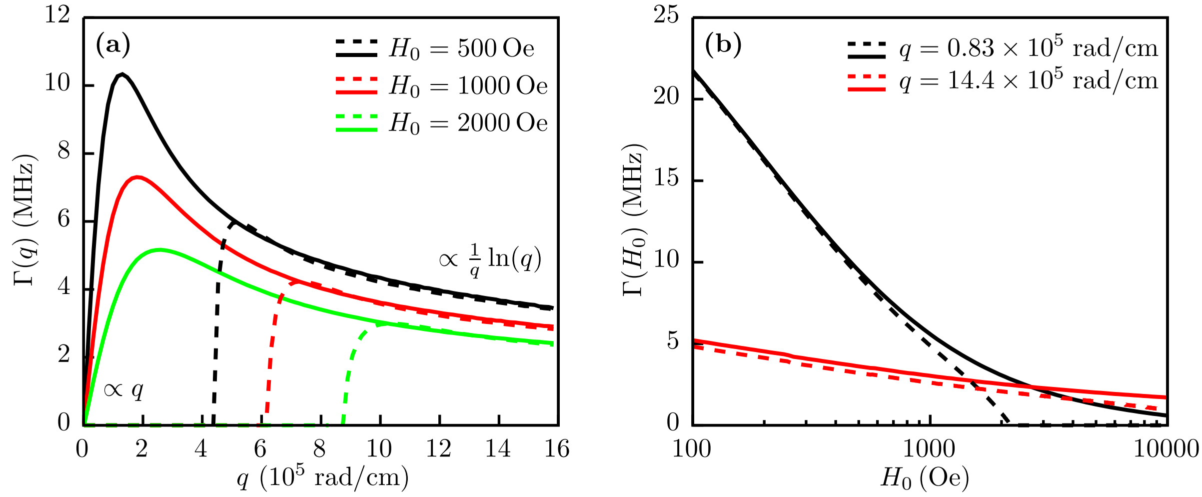

Figure 3.3: (a) Relaxation rates of the three-magnon process as a function of the wave vector for three different applied magnetic fields. The solid lines correspond to the confluence process whereas the dashed lines correspond to the splitting process. (b) Relaxation rates of the confluence process as a function of the applied magnetic field at two different wave vectors. The solid lines correspond to the common cut-off energy of $E_{\text{cut}} \approx 14.4$ THz, whereas the dashed lines correspond to a reduced cut-off energy of $E_{\text{cut}} = 100$ GHz above the minimal energy state.

the three-magnon process strongly depend on the applied magnetic field, at least at small wave vectors. The reason for this behavior can be found in the energy conservation laws in Eqs. (3.9a) and (3.9b), which in contrast to the four-magnon process depend on the applied magnetic field. Figure 3.3(a) shows the calculated relaxation rates as a function of the wave vector at three different magnetic fields. We begin with the confluence process, denoted by the solid lines, which vanishes at zero wave vector because the simultaneous fulfillment of energy and momentum conservation is not possible in this case. However, at small but nonzero wave vectors, the relaxation rates exhibit a characteristic linear dependence on the wave vector and reach a maximum between $q = 1 \times 10^5$ rad/cm and $q = 3 \times 10^5$ rad/cm for the applied magnetic fields used in the calculations. Apparently, as has also been revealed in Refs. [68,99], the three-magnon confluence process explains the linear increase of the relaxation rates as a function of the wave vector and the bend-over region as measured in the Kasuya-LeCraw experiment [48], although in our calculations the relaxation rates at the wave vector $q_0 = |\boldsymbol{q}_0|$ are averaged over the solid angle Ω_0 due to the isotropic approximation (cf. Sec. 2.2 and Appendix A.4). We nevertheless get a good qualitative agreement with the experiment. At large wave vectors, the relaxation rates gradually decrease and are proportional to $q^{-1}\ln(q)$, similar to the estimates made in Ref. [68].

We now turn to the splitting process, which is shown by the dashed lines in Fig. 3.3(a). We clearly see that there exists a sharp field-dependent threshold for the wave vector q_{crit} below which the splitting process is forbidden by the conservation laws. The minimal energy for the splitting magnon has to be at least twice the minimal energy of the system E_{min} in order to ensure the energy conservation. However, in this case, the momentum conservation is violated. Therefore, the minimal energy of the splitting magnon has to be larger and can be calculated by means of the conservation laws

$$\hbar\omega(q_{\text{crit}}) = \hbar\omega(q_1) + \hbar\omega(q_2), \tag{3.10a}$$

$$q_{\text{crit}} = q_1 + q_2. \tag{3.10b}$$

Minimizing q_{crit} in the above equations yields $q_{\mathrm{crit}} = 2\sqrt{g\mu_{\mathrm{B}}\mu_0 H_0/4JSa_0^2}$ and hence $\hbar\omega(q_{\mathrm{crit}}) = 3g\mu_{\mathrm{B}}\mu_0 H_0 = 3E_{\mathrm{min}}$. The relaxation rates strongly increase slightly above q_{crit} and then also gradually decrease proportional to $q^{-1}\ln(q)$, so that at large wave vectors both the splitting and confluence process contribute equally to the total three-magnon relaxation rate.

As we have just seen, at small wave vectors, both the confluence and the splitting process strongly depend on the applied magnetic field, whereas the relaxation rates at larger wave vectors are rather unaffected by variation of the latter. In order to investigate this dependence more thoroughly, we plot in Fig. 3.3(b) the relaxation rates of the confluence process as a function of the magnetic field at two different wave vectors. The solid lines correspond to the cut-off energy of $E_{\mathrm{cut}} \approx 14.4$ THz, following from Eq. (2.82b), which we employ throughout this thesis. In order to see which magnons contribute in the scattering processes and if a smaller cut-off energy would give the same results, we decrease the cut-off energy to $E_{\mathrm{cut}} = 100$ GHz above the minimum for the moment. The resulting relaxation rates are shown by the dashed lines. At $q = 0.83 \times 10^5$ rad/cm, which corresponds to an energy of 100 MHz above the minimum, the relaxation rates exhibit a significant dependence on the magnetic field below $H_0 \approx 1000\,\mathrm{Oe}$ and coincide for the two different cut-off energies. However, at magnetic fields above $H_0 \approx 1000\,\mathrm{Oe}$, there are large deviations which remarkably manifest in the disappearance of the confluence process for magnetic fields of $H_0 \gtrsim 2000\,\mathrm{Oe}$ in the case of the smaller cut-off energy. This can be realized by means of the conservation laws

$$\hbar\omega(q) + \hbar\omega(q_1) = \hbar\omega(q_2), \tag{3.11a}$$

$$q_2 - q_1 < q, \tag{3.11b}$$

which require that the energies of the confluent magnons have to obey

$$[\hbar\omega(q) - E_{\mathrm{min}}]\,[\hbar\omega(q_1) - E_{\mathrm{min}}] > \frac{1}{4}E_{\mathrm{min}}^2, \tag{3.12}$$

which indeed yields $\hbar\omega(q_1) > 100$ GHz for an applied magnetic field of $H_0 \approx 2186\,\mathrm{Oe}$. In contrast, at $q = 14.4 \times 10^5$ rad/cm, which corresponds to an energy of 30 GHz above the minimum, the relaxation rates only gradually decrease and the deviations resulting from the smaller cut-off energy barely depend on the magnetic field, at least for fields of $H_0 \lesssim 4000\,\mathrm{Oe}$. This shows, in accordance with Eq. (3.12), that the conservation laws in this case permit scattering processes with magnons having energies below $\hbar\omega(q_1) = 100$ GHz which contribute the most to the relaxation rate. Besides, the reason for the different degree of influence on the magnetic field can also be explained by the conservation laws, which, according to Eq. (3.12), considerably prohibit the scattering with magnons having small energies in the confluence process at small wave vectors. Therefore, the relaxation rates significantly decrease with increasing magnetic field, in contrast to the relaxation rates of the confluence process at large wave vectors, where the conservation laws do not restrict severely the scattering with low energy magnons. The slight decrease of the relaxation rates in this case, however, is mainly caused by the equilibrium Bose-Einstein distributions in Eq. (3.9b), which slightly decrease with increasing magnetic field.

In conclusion, we have seen that magnons having energies $E > 100$ GHz are responsible for the confluence process to occur at small wave vectors $q \lesssim 0.83 \times 10^5$ rad/cm and moderate magnetic fields of $H_0 \approx 2000\,\mathrm{Oe}$. This fact is especially important for the damping of the condensate in thin magnetic films, in which the dipolar interaction leads to a minimal energy state exhibiting a nonzero wave vector q_{min}, which in the case of the dipole-exchange dispersion in Fig. 2.1(b) amounts to $q_{\mathrm{min}} \approx 0.5 \times 10^5$ rad/cm. In addition, it is possible to reduce the damping of magnons with small wave vectors by increasing the applied magnetic field.

3.1.4 Magnon-Phonon Coupling: Cherenkov Process

In a first step, we analyze the relaxation rates of the Cherenkov process in order to see in which wave vector range this process is strong and where it is negligible or even forbidden due to the conservation laws. As in the case of the three-magnon process, the Cherenkov process can also be separated into a splitting process, whose relaxation rates are given by

$$\Gamma(\boldsymbol{q}_0) = \frac{2\pi}{\hbar}\frac{a_0^3}{(2\,\pi)^3}\sum_{\sigma}\iint \mathrm{d}^3q_1\mathrm{d}^3q_2\Big[\,|V_\sigma(\boldsymbol{q}_1,\boldsymbol{q}_2)|^2\,\delta(\hbar\omega(\boldsymbol{q}_0)-\hbar\omega(\boldsymbol{q}_1)-\hbar\omega_\sigma(\boldsymbol{q}_2)) \\ \times\,\delta(\boldsymbol{q}_0-\boldsymbol{q}_1-\boldsymbol{q}_2)\,\Big(\,(1+f(\boldsymbol{q}_1))\,(1+f_\sigma(\boldsymbol{q}_2))-f(\boldsymbol{q}_1)f_\sigma(\boldsymbol{q}_2)\Big)\Big], \tag{3.13a}$$

and a confluence process, whose relaxation rates are given by

$$\Gamma(\boldsymbol{q}_0) = \frac{2\pi}{\hbar}\frac{a_0^3}{(2\,\pi)^3}\sum_{\sigma}\iint \mathrm{d}^3q_1\mathrm{d}^3q_2\Big[\,|V_\sigma(\boldsymbol{q}_0,\boldsymbol{q}_2)|^2\,\delta(\hbar\omega(\boldsymbol{q}_0)+\hbar\omega_\sigma(\boldsymbol{q}_2)-\hbar\omega(\boldsymbol{q}_1)) \\ \times\,\delta(\boldsymbol{q}_0+\boldsymbol{q}_2-\boldsymbol{q}_1)\,\Big(f_\sigma(\boldsymbol{q}_2)\,(1+f(\boldsymbol{q}_1))-f(\boldsymbol{q}_1)\,(1+f_\sigma(\boldsymbol{q}_2))\,\Big)\Big], \tag{3.13b}$$

where both magnon and phonon distribution functions are fixed Bose-Einstein distributions at room temperature equilibrium. Due to the conservation laws in Eqs. (3.13a) and (3.13b), the relaxation rates are, as in the four-magnon process, almost independent on the external magnetic field which we set to be $H_0 = 1000\,\mathrm{Oe}$. The Figs. 3.4(a) and 3.4(b) show the calculated relaxation rates as a function of the wave vector. We see that at large wave vectors the confluence process, denoted by the black lines, and the splitting process, denoted by the red lines, exhibit similarly high relaxation rates in the gigahertz range (Fig. 3.4(b)), whereas the relaxation rates of both processes strongly diminish at smaller wave vectors and fall into the sub-megahertz range (Fig. 3.4(a)). On the one hand, the reason for this behavior can be found in the Cherenkov interaction potential V_σ, given in Eq. (2.41), which decreases with decreasing wave vector of the participating particles and even vanishes at zero momentum. On the other hand, the momentum and energy conservation laws restrict the allowed scattering processes in the low wave vector regime. This fact is considerably manifested in the splitting process, which is forbidden below a critical wave vector q_1, as indicated in Fig. 3.4(a) by the left dashed line. Since the differences of both energy and momentum between the splitting magnon and the resulting magnon after the scattering have to be equal to the energy and momentum of the emitted phonon, respectively, the gradient and hence the group velocity of the magnons has to be larger than the group velocity of the phonons for the Cherenkov splitting process to be effective. The lowest possible wave vector q_1 of the splitting magnon is thus determined via

$$\frac{\mathrm{d}}{\mathrm{d}q}\omega(q)\bigg|_{q_1} = v_\perp, \tag{3.14}$$

which gives $q_1 \approx 21.1 \times 10^5$ rad/cm. Figure 3.5 shows the dispersion relation of the magnons and the transverse and longitudinal phonon branches. The critical wave vector q_1 is indicated

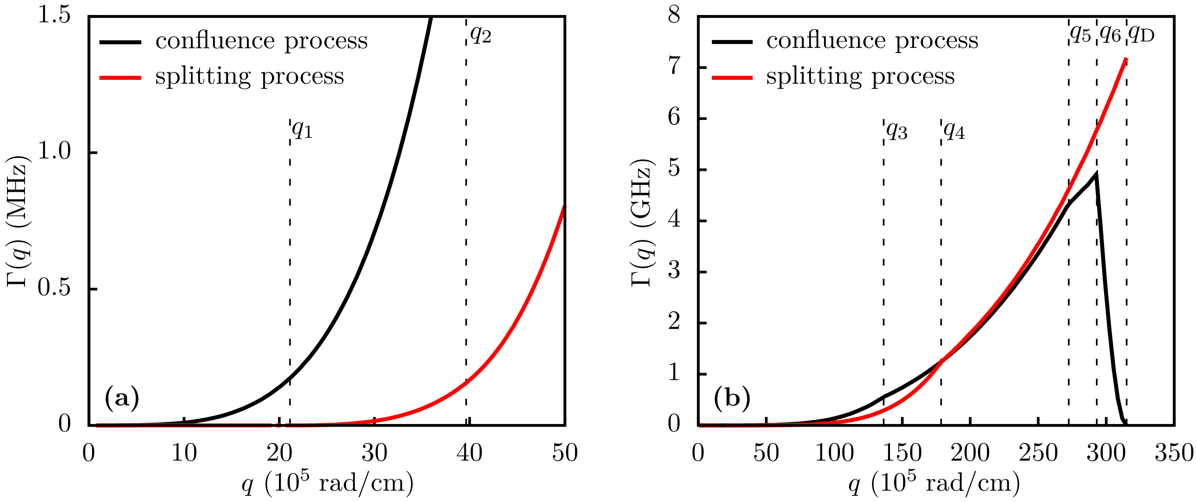

Figure 3.4: Relaxation rates of the Cherenkov process as a function of the wave vector. The black lines correspond to the confluence process while the red lines correspond to the splitting process. The dashed lines indicate the wave vectors q_1 to q_6 at which qualitative changes of the relaxation processes occur. q_D is the Debye wave vector.

in the inset of Fig. 3.5 which corresponds to a magnon energy of $E_1 \approx 67$ GHz. Above a second critical wave vector determined by

$$\frac{\mathrm{d}}{\mathrm{d}q}\omega(q)\bigg|_{q_2} = v_\parallel, \tag{3.15}$$

also the scattering with longitudinal phonons contributes to the splitting process. The wave vector $q_2 \approx 39.6 \times 10^5$ rad/cm corresponds to a considerably higher magnon energy of $E_2 \approx$ 230 GHz, also indicated in the inset of Fig. 3.5. In general, the condition (3.14) limits the minimal possible wave vector of the magnon with the larger energy participating in the Cherenkov process. As a consequence, also in the confluence process, the wave vector of the resulting magnon after the scattering does not fall below q_1. For this reason, the splitting and also the confluence process are called *Cherenkov processes* [20] in analogy to charged particles moving faster than light in a dielectric medium and thus emitting *Cherenkov radiation* [100]. Furthermore, as it is apparent in Fig. 3.4(b), there are pronounced corners in the relaxation rates in both the splitting process and the confluence process which mark some qualitative changes in the scattering processes. These changes are easiest to understand by following the graph of the confluence process from large to small wave vectors. Beginning at the Debye wave vector q_D, the relaxation rates grow since more and more scattering processes are enabled due to the increasing amount of magnon states lying above the state of the confluent magnon. The increase of the relaxation rates stops at the wave vector q_6, where scattering processes into the highest magnon states are only just possible by absorbtion of a transverse phonon with the highest energy. The critical wave vector q_6 is thus determined by

$$\hbar\omega(q_\mathrm{D}) - \hbar\omega(q_6) = \hbar\omega_\perp(q_\mathrm{D}), \tag{3.16}$$

which gives $q_6 \approx 293.1 \times 10^5$ rad/cm. The explanation of the next corner at q_5 is the same as before but here the corner is caused by the prohibition of the relaxation channel through longitudinal phonons into the highest magnon states. The critical wave vector q_5 is thus

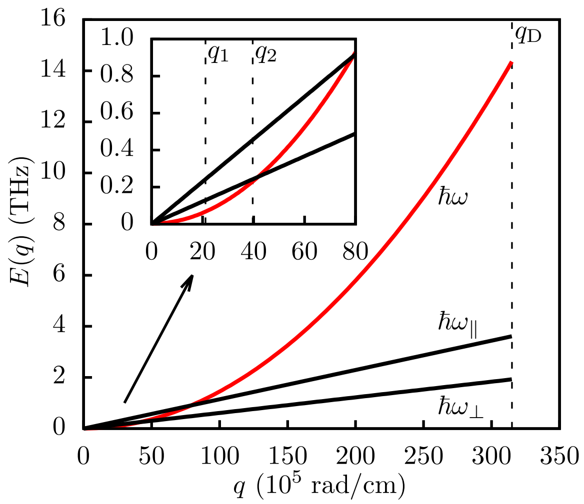

Figure 3.5: Dispersion relations of the magnons (2.78a) and of the phonons (2.78b). The red line shows the magnon dispersion $\hbar\omega$, while the black lines denote the transverse $\hbar\omega_{\perp}$ and longitudinal $\hbar\omega_{\|}$ branches of the phonons, as indicated. The dashed black line indicates the Debye wave vector q_{D}. The inset shows a zoom into the region with smaller wave vectors, where the dashed lines indicate the critical wave vectors q_1 and q_2, respectively.

determined by

$$\hbar\omega(q_{\mathrm{D}}) - \hbar\omega(q_5) = \hbar\omega_{\|}(q_{\mathrm{D}}), \tag{3.17}$$

which gives $q_5 \approx 272.4 \times 10^5$ rad/cm. By further decreasing the wave vector, we reach the next critical wave vector q_3 of the confluence process. At this wave vector, a magnon can only just absorb a transverse phonon with the highest energy if the confluent magnon and the resulting magnon have momenta in opposite directions. Therefore, we determine q_3 via

$$\hbar\omega(q_{\mathrm{D}} - q_3) - \hbar\omega(q_3) = \hbar\omega_{\perp}(q_{\mathrm{D}}), \tag{3.18}$$

and we obtain $q_3 \approx 136.3 \times 10^5$ rad/cm. The reversed process is a splitting of a magnon having the critical wave vector $q_4 = q_{\mathrm{D}} - q_3 \approx 178.6 \times 10^5$ rad/cm at which the corner in the graph of the splitting process occurs.

As we have just seen, it is possible to explain the corners in the relaxation rates by geometrical arguments concerning the conservation laws. In summary, the Cherenkov process is negligible at small wave vectors, where the four-magnon and the three-magnon processes dominate, but it has a strong influence on the relaxation rates at large wave vectors, nevertheless remaining below the rates of the four-magnon process.

3.2 Magnon Equilibration

This section discusses dynamic relaxation processes of non-equilibrium initial conditions in the case of the three magnon interactions which we are considering. A remarkable property of the Boltzmann equation is its irreversible time evolution towards the equilibrium which is manifested in Boltzmann's H-theorem (cf. Sec. 2.2). For all three interactions, we demonstrate this property by means of the non-equilibrium entropy in the closed magnon system and the non-equilibrium free energy in the open magnon system, coupled to a phonon heat bath. Furthermore, we compare the nonlinear dynamics in the closed magnon system with the linear relaxation rates determined in the preceding section and we show the strong dependence of the four-magnon process on the local magnon density, which is not as pronounced as in the case of the three-magnon process. We begin the analysis with the four-magnon process and show its importance for the magnon Bose-Einstein condensation, which solely depends on the initial conditions. After that, we consider the three-magnon process and discuss its role in the damping of the magnetic system. Finally, we investigate the magnon dynamics under the Cherenkov process, which admits an energy transfer between the magnetic system and the lattice.

3.2.1 Four-Magnon Scattering

The most important interaction for the internal thermalization is the four-magnon scattering process, where two magnons are annihilated and two magnons are created under energy conservation (2 in, 2 out). Therefore, this process also conserves the total magnon number which is a prerequisite for the establishment of a Bose-Einstein condensation.

First of all, we demonstrate the relaxation dynamics of a non-equilibrium distribution under the four-magnon process, described by the kinetic equations (2.83), (2.88) and (2.89). For this purpose, we choose the external magnetic field to be $H_0 = 1000\,\mathrm{Oe}$, which shifts the minimal energy state to $E_{\mathrm{min}} \approx 2.8$ GHz, and we set an initial magnon distribution at room temperature equilibrium, that is $T_{\mathrm{m}} = 300$ K and $\mu_{\mathrm{m}} = 0$. We further add a broad peak

$$f_{\mathrm{peak}}(\boldsymbol{q}) = \rho_0 \, \exp\Big(-(2\,(\hbar\omega(\boldsymbol{q}) - E_{\mathrm{peak}})\,/\Delta E)^2\Big) \tag{3.19}$$

to the distribution function, where we choose $\Delta E = 115$ GHz, $E_{\mathrm{peak}} = 400$ GHz and $\rho_0 = 50$. For the moment, we reduce the cut-off energy to $E_{\mathrm{cut}} = 1$ THz above the minimal energy state for numerical reasons. As we have shown in Sec. 2.2, we have to give a seed for the condensate which we choose to be $n_c(t = 0) = 10^{-10}$. The total magnon number N_{tot} and the internal energy U are determined via

$$N_{\mathrm{tot}} = n_c + \frac{a_0^3}{(2\,\pi)^3} \int \mathrm{d}^3q\, f(\boldsymbol{q}), \tag{3.20a}$$

$$U = n_c E_{\mathrm{min}} + \frac{a_0^3}{(2\,\pi)^3} \int \mathrm{d}^3q\, f(\boldsymbol{q})\, \hbar\omega(\boldsymbol{q}), \tag{3.20b}$$

which give $N_{\mathrm{tot}} \approx 0.4$ and $U \approx 145$ GHz. These two quantities are collisional invariants since the four-magnon process conserves both magnon number and magnon energy. As we have also shown in Sec. 2.2, the equilibrium states of the four-magnon process are Bose-Einstein distribution functions f_{BE} with the magnon temperature T_{m} and a generally nonzero chemical potential $\mu_{\mathrm{m}} \neq 0$ which are given implicitly via the relations

$$N_{\mathrm{tot}} = n_c + \frac{a_0^3}{(2\,\pi)^3} \int \mathrm{d}^3q\, f_{\mathrm{BE}}(\boldsymbol{q}, T_{\mathrm{m}}, \mu_{\mathrm{m}}), \tag{3.21a}$$

$$U = n_c E_{\mathrm{min}} + \frac{a_0^3}{(2\,\pi)^3} \int \mathrm{d}^3q\, f_{\mathrm{BE}}(\boldsymbol{q}, T_{\mathrm{m}}, \mu_{\mathrm{m}})\, \hbar\omega(\boldsymbol{q}). \tag{3.21b}$$

Solving these equations, we obtain $T_{\mathrm{m}} \approx 395$ K and $\mu_{\mathrm{m}} \approx -2.3$ GHz, so the chemical potential does not reach the minimal energy state. Thus, the initial conditions are subcritical and the magnon system does not undergo Bose-Einstein condensation, therefore n_c will vanish in equilibrium. We now investigate the time evolution of the initial magnon distribution towards the equilibrium state which is shown in Fig. 3.6(a). The initial peak at $E_{\mathrm{peak}} = 400$ GHz is damped very quickly within several nanoseconds which just reflects the large relaxation rates in the gigahertz-range as calculated in the preceding section. The magnons which scatter to even larger energy states immediately reach the equilibrium state. In contrast to this, the

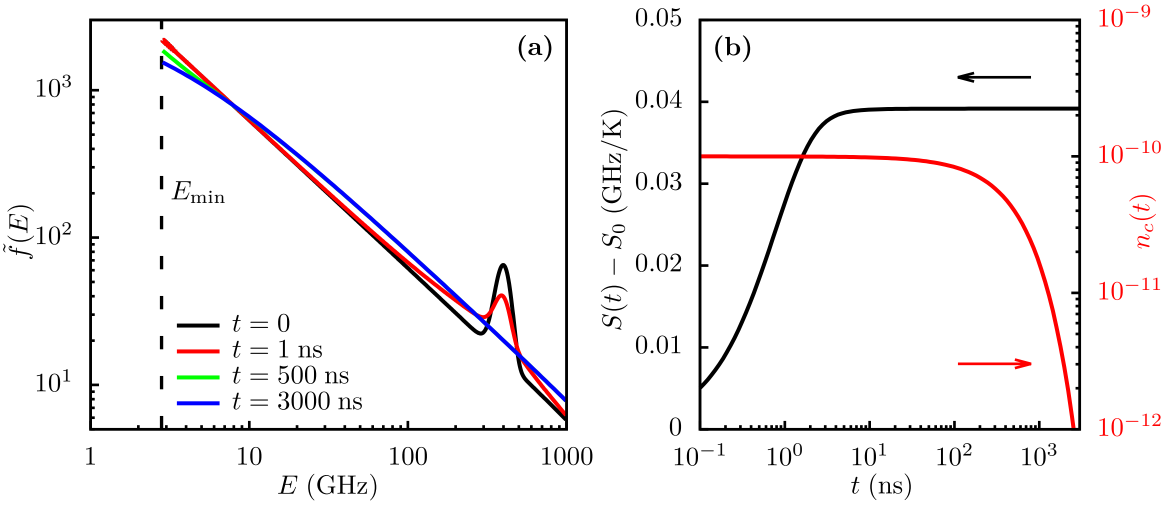

Figure 3.6: (a) Time evolution of the magnon distribution under the four-magnon process in the case of subcritical initial conditions. The black line shows the initial magnon distribution at room temperature equilibrium augmented by a broad peak at $E_{\rm peak} = 400$ GHz, described by Eq. (3.19). The dashed black line indicates the minimal energy state $E_{\rm min} \approx 2.8$ GHz. (b) Magnon condensate n_c, denoted by the red line, and the non-equilibrium entropy S, as defined in Eq. (2.71) and denoted by the black line, as a function of time.

scattering to lower energy states takes place on a considerably larger timescale of several hundreds of nanoseconds until the equilibrium state, as determined above, is achieved at about $t \approx 3000$ ns. Figure 3.6(b) shows the time evolution of the condensate. The initial seed of $n_c = 10^{-10}$ gradually decreases and eventually vanishes in equilibrium, which is caused by magnons scattering out of the condensate into the gaseous magnon phase. As also shown in Fig. 3.6(b), the whole dynamic process is irreversible since the non-equilibrium entropy, as defined in Eq. (2.71), monotonically increases and saturates when the system approaches the equilibrium state.

We now study the supercritical case in which Bose-Einstein condensation takes place. In order to establish these conditions, we move the initial peak to smaller energies and choose $\Delta E = 36$ GHz, $E_{\rm peak} = 100$ GHz and $\rho_0 = 323$ in Eq. (3.19). Using Eqs. (3.20a) and (3.20b), we obtain the same total magnon number as in the previous case $N_{\rm tot} \approx 0.4$, but a smaller internal energy of $U \approx 118$ GHz, as intended. Using again Eqs. (3.21a) and (3.21b), we see that these initial conditions indeed fulfill the critical conditions for BEC and belong to an equilibrium state with $T_{\rm m} \approx 320$ K and $\mu_{\rm m} = E_{\rm min}$, exhibiting a condensate $n_c \approx 0.04$. The time evolution of the magnon distribution is shown in Fig. 3.7(a). A little slower than in the previous case, the initial peak is damped within some tens of nanoseconds, which is also explained by the smaller relaxation rates in this energy region, and the magnons again redistribute over the entire spectrum. In this case however, a big fraction accommodates the low lying energy part of the spectrum, smaller than $E \approx 10$ GHz at about $t \approx 1000$ ns. These magnons then begin to scatter into the condensate which immediately grows, as shown by the solid red line in Fig. 3.7(b), and which saturates at about $t \approx 3000$ ns thus reaching the equilibrium state. This whole process is again irreversible as shown by the monotonic increase and saturation of the non-equilibrium entropy, represented by the solid black line.

At room temperature, where the thermal energy $k_{\rm B}T_{\rm m} \approx 6$ THz is much larger than the energies of the low lying magnon states, the Bose-Einstein distribution reduces to a Rayleigh-

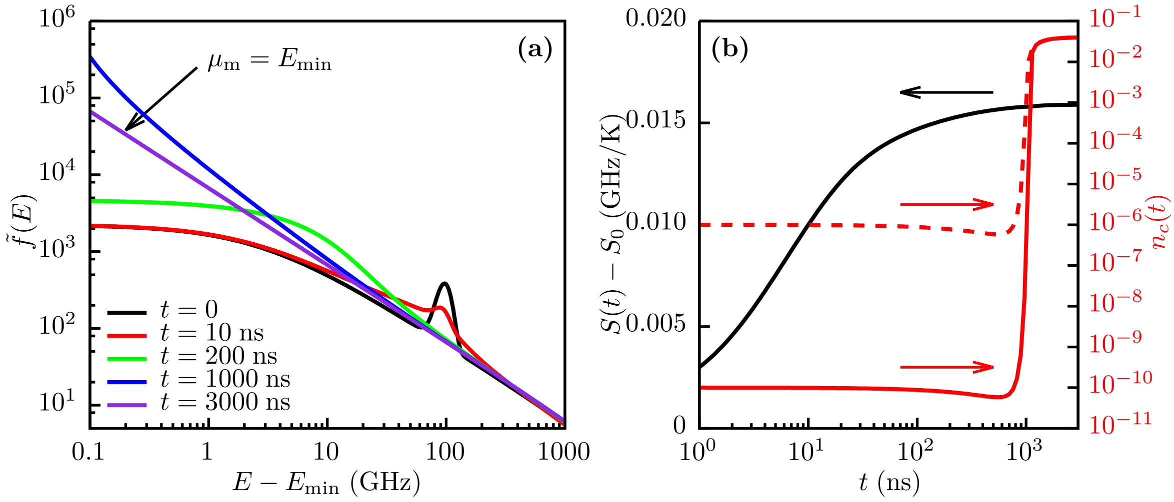

Figure 3.7: (a) Time evolution of the magnon distribution under the four-magnon process in the case of supercritical initial conditions. The black line shows the initial magnon distribution at room temperature equilibrium augmented by a broad peak at $E_{peak} = 100$ GHz, described by Eq. (3.19). (b) Time evolution of the magnon condensate n_c (red lines) and the non-equilibrium entropy S (black line). The condensate with an initial seed of $n_c(t = 0) = 10^{-10}$ is denoted by the solid red line, whereas the condensate with an initial seed of $n_c(t = 0) = 10^{-6}$ is denoted by the dashed red line.

Jeans distribution

$$\tilde{f}(E) = \frac{k_B T_m}{E - \mu_m}. \tag{3.22}$$

Therefore, the critical magnon distribution with $\mu_m = E_{min}$ appears as a straight line in a double-logarithmic plot as indicated in Fig. 3.7(a). In this sense, it is just a matter of semantics if one calls the magnon condensation a Rayleigh-Jeans rather than a Bose-Einstein condensation (cf. Ref. [45]).

In addition, we briefly check the dependence of the initial value of the condensate $n_c(t = 0)$, which is chosen arbitrarily, on the condensation process. Therefore, we repeat the simulation with a larger seed of $n_c(t = 0) = 10^{-6}$. The result is shown by the dashed red line in Fig. 3.7(b). The condensate stays rather constant at the initial value until about $t \approx 1000$ ns and then promptly increases and saturates at the equilibrium occupation with $n_c \approx 0.04$, exactly as in the case with the smaller seed of $n_c(t = 0) = 10^{-10}$, illustrated by the solid red line. Therefore, we conclude that the particular choice of the seed is not important as far as the condition $n_c(t = 0) \ll N_{tot}$ is satisfied [85,86]. A deeper analysis [86,88] shows that the condensate increases with a power law $n_c(t) \propto (t - t_*)^\alpha$ just after the moment of condensation t_* which in our case is at $t_* \approx 1000$ ns. The moment of condensation generally depends on the initial conditions of the gaseous magnon phase, provided that these are supercritical.

So far, we have dealt with non-equilibrium initial conditions which are difficult to realize in practice. In experiments, magnons are excited via microwave pumping in the low energy region ($E < 10$ GHz) of the spectrum and the time evolution of these primary magnons is studied via Brillouin light scattering [22]. In the following, we thus consider non-equilibrium situations which resemble real situations in experiments after the pumping stops and we investigate the relaxation of primary magnons located narrowly in energy space which we add to the room temperature equilibrium distribution. We describe these primary magnons by means of Eq. (3.19), where we choose $\Delta E = 0.5$ GHz and $E_{peak} = 4.05$ GHz in order to come close to the experimental conditions [24,25]. From now on, we employ again the common cut-

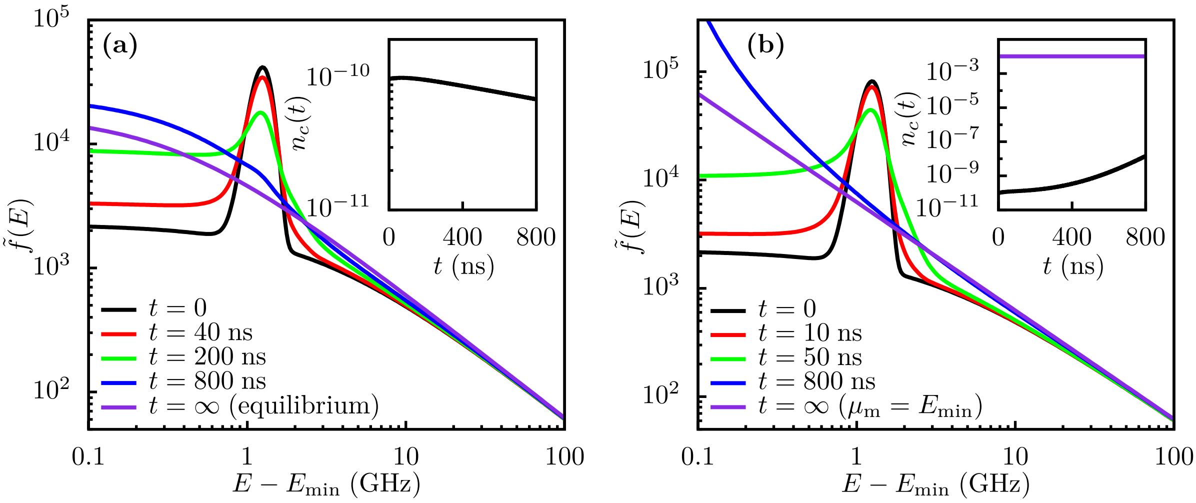

Figure 3.8: Time evolution of the magnon distribution under the four-magnon process. The black lines show the initial magnon distributions at room temperature equilibrium augmented by a narrow peak at $E_{\mathrm{peak}} = 4.05$ GHz, described by Eq. (3.19), respectively. The insets show the time evolution of the magnon condensate. (a) Subcritical density. (b) Supercritical density.

off energy given by Eq. (2.82b). First, we consider a subcritical density with $\rho_0 = \rho_{\mathrm{sub}} = 4 \times 10^4$ and calculate the time evolution of this initial peak which is shown in Fig. 3.8(a). The peak is broadened due to the scattering of magnons to higher and lower energy states respectively on a timescale of several hundreds of nanoseconds, where the equilibrium distribution with $\mu_{\mathrm{m}} < E_{\min}$, which we have calculated by means of Eqs. (3.20a), (3.20b), (3.21a) and (3.21b), is shown by the purple line. The inset of Fig. 3.8(a) shows the occupation of the condensate which decays because the critical condition for BEC is not fulfilled. However, by choosing $\rho_0 = \rho_{\mathrm{sup}} = 8 \times 10^4$, we double the density of primary magnons and thus exceed the critical density necessary for condensation. This situation is shown in Fig. 3.8(b) where the magnons quickly redistribute similarly as in the previous case and where the equilibrium distribution with $\mu_{\mathrm{m}} = E_{\min}$ is indicated by the straight purple line. During this redistribution process the condensate increases, as shown in the inset of Fig. 3.8(b), and finally saturates at the equilibrium occupation, also denoted by the purple line. As distinguished from the previous case with half amount of primary magnons, we see that in this case the time evolution is much faster. In order to demonstrate this behavior more thoroughly, we plot the amount of magnons located in the peak region

$$N_{\mathrm{peak}} = \frac{a_0^3}{(2\,\pi)^3} \int \mathrm{d}^3 q \; \left(f(\boldsymbol{q}) - f_{\mathrm{BE}}(\boldsymbol{q})\right) \frac{f_{\mathrm{peak}}(\boldsymbol{q})}{\rho_0}, \tag{3.23}$$

as a function of time for both cases, respectively, where f_{peak} is defined in Eq. (3.19). The function f_{BE} in Eq. (3.23) denotes the equilibrium distribution in both cases, respectively. In order to compare both situations, we normalize the densities to their maximal values, respectively, and we compare the nonlinear relaxation rates with the linear relaxation rate at $q_{\mathrm{peak}} \approx 2.94 \times 10^5$ rad/cm, according to the position of the peak (3.19) in energy space at $E_{\mathrm{peak}} = 4.05$ GHz, which we have already determined in the preceding section. The result is shown in Fig. 3.9, where the solid red line corresponds to the subcritical density and the solid black line corresponds to the supercritical density. In addition, we also indicate the initial nonlinear rates by the straight dashed lines, respectively. As expected, the relaxation rates in the case of the supercritical density are initially larger than in the case of the subcritical

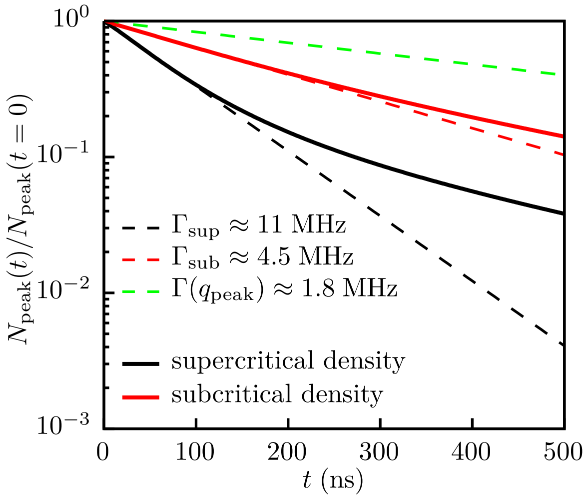

Figure 3.9: Nonlinear relaxation of primary magnons calculated by means of Eq. (3.23). The black lines denote the nonlinear relaxation in the supercritical case (sup), whereas the red lines denote the nonlinear relaxation in the subcritical case (sub). The straight dashed lines correspond to the initial relaxation rates Γ_{sup} and Γ_{sub} in the temporal interval between $t = 0$ and $t = 80$ ns, respectively. The straight dashed green line indicates the linear relaxation with the relaxation rate $\Gamma(q_{\text{peak}})$, calculated by means of Eq. (3.5). The wave vector $q_{\text{peak}} \approx 2.94 \times 10^5$ rad/cm corresponds to the location of the initial peak at $E_{\text{peak}} = 4.05$ GHz, described by Eq. (3.19).

density whereas during the time evolution both rates decrease and saturate at about $t \approx 500$ ns approximately at the linear relaxation rate $\Gamma(q_{\text{peak}}) \approx 1.8$ MHz. We determine the initial rate in the case of the supercritical density to be approximately $\Gamma_{\text{sup}} \approx 11$ MHz which is more than twice as large as the initial rate in the subcritical case $\Gamma_{\text{sub}} \approx 4.5$ MHz. This is an essential property of the four-magnon process becoming stronger at higher densities which is a direct consequence of the conservation laws being always satisfied in a narrow region in wave vector space. In order to show this last statement, we linearize the (arbitrary) magnon dispersion about a certain wave vector $\boldsymbol{q}$ and we consider the resulting conservation laws in the four-magnon process which thus read

$$\boldsymbol{q}_0 \cdot \boldsymbol{\nabla} \hbar\omega(\boldsymbol{q}) + \boldsymbol{q}_1 \cdot \boldsymbol{\nabla} \hbar\omega(\boldsymbol{q}) = \boldsymbol{q}_2 \cdot \boldsymbol{\nabla} \hbar\omega(\boldsymbol{q}) + \boldsymbol{q}_3 \cdot \boldsymbol{\nabla} \hbar\omega(\boldsymbol{q}), \tag{3.24a}$$

$$\boldsymbol{q}_0 + \boldsymbol{q}_1 = \boldsymbol{q}_2 + \boldsymbol{q}_3. \tag{3.24b}$$

We see that in this case the energy conservation (3.24a) holds by default if only the momentum conservation (3.24b) is satisfied, which considerably facilitates the fulfillment of the conservation laws in the four-magnon process. Because of this relation, most of the scattering processes are strongly located in energy space and are thus enhanced by a higher local density. This is in contrast to both the three-magnon process and the Cherenkov process which are generally nonlocal in energy space due to the severe restrictions of the conservation laws for these processes. Turning again to Fig. 3.9, the initially larger relaxation rate in the supercritical case is caused by the larger density of scattering partners of a primary magnon which are predominantly located in the initial peak. Therefore, by doubling the magnon density in the peak, the density of the scattering partners $f(\boldsymbol{q}_1)$ will also be doubled roughly, which results in an increase of the four-magnon relaxation rate (3.5) by a factor of two, approximately. Gradually, the nonlinear relaxation rates of both the subcritical and supercritical cases decrease and approximately approach the linear relaxation rate since the initial peak is broadened during the time evolution as shown in Figs. 3.8(a) and 3.8(b), resulting in a weakening of the local scattering in the peak.

In this sense, it is reasonable to attribute a strong nonlinearity to the four-magnon process. This property is exploited in the experiments of pumped magnons [19, 23–33], where the four-magnon process has to prevail over the three-magnon process in order to satisfy the conditions for Bose-Einstein condensation. We focus on this dynamical interplay in Sec. 4.1 of the subsequent chapter.

3.2.2 Three-Magnon Scattering

The most important process for the damping of the magnetic system is the three-magnon process, which in contrast to the four-magnon process does not conserve the total magnon number. Nevertheless, the three-magnon process conserves the internal energy being an inherent process in the closed magnon system.

In order to study this process, which is described by the kinetic equation (A.41) in Appendix A.4, we keep the magnetic field of $H_0 = 1000\,\mathrm{Oe}$ and we set an initial magnon distribution with $T_\mathrm{m} = 300$ K and $\mu_\mathrm{m} = E_\mathrm{min}$ which corresponds to the critical condition for BEC. This situation is very important since experiments in the field of magnon BEC are commonly performed at room temperature [19,23–33]. As already shown in Sec. 2.2, the equilibrium state of the three-magnon process is a Bose-Einstein distribution function with zero chemical potential. Figure 3.10(a) shows the time evolution of this initial magnon distribution under the three-magnon scattering. The magnons are gradually damped on a timescale of several hundreds of nanoseconds and the equilibrium state is approached approximately at $t \approx 2$ µs. The total magnon number, as shown in Fig. 3.10(b), decreases non-exponentially due to the different energy-dependent relaxation rates involved in the scattering, which we have discussed in the previous section. In addition, also the changes in the magnon distributions during the time evolution influence the relaxation process. In order to quantify the depletion of the total magnon number, we consider a fall time τ_fall defined by

$$N_\mathrm{tot}(\tau_\mathrm{fall}) = N_\mathrm{tot}(\mu_\mathrm{m} = 0) + \exp(-1)\,[\,N_\mathrm{tot}(\mu_\mathrm{m} = E_\mathrm{min}) - N_\mathrm{tot}(\mu_\mathrm{m} = 0)\,]\,, \tag{3.25}$$

which gives $\tau_\mathrm{fall} \approx 525$ ns. The reason for the decrease of the total magnon number is the three-magnon confluence process, in which two magnons in the low energy part of the spectrum coalesce under creation of a high energy magnon. Due to the energy conservation in the three-magnon process, the temperature in the equilibrium state will be larger than the initial $T_\mathrm{m} = 300$ K. By means of Eq. (3.20b), we determine the internal energy to be $U \approx 3.06$ THz, which is a collisional invariant. Knowing the chemical potential in equilibrium,

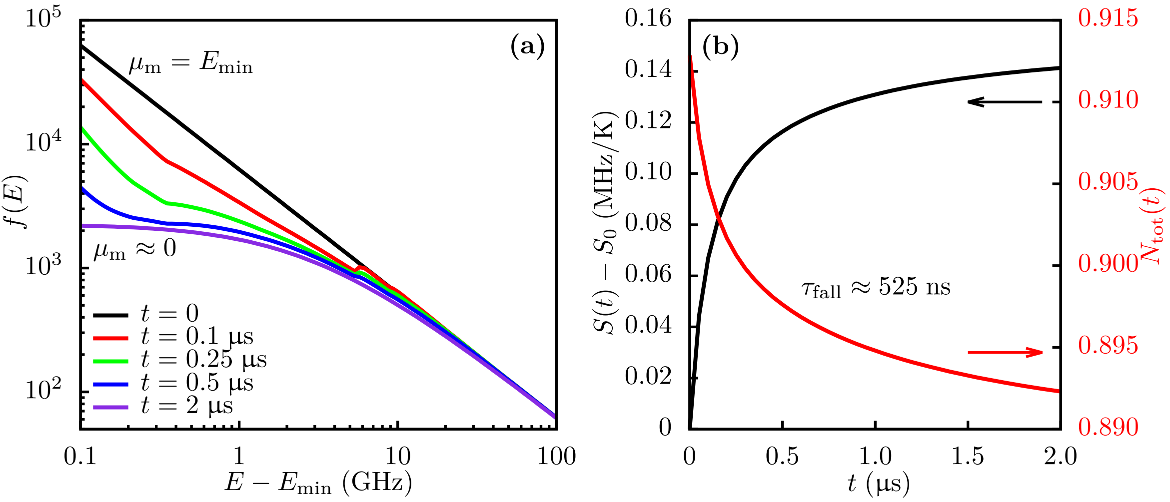

Figure 3.10: (a) Time evolution of the magnon distribution under the three-magnon process. The black line shows the initial magnon distribution with $T_\mathrm{m} = 300$ K and $\mu_\mathrm{m} = E_\mathrm{min}$. (b) Total magnon number N_tot (red line) and non-equilibrium entropy S (black line) as a function of time. τ_fall is the fall time of the total magnon number as defined in Eq. (3.25).

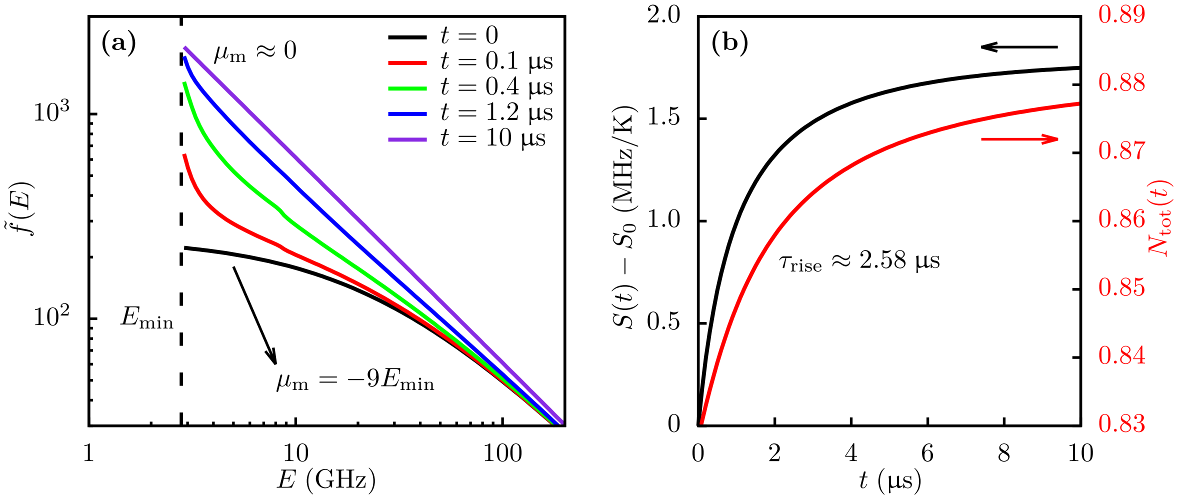

Figure 3.11: (a) Time evolution of the magnon distribution under the three-magnon process. The black line shows the initial magnon distribution with $T_m = 300$ K and $\mu_m = -9E_{\min}$. The dashed black line indicates the minimal energy of the system $E_{\min}$. (b) Total magnon number N_{tot} (red line) and non-equilibrium entropy S (black line) as a function of time. τ_{rise} is the rise time of the total magnon number as defined in Eq. (3.27).

that is $\mu_m = 0$, the equilibrium magnon temperature is given implicitly via

$$U = \frac{a_0^3}{(2\pi)^3} \int \mathrm{d}^3q \, f_{\text{BE}}(\boldsymbol{q}, T_m, \mu_m = 0) \, \hbar\omega(\boldsymbol{q}), \tag{3.26}$$

which yields $T_m = 300.2$ K, so only 0.2 K above the initial temperature. Because the room temperature equilibrium state is only slightly perturbed by approaching the critical condition for BEC, the magnon temperature remains rather unaffected in this case. As well as the four-magnon process, the three-magnon process is also irreversible which is demonstrated by the monotonic increase of the non-equilibrium entropy, shown in Fig. 3.10(b).

In the above simulation, the three-magnon process leads to a reduction of the total magnon number due to the confluence of two magnons. However, there are also cases in which the total magnon number increases due to the splitting of magnons. We study this case by setting an initial magnon distribution with $T_m = 300$ K and $\mu_m = -9E_{\min}$. The time evolution of this magnon distribution is shown in Fig. 3.11(a). Due to the negative chemical potential in the initial condition, there is a lack of magnons in the low energy part of the spectrum for attaining the equilibrium state with $\mu_m = 0$. This gap is filled via the splitting of magnons with high energy into two magnons with low energy. Due to the energy conservation, the temperature in the equilibrium state will be smaller than the initial $T_m = 300$ K. In order to show this, we again determine the internal energy by means of Eq. (3.20b) to be $U \approx 3.03$ THz in this case, and calculate the magnon temperature in equilibrium via Eq. (3.26) which yields $T_m = 298.4$ K. As different from the first case, the magnon dynamics occurs on a larger timescale of several microseconds, which is caused by two reasons. On the one hand, the slowed relaxation is due to the significantly smaller magnon distributions in the low energy region, which enter the kinetic equation. On the other hand, the negative chemical potential in this case also reduces the magnon distribution at higher magnon energies $E > 10$ GHz, as can be seen in Fig. 3.11(a) by comparing the initial and final distributions, respectively. The high energy magnons naturally have a smaller relaxation rate as we have demonstrated in the previous section, which additionally contributes to a retardation of the relaxation dynamics.

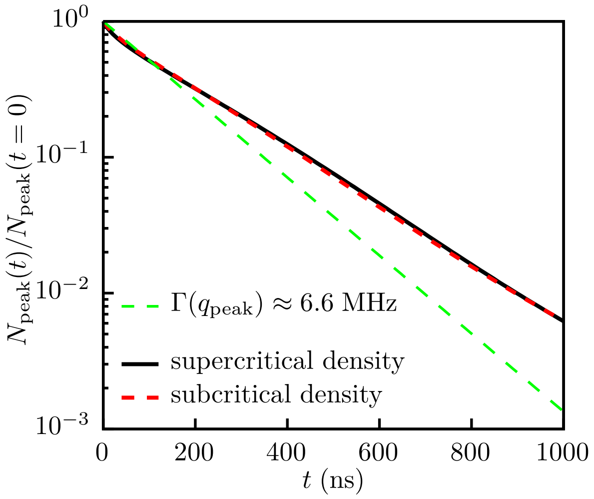

Figure 3.12: Relaxation of primary magnons calculated by means of Eq. (3.23) under the three-magnon process. The solid black line denotes the relaxation in the supercritical case, whereas the dashed red line denotes the relaxation in the subcritical case. The straight dashed green line indicates the linear relaxation with the relaxation rate $\Gamma(q_{\rm peak})$, calculated by means of Eq. (3.9b). The wave vector $q_{\rm peak} \approx 2.94 \times 10^5$ rad/cm corresponds to the location of the initial peak (3.19).

As a consequence, these two effects also manifest in the time evolution of the total magnon number, as shown in Fig. 3.11(b), which gradually increases and saturates as soon as the equilibrium state is reached at about $t \approx 10$ µs. In this case, we consider a rise time $\tau_{\rm rise}$ of the total magnon number defined by

$$N_{\rm tot}(\tau_{\rm rise}) = N_{\rm tot}(\mu_{\rm m} = 0) - \exp(-1)\,[\,N_{\rm tot}(\mu_{\rm m} = 0) - N_{\rm tot}(\mu_{\rm m} = -9E_{\rm min})\,]\,, \tag{3.27}$$

which gives $\tau_{\rm rise} \approx 2.58$ µs. The whole process is again irreversible as shown by the monotonic increase of the non-equilibrium entropy in Fig. 3.11(b).

As in the case of the four-magnon process, we also investigate nonlinear effects of the three-magnon process. We therefore repeat the simulations of the relaxation of primary magnons located in a narrow peak (3.19) for both the subcritical ($\rho_0 = \rho_{\rm sub}$) and the supercritical densities ($\rho_0 = \rho_{\rm sup}$) under the three-magnon process. The results are shown in Fig. 3.12 where we again normalize the amount of magnons in the peak region (3.23) with respect to the initial values, respectively. We see that in contrast to the four-magnon process, the graphs of the supercritical and of the subcritical densities coincide almost perfectly which shows that the three-magnon process is a linear process for perturbations located narrowly in energy space. This behavior can again be explained with the conservation laws of the three-magnon process, which prohibit the localized scattering of two or three magnons in most situations. The calculated rates are nevertheless somewhat smaller than the linear relaxation rate $\Gamma(q_{\rm peak})$ of the three-magnon confluence process, denoted by the dashed green line. This deviation can be explained with the total changes of the magnon distribution during the time evolution, which by default is not taken into account in the calculation of the linear relaxation rates (3.9b). As a consequence, the inverse process of splitting of magnons into the peak region is enhanced resulting in a reduction of the net relaxation rate. As can be seen in Fig. 3.12, the deviation begins not until $t \approx 100$ ns, where the total changes in the magnon distribution beyond the peak region are not negligible anymore.

In conclusion, it is possible to shift the relative strength of the three-magnon and four-magnon processes by varying the local magnon density, since the four-magnon process is nonlinear opposed to the three-magnon process, as we have just shown. We exploit this property in the discussion of the thermalization of magnons in Sec. 4.1.

3.2.3 Cherenkov Process

The four-magnon and three-magnon processes are inherent processes in the closed magnetic system where always energy conservation holds. The strongest coupling of the magnetic system to the environment with allowance for an energy transfer is due to phonons, where the most important magnon-phonon interaction is the Cherenkov process. In this process, a phonon is either absorbed (confluence process) or emitted (splitting process) by a magnon so that the total magnon number is conserved. As we have shown already in Sec. 2.2, the energy transfer between the magnetic system and the lattice is finished as soon as the magnon temperature is equal to the fixed phonon temperature. Since the Cherenkov process conserves the total magnon number, the magnetic system is not damped under this process, the magnons just redistribute over the spectrum and finally reach a Bose-Einstein distribution with a generally nonzero chemical potential, determining the total magnon number.

We analyze this process, which is described by the kinetic equation (A.42) in Appendix A.4, by setting an initial magnon distribution with $T_\mathrm{m} = 200$ K and $\mu_\mathrm{m} = 0$ and we calculate the time evolution of the magnons coupled to a phonon heat bath at a fixed temperature of $T_\mathrm{ph} = 300$ K. We again keep the magnetic field of $H_0 = 1000\,\mathrm{Oe}$. As we see in Fig. 3.13(a), the Cherenkov process is very strong at large energies in the terahertz-range where the magnons reach the equilibrium state within $t = 100$ ns, reflecting the large relaxation rates in Fig. 3.4(b). However, the Cherenkov process is negligible at small magnon energies in the gigahertz-range with relaxation times about 100 µs, also reflecting the small relaxation rates in Fig. 3.4(a). As already mentioned, the chemical potential of the magnons in the equilibrium state is nonzero and has to be negative in our case since magnons with low energies are redistributed to larger energies under absorption of phonons. By means of Eq. (3.20a), we determine the total magnon number to be $N_\mathrm{tot} \approx 0.51$, which is a collisional invariant. Knowing the magnon temperature in equilibrium, that is $T_\mathrm{m} = T_\mathrm{ph} = 300$ K, the chemical

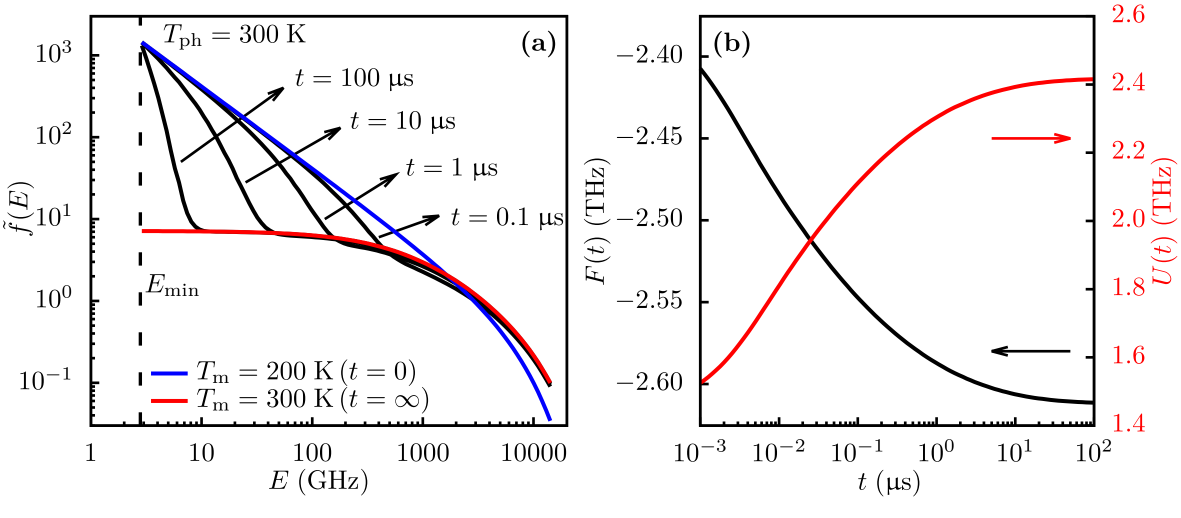

Figure 3.13: (a) Time evolution of the magnon distribution under the Cherenkov process. The blue line shows the initial magnon distribution with $T_\mathrm{m} = 200$ K and $\mu_\mathrm{m} = 0$ and the red line shows the equilibrium state with $T_\mathrm{m} = 300$ K and $\mu_\mathrm{m} = -0.82$ THz. The dashed black line indicates the minimal magnon energy E_min. The temperature of the phonon heat bath is fixed at $T_\mathrm{ph} = 300$ K. (b) Internal magnon energy U and non-equilibrium free energy F as a function of time.

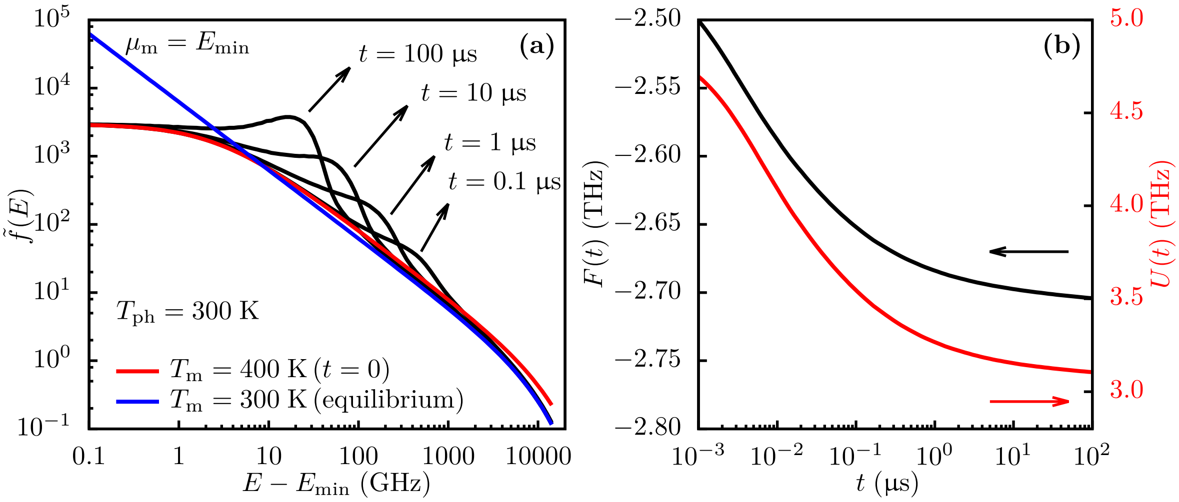

Figure 3.14: (a) Time evolution of the magnon distribution under the Cherenkov process. The red line shows the initial magnon distribution with $T_m = 400$ K and $\mu_m = 0$ and the blue line shows the equilibrium state with $T_m = 300$ K and $\mu_m = E_{min}$. The temperature of the phonon heat bath is fixed at $T_{ph} = 300$ K. (b) Internal magnon energy U and non-equilibrium free energy F as a function of time.

potential in equilibrium is given implicitly via

$$N_{tot} = n_c + \frac{a_0^3}{(2\pi)^3} \int d^3q\, f_{BE}(\boldsymbol{q}, T_m = 300\text{ K}, \mu_m), \tag{3.28}$$

which yields $n_c = 0$ and $\mu_m \approx -0.82$ THz. Figure 3.13(b) shows the internal magnon energy U which increases during the time evolution since the magnetic system is heated from $T_m = 200$ K to $T_m = 300$ K. The internal energy finally saturates at about $t \approx 100$ µs where the magnon temperature coincides with the phonon temperature. The whole process is irreversible as shown in Fig. 3.13(b) by the non-equilibrium free energy F, defined in Eq. (2.74), which monotonically decreases despite the increase of the internal energy. Therefore, the increase of the term $T_{ph}S$ in the non-equilibrium free energy prevails over the increase of U.

We now set an initial magnon distribution with $T_m = 400$ K and $\mu_m = 0$ and repeat the simulation. In this case, the magnon system will be cooled by the phonon heat bath and the chemical potential in the equilibrium state will be larger than the initial $\mu_m = 0$. We again calculate the total magnon number by means of Eq. (3.20a) which yields $N_{tot} \approx 1.29$. In equilibrium, the chemical potential is determined via the relation (3.28), where in this case the chemical potential even takes the maximal value equal to the minimal energy of the system $\mu_m = E_{min}$ and the magnetic system exhibits a condensate $n_c \approx 0.37$. Figure 3.14(a) shows the time evolution of the magnons in this case. Again, the high energy part of the spectrum in the terahertz-range rapidly reaches the equilibrium state, denoted by the blue line, within $t = 100$ ns. Due to the conservation of the total magnon number in the Cherenkov process, the high energy magnons are redistributed to smaller energies under emission of phonons which leads to a cooling of the magnetic system. According to Eq. (3.28), a big fraction of the magnons of $n_c \approx 0.37$ even has to occupy the lowest energy state in order to establish the equilibrium state with $T_m = 300$ K. However, the magnons gather at about $E \approx 20$ GHz and do not occupy the condensate. The reason for this behavior can be found in the interaction potential of the Cherenkov process (2.41), which vanishes in the limit of zero wave vectors. Therefore, the Cherenkov process does not couple the condensate to the thermal magnons and, as a consequence, the equilibrium state can not be reached in this case. Instead, a stationary non-equilibrium state is developed. Both, the internal energy U and the non-equilibrium free energy F decrease during the time-evolution, as shown in Fig. 3.14(b), and saturate at about $t \approx 100$ µs in the stationary non-equilibrium state.

The consideration of the four-magnon process in this simulation would indeed result in a Bose-Einstein condensation since the magnons are thus enabled to reach the equilibrium state as calculated by means of Eq. (3.28). However, in real situations, the damping of the magnetic system due to the three-magnon process also strongly influences the magnon dynamics and inhibits the formation of a condensate under certain conditions, which we will discuss in Sec. 4.3 of the subsequent chapter.

3.3 Concluding Remarks

This chapter gave an overview of the linear and dynamical properties of the four-magnon process, three-magnon process and the Cherenkov process, individually. In this section, we briefly recapitulate the main results of this chapter.

In the first section, we have discussed the linear relaxation rates of each interaction process at room temperature and we compared the results with the Kasuya-LeCraw experiment [48]. We have seen that the modified four-magnon process augmented by the quantum mechanical correction term $S_0 \neq 0$ also leads to a constant upshift of the relaxation rates at small wave vectors, as measured in the experiment [48]. However, the modified four-magnon process overestimates the experimental value by a factor of approximately five and also the dependence of the uniform mode relaxation rate on the saturation magnetization strongly deviates from the experiment. We thus modified the four-magnon process by substituting S_0 with αS_0, where we chose the correction factor to be $\alpha = 0.3$, which thus weakens the modified four-magnon process in order to be compatible with the experiment at least in magnitude. However, the source of the resulting four-magnon process, exhibiting a uniform mode relaxation rate of $\Gamma_0 \approx 1.1$ MHz, is yet unknown since the term S_0 vanishes in the t-matrix approach (cf. Sec. 2.2) and is thus an artifact of the first Born approximation. We nevertheless kept this four-magnon process since the common exchange four-magnon process, augmented by the dipolar contribution to the scattering amplitude, is far too weak in order to account for the dynamical processes at reasonable timescales in our isotropic model. Furthermore, we have shown that the linear increase of the relaxation rate with the wave vector in Ref. [48] is due to the three-magnon confluence process, as has been already revealed in Refs. [68, 99]. In contrast, the three-magnon splitting process sets in not until a certain threshold for the wave vector, determined by the conservation laws, whereas at larger wave vectors both the confluence and the splitting process contribute equally to the total three-magnon relaxation rate in the megahertz-range. In addition, we have seen that the Cherenkov process, induced by the exchange interaction, vanishes at small wave vectors so that the low energy part of the magnetic system is almost decoupled from the underlying lattice. However, at large wave vectors, the Cherenkov process gets stronger with relaxation rates in the gigahertz-range nevertheless staying below the relaxation rates of the four-magnon process which yields the strongest relaxation mechanism at large wave vectors.

In the second section, we have studied the equilibration dynamics of the magnetic system, being initially in non-equilibrium, for each interaction process. As we have already shown in Sec. 2.2, the equilibrium states of the kinetic equations are Bose-Einstein distributions, where the chemical potential μ_{m} and the temperature T_{m} of the magnon system in equilibrium depend on both the initial conditions and also the particular interaction process. Since the four-magnon process conserves both magnon energy and magnon number, the initial conditions determine the pair (μ_{m},T_{m}) in equilibrium, exclusively. As we have seen, the four-magnon process yields an important mechanism for the internal magnon thermalization which takes place on a timescale of several hundreds of nanoseconds and even leads to Bose-Einstein condensation as soon as the initial conditions are supercritical ($\mu_{\mathrm{m}} = E_{\mathrm{min}}$). Due to the structure of the kinetic equation describing the condensate (2.88), we had to give an initial seed for the condensate whose particular choice is not important as long as the condition $n_c(t = 0) \ll N_{\mathrm{tot}}$ holds. We have also demonstrated the strong nonlinearity of the four-magnon process which manifests itself in a faster relaxation dynamics by increasing the local magnon density. The reason for this behavior are the conservation laws of the four-magnon process, which are always easily fulfilled in a narrow region in wave vector space. We then turned to the three-magnon process which yields the most important damping mechanism since this process does not conserve the total magnon number. The equilibrium states are thus always Bose-Einstein distributions with zero chemical potential. We showed in two examples that the three-magnon process either decreases or even increases the total magnon number for attaining the equilibrium state on a timescale of several hundreds of nanoseconds to several microseconds, respectively. As we have also demonstrated, the three-magnon process only acts linearly on a local magnon density due to the severe restrictions of the conservation laws in contrast to the four-magnon process. Finally, we discussed the Cherenkov process, which admits an energy transfer between the magnetic system and the lattice, until the temperature of the magnons approaches the temperature of the phonons. However, the Cherenkov process only affects the magnetic system considerably at large wave vectors on a timescale of several hundreds of nanoseconds and even vanishes at small wave vectors due to the vanishing interaction potential in this region. Therefore, as already noted, the Cherenkov process is negligible in the low energy region of the spectrum. In addition, we have demonstrated the irreversibility of the time evolution resulting from the kinetic equations in each process. In the closed magnon system, we have shown that the non-equilibrium entropy always monotonically increases and saturates in equilibrium, independent of the initial conditions. In the case of the Cherenkov process, we were dealing with an open magnon system, and we have shown that the non-equilibrium free energy monotonically decreases and eventually saturates in equilibrium.

Finally, we stress that the three-magnon process in combination with the Cherenkov process necessarily leads to an equilibrium Bose-Einstein distribution with $\mu_{\mathrm{m}} = 0$ and $T_{\mathrm{m}} = T_{\mathrm{ph}}$, which indeed describes the thermal equilibrium of quasiparticles, in our case magnons. The thermal equilibrium is also the equilibrium state of the full model being a special case of the various equilibrium states of the four-magnon process. This fact becomes relevant in the subsequent chapter.

4

Bose-Einstein Condensation of Magnons

This chapter discusses the magnon dynamics of the full model including all interaction processes which already have been discussed individually in the preceding chapter. We focus on Bose-Einstein condensation of magnons and investigate the prerequisites necessary for the phase transition to occur in different situations. First, we study the dynamics of the magnetic system brought out of equilibrium via short parallel pumping pulses. We discuss the strength of the four-magnon process required to reproduce the experimental results and we also consider a modified Cherenkov process as a possible thermalization channel in the low energy region of the magnon spectrum. The second section is dedicated to the case of continuous magnon pumping, where the special attributes of the resulting stationary magnon distributions and the emerging condensates are studied in particular. Based on these results, we present an alternative explanation for the specific behavior of the magnon condensate at high pumping powers. Finally, in the third section, we discuss the possibility of magnon condensation via a rapid temperature decrease in the phonon system without the use of external microwave pumping.

4.1 Dynamics of Pumped Magnons

In this section, we consider the dynamics of pumped magnons which has also been investigated experimentally [24, 25]. In these experiments, thin YIG films with a thickness of 5 µm and lateral dimensions 1.5 mm × 30 mm are used which are magnetized in-plane with an external magnetic field of $H_0 = 1000\,\mathrm{Oe}$ leading to a minimal magnon energy of about $E_{\mathrm{min}} \approx 2.9$ GHz (cf. Fig. 2.1(b)). In order to bring the magnetic system out of the room temperature equilibrium, short microwave pulses with a pump frequency of $f_{\mathrm{pump}} = \omega_{\mathrm{pump}}/2\pi = 8.1$ GHz and a duration of 30 ns are applied parallel to the applied magnetic field, resulting in the appearance of pumped magnons at $f_{\mathrm{peak}} = \omega_{\mathrm{peak}}/2\pi = 4.05$ GHz. The time evolution of these primary magnons is then investigated by means of time-resolved inelastic Brillouin light scattering (BLS) [22]. Figure 4.1 shows the detected BLS intensity as a function of frequency and delay time corresponding to the start of the pumping with a pump power of $P = 3$ W. As indicated, the magnon dynamics can be separated into three different stages. In the first stage (i), the parallel pumping leads to a rapid increase of primary magnons at about $E \approx 4$ GHz within $t = 20$ ns, which then redistribute over the whole spectrum in the second stage (ii). This redistribution process takes about 60 ns and results in a considerable population of the minimal energy state E_{min} in the third stage (iii), which is interpreted as a quasi-equilibrium magnon Bose-Einstein condensation. After the pumping stops at $t = 30$ ns, the magnon system freely evolves demonstrating that the BEC transition is caused by inherent scattering processes rather than being induced purely through the external magnon driving.

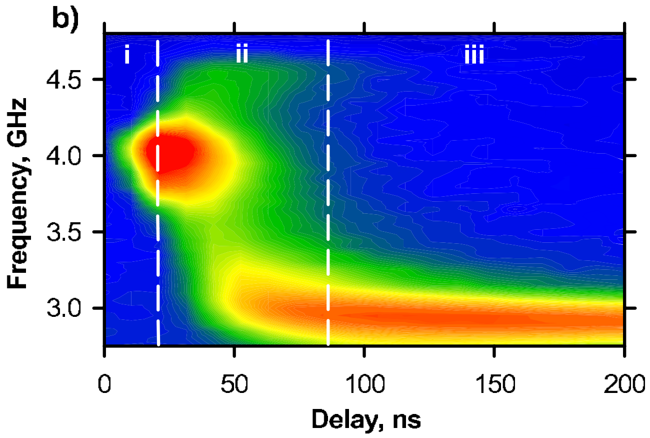

Figure 4.1: Detected BLS intensity of pumped magnons as a function of magnon frequency and delay time with respect to the start of the pumping. The figure is taken from Ref. [25] (Reprinted with permission from V. E. Demidov, O. Dzyapko, S. O. Demokritov, G. A. Melkov, and A. N. Slavin, Phys. Rev. Lett. 100, 047205 (2008) Copyright 2008 by the American Physical Society.)

We simulate this experiment by using the full model and we employ the modified four-magnon scattering process in addition with the correction factor $\alpha = 0.3$, introduced in Sec. 3.1, which thus meets the restrictions of the Kasuya-LeCraw experiment [48]. Furthermore, we augment the model by the parallel pumping process (A.43) and we estimate the power absorbtion by the sample via the relation

$$P = \frac{V_\mathrm{s}}{(2\,\pi)^3} \int \mathrm{d}^3 q \, \frac{\mathrm{d}}{\mathrm{d}t} f(\boldsymbol{q}) \Big|_{\mathrm{pump}} \hbar\omega(\boldsymbol{q}), \tag{4.1}$$

where the time derivative only corresponds to the parallel pumping process and $V_\mathrm{s} = 1.5\ \mathrm{mm} \times 30\ \mathrm{mm} \times 5\ \mu\mathrm{m}$ is the volume of the samples used in the experiments. We determine the time evolution of the magnon spectral density which is defined by

$$\rho(E) = D(E)\,\tilde{f}(E), \tag{4.2}$$

where

$$D(E) = \frac{2\pi}{(8\pi^2 JS)^{3/2}} \sqrt{E - E_\mathrm{min}} \tag{4.3}$$

denotes the magnon density of states of the isotropic dispersion. Since the spectral density (4.2) is proportional to the detected BLS signal, we can directly compare our results with the experiment. In order to get close to the experimental conditions, we set an initial magnon distribution at room temperature equilibrium and apply a static magnetic field of $H_0 = 1000\,\mathrm{Oe}$, which shifts the minimal magnon energy to $E_\mathrm{min} \approx 2.8$ GHz, so only slightly below the minimal energy in the experiment.

In the first example, we apply a pumping field of $h_\mathrm{pump} = 55.9\,\mathrm{Oe}$ with the frequency $f_\mathrm{pump} = \omega_\mathrm{pump}/2\pi = 8.1$ GHz, resulting in the creation of primary magnons in the energy region about $E_\mathrm{peak} = 4.05$ GHz, as can be seen in Fig. 4.2. The pumping field leads to a peak power of $P \approx 6.6$ W, which is defined as the maximal value of the absorbed power in Eq. (4.1). In comparison with the experiment, this value overestimates the measured power absorption which is probably caused by the assumption we made in Eq. (4.1) that the power is absorbed homogenously by the whole sample. In the experiments, a microwave stripe or wire with a width of 25 µm is attached to the surface of the sample, which first excites magnons in a locally restricted region, not covering the whole sample. Therefore, Eq. (4.1) has to be understood as a rough estimate of the absorbed power. After the pumping stops at $t = 30$ ns, magnons begin to redistribute over the spectrum due to the four-magnon

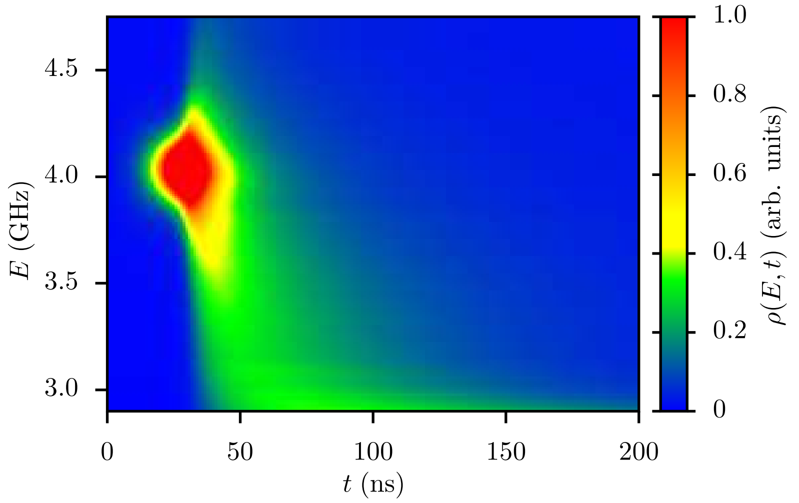

Figure 4.2: Time evolution of primary magnons pumped into a narrow region in energy space at $E_{\mathrm{peak}} = 4.05$ GHz with a pumping field of $h_{\mathrm{pump}} = 55.9$ Oe. The plot shows the color-coded magnon spectral density (4.2) as a function of energy and time.

process and considerably populate the low lying energy region up to the minimum. The thermalization process lasts until about $t = 100$ ns and afterwards the magnons gradually disappear due to the three-magnon process and the whole magnon system approaches the room temperature equilibrium again.

In order to study the time evolution more quantitatively and to see whether the magnon system undergoes Bose-Einstein condensation in this example, we plot in Fig. 4.3 the population of magnons in distinct regions of the spectrum as a function of time. Figure 4.3(a) shows the total magnon number, as defined in Eq. (2.90a), which increases from the equilibrium magnon occupation $N_{\mathrm{eq}} \approx 0.9$ with $\mu_{\mathrm{m}} = 0$ to $N_{\mathrm{tot}} \approx 1.03$ at the end of the pumping at $t = 30$ ns. The critical magnon density ($\mu_{\mathrm{m}} = E_{\mathrm{min}}$) of $N_{\mathrm{crit}} \approx 0.93$, denoted by the dashed red line, lies only slightly above the equilibrium value, so from the thermodynamic point of view, this small density of pumped magnons is already sufficient to cause the BEC transition. After the pumping stops, the total magnon number continuously decreases due to the three-magnon interaction. Figure 4.3(b) shows the population of magnons in the pumping area

$$N_{\mathrm{pump}} = \frac{a_0^3}{(2\,\pi)^3} \int \mathrm{d}^3 q\, f(\boldsymbol{q})\, c(\boldsymbol{q}), \tag{4.4}$$

where the function $c(\boldsymbol{q})$ approximately covers the pumping region and reads

$$c(\boldsymbol{q}) = \exp\left(-(2\,(\hbar\omega(\boldsymbol{q}) - E_{\mathrm{peak}})\,/\Delta E)^2\right), \tag{4.5}$$

where we choose $\Delta E = 0.5$ GHz and $E_{\mathrm{peak}} = 4.05$ GHz. In this region, the magnon population increases exponentially due to the parallel pumping process and quickly diminishes after the pumping ends at $t = 30$ ns due to the four-magnon scattering process, which redistributes the pumped magnons over the spectrum. Simultaneously, the amount of magnons in the low lying energy part of the spectrum, N_{min}, which we define as

$$N_{\mathrm{min}} = \int\limits_{E_{\mathrm{min}}}^{E_{\mathrm{min}}+E_{\mathrm{low}}} \mathrm{d}E\, \tilde{f}(E) D(E), \tag{4.6}$$

and where we set $E_{\mathrm{low}} = 100$ MHz, increases as shown in Fig. 4.3(c), and reaches a maximum at about $t \approx 84$ ns. The subsequent decrease is exponential and exhibits a characteristic time

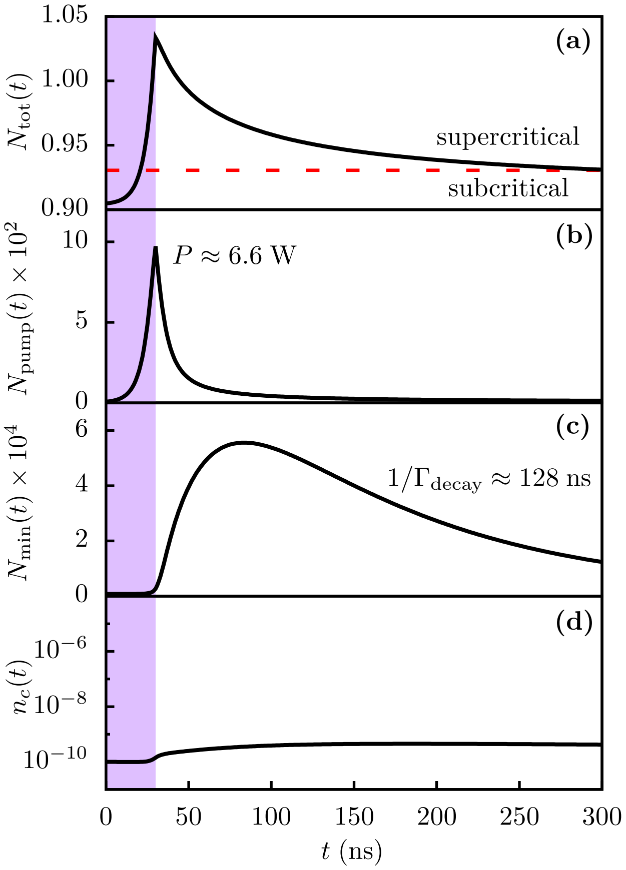

Figure 4.3: Time evolution of the pumped magnons in different regions of the spectrum at a pumping field of $h_{\mathrm{pump}} = 55.9\,\mathrm{Oe}$. The purple shaded area denotes the duration of the pumping. (a) Total magnon number. The dashed red line separates the subcritical and the supercritical magnon densities. (b) Amount of magnons in the pumping area, defined by Eq. (4.4). The absorbed peak power, defined by Eq. (4.1), amounts to $P \approx 6.6$ W. (c) Amount of magnons in the low energy part of the spectrum, defined by Eq. (4.6). The characteristic time of the exponential decrease amounts to $1/\Gamma_{\mathrm{decay}} \approx 128$ ns. (d) Time evolution of the magnon condensate.

of about $1/\Gamma_{\mathrm{decay}} \approx 128$ ns. Figure 4.3(d) shows the population of the condensate, where we set a condensate seed $n_c(t = 0) = 10^{-10}$ at the beginning of the simulation. Although the magnon system exceeds the critical density necessary for BEC and the low lying energy part is being populated, the condensate only increases weakly and stays below a population of $n_c \approx 10^{-9}$. The reason for this counterintuitive behavior is the weakness of the four-magnon process, which admittedly redistributes the magnons but nevertheless does not lead to the thermalization of the magnetic system, which means that the magnon distribution can not be described by a Bose-Einstein distribution with a nonzero chemical potential. In the absence of the three-magnon process, a critical Bose-Einstein distribution would indeed be established at large delay times $t > 200$ ns. However, in this example, the three-magnon process prevails over the four-magnon process and prohibits the development of a critical Bose-Einstein distribution preventing the formation of a magnon BEC.

As we have seen in Sec. 3.2 of the previous chapter, the four-magnon process is a strongly nonlinear process which can be enhanced by increasing the magnon density. Therefore, at a second threshold for the magnon density, larger than the critical density for BEC, the four-magnon process should be stronger than the three-magnon process and a non-equilibrium BEC should be possible. In order to proof this assertion, we repeat the simulation and apply a stronger pumping field of $h_{\mathrm{pump}} = 60.2\,\mathrm{Oe}$. This pumping field leads to an increase of the peak power to $P \approx 8.9$ W. Figure 4.4 shows the time evolution of the magnon spectral density in this example. The pumped magnons now immediately begin to redistribute over the spectrum after the pumping ends at $t = 30$ ns and a big fraction of the primary magnons scatter to the low lying energy part of the spectrum. During the time evolution, the magnons

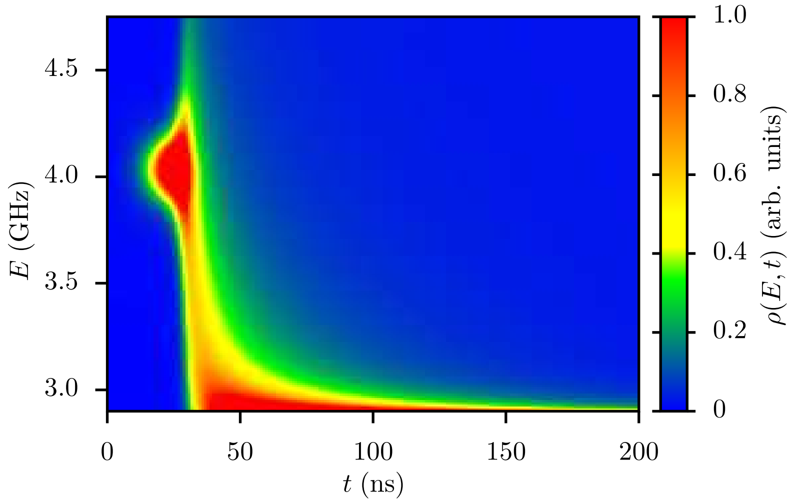

Figure 4.4: Time evolution of primary magnons pumped into a narrow region in energy space at $E_{\text{peak}} = 4.05$ GHz with a pumping field of $h_{\text{pump}} = 60.2\,\text{Oe}$. The plot shows the color-coded magnon spectral density (4.2) as a function of energy and time.

are again continuously damped which significantly manifests itself in the disappearance of magnons at about $t = 200$ ns in Fig. 4.4. The magnon populations in the distinct parts of the spectrum are given in Fig. 4.5. As can be seen in Fig. 4.5(a), the total magnon number increases from the equilibrium occupation $N_{\text{eq}} \approx 0.9$ to $N_{\text{tot}} \approx 1.12$ at the end of the pumping and afterwards continuously decreases due to the three-magnon damping. By taking a closer look at Fig. 4.5(b), we see that the moment of maximal population of magnons in the pumping area is slightly before the end of the pumping. The reason for this behavior is the four-magnon process, which leads to a scattering of magnons out of the pumping region and therefore provides a nonlinear damping mechanism which limits the exponential growth of magnons due to the parallel pumping instability. Simultaneously, the amount of magnons in the low lying energy part of the spectrum N_{min} increases as shown in Fig. 4.5(c), and reaches a maximum at about $t \approx 90$ ns. The subsequent exponential decrease has a characteristic time of about $1/\Gamma_{\text{decay}} \approx 105$ ns, which is considerably smaller than the linear relaxation time of the three-magnon confluence process at $q \approx 0.83 \times 10^5$ rad/cm, corresponding to an energy $E = E_{\text{min}} + E_{\text{low}}$, which amounts to $1/\Gamma(q) \approx 166$ ns, as calculated in Fig. 3.3(b). The reason for this discrepancy is again the four-magnon process which redistributes the magnons in the low lying energy part back to states with higher energies, where the three-magnon process also damps the system. Via this mechanism, the critical condition $\mu_{\text{m}} = E_{\text{min}}$ is maintained until the total magnon number falls below the critical density. During the population of the minimum region of the spectrum, magnons begin to scatter into the condensate, as shown in Fig. 4.5(d), forming a non-equilibrium BEC. In this example, the density of condensed magnons is roughly two orders of magnitude smaller than the non-condensed magnons in the low energy part. However, by applying an even stronger pumping field h_{pump}, the density of condensed magnons will increase and dominate over the non-condensed magnons at a sufficient high pumping power.

The current example illustrates that our kinetic theory supports the formation of a magnon BEC providing that the pumped magnon density is sufficiently large. However, by comparing the above results corresponding to the case of a very weak condensate with the experiments [24,25], we see that the decay time of magnons in the minimum region, which has been measured to be $1/\Gamma_{\text{decay}} \approx 260$ ns, is in contrast with our result of $1/\Gamma_{\text{decay}} \approx 105$ ns, as shown in Fig. 4.5(c). This discrepancy has its origin in the isotropic approximation as

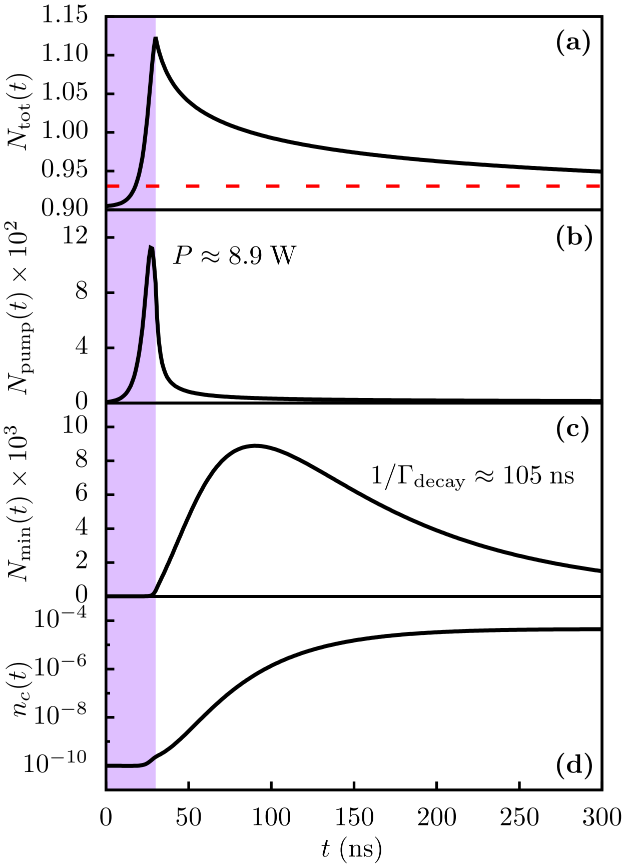

Figure 4.5: Time evolution of the pumped magnons in different regions of the spectrum at a pumping field of $h_{\mathrm{pump}} = 60.2\,\mathrm{Oe}$. The purple shaded area denotes the duration of the pumping. (a) Total magnon number. The dashed red line separates the subcritical and the supercritical magnon densities. (b) Amount of magnons in the pumping area, defined by Eq. (4.4). The absorbed peak power, defined by Eq. (4.1), amounts to $P \approx 8.9$ W. (c) Amount of magnons in the low energy part of the spectrum, defined by Eq. (4.6). The characteristic time of the exponential decrease amounts to $1/\Gamma_{\mathrm{decay}} \approx 105$ ns. (d) Time evolution of the magnon condensate.

we indicate subsequently. As shown in Appendix A.4, we average the kinetic equation resulting from the three-magnon interaction over the solid angle Ω_0. In the experiments, the minimum lies at the angle $\theta_{\boldsymbol{q}_0} = 0$ due to the dipolar anisotropy, where the three-magnon confluence process is about a factor of two smaller than averaged over the solid angles which follows from the three-magnon interaction potential (2.26). Because of the generally smaller damping in the low energy part of the spectrum, the four-magnon process less redistributes the magnons back to states with higher energies, which additionally contributes to a higher magnon lifetime in the minimum region.

In order to adjust the attenuation of magnons in the low energy part to the experiment, we decrease the influence of the three-magnon process on a trial basis by multiplying the corresponding kinetic equation (A.41) by a factor of 1/2. The influence of the three-magnon process in an anisotropic spectrum in the minimum region should thus be comparable with our artificial manipulation of the damping. We apply a slightly larger pumping field of $h_{\mathrm{pump}} = 56\,\mathrm{Oe}$ than in the first example, which leads to a slightly larger peak power of $P \approx 6.9$ W. The time evolution of the magnon spectral density in this case is shown in Fig. 4.6. As can be seen, the magnons in the pumping region scatter to the low energy part more slowly than in the previous example (cf. Fig. 4.4) due to the weaker four-magnon process caused by the smaller amount of pumped magnons. Nevertheless, the pumped magnons reach the minimum region and strongly accumulate there even at delay times $t \approx 200$ ns which is due to the smaller damping during the thermalization process. The time evolution of the spectral density in this case visibly resembles the measured BLS data shown in Fig. 4.1. Figure 4.7 shows the populations of different parts of the spectrum. As can be seen in Fig. 4.7(a), the pumping

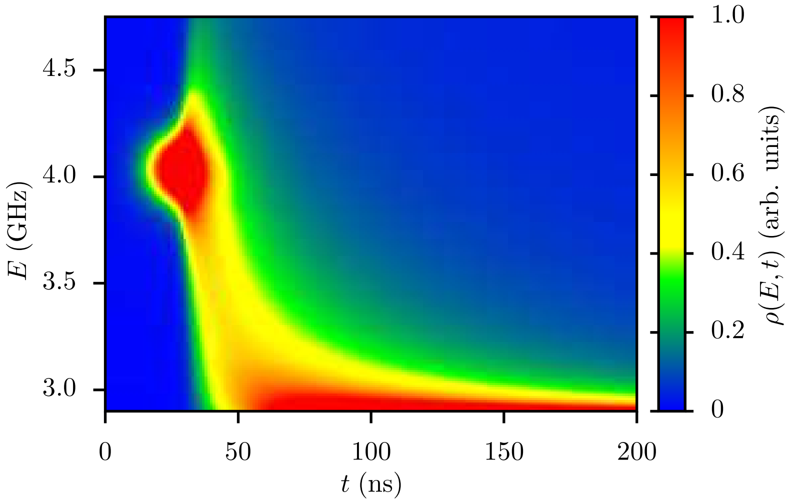

Figure 4.6: Time evolution of primary magnons pumped into a narrow region in energy space at $E_{\text{peak}} = 4.05$ GHz with a pumping field of $h_{\text{pump}} = 56\,\text{Oe}$ in the case of the artificially manipulated three-magnon process. The plot shows the color-coded magnon spectral density (4.2) as a function of energy and time.

leads to a maximal total magnon number which is similar to the magnon number in the first example (cf. Fig. 4.3), which nevertheless decreases more slowly after the pumping stops at $t = 30$ ns due to the weaker three-magnon process. By investigating the time evolution of the magnon population in the minimum region, as shown in Fig. 4.7(c), we see that the maximum amount of magnons is reached not until $t \approx 188$ ns and that the subsequent exponential decrease exhibits a characteristic time of $1/\Gamma_{\text{decay}} \approx 223$ ns, which indeed comes closer to the measured $1/\Gamma_{\text{decay}} \approx 260$ ns. During the population of the minimum region, magnons begin to scatter into the condensate as shown in Fig. 4.7(d), which gains a population also two orders of magnitude smaller than the amount of non-condensed magnons in the minimum region. As opposed to the first example, the total increase of magnons to $N_{\text{tot}} \approx 1.04$ is already sufficient to cause the BEC transition in this case.

As a concluding remark, we get a good agreement with the experiments [24, 25] by artificially weakening the angle-averaged kinetic equation of the three-magnon process. However, we keep the averaged version of the three-magnon process for the subsequent simulations being part of the isotropic approximation.

Until now, we have only considered the modified four-magnon process with $\alpha S_0 \neq 0$, where we have introduced the correction factor $\alpha = 0.3$ in order to be compatible with the measured relaxation rates in the Kasuya-LeCraw experiment [48], discussed in Sec. 3.1 of the previous chapter. As we have seen in the last examples of this section, this modified four-magnon process has just the right order of magnitude in order to reproduce the experimental results reasonably. In the following, we vary the four-magnon process in order to see in which way the strength of this process influences the magnon dynamics. We thus repeat the simulation with the same parameters but we replace the modified four-magnon process ($\alpha S_0 \neq 0$) with the common exchange four-magnon process ($\alpha S_0 = 0$) augmented by the dipolar contribution to the scattering amplitude (A.49), derived in Appendix A.5. We apply the same pumping field of $h_{\text{pump}} = 60.2\,\text{Oe}$ as in the second example (cf. Fig. 4.4) and calculate the time evolution of the magnon spectral density. The result is shown in Fig. 4.8(a). In this case, the magnons do not redistribute over the spectrum but instead remain at the pumping region after the pumping stops. The three-magnon process then gradually damps the pumped magnons similarly to the damping shown in Fig. 3.12 in Sec. 3.2. Obviously, the common four-magnon process is far too weak in order to redistribute the magnons efficiently. As we have shown

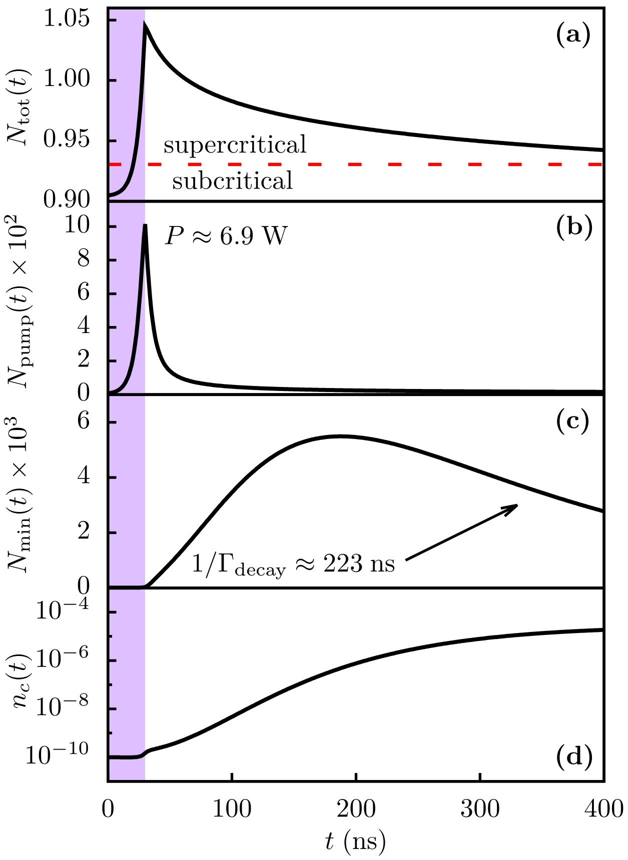

Figure 4.7: Time evolution of the pumped magnons in different regions of the spectrum at a pumping field of $h_{\mathrm{pump}} = 56\,\mathrm{Oe}$ in the case of the artificially manipulated three-magnon process. The purple shaded area denotes the duration of the pumping. (a) Total magnon number. The dashed red line separates the subcritical and the supercritical magnon densities. (b) Amount of magnons in the pumping area, defined by Eq. (4.4). The absorbed peak power, defined by Eq. (4.1), amounts to $P \approx 6.9\,\mathrm{W}$. (c) Amount of magnons in the low energy part of the spectrum, defined by Eq. (4.6). The characteristic time of the exponential decrease amounts to $1/\Gamma_{\mathrm{decay}} \approx 223$ ns. (d) Time evolution of the magnon condensate.

in Sec. 3.2, the four-magnon process is a strongly nonlinear process and can be enhanced by increasing the local magnon density. By comparing the scattering amplitudes (A.46) and (A.50) in the limit of vanishing wave vectors between the modified and the common four-magnon process

$$\lim_{\boldsymbol{q}_0,\boldsymbol{q}_1\to 0} \frac{A_4^{\mathrm{mod}}(\boldsymbol{q}_0,\boldsymbol{q}_1)^2}{A_4^{\mathrm{com}}(\boldsymbol{q}_0,\boldsymbol{q}_1)^2} = \frac{(96\,\alpha S_0\,J)^2}{\frac{1}{5}\left(\frac{\mu_0(g\mu_{\mathrm{B}})^2}{a_0^3}\right)^2} \approx 193, \tag{4.7}$$

we see that we have to increase the pumped magnon density by a factor of approximately $\sqrt{193} \approx 14$ in order to ensure the dipolar four-magnon process to be effective, since the product of occupations of the two incoming magnons in the scattering process has to compensate the smaller scattering amplitude, as discussed in Sec. 3.2. We again repeat the simulation and apply a pumping field of $h_{\mathrm{pump}} = 78.5\,\mathrm{Oe}$ which leads to a peak power of $P \approx 266$ W and an increase of the total magnon number to $N_{\mathrm{tot}} \approx 4.02$. It is worth noting that this value of pumped magnons is unreasonably high, since it exceeds the number of magnons at room temperature equilibrium $N_{\mathrm{eq}} \approx 0.9$ by more than a factor of three. Anyhow, we calculate the time evolution of the spectral density which is shown in Fig. 4.8(b). As can be seen, the pumped magnons in this case indeed begin to redistribute over the spectrum after the pumping ends. Nevertheless, due to the high magnon density, the three-magnon process also becomes stronger as soon as the pumped magnons begin to redistribute, and thus leads to an immediate damping of the magnetic system within $t \approx 20$ ns preventing the pumped magnons to reach the minimal energy region. Therefore, even in this case, the Bose-Einstein condensation of magnons is not possible with the common four-magnon process.

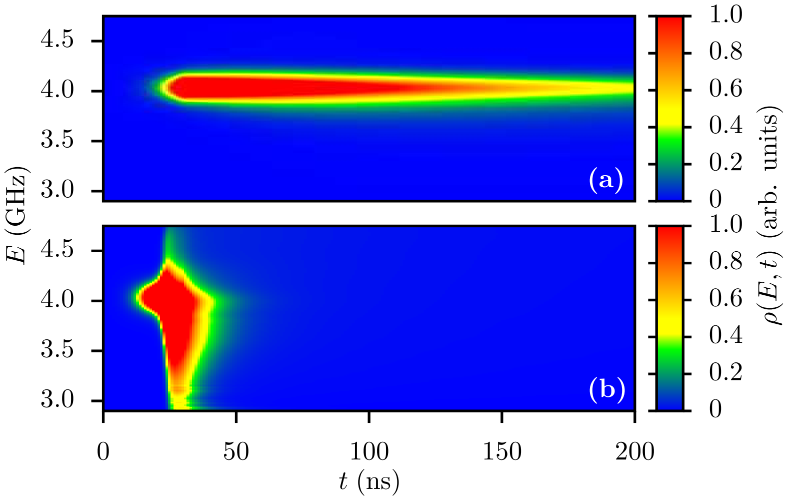

Figure 4.8: Time evolution of primary magnons pumped into a narrow region in energy space at $E_{\text{peak}} = 4.05$ GHz in the case of the common four-magnon process ($\alpha S_0 = 0$). The plots show the color-coded magnon spectral density (4.2) as a function of energy and time. (a) Pumping field: $h_{\text{pump}} = 60.2$ Oe. (b) Pumping field: $h_{\text{pump}} = 78.5$ Oe.

We now turn again to the modified four-magnon process and reduce the correction factor to $\alpha = 0.1$ in order to see, if the four-magnon process is still strong enough to redistribute the pumped magnons. We apply a pumping field of $h_{\text{pump}} = 64.2$ Oe which leads to a peak power of $P \approx 34$ W and which is necessary to ensure the four-magnon process to be effective. Figure 4.9 shows the time evolution of the magnon spectral density. The pumped magnons indeed scatter to the low lying energy part shortly after the pumping ends and populate the minimum region. However, due to the very high magnon density, the magnons are strongly damped and disappear already at about $t \approx 100$ ns. At a first glance, the time evolution of the spectral density resembles the case of the common four-magnon process shown in Fig. 4.8(b). Figure 4.10 shows the magnon population of the distinct regions of the spectrum. In Fig. 4.10(a), we see that the total magnon density increases to $N_{\text{tot}} \approx 1.55$, a value well above the critical density as indicated by the dashed red line. Due to this high magnon density the three-magnon process is also enhanced and strongly damps the magnetic system in the first 100 ns. Afterwards, the density still lies above the critical density but is small enough for the pumped magnons to be only moderately damped. Figure 4.10(c) shows the magnon population in the minimum region. The maximal population is already reached at a delay time of $t \approx 45$ ns, so only 15 ns after the pumping ends, which is caused by the initially strong four-magnon process. The subsequent exponential decrease has a characteristic time of only $1/\Gamma_{\text{decay}} \approx 64$ ns, which is due to the strong three-magnon damping and the following redistribution of magnons back to the high energy part of the spectrum where the three-magnon process also damps the magnetic system. As can be seen in Fig. 4.10(d), the condensate barely increases and stays at a population below $n_c \approx 10^{-9}$. So also in the case of $\alpha = 0.1$, the modified four-magnon process is too weak in order to cause the BEC transition.

By taking into account all the above performed simulations, we conclude that, provided the four-magnon process is responsible for the thermalization process and the build up of a magnon condensate, the four-magnon scattering amplitude has to exhibit a non-vanishing constant in the limit of zero wave vector which should have a magnitude of about

$$A_4 = 96\alpha S_0 J \approx 2.1 \text{ GHz}, \tag{4.8}$$

following from Eq. (2.93), with the common correction factor $\alpha = 0.3$. Only with a scattering

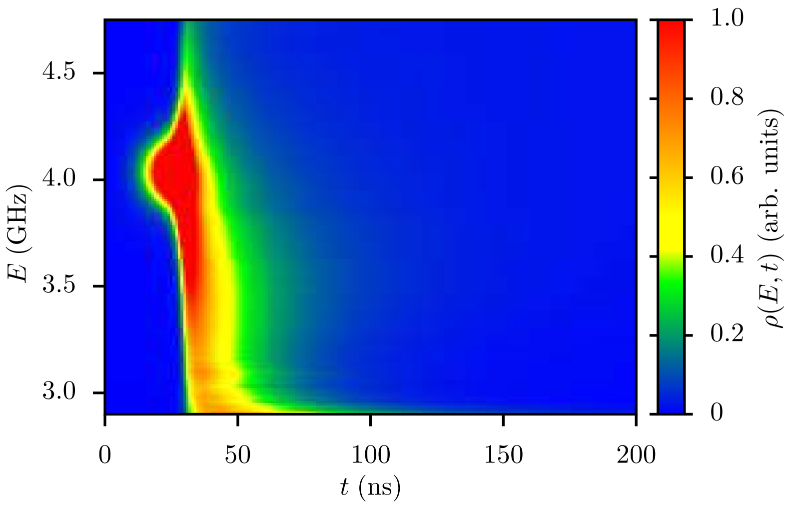

Figure 4.9: Time evolution of primary magnons pumped into a narrow region in energy space at $E_{\text{peak}} = 4.05$ GHz in the case of the modified four-magnon process ($\alpha S_0 \neq 0$) with $\alpha = 0.1$. The plot shows the color-coded magnon spectral density (4.2) as a function of energy and time at a pumping field of $h_{\text{pump}} = 64.2\,\text{Oe}$.

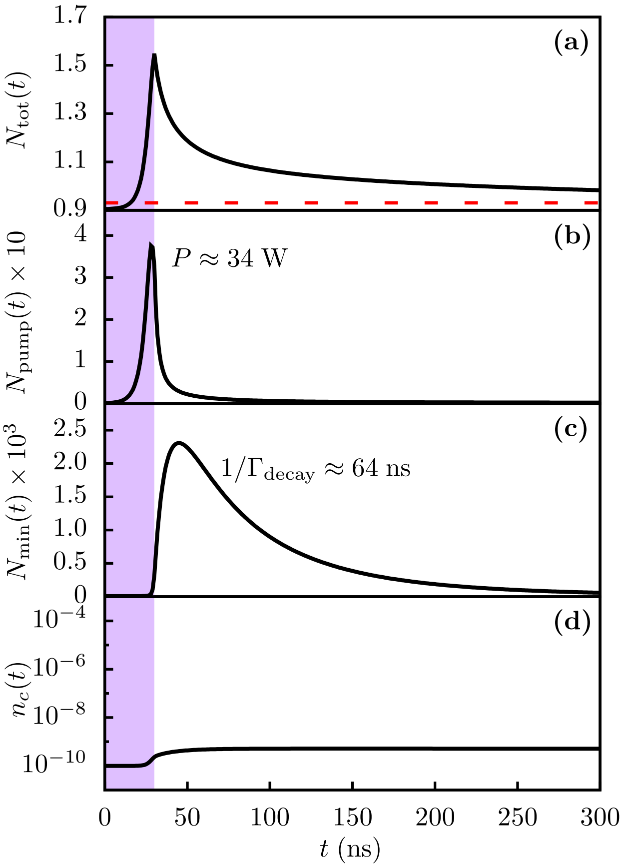

Figure 4.10: Time evolution of the pumped magnons in different regions of the spectrum at a pumping field of $h_{\text{pump}} = 64.2\,\text{Oe}$ in the case of the modified four-magnon process ($\alpha S_0 \neq 0$) with $\alpha = 0.1$. The purple shaded area denotes the duration of the pumping. (a) Total magnon number. The dashed red line separates the subcritical and the supercritical magnon densities. (b) Amount of magnons in the pumping area, defined by Eq. (4.4). The absorbed peak power, defined by Eq. (4.1), amounts to $P \approx 34$ W. (c) Amount of magnons in the low energy part of the spectrum, defined by Eq. (4.6). The characteristic time of the exponential decrease amounts to $1/\Gamma_{\text{decay}} \approx 64$ ns. (d) Time evolution of the magnon condensate.

amplitude exhibiting this magnitude, a good agreement between theory and experiment is achievable, at least in our model, as we have shown in this section.

4.1.1 Thermalization through Magnon-Phonon Interaction

Finally, we seek for other possible thermalization mechanisms. The Cherenkov process, as already mentioned in Sec. 3.2 of the previous chapter, also conserves the total magnon number and therefore principally also leads to a thermalization of the magnetic system. In a recent

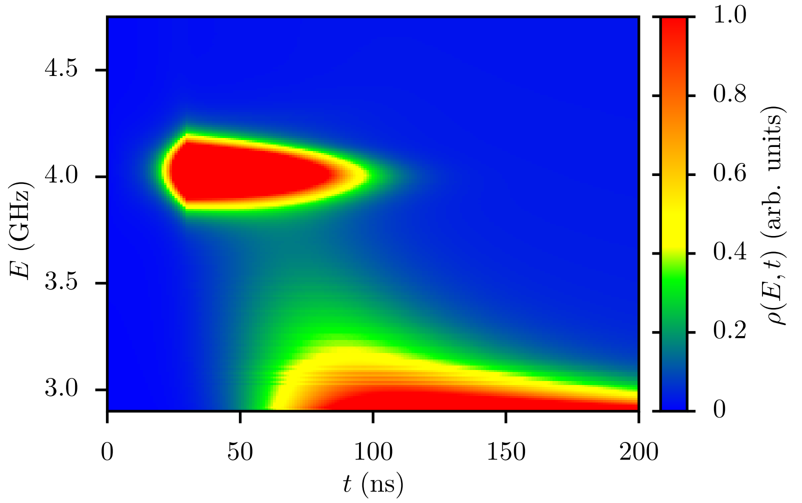

Figure 4.11: Time evolution of primary magnons pumped into a narrow region in energy space at $E_{\text{peak}} = 4.05$ GHz in the case of the modified Cherenkov process. The plot shows the color-coded magnon spectral density (4.2) as a function of energy and time at a pumping field of $h_{\text{pump}} = 73.3$ Oe.

publication [45], the authors propose a stochastic version of the Landau-Lifshitz equation which is based on the Cherenkov process induced by the spin-orbit interaction in order to explain the thermalization process. As we have shown in Sec. 3.1, the Cherenkov process induced by the exchange interaction vanishes in the limit of zero wave vectors and is hence negligible in the low energy part of the spectrum. Nevertheless, similarly to the case of the four-magnon scattering, we just modify the interaction process by setting a non-vanishing constant at zero wave vectors c_σ in the original Cherenkov interaction potential (2.41) and determine its strength necessary for explaining the experiments. The modified interaction potential then reads

$$V_\sigma(\boldsymbol{q},\boldsymbol{q}') = \left(c_\sigma + JSa_0^2\sqrt{\frac{2\hbar}{mv_\sigma}}\,q\,k\sqrt{q'}\right)\phi_\sigma(\boldsymbol{q},\boldsymbol{q}'), \tag{4.9}$$

where the angle-dependent quantity ϕ_σ is defined in Eq. (2.42) which we again neglect for deriving the kinetic equation and we proceed just as in the calculations made in the Appendixes A.4 and A.5. In the following simulation, we set $c_\perp = c_\parallel = 20$ GHz on trial and also neglect the four-magnon scattering process. We apply a pumping field of $h_{\text{pump}} = 73.3$ Oe and calculate the time evolution of the pumped magnons which is shown in Fig. 4.11. Although the pumping stops at $t = 30$ ns, the pumped magnons stay very long, up to $t \approx 100$ ns, in the pumping region. The population of the low lying energy part begins at about $t \approx 50$ ns, which qualitatively distinguishes from the thermalization process caused by the four-magnon scattering process which we have studied in the previous examples. In contrast to these simulations, the thermalization does not take place in a cascade of scattering events from the pumping region down to the minimal energy state but rather in a way skipping the energy interval between these two regions. The reason for this difference are the energy and momentum conservation laws of the Cherenkov process which forbid a scattering of two magnons located in the low energy region. As already mentioned in Sec. 3.1, the Cherenkov scattering process always involves a magnon having energy $E \approx 67$ GHz or larger (cf. Eq. (3.14)). Therefore, magnons in the pumping region are annihilated in a confluence process resulting in the creation of magnons with energies $E > 67$ GHz. Via a splitting of these high energy magnons, magnons are in turn created which directly populate the low energy part. Therefore, instead of a downward cascade originating from the four-magnon scattering, the thermalization induced by the Cherenkov process takes place in two steps involving high energy magnons. In

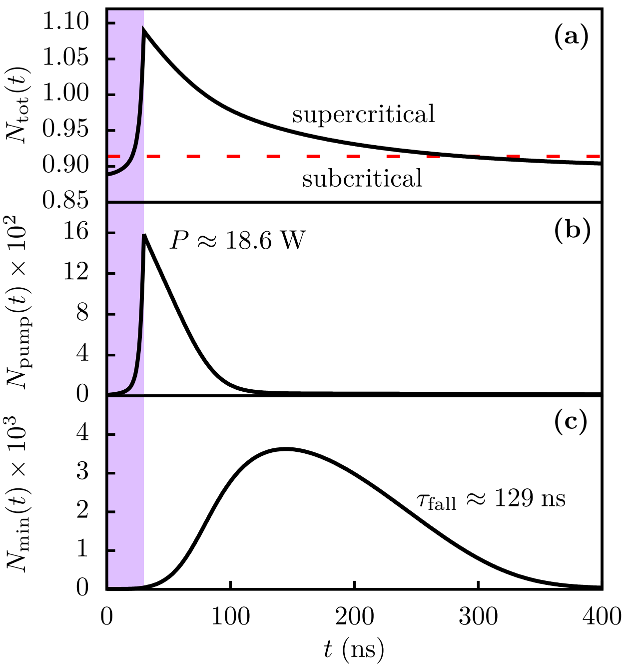

Figure 4.12: Time evolution of the pumped magnons in different regions of the spectrum at a pumping field of $h_{\mathrm{pump}} = 73.3\,\mathrm{Oe}$ in the case of the modified Cherenkov process. The purple shaded area denotes the duration of the pumping. (a) Total magnon number. The dashed red line separates the subcritical and the supercritical magnon densities. (b) Amount of magnons in the pumping area, defined by Eq. (4.4). The absorbed peak power, defined by Eq. (4.1), amounts to $P \approx 18.6\,\mathrm{W}$. (c) Amount of magnons in the low energy part of the spectrum, defined by Eq. (4.6). The fall time of the attenuation amounts to $\tau_{\mathrm{fall}} \approx 129$ ns.

Fig. 4.12, we plot the population of magnons in different spectral regions, excepting the population of the condensate, which is not affected by the Cherenkov process and therefore stays constant. Figure 4.12(a) shows the total magnon number which is comparable to the magnon density in the case described by Fig. 4.5. In Fig. 4.12(b) however, we indeed see that the pumped magnons are gradually damped within a long period of 70 ns after reaching a peak power of $P \approx 18.6$ W at $t = 30$ ns. This is in severe contrast to the prompt attenuation of pumped magnons found in the case of the four-magnon scattering. Also contrary to the simulation described by Fig. 4.5, the population of the minimal energy part reaches its maximum at about $t \approx 145$ ns where the maximal value in this case is smaller by a factor of ≈ 2.5. The subsequent attenuation is, in contrast to the simulations including the four-magnon process, non-exponential and exhibits a fall time of about $\tau_{\mathrm{fall}} \approx 129$ ns (time at which the population in the minimum region is decreased to $1/e$ of the maximal value at $t = 145$ ns).

As concluding remarks, we have seen that the thermalization caused by a modified Cherenkov process qualitatively distinguishes from the thermalization induced by the four-magnon process and therefore also deviates from the experimental findings [24, 25]. We have adapted the hypothetic constant c_σ in the interaction potential in a way that the timescales of the thermalization process resembles those found in the experiment. However, by calculating the relaxation rate of the uniform mode which results from this modification of the Cherenkov process, we obtain $\Gamma_0 \approx 247$ MHz, which is about two orders of magnitude above the measured value in the Kasuya-LeCraw experiment [48] (cf. Sec. 3.1). Therefore, we can beyond doubt rule out the possibility of a magnon-phonon induced thermalization, at least in our isotropic model.

4.2 Bose-Einstein Condensation under Continuous Pumping

In this section, we investigate the dynamics of magnons under continuous pumping which is a technique also used in the seminal work of Demokritov *et al.* [19]. Instead of short intensive pumping pulses as considered in the previous section, the parallel pumping process is applied continuously during the experiment and the formation of a magnon Bose-Einstein condensate is studied in frequency space at different delay times with respect to the start of the pumping. Recently, Serga *et al.* found unexpected behavior of the condensate at high pumping powers [32] which we will also address at the end of this section. Throughout this section, we adapt the applied magnetic field of $H_0 = 1735\,\mathrm{Oe}$ used in this experiment, which shifts the minimal energy of the spectrum to $E_{\mathrm{min}} \approx 4.86$ GHz. In the experiment, the parallel pumping is applied with a pump frequency of $f_{\mathrm{pump}} = \omega_{\mathrm{pump}}/2\pi = 14$ GHz resulting in the appearance of pumped magnons at $f_{\mathrm{peak}} = \omega_{\mathrm{peak}}/2\pi = 7$ GHz. We therefore adapt the parallel pumping process (A.43) and also set $\hbar\omega_{\mathrm{pump}} = 14$ GHz in order to get close to the experimental conditions. We again simulate the time evolution at room temperature by means of the full model with the modified four-magnon scattering process in addition with the correction factor $\alpha = 0.3$.

In the first example, we start by applying a very small pumping field of $h_{\mathrm{pump}} \approx 6.7\,\mathrm{Oe}$. Figure 4.13(a) shows the magnon distribution function in the pumping region in the range of $E = 6$ GHz to $E = 8$ GHz at different delay times. It is visible that magnons appear at the beginning of the pumping process but the pumped magnon density gets stuck and does not grow exponentially as it is intended in the parallel pumping process in order to excite magnons. To be more precise, we plot in Fig. 4.13(b) the time evolution of the magnon number in the pumping region by means of Eq. (4.4), where we choose $\Delta E = 0.5$ GHz and $E_{\mathrm{peak}} = 7$ GHz. The pumped magnon density only gradually increases and even saturates at about $t \approx 1$ µs. As a consequence, also the absorbed power by the sample does not exceed $P = 1$ mW due to the small amount of magnons. In order to understand this result we set up a simplified model for the pumped magnons

$$\frac{\mathrm{d}}{\mathrm{d}t} N_{\mathrm{pump}} = -\Gamma \left(N_{\mathrm{pump}} - N_0\right) + \beta N_{\mathrm{pump}}, \tag{4.10}$$

where the first term on the right-hand side describes the linear relaxation caused by the three-magnon and four-magnon processes and the second term describes the parallel pumping process, where N_0 denotes the equilibrium amount of magnons in the pumping region. This equation can easily be solved by

$$N_{\mathrm{pump}}(t) = N_0 + \frac{\beta N_0}{\Gamma - \beta}\Big(1 - \exp(-(\Gamma - \beta)t)\Big), \tag{4.11}$$

which only yields an exponential increase of the pumped magnons if the pumping overcomes the linear damping of the system, that is $\Gamma < \beta$. This condition marks the threshold for the parallel pumping process to be effective. By measuring this threshold in parallel pumping experiments, it is possible to determine the linear relaxation rates as it has been done in the Kasuya-LeCraw experiment [48], already discussed in Sec. 3.1. In our case, the pumping field is below the threshold for the spin wave instability which results in a saturation of the pumped magnons described by Eq. (4.11). Therefore, we adapt the model (4.11) to the numerical result and use the constants Γ and β as fit parameters. The dashed black line in Fig. 4.13(b) shows the resulting fit which is in excellent agreement with the simulation.

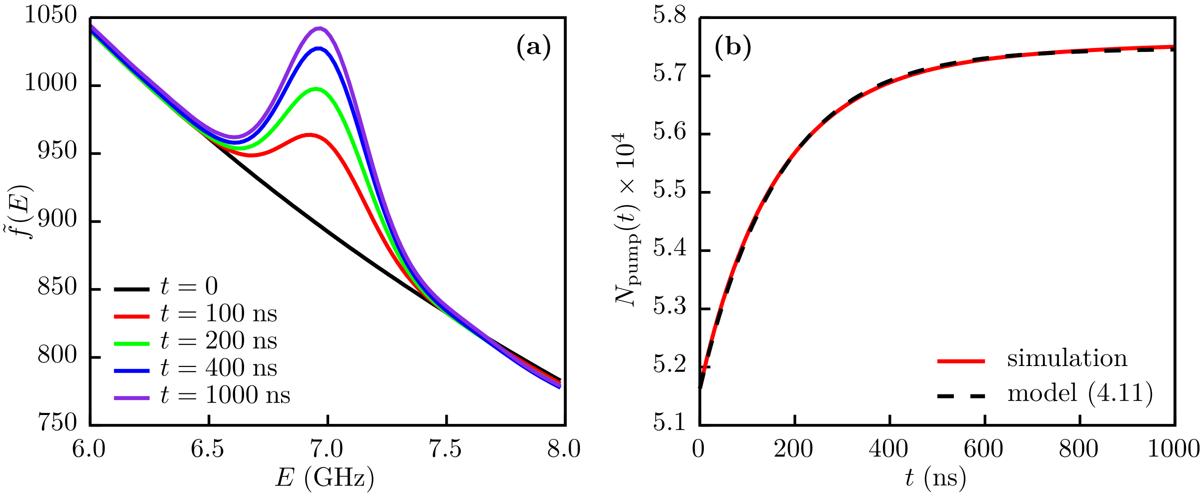

Figure 4.13: (a) Magnon distribution function at different delay times corresponding to the start of the pumping process with a pumping field of $h_{\mathrm{pump}} \approx 6.7\,\mathrm{Oe}$. (b) Population of magnons in the pumping region (4.4) as a function of time. The solid red line shows the numerical result, whereas the dashed black line shows a fit with the model (4.11).

In the next example, we increase the pumping field to $h_{\mathrm{pump}} \approx 26.6\,\mathrm{Oe}$, which is sufficient to exceed the threshold for the parallel pumping instability. Indeed, as shown in Fig. 4.14 by the solid red line, the amount of pumped magnons increases exponentially at the beginning of the pumping, which is corroborated by a fit of the model (4.11) with the numerical data in the temporal interval between $t = 0$ and $t = 200$ ns, shown by the dashed black line. As also visible in Fig. 4.14, this exponential increase of pumped magnons does not remain unlimited and stops at about $t \approx 500$ ns with a peak power of $P \approx 0.23$ W. The reason for this behavior is the four-magnon process which leads to a scattering of magnons out of the pumping region thus providing a nonlinear damping mechanism. Therefore, the model (4.10) is not adequate to describe the dynamics of pumped magnons far above the threshold. As we have shown in Sec. 3.2, the relaxation rates of the four-magnon process are roughly doubled by increasing the magnon density in the peak by a factor of two. On a trial basis, we thus augment the model (4.10) by a nonlinear damping term in order to limit the growth of magnons

$$\frac{\mathrm{d}}{\mathrm{d}t} N_{\mathrm{pump}} = -\Gamma \left(N_{\mathrm{pump}} - N_0\right) - \Gamma_2 \left(N_{\mathrm{pump}} - N_0\right)^2 + \beta N_{\mathrm{pump}}, \tag{4.12}$$

where Γ_2 is a constant describing the strength of the nonlinear damping. A solution of this equation can be obtained by completing the square which yields

$$N_{\mathrm{pump}}(t) = N_0 - x + \sqrt{y}\,\tanh(\sqrt{y}\,\Gamma_2 t + z), \quad \text{with} \tag{4.13a}$$

$$x = \frac{\Gamma - \beta}{2\,\Gamma_2}, \tag{4.13b}$$

$$y = \frac{(\Gamma - \beta)^2}{4\,\Gamma_2^2} + \frac{\beta N_0}{\Gamma_2}, \tag{4.13c}$$

$$z = \operatorname{arctanh}\left(\frac{x}{\sqrt{y}}\right). \tag{4.13d}$$

Using the constants Γ, Γ_2 and β as fit parameters in the temporal interval between $t = 0$ and $t = 500$ ns, we obtain the solution of Eq. (4.12) shown by the dotted black line in Fig. 4.14. At

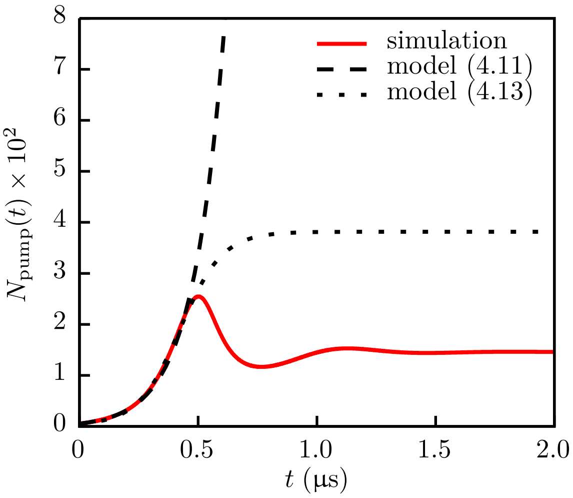

Figure 4.14: Population of magnons in the pumping region (4.4) as a function of time at a pumping field of $h_{\mathrm{pump}} \approx 26.6\,\mathrm{Oe}$. The solid red line shows the numerical result, whereas the dashed black line shows a fit with the model (4.11) and the dotted black line shows a fit with the model (4.13).

the beginning of the pumping, the magnon density again increases exponentially as described by the model (4.11), showing that this limiting case is also incorporated in the model (4.13). As also intended by the implementation of the nonlinear damping term, the growth of the pumped magnons in this augmented model is indeed limited and the magnon density finally saturates at a certain level. Nevertheless, in the simulation, the amount of pumped magnons first reaches a maximum and again decreases in contrast to the monotonic increase predicted by the augmented model. The reason for this behavior is the fact that the magnons which are scattered out of the pumping region gather at the low energy part of the spectrum as shown in Fig. 4.15(c) thus enhancing the scattering of magnons out of the pumping region. An even more realistic model which also takes into account this initial overshoot of the pumped magnon density should allow for a variable Γ_2, which depends on the amount of magnons already scattered out of the pumping region.

Although the parallel pumping threshold is exceeded in this example and an exponential increase of magnons sets in, the magnon system does not undergo Bose-Einstein condensation. Figure 4.15(a) shows the temporal evolution of the total magnon number. After about $t \approx 0.5$ μs, when the maximum of magnons in the pumping region is reached (cf. Fig. 4.14), the total magnon number exceeds the critical magnon density, denoted by the dashed red line, and saturates at about $t \approx 1.5$ μs, where a non-equilibrium steady state is established. However, the condensate, shown in Fig. 4.15(b), rather stays at the initial value of $n_c(t = 0) = 10^{-10}$. This surprising result can be understood by taking a look at the magnon distribution function at different delay times, shown in Fig. 4.15(c). Although magnons scatter to the low lying energy part of the spectrum during the pumping process, the magnon density is not large enough for the four-magnon process to efficiently redistribute the magnons and to overcome the damping due to the three-magnon process. Consequently, at $t = 2$ μs, a stationary non-equilibrium magnon distribution is reached, shown by the purple line, which does not exceed the critical magnon distribution in the low energy part, shown by the dashed black line.

We now further increase the pumping field to $h_{\mathrm{pump}} \approx 59.9\,\mathrm{Oe}$, in order to cause the BEC transition. Figure 4.16 shows the time evolution of the magnon distribution function at different delay times corresponding to the start of the pumping. We see that at $t = 200$ ns a supercritical magnon distribution is formed which significantly lies above the critical distribution, shown by the dashed black line. Obviously, in this case, the magnon density is

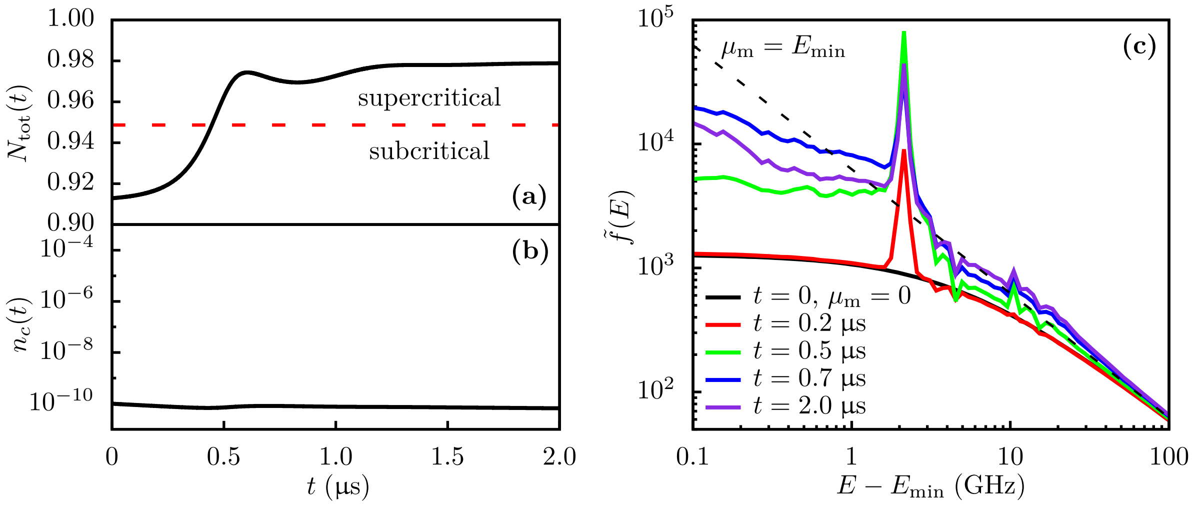

Figure 4.15: (a) Total magnon number as a function of time. The dashed red line denotes the critical magnon density. (b) Time evolution of the magnon condensate. (c) Magnon distribution function at different delay times. The dashed black line denotes the critical magnon distribution with $\mu_{\rm m} = E_{\rm min}$ and $T_{\rm m} = 300$ K.

large enough for the four-magnon process to prevail over the three-magnon process. At delay times $t > 200$ ns, the magnons in the low energy part of the spectrum begin to scatter to the lowest energy state where a magnon condensate is formed, as we will show subsequently. During this process, the magnon distribution function asymptotically approaches the critical distribution with $\mu_{\rm m} = E_{\rm min}$ and $T_{\rm m} = 300$ K, ending in a steady state. In order to investigate the interplay between the magnons in the condensate and the magnons in the gaseous phase, we define the latter as

$$N_{\rm gas} = N_{\rm tot} - N_{\rm pump} - n_c. \tag{4.14}$$

Figure 4.17 shows the time evolution of the quantities arising in Eq. (4.14) by the solid black lines. In Fig. 4.17(b), we show the occupation of magnons in the pumping region where the initial overshoot of pumped magnons at $t \approx 83$ ns, also discussed in the previous example, is even more pronounced due to the higher pumping field which leads to a peak power of $P \approx 3.8$ W. The population of magnons in the gaseous phase thus strongly increases in the temporal interval between $t \approx 70$ ns and $t \approx 108$ ns due to the scattering of magnons out of the pumping region. Subsequently, the population decreases by a small amount due to the three-magnon process which briefly dominates over the pumping process because a lot of magnons which originally enhanced the pumping left the pumping region after the overshoot. At about $t \approx 250$ ns, the population of the gaseous phase begins to decrease significantly because a supercritical magnon occupation is formed (cf. Fig. 4.16) and magnons scatter into the condensate which likewise increases as shown in Fig. 4.17(d). In contrast to the population of the gaseous phase, which eventually saturates at the critical magnon density, shown by the solid green line in Fig. 4.17(c), the condensate does not saturate and increases linearly at large delay times $t \gg 2$ µs due to a constant flux of magnons left from the pumping process which remains undamped by the three-magnon process. This linear increase of the total magnon number, shown in Fig. 4.17(a), is clearly visible already at delay times $t > 0.5$ µs, so that the magnon population will diverge as time passes.

This unphysical behavior is an artifact of the isotropic approximation since the only process affecting the condensate in this approximation is the four-magnon process. In real

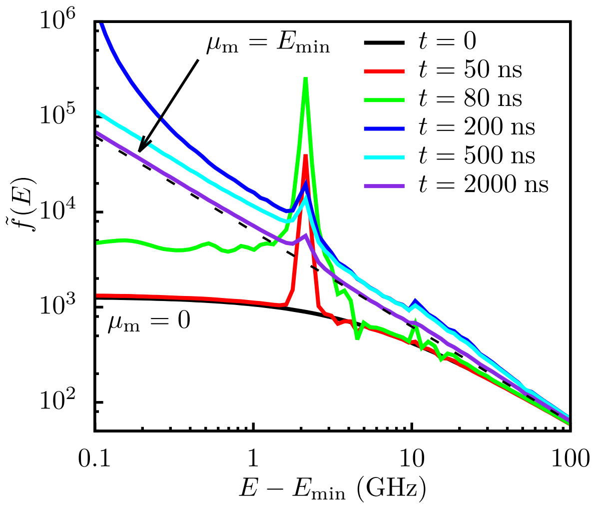

Figure 4.16: Magnon distribution function at different delay times at a pumping field of $h_\mathrm{pump} \approx 59.9\,\mathrm{Oe}$. The dashed black line denotes the critical magnon distribution with $\mu_\mathrm{m} = E_\mathrm{min}$ and $T_\mathrm{m} = 300$ K.

situations, the magnons in the condensate are additionally damped by the three-magnon confluence process which is indeed effective because the minimal energy state of dipolar-exchange dispersion relations does not lie at zero wave vectors in contrast to the isotropic dispersion. In order to take this damping of the condensate into account, even in our isotropic model, we phenomenologically set up a kinetic equation for the condensate resulting from the three-magnon confluence process by treating the condensate as it would be lying at nonzero wave vector $\boldsymbol{q}_\mathrm{min}$. We therefore, similarly as in Eq. (2.87), separate the lowest energy state from the distribution function

$$f_\mathrm{tot}(\boldsymbol{q}) = f(\boldsymbol{q}) + n_c^+ \, \frac{(2\pi)^3}{a_0^3} \, \delta(\boldsymbol{q} - q_\mathrm{min}\, \boldsymbol{e}_z) + n_c^- \, \frac{(2\pi)^3}{a_0^3} \, \delta(\boldsymbol{q} + q_\mathrm{min}\, \boldsymbol{e}_z), \tag{4.15}$$

corresponding to the respective positions of the minima in dipolar-exchange dispersions. Inserting this ansatz into the original kinetic equation resulting from the three-magnon confluence process (second term in Eq. (2.63)) and repeating the calculations in Appendix A.4 without averaging over the solid angle Ω_0, the resulting kinetic equation reads

$$\frac{\mathrm{d}}{\mathrm{d}t} n_c = \frac{n_c}{16\pi^2\hbar\,(2JS)^{3/2}} \int\limits_{E_\mathrm{min}+\frac{E_\mathrm{min}^2}{8JS(q_\mathrm{min}a_0)^2}}^{E_\mathrm{cut}-E(q_\mathrm{min})} \mathrm{d}E_1 \Bigg[\frac{\tilde{F}_3^c(E(q_\mathrm{min}), E_1, E(q_\mathrm{min}) + E_1)}{\sqrt{E(q_\mathrm{min}) - E_\mathrm{min}}}$$

$$\times \Big(\tilde{f}(E(q_\mathrm{min}) + E_1) \Big(1 + \tilde{f}(E_1)\Big) - \tilde{f}(E_1) \Big(1 + \tilde{f}(E(q_\mathrm{min}) + E_1)\Big) \Big) \Bigg], \tag{4.16}$$

where $n_c = n_c^+ + n_c^-$. The quantity $\tilde{F}_3^c$ as well as the lower bound of integration are given and evaluated in Appendix A.5. Note that $E(q_\mathrm{min}) > E_\mathrm{min}$. According to the wave vector of the energy minimum of an 5 µm-thick film, which we have determined in Fig. 2.1(b) in Sec. 2.1, we set $q_\mathrm{min} = 0.5 \times 10^5$ rad/cm. Since $\tilde{f}(E(q_\mathrm{min}) + E_1) < \tilde{f}(E_1)$ is valid for large E_1 in most cases, Eq. (4.16) indeed leads to a damping of the condensate.

We now repeat the simulation and include this linear damping term for the condensate. The result is shown in Fig. 4.17 by the dashed red lines. In this case, the condensate (d) indeed saturates at a certain level rising with increasing strength of the pumping field h_pump. The divergence of the total magnon number (a) thus fails to appear and a steady population is reached already at $t \approx 0.5$ µs. The limited increase of the condensate also influences the

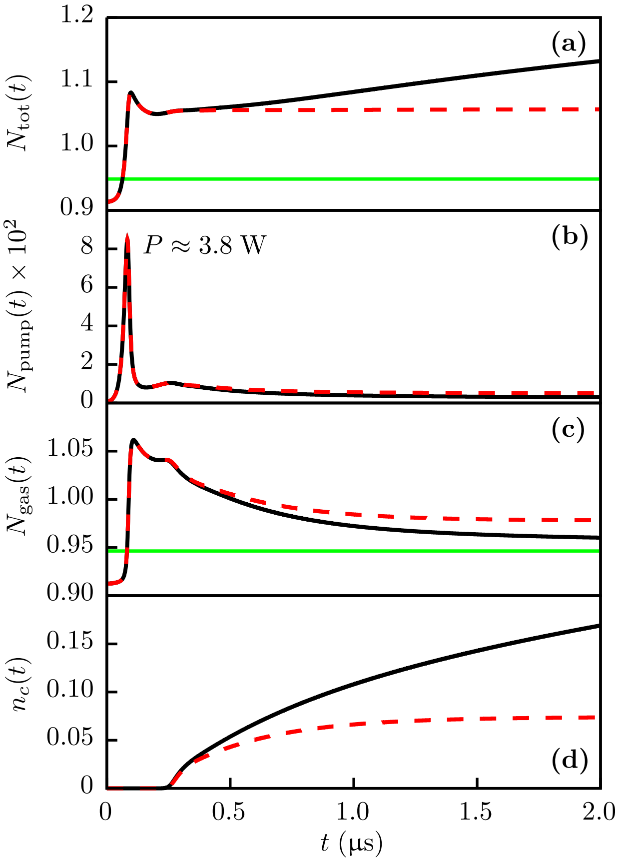

Figure 4.17: Time evolution of magnon populations in different regions of the spectrum at a pumping field of $h_{\mathrm{pump}} \approx 59.9\,\mathrm{Oe}$. The dashed red lines correspond to the case incorporating the phenomenological linear damping of the condensate described by Eq. (4.16), whereas the solid black lines correspond to the case neglecting this damping as in the previous simulations. (a) Total magnon number as a function of time. The solid green line denotes the critical density. (b) Magnons in the pumping region as a function of time. The peak power at $t \approx 83$ ns amounts to $P \approx 3.8$ W. (c) Magnon population of the gaseous phase defined by Eq. (4.14) as a function of time. The solid green line denotes the critical density. (d) Time evolution of the condensate.

population of the gaseous magnon phase (c) which lies slightly above the population in the case without the linear damping of the condensate, shown by the solid black line. Due to the smaller amount of magnons in the condensate, the scattering of magnons in the gaseous phase into the condensate is weaker than in the case without the condensate damping which results into a slightly larger population of the gaseous phase. In order to see how the magnons which are responsible for this difference in populations are distributed over the spectrum, we plot in Fig. 4.18 the stationary distributions at $t = 2$ µs in both the case including the linear damping of the condensate, indicated by the solid red line, and in the case without the linear condensate damping, indicated by the solid green line. As already pointed out in Fig. 4.16, the latter distribution gradually approaches the critical distribution with $\mu_{\mathrm{m}} = E_{\mathrm{min}}$ and $T_{\mathrm{m}} = 300$ K, shown by the dashed black line. However, the stationary distribution in the case including the condensate damping lies above the critical distribution and appears as a straight line which is parallel to the straight line indicating the critical distribution. Therefore, we can describe this steady state at low magnon energies $E < 6$ GHz by $\mu_{\mathrm{m}} = E_{\mathrm{min}}$ and an effective temperature of $T_{\mathrm{m}} = 435$ K, denoted by the dotted black line. At magnon energies above the pumping region $E > 8$ GHz ($E_{\mathrm{min}} \approx 5$ GHz), the stationary distribution quickly approaches the critical distribution with $T_{\mathrm{m}} = 300$ K.

Interestingly, the effective temperature does not increase by applying a stronger pumping field, only the condensate saturates at a higher level. This behavior is reasonable since the scattering of gaseous magnons into the condensate scales linearly with n_c (cf. Eq.(2.88)), just as the damping of the condensate (4.16). In a simple manner, we can write the time evolution

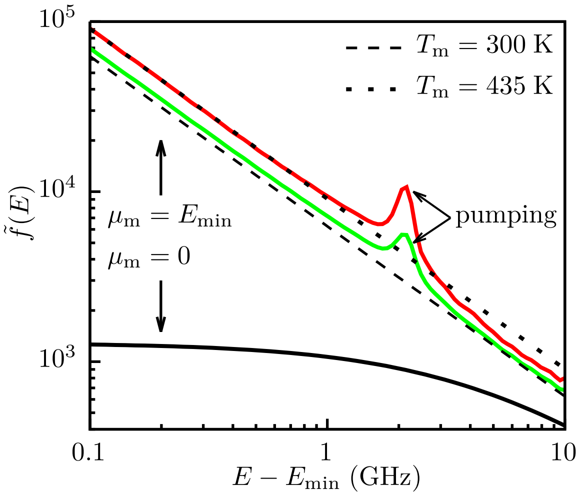

Figure 4.18: Stationary magnon distributions at $t = 2$ µs in the case including the linear damping of the condensate (cf. Eq. (4.16)), denoted by the solid red line, and in the case excluding the condensate damping, denoted by the solid green line. The solid black line shows the distribution at room temperature equilibrium at $t = 0$. The dashed black line corresponds to the critical distribution with $\mu_\mathrm{m} = E_\mathrm{min}$ and $T_\mathrm{m} = 300$ K, whereas the dotted black line corresponds to a distribution with $\mu_\mathrm{m} = E_\mathrm{min}$ and $T_\mathrm{m} = 435$ K.

of the condensate as

$$\frac{\mathrm{d}}{\mathrm{d}t} n_c = \gamma(T_\mathrm{eff})\, n_c - \Gamma(T_\mathrm{ph})\, n_c, \tag{4.17}$$

where γ is the rate of magnons entering the condensate which depends on the effective temperature T_eff and Γ is the damping rate of the condensate which almost exclusively depends on the overall magnon temperature at higher energies, which coincides with the phonon temperature T_ph due to the Cherenkov process. In a steady state, T_eff adjusts in a way that these two contributions cancel out, that is

$$\gamma(T_\mathrm{eff}) = \Gamma(T_\mathrm{ph}), \tag{4.18}$$

which shows that the effective temperature only depends on T_ph rather than on the pumping field. The emerging stationary condensate level is therefore only determined by the constant flux of magnons F into the condensate

$$\gamma(T_\mathrm{eff})\, n_c = F(h_\mathrm{pump}), \tag{4.19}$$

which indeed depends on the strength of the pumping. Noteworthy, the damping rate of the condensate Γ can also be altered by varying the applied magnetic field since the lower bound of integration in Eq. (4.16) quickly increases with increasing magnetic field, just as in the confluence process at small wave vectors, discussed in Sec. 3.1. By means of this linear damping, the divergence of the total magnon number in the case of continuous pumping is remedied and we thus include this damping in the remaining simulations.

4.2.1 Bose-Einstein Condensation at High Pumping Powers

As already mentioned in the beginning of this section, Serga *et al.* found unexpected behavior of the condensate at large pumping powers [32]. In this experiment, a strong pumping pulse with a pump frequency of $f_\mathrm{pump} = \omega_\mathrm{pump}/2\pi = 14$ GHz is applied with a duration of 2 µs which leads to the appearance of primary magnons at $f_\mathrm{peak} = \omega_\mathrm{peak}/2\pi = 7$ GHz exhibiting a high peak power of $P = 25$ W. The time evolution of the pumped magnons and the build up of a magnon condensate in the lowest energy state at $E_\mathrm{min} \approx 5$ GHz is then measured via BLS. Figure 4.19 shows the measured BLS intensities of (a) the pumping region, (b) the gaseous magnons measured at $E_\mathrm{gas} = 6$ GHz and (c) the magnon condensate, respectively. All

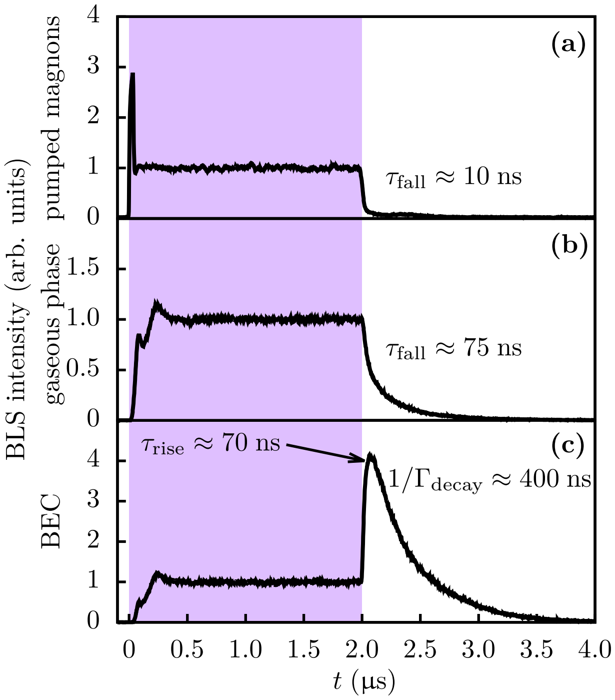

Figure 4.19: BLS intensities as measured in Ref. [32] of (a) pumped magnons at $E_{\mathrm{peak}} = 7$ GHz, (b) gaseous magnons at $E_{\mathrm{gas}} = 6$ GHz and (c) BEC magnons in the lowest energy state at $E_{\mathrm{min}} = 5$ GHz as a function of time. The purple shaded area denotes the action of the pumping. All quantities are normalized to their respective stationary values before the pumping stops at $t = 2$ µs. The decay of the pumped magnons and of the gaseous magnons is non-exponential and the corresponding fall times correspond to a decrease by half of the original populations, respectively. Experimental data by courtesy of A. A. Serga, originally published in Serga *et al.*, Nat. Commun. 5, 3452 (2014).

intensities are normalized to their respective stationary values, which are approached several hundreds of nanoseconds after the pumping has started. The pronounced peak in the density of pumped magnons at the beginning of the pumping, which we have already discussed in this section, also appears in this experiment, as can be seen in Fig. 4.19(a). At $t = 2$ µs, the pumping stops and the population of the pumping region decreases non-exponentially by half within $\tau_{\mathrm{fall}} \approx 10$ ns, also the population of the gaseous magnon phase decreases non-exponentially by half within $\tau_{\mathrm{fall}} \approx 75$ ns. Surprisingly, the condensate behaves differently and jumps upward in population by a factor of four instead of decaying directly after the end of the pumping. The rise time of the condensate was determined to be $\tau_{\mathrm{rise}} \approx 70$ ns which is correlated in time with the decay of the gaseous magnon phase. After the condensate reaches the maximum value in the upward jump, it relaxes again with a characteristic time of $1/\Gamma_{\mathrm{decay}} \approx 400$ ns. Noteworthy, shortly before interrupting the pumping at $t = 2$ µs, the density of the gaseous phase was found to be about a factor of 666 larger than the density at room temperature equilibrium. Since the magnon energies in the low energy part of the spectrum are much smaller than the thermal energy at room temperature $E \ll k_{\mathrm{B}} T_{\mathrm{m}}$, the occupation of the gaseous phase at $E_{\mathrm{gas}} = 6$ GHz can be described by a Rayleigh-Jeans distribution (3.22), as we have already seen in Sec. 3.2. By assuming that the stationary distribution of the gaseous phase at $t = 2$ µs can be described by a chemical potential $\mu_{\mathrm{m}} = E_{\mathrm{min}}$ and an effective temperature T_{eff}, it is possible to compare the distribution shortly before the pumping stops with the distribution at room temperature equilibrium,

$$\frac{\tilde{f}(E_{\mathrm{gas}}, t = 2\ \mu\mathrm{s})}{\tilde{f}(E_{\mathrm{gas}}, t = 0)} = 666 = \frac{E_{\mathrm{gas}}}{E_{\mathrm{gas}} - E_{\mathrm{min}}} \frac{T_{\mathrm{eff}}}{300\ \mathrm{K}}. \tag{4.20}$$

Via this relation, the effective temperature in the low energy region about $E \approx 6$ GHz can be estimated to be $T_{\mathrm{eff}} \approx 30000$ K.

Since this high effective temperature is reasonable only in a small spectral region, the authors consequently argue with a two-temperature model and interpret this experiment

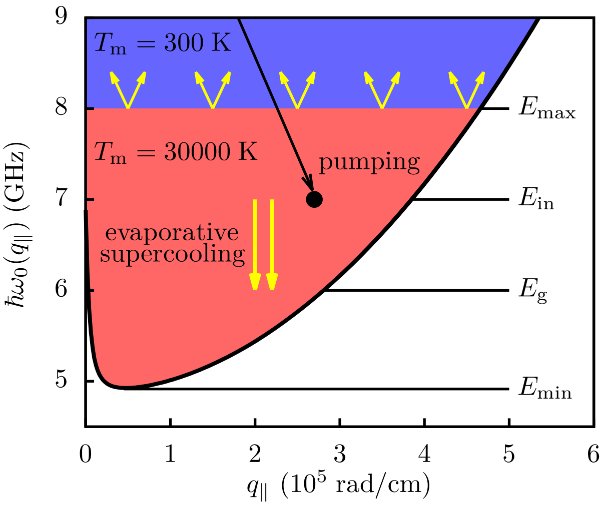

Figure 4.20: Schematic illustration of the evaporative supercooling mechanism. The black line shows the dispersion (2.24) of the lowest mode of a 5 µm-thick YIG film parallel to the external field of $H_0 = 1735\,\mathrm{Oe}$. E_max separates the low energy part at $T_\mathrm{m} = 30000$ K from the rest of the spectrum at $T_\mathrm{m} = 300$ K. The pumping injects magnons with energy E_in and the small yellow arrows denote the scattering of magnons from the edge of the low energy part into the room temperature part of the spectrum. The two thick yellow arrows indicate the reduction of the average energy from E_in to E_g.

by means of an evaporative supercooling mechanism. As depicted in Fig. 4.20, the strong pumping creates an overheated magnon gas in the low energy region with energies $E \lesssim 8$ GHz. The authors then introduce a hypothetic energy boundary E_max, which separates the overheated low energy part from the rest of the magnon spectrum still remaining at room temperature equilibrium. By considering only the low energy part, the pumping injects hot magnons at the energy E_in which increase the average energy of this region, therefore the pumping acts as a heating source. This heating is compensated by magnons which scatter from the edge of the low energy region at E_max to states with higher energies in the room temperature part of the spectrum, thus providing an evaporative cooling of the overheated low energy part. As a result, the average energy of the low energy part decreases from the injection energy E_in to a smaller energy E_g, as indicated by the two yellow arrows in Fig. 4.20. When the pumping is on, these two mechanisms balance each other so that a moderate condensate is formed, described by the steady population in Fig. 4.19(c). However, when the pumping is switched off, the associated heating also vanishes and the evaporative cooling mechanism leads to a further decrease of the average energy and also leads to an increase of the chemical potential. Therefore, as soon as the pumping is switched off, the scattering of magnons from the gaseous phase into the condensate is enhanced which explains the decrease of the magnon population in the gaseous phase and the likewise increase of the condensate, as seen in Fig. 4.19(c).

However, within the scope of our kinetic approach, it is not possible to reproduce the results of this experiment based on the (plausible) explanation provided by the authors. The reason is that the low lying energy part is only considerably decoupled from the rest of the spectrum if the timescale of dynamical processes in the low energy region is essentially smaller than the timescale in the energy region above a certain boundary, which would separate these two regions. Only if this requirement is met, the low energy part behaves autonomously revealing properties as pumping-induced heating and evaporative cooling. However, as already discussed in Sec. 3.1, the four-magnon process even becomes stronger with increasing wave vector, so that the low lying energy part actually does not behave as being separated from the rest of the spectrum, at least in our model. Therefore, a higher pumping power would only result in a higher saturation level of the condensate without overheating the low energy part, as already discussed in this section.

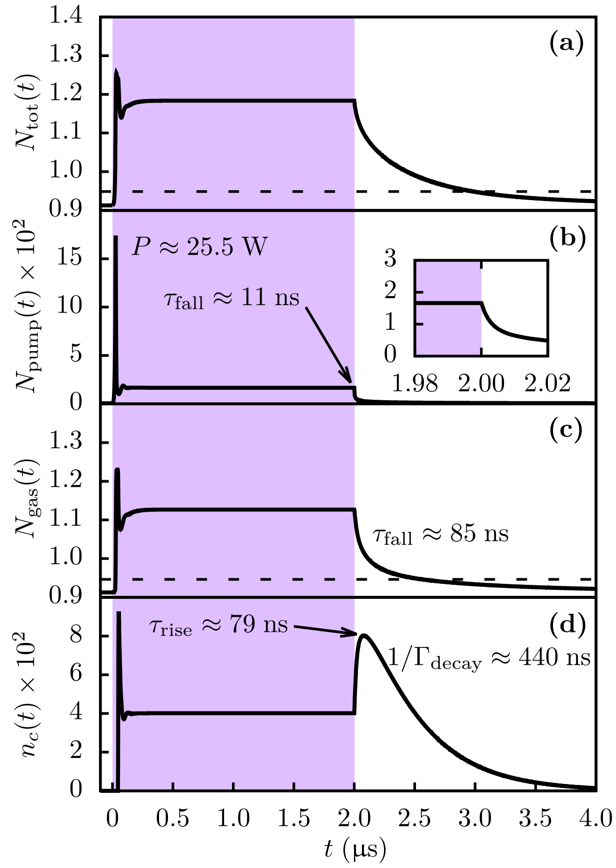

Figure 4.21: Time evolution of magnon populations in different parts of the spectrum. The purple shaded area denotes the action of the pumping. (a) Total magnon number. The dashed black line indicates the critical magnon density at room temperature. (b) Magnon population in the pumping region. P is the absorbed peak power. The inset shows a zoom into the end of the pumping. τ_{fall} follows by determining the time at which the population is decreased to $1/e$ of the original population before the pumping has stopped. (c) Magnon population of the gaseous phase. The dashed black line indicates the critical magnon density at room temperature. τ_{fall} follows by determining the time at which the population in the gaseous phase is decreased to $1/e$ of the original population at $t = 2$ µs deducting the critical density. (d) Time evolution of the condensate. τ_{rise} is defined as the time difference between the maximum of the peak and the end of the pumping. Γ_{decay} is the rate of the subsequent exponential decay.

We nevertheless present an alternative explanation for the experimental findings. As we have seen in this section, the steady state of the gaseous phase in the case of continuous pumping can be described by an effective temperature in the low energy part of the spectrum, which depends on the strength of the condensate damping (cf. Eq. (4.18)). Since the rate at which magnons scatter into the condensate increases with increasing difference between the effective temperature and the phonon temperature, a stronger condensate damping would consequently result in a higher effective temperature, provided the pumping is strong enough to establish this magnon distribution far from equilibrium. In the case of the linear damping of the condensate (4.16), induced by the three-magnon confluence process, we have shown that this effective temperature is about $T_{\mathrm{eff}} \approx 435$ K at room temperature. In order to reproduce the experimental results, we thus postulate a strong nonlinear damping of the condensate

$$\frac{\mathrm{d}}{\mathrm{d}t} n_c = -\Gamma_{\mathrm{pump}}\, n_c^2, \tag{4.21}$$

which is only present as long as the strong pumping is active. We set $\Gamma_{\mathrm{pump}} = 1/\mathrm{ns}$, which describes the strength of the pumping-induced condensate damping. As a consequence, this damping vanishes by switching off the pumping in our simulation. The source of this kind of damping could be a direct interaction between a microwave photon during the pumping and two condensate magnons lying at wave vectors $\boldsymbol{q}_{\mathrm{min}}$ and $-\boldsymbol{q}_{\mathrm{min}}$, respectively.

We start the simulation by applying a strong pumping field of $h_{\mathrm{pump}} = 108\,\mathrm{Oe}$ with a duration of 2 µs. Figure 4.21 shows the time evolution of (a) the total magnon number, (b) the magnons in the pumping region, (c) the magnons in the gaseous phase, as defined in Eq. (4.14), and (d) the population of the condensate, where the purple shaded area denotes

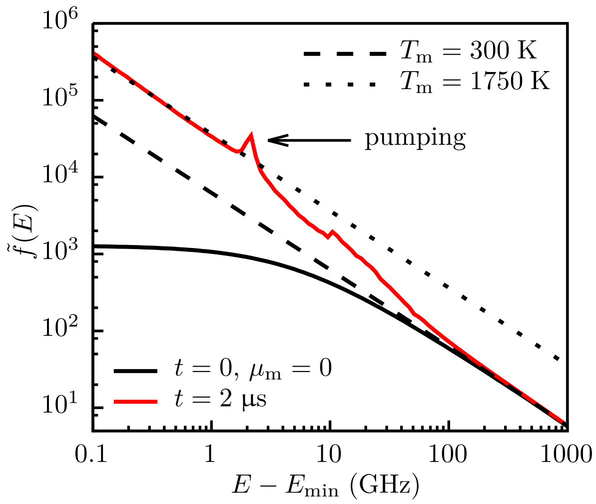

Figure 4.22: Magnon distribution as a function of energy. The solid black line shows the initial magnon distribution at room temperature equilibrium, whereas the solid red line shows the stationary magnon distribution at $t = 2$ µs. The dashed black line corresponds to the critical distribution with $\mu_\mathrm{m} = E_\mathrm{min}$ and $T_\mathrm{m} = 300$ K, whereas the dotted black line corresponds to a distribution with $\mu_\mathrm{m} = E_\mathrm{min}$ and $T_\mathrm{m} = 1750$ K.

the time interval in which the pumping is active. The characteristic overshoot of magnons in the pumping region is very pronounced in this case due to the large pumping field and results in a peak power of $P \approx 25.5$ W, similarly to the power absorption achieved in the experiment. Also the condensate initially overshoots due to both the strong pumping and the strong damping and reaches a steady population after a transient process which takes about $t \approx 200$ ns. The magnons in the gaseous phase and in the pumping region also approach steady populations which are maintained until the pumping is switched off at $t = 2$ µs. Therefore, the creation of magnons via microwave pumping is balanced through both the nonlinear damping of magnons entering the condensate and the three-magnon process which damps the magnons in the gaseous phase. As can be seen in Fig. 4.22, the stationary magnon distribution at $t = 2$ µs, shown by the solid red line, can indeed be described in the low energy part ($E < 6$ GHz) by a chemical potential $\mu_\mathrm{m} = E_\mathrm{min}$ and by an elevated effective temperature of about $T_\mathrm{eff} \approx 1750$ K, denoted by the dotted black line, which nevertheless does not approach the estimated temperature of $T_\mathrm{eff} \approx 30000$ K in the experiment. At high magnon energies $E > 100$ GHz, the magnon distribution again follows the room temperature distribution, denoted by the dashed black line, as a result of the Cherenkov process. Thus, at intermediate energies, the magnon distribution can not be described by any Bose-Einstein distribution and a gradual transition between these two temperature regions takes place in contrast to a more or less sharp boundary E_max, as assumed in Ref. [32]. At $t = 2$ µs, the pumping is switched off and the nonlinear damping of the condensate (4.21) vanishes simultaneously. Turning again to Fig. 4.21, we see that the magnon population in the pumping region (b) immediately falls down due to a strong four-magnon process. The inset shows a zoom into the end of the pumping, which reveals a clearly non-exponential decrease of the pumped magnons with a fall time of $\tau_\mathrm{fall} \approx 11$ ns, in good agreement with the experiment. The total magnon number (a) instantaneously begins to decrease due to the three-magnon process which is reasonable in the absence of any magnon pumping. However, the magnon population in the gaseous phase (c) decreases even more rapidly, because magnons in the overheated low energy part are still scattering into the condensate. This process is finished not until the critical magnon distribution at room temperature is reached. The resulting decay in the gaseous magnon phase is also non-exponential and we calculate a fall time of $\tau_\mathrm{fall} \approx 85$ ns. In the absence of the nonlinear damping, the condensate (d) thus jumps in population by a factor of two, with a rise time of about $\tau_{\text{rise}} \approx 79$ ns, which is also in reasonable agreement with the experiment. After the rise of the condensate, the low energy part is cooled again to room temperature and the condensate relaxes with a characteristic time of about $1/\Gamma_{\text{decay}} \approx 440$ ns, similarly to the measured characteristic time of $1/\Gamma_{\text{decay}} \approx 400$ ns in the experiment (cf. Fig. 4.19).

As we have seen, by means of a pumping-induced nonlinear damping of the condensate (4.21), it is possible to reproduce the experimental results of Ref. [32] remarkably well in the framework of our kinetic theory, although the effective temperature of the overheated low energy part is significantly smaller in the simulation than the estimated temperature based on the experiment.

Pumping-Induced Destruction of the Condensate

In a second experiment [32], a freely decaying magnon BEC was observed to rapidly decrease by applying an additional strong pumping pulse. By the same means as in the previous experiment, a long pumping pulse creates an overheated magnon gas and a moderate condensate so that steady populations are reached. Figure 4.23 shows the normalized BLS intensity as a function of time for the gaseous magnons (blue line in Fig. 4.23(a)) and for the condensate (red line in Fig. 4.23(b)), where the purple shaded area again denotes the action of the pumping. At $t = 0$, the pumping is switched off resulting in an upward jump of the condensate and a strong decrease of the gaseous magnons which is similar to the behavior of the magnetic system in the previous experiment. After the rise time of the condensate, the freely decaying BEC is again disturbed at a delay time of $t = 100$ ns by application of an additional pumping pulse with a duration of 150 ns. As can be seen in Fig. 4.23, the condensate immediately decreases, even below the steady population, and the gaseous magnon density promptly increases with comparable timescales thereby quickly approaching again the original population. However, the condensate reaches its steady population only after a short transient time of about 50 ns and still increases slightly afterwards. At a delay time of $t = 250$ ns, the pumping is again switched off resulting in a prompt decrease of the gaseous magnons and a jump in the condensate which slightly exceeds the maximum value of the first jump. After reaching the maximal value, the condensate again relaxes, in this experiment, however, with a significantly smaller characteristic time of about $1/\Gamma_{\text{decay}} \approx 220$ ns in comparison with the previous experiment.

The interpretation provided by the authors of Ref. [32] is similar as in the previous experiment. By applying the pumping to the freely decaying BEC again, hot magnons are injected into the low lying energy part which increase the average energy in the absence of the evaporative cooling which requires some time to fully develop due to the lack of magnons in the gaseous phase. The cooling of the gaseous phase is thus taken over by the magnons in the condensate which scatter into the gaseous phase.

By the same reasons as given above we are not able to reproduce this experiment based on the explanation provided by the authors. Nevertheless, we again take the postulated nonlinear damping of the condensate (4.21) into account and we start the simulation by applying the same pumping sequence as in the experiment by using the same physical parameters as in the previous simulation. The result is shown in Fig. 4.23 by the black lines. We use a long pumping pulse in order to a achieve the steady populations of the gaseous phase (a) and of the condensate (b). In the case of the gaseous magnons, we deduct the critical magnon

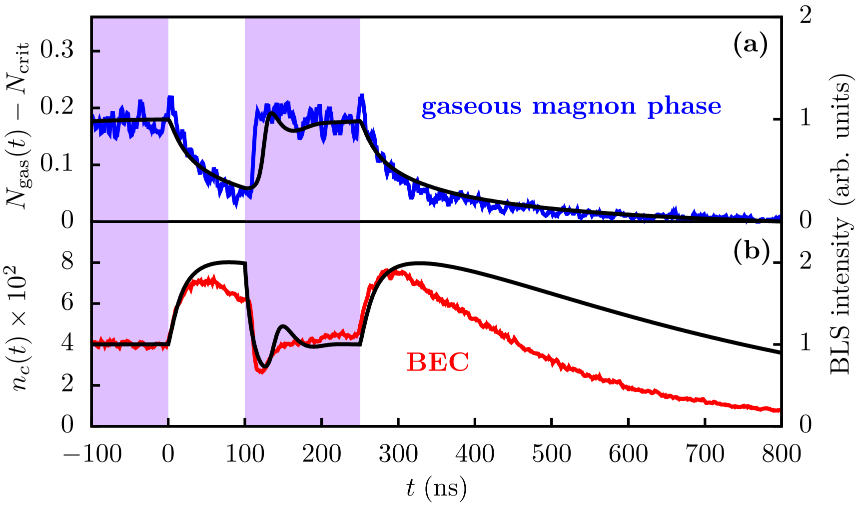

Figure 4.23: Magnon populations of the gaseous phase (a) and of the condensate (b) as a function of time. The purple shaded area denotes the action of the pumping. The black lines show the results based on our theoretical model, whereas the blue and red lines respectively show the measured BLS intensities of Ref. [32] which are normalized to the respective stationary values. Experimental data by courtesy of A. A. Serga, originally published in Serga *et al.*, Nat. Commun. 5, 3452 (2014).

density N_{crit} since only these non-equilibrium magnons finally enter the condensate. At $t = 0$, the pumping is interrupted which results in the jump of the condensate and the simultaneous decrease of the gaseous magnon phase which very well coincide with the respective jumps of the populations in the experiment. At a delay time of $t = 100$ ns, the pumping and consequently the nonlinear damping are again activated resulting in both a dramatic downward jump of the condensate which even falls below the original population, and a comparable increase in the population of the gaseous magnon phase, just as in the experiment. After a transient time of about 100 ns, both the gaseous phase and the condensate again approach their steady populations which persist until the pumping is again switched off at $t = 250$ ns. The subsequent time evolution is again the same as in the previous simulation after the end of the pumping at $t = 2$ µs (cf. Fig. 4.21), which in the case of the gaseous magnons is in excellent agreement with the experiment, as can be seen in Fig. 4.23(a). However, the decay time of the condensate in this experiment, as mentioned above, is significantly smaller than the decay times of both the previous experiment and the simulation.

As we have seen, the agreement between the simulation and this experiment is also remarkable, although we are not able to reproduce correctly the transient behavior of the condensate in the temporal interval between $t = 100$ ns and $t = 250$ ns, in which the condensate even exceeds the original population in the experiment. As a consequence, the second jump of the condensate in the simulation does not exceed the maximal value of the first jump in contrast to the experiment. Furthermore, we are not able to reproduce correctly the decay of the condensate after the pumping stops. However, the time evolution of the gaseous magnons is in perfect agreement with the experiment.

4.3 Phonon-Mediated Bose-Einstein Condensation

This section discusses the possibility of magnon Bose-Einstein condensation via a temperature decrease in the magnetic system as opposed to the usual approach of pumping non-equilibrium magnons into the spectrum for reaching the critical condition for BEC. An easy estimate shows that for a magnetic system at room temperature, a temperature decrease of $\Delta T_{\mathrm{m}} \approx 10$ K is already sufficient to cause the BEC transition, provided the magnon number conservation holds. The question now arises, how to cool the magnetic system. As we know, the magnetic system is coupled to the phonon heat bath via the Cherenkov process which leads to an energy transfer between the two subsystems until the temperatures of both magnons and phonons coincide. In Fig. 3.14 in Sec. 3.2, we already discussed the response of the magnetic system initially exhibiting a temperature of $T_{\mathrm{m}} = 400$ K which is coupled to a phonon heat bath at $T_{\mathrm{ph}} = 300$ K under the Cherenkov process only. Indeed, as we have seen, the Cherenkov process leads to a cooling of the magnetic system by emission of phonons, so that high energy magnons are scattered to lower energies under magnon number conservation. However, the timescales of the scattering processes strongly increase at lower magnon energies so that the hot magnons are not able to reach the lowest energy state and therefore a magnon BEC is prohibited. Nevertheless, by including the four-magnon process in the simulation, magnons in the low energy part are again enabled to scatter further to lower energies including the lowest energy state. This combination of interaction processes would indeed result in the equilibrium state exhibiting a magnon condensate predicted by means of Eq. (3.28). However, in real situations, the initially hot magnons are continuously damped via the three-magnon process on their way down to the lowest energy state. We therefore investigate in this section, under which conditions a temperature difference between the magnons and the phonons results in a magnon BEC. While doing so, we assume that the magnetic properties, i. a. the saturation magnetization and the effective coupling constants, do not differ at larger magnon temperatures from those at room temperature.

We start by simulating the full dynamics of the magnetic system which initially has a temperature of $T_{\mathrm{m}} = 400$ K and $\mu_{\mathrm{m}} = 0$ and is coupled to a phonon heat bath at $T_{\mathrm{ph}} = 300$ K. We set the external magnetic field to $H_0 = 1735\,\mathrm{Oe}$, equal to the field used in the previous section. The time evolution of the magnon distribution is shown in Fig. 4.24. After a delay time of $t = 25$ ns, the high energy part of the spectrum with energies $E > 500$ GHz has already adopted the temperature of the phonon heat bath, as indicated by the dashed black line. As a consequence of the Cherenkov process, the hot magnons scatter to lower energies $E < 100$ GHz and are further redistributed by the four-magnon process. At a delay time of $t = 100$ ns, a considerable fraction of the hot magnons reaches the low energy part of the spectrum, which is nevertheless too small in order to exceed the critical distribution, as indicated by the dashed black line. In the subsequent time evolution, the three-magnon process prevails over the four-magnon process and the magnon distribution gradually approaches the equilibrium distribution at room temperature and vanishing chemical potential $\mu_{\mathrm{m}} = 0$. We now take a closer look to the magnon populations in different regions of the spectrum, shown in Fig. 4.25 by the solid black lines. The cooling of the magnetic system takes place very quickly as shown by the internal energy U in Fig. 4.25(b), which approaches the room temperature internal energy, as indicated by the solid green line, within $t = 50$ ns. This rapid cooling is a result of the strong Cherenkov process at high magnon energies $E > 500$ GHz, which are most responsible for the total energy of the magnetic system since the energy density, defined as

$$w(E) = \rho(E)\, E = D(E)\, \tilde{f}(E)\, E, \tag{4.22}$$

behaves as $w(E) \propto \sqrt{E}$ at large energies. Figure 4.25(a) shows the total magnon number, where the solid green line indicates the critical magnon density at room temperature. It

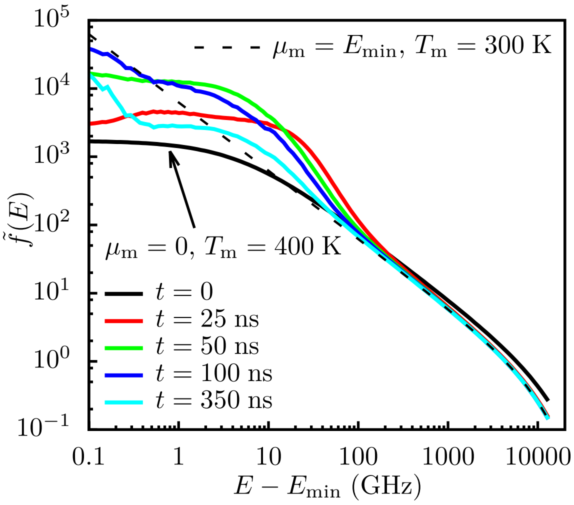

Figure 4.24: Magnon distribution function at different delay times. The solid black line shows the initial magnon distribution with $T_\mathrm{m} = 400$ K and vanishing chemical potential, whereas the dashed black line indicates the critical magnon distribution with $T_\mathrm{m} = 300$ K and $\mu_\mathrm{m} = E_\mathrm{min}$. The magnetic system is coupled to a phonon heat bath at room temperature.

is visible that not until a delay time of about $t \approx 50$ ns, the total magnon number strongly decreases. Obviously, this delay time coincides with the duration of the cooling process, which is reasonable since the delay time is determined by the onset of the three-magnon confluence process, which considerably becomes effective, when the initially hot magnons strongly gather in the low energy part of the spectrum with $E < 10$ GHz. Meanwhile, magnons indeed begin to populate the minimum region, as can be seen in Fig. 4.25(c), which is caused by the four-magnon process, being absent in the simulation shown in Fig. 3.14 in Sec. 3.2. At $t \approx 120$ ns, the maximum of magnon population in the minimum region is reached, which nevertheless is too small for the magnons to populate the condensate as shown in Fig. 4.25(d). Thus, the condensate stays below the initial seed of $n_c(t = 0) = 10^{-10}$ and decreases due to both the linear damping and also the scattering of magnons out of the condensate. As we have seen, a temperature decrease of $\Delta T_\mathrm{m} = 100$ K leads to a scattering of hot magnons down to the lowest energy state which is nevertheless still too slow so that the three-magnon process effectively damps the hot magnons, resulting in a prevention of the BEC transition.

We therefore increase the initial magnon temperature to $T_\mathrm{m} = 500$ K and repeat the simulation. The time evolution of the magnon distribution in this case is shown in Fig. 4.26. The high energy part of the spectrum again adopts the phonon temperature within $t = 25$ ns, and the hot magnons already gather in the low energy part. At $t = 100$ ns, a supercritical magnon distribution is formed, before the three-magnon damping again leads to a depletion of magnons in the low energy part resulting in an equilibrium distribution with $\mu_\mathrm{m} = 0$. In order to see if a magnon condensate is formed, we additionally plot in Fig. 4.25 the populations of different parts of the spectrum in the case including an initial magnon temperature of $T_\mathrm{m} = 500$ K, shown by the dashed red lines. The cooling process is again very fast, as can be seen in Fig. 4.25(b), so that the internal energy at room temperature is approached within $t = 50$ ns, similar to the previous simulation. The pronounced decrease of the total magnon number, shown in Fig. 4.25(a), nevertheless sets in already at a delay time of about $t \approx 25$ ns. This is caused by the four-magnon process which is stronger due to the higher magnon density and leads to a faster redistribution of hot magnons in the low energy part, as we have already seen in Fig. 4.26. Thus, also the damping sets in earlier. After a delay time of $t \approx 100$ ns, the total magnon numbers in both cases again coincide and gradually decrease on a timescale of several hundreds of nanoseconds, corresponding to the three-magnon process at moderate

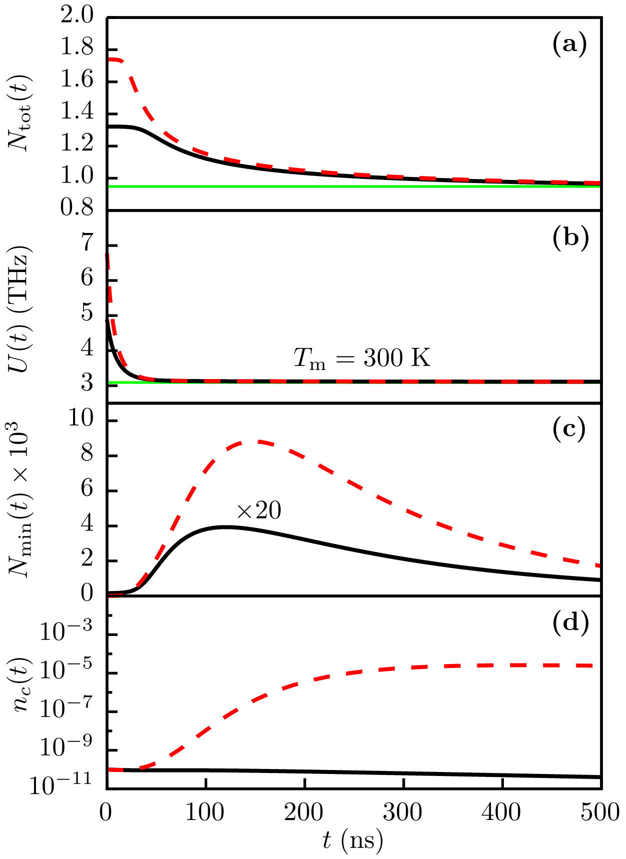

Figure 4.25: Time evolution of the hot magnons in different regions of the spectrum. The solid black lines correspond to an initial magnon temperature of $T_{\mathrm{m}} = 400$ K, whereas the dashed red lines correspond to an initial magnon temperature of $T_{\mathrm{m}} = 500$ K. (a) Total magnon number as a function of time. The solid green line indicates the critical magnon density at room temperature. (b) Internal magnon energy. The solid green line indicates the internal magnon energy at room temperature. (c) Amount of magnons in the low energy part of the spectrum, defined in Eq. (4.6). The magnon population which is represented by the solid black line is multiplied by a factor of 20. (d) Occupation of the magnon condensate as a function of time.

magnon densities. As can be seen in Fig. 4.25(c), the magnon population in the minimum region strongly increases in the meantime and reaches a maximum at about $t \approx 150$ ns which is comparable to the density of magnons achieved in the parallel pump simulations (cf. Fig. 4.5 and Fig. 4.7), in the case of condensation. In accordance with these simulations, the magnon system undergoes Bose-Einstein condensation, as shown in Fig. 4.25(d), and the condensate reaches a maximum at about $t \approx 420$ ns which is also two orders of magnitude smaller than the non-condensed magnons in the minimum region, as in the parallel pump simulations.

By further increasing the initial temperature difference between the magnons and the phonons, the simulations predict an even stronger condensate. However, the spin wave approximation loses its validity in the vicinity of the Curie temperature, which amounts to $T_{\mathrm{C}} \approx 559$ K in YIG [51]. Therefore, we keep $T_{\mathrm{m}} = 500$ K as an upper limit for the magnon temperature, which we are able to treat within the framework of our kinetic theory. Noteworthy, the magnetic system, initially being at room temperature equilibrium, does not undergo Bose-Einstein condensation by coupling to a phonon bath at $T_{\mathrm{ph}} = 3$ K since the magnon density at room temperature is too small for the four-magnon process to redistribute the hot magnons sufficiently fast.

In real situations, the temperature difference is not present instantaneously, as we have assumed in the previous simulations. The phonon system can be rather cooled on a certain timescale and the magnetic system then follows this temperature. We suppose this temperature decrease in the phonon heat bath to be exponential and we therefore make an ansatz

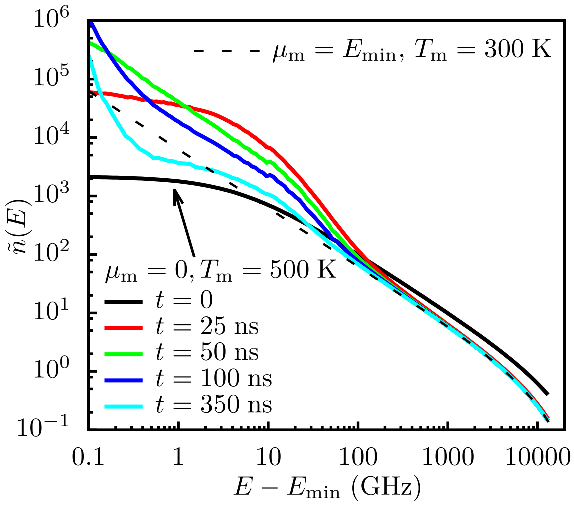

Figure 4.26: Magnon distribution function at different delay times. The solid black line shows the initial magnon distribution with $T_\mathrm{m} = 500$ K and vanishing chemical potential, whereas the dashed black line indicates the critical magnon distribution with $T_\mathrm{m} = 300$ K and $\mu_\mathrm{m} = E_\mathrm{min}$. The magnetic system is coupled to a phonon heat bath at room temperature.

for the phonon temperature

$$\frac{\mathrm{d}}{\mathrm{d}t} T_\mathrm{ph} = -\Gamma_\mathrm{ph}\,(T_\mathrm{ph} - T_0), \tag{4.23}$$

where we set $T_0 = 300$ K and $T_\mathrm{ph} = T_\mathrm{m} = 500$ K as initial conditions. This time-dependent phonon temperature now enters the Planck distribution of the phonons in the kinetic equation resulting from the Cherenkov process (A.42). We then repeat the simulation with different characteristic times $1/\Gamma_\mathrm{ph}$ in order to see on which timescale the temperature decrease has to occur for ensuring the magnon condensation. The result is shown in Fig. 4.27, where we plot the maximum value of the condensate $\max\{n_c(t)\}$ as a function of the characteristic time $1/\Gamma_\mathrm{ph}$. It follows that the maximum value of the condensate strongly depends on the timescale of the temperature decrease and that the maximum value even does not exceed the initial seed for characteristic times $1/\Gamma_\mathrm{ph} \gtrsim 50$ ns. As we see, the temperature decrease has to occur on a timescale of only several nanoseconds for ensuring the formation of a moderate condensate of $\max\{n_c(t)\} \approx 10^{-5}$. The reason is that the four-magnon process only prevails over the three-magnon process under creation of a magnon condensate above a certain magnon density in the low energy region. If the temperature decrease of the phonon system from initially $T_\mathrm{ph} = 500$ K to $T_\mathrm{ph} = 300$ K is present instantaneously, the magnon density required for condensation is only just reached so that a small condensate emerges. However, if this temperature decrease follows the law (4.23) with $1/\Gamma_\mathrm{ph} \gtrsim 10$ ns, the required magnon density can not be reached anymore because the three-magnon process permanently damps the magnetic system also during the temperature decrease, when the scattering of hot magnons to the low lying energy part is not finished yet. At even larger characteristic times of $1/\Gamma_\mathrm{ph} \gg 500$ ns, much larger than the timescale of the three-magnon damping, the magnetic system adiabatically follows the phonon temperature prohibiting even the formation of a non-equilibrium state.

As we have seen, from the theoretical point of view, a fast temperature decrease in the phonon heat bath leads to a Bose-Einstein condensation in the magnetic system under certain conditions. However, only a temperature decrease in the phonon system from initially $T_\mathrm{ph} = 500$ K to $T_\mathrm{ph} = 300$ K which takes place within several nanoseconds results in a magnon density which is sufficient for the four-magnon process to prevail over the three-magnon damping for a short period of time so that a weak magnon condensate is finally established. Therefore, from the experimental point of view, we can rule out the possibility of a phonon

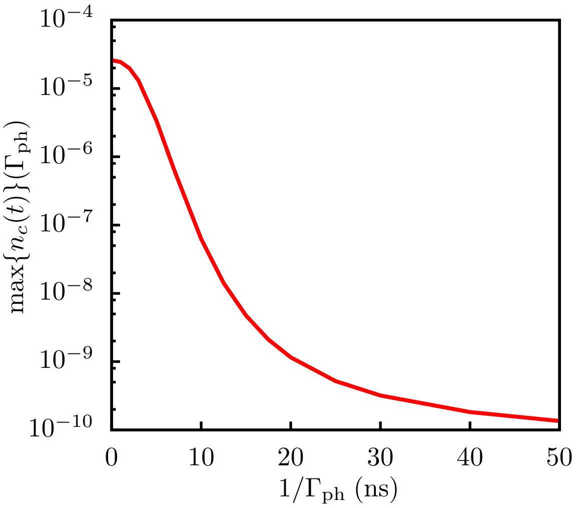

Figure 4.27: Maximum value of the condensate $\max\{n_c(t)\}$ as a function of the characteristic time $1/\Gamma_{\mathrm{ph}}$, defined in Eq. (4.23).

mediated BEC without external microwave pumping.

4.4 Concluding Remarks

In this chapter, we have discussed the magnon dynamics and Bose-Einstein condensation in different situations by means of the full model with all interaction processes included. Here, we briefly recapitulate the main results of this chapter.

In the first section, we have considered the Bose-Einstein condensation of magnons pumped via short microwave pulses into the low energy part of the spectrum. The magnon dynamics in this region is mainly governed by the three-magnon and four-magnon processes which are in competition to redistribute the pumped magnons. As we have seen, we get a good agreement with the experiments [24, 25] by means of the proposed modified four-magnon process with $\alpha S_0 \neq 0$ and $\alpha = 0.3$ which has just the right order of magnitude to reproduce the experimental results reasonably. However, the source of this hypothetic four-magnon process exhibiting an scattering amplitude of $A_4 \approx 2$ GHz in the low wave vector regime is yet unknown. In contrast, the common exchange four-magnon process ($\alpha S_0 = 0$) augmented by the dipolar contribution to the scattering amplitude is far too weak in order to explain the observed magnon thermalization. We have also considered the possibility of the magnon thermalization caused by a modified Cherenkov process. In this case, the thermalization process qualitatively distinguishes from the observed downward cascade of magnons in the experiment and the uniform mode relaxation rate originating from the modification of the Cherenkov interaction potential would exceed the observed value in the Kasuya-LeCraw experiment [48] by two orders of magnitude. Therefore, we can exclude the Cherenkov process as a possible thermalization mechanism in the isotropic model. On the other hand, the magnon damping caused by the three-magnon process which is induced by the dipolar interaction between the spins reasonably reproduces the observed attenuation of magnons in the experiment, though the isotropic approximation leads to an overestimation of the damping in the low energy part by a factor of approximately two.

In the second section, we have considered the case of continuous magnon pumping and discussed the magnon dynamics at different pumping fields. We have seen that there are two thresholds for the pumping field which qualitatively separate the magnon dynamics. Below the first threshold, the pumping is too weak in order to overcome the damping caused by the linear contributions of the three-magnon and four-magnon processes. Therefore, the pumped magnon density does not increase exponentially but saturates at a certain level. At a higher pumping field, exceeding the first threshold, the pumped magnons indeed begin to increase exponentially. However, the exponential increase is limited due to the nonlinear damping caused by the four-magnon process which results in an initial overshoot of the pumped magnon density, also observed in the experiment [32]. Above a second threshold for the pumping field, a magnon BEC emerges which increases unlimitedly while the population of the gaseous phase of the magnon system saturates and can be described by the critical magnon distribution with a magnon temperature equal to the phonon temperature. This unphysical behavior of the condensate is an artifact of the isotropic approximation which prohibits the three-magnon confluence process to affect the condensate by the conservation laws which is not the case in real dipolar-exchange dispersions. By phenomenologically including this linear damping into the model, the condensate indeed saturates at a certain level, depending on the strength of the pumping, and the damping also influences the gaseous phase of the magnetic system which can be described by an effective temperature in the low energy part of the spectrum exceeding the phonon temperature. Noteworthy, in the case of the linear condensate damping via the three-magnon confluence process, this effective temperature only depends on the phonon temperature and the external magnetic field, independent of the magnon pumping. Since a stronger condensate damping results in a higher effective temperature of the gaseous magnon phase, we exploited this property in order to present an alternative explanation for the unexpected behavior of the condensate found in the experiment [32] at high pumping powers. By switching off the strong pumping, the condensate was found to immediately jump upward in population against the expectation. Just before the end of the pumping, an effective magnon temperature of $T_{\mathrm{m}} \approx 30000$ K was estimated in the low energy part of the spectrum. We thus postulated a strong nonlinear damping of the condensate which is only present as long as the pumping is on, and which could probably be caused by an interaction between the condensate magnons and the microwave photons. By means of this nonlinear damping, we were able to explain both the upward jump of the condensate with timescales of the magnon dynamics in reasonable agreement with the experiment and also the elevated effective magnon temperature in the low energy part of the spectrum which nevertheless significantly falls below the estimated value.

In the final section, we finally discussed the possibility of a magnon Bose-Einstein condensation caused by a temperature decrease in the magnetic system in the absence of any external magnon pumping. The temperature decrease in the magnetic system is initiated by an abrupt decrease of the phonon temperature and is mediated by the Cherenkov process which cools the magnetic system by the redistribution of high energy magnons to the low energy part of the spectrum under particle number conservation. We have shown that an instantaneous decrease in the phonon temperature from $T_{\mathrm{ph}} = 400$ K to $T_{\mathrm{ph}} = 300$ K does not lead to a BEC in the magnetic system, initially being in equilibrium with the lattice at $T_{\mathrm{m}} = 400$ K. However, an instantaneous jump in the phonon temperature from $T_{\mathrm{ph}} = 500$ K to $T_{\mathrm{ph}} = 300$ K indeed results in a weak magnon condensate in the magnetic system, initially exhibiting a temperature of $T_{\mathrm{m}} = 500$ K. However, in real situations, the temperature decrease in the phonon system occurs on a certain timescale rather than taking place immediately. Therefore, we assumed an exponential decrease in the phonon temperature from initially $T_{\mathrm{ph}} = 500$ K to $T_{\mathrm{ph}} = 300$ K and we varied the characteristic time $1/\Gamma_{\mathrm{ph}}$ of the temperature decrease. We have seen that the magnitude of the condensate strongly depends on the timescale of the phonon temperature decrease, which has to take place at characteristic times below $1/\Gamma_{\mathrm{ph}} \approx 10\,\mathrm{ns}$ in order to cause the BEC transition in the magnetic system. Therefore, from the experimental point of view, we can rule out the possibility of a phonon mediated magnon condensation.

5

Conclusions

In this thesis a kinetic theory of the magnon Bose-Einstein condensation in YIG has been presented. We have developed a kinetic model for the simulation of the time evolution of the magnetic system, which takes into account the basic interactions between magnons themselves and between magnons and phonons. In the following, we summarize the main results of this thesis.

At the beginning, the theoretical model has been introduced in detail. Starting from an effective spin Hamiltonian in YIG, the spectrum of non-interacting magnons as well as the most important inherent magnon interactions, which are the three-magnon and four-magnon processes, have been derived. Furthermore, we presented both the magnon-phonon Cherenkov process, resulting from the coupling between the magnetic system and the lattice, and also the parallel pumping process, which is essential for describing the creation of non-equilibrium magnons. Moreover, we established the kinetic theory based on the Boltzmann equation and we derived the kinetic equations resulting from the respective magnon interactions. In addition, we revealed the equilibrium states of the individual kinetic equations and we introduced the non-equilibrium entropy in the closed magnetic system as well as the non-equilibrium free energy in the open magnetic system, which constitute the irreversibility of the time evolution towards the equilibrium. In the derivation of the four-magnon process, we found a quantum mechanical correction term which leads to a non-vanishing contribution in the interaction potential in the limit of zero wave vector, which strongly modifies the four-magnon scattering amplitude in the first Born approximation, but which nevertheless vanishes in the t-matrix approach.

In the subsequent chapter, we analyzed the magnon interaction processes individually. At first, we studied the linear properties of the kinetic equations by considering the respective relaxation rates. We compared the rates resulting from our kinetic model with the relaxation rates determined in the Kasuya-LeCraw experiment. It was shown that the four-magnon relaxation rate, which follows from the scattering amplitude augmented by the quantum mechanical correction term, exceeds the measured rates at small wave vectors by a factor of five, approximately. We thus introduced a correction factor in order to weaken the four-magnon process to be compatible with the experiment. As we have shown in the subsequent chapter, the resulting four-magnon process exhibits just the right order of magnitude for describing the experiments of pumped magnons reasonably. We further studied the equilibration processes of non-equilibrium initial conditions individually for the different interaction processes, revealing that the four-magnon process is responsible for both the internal thermalization of the magnetic system and for the formation of a magnon condensate. In contrast, we have demonstrated that the three-magnon process yields the main mechanism for the damping of the magnetic system. Moreover, it was shown that the Cherenkov process leads to an energy transfer between the magnetic system and the lattice which is finished as soon as the magnetic system adopts the lattice temperature. However, due to the interaction potential, this process only affects the magnetic system considerably at large wave vectors and is negligible in the low energy part of the spectrum.

In the final part of this thesis, we considered the full model with all interaction processes combined and we focussed on magnon Bose-Einstein condensation in different cases. First, we studied the dynamics of the magnetic system brought out of equilibrium by means of short intense pumping. We demonstrated that the agreement between our kinetic theory and the experiment is remarkable by employing the modified four-magnon process, introduced in the preceding chapter. In contrast, the dipolar contribution to the four-magnon scattering amplitude is far too weak in order to explain the fast magnon thermalization. Even at very large magnon densities the BEC transition can not be reached due to a strong three-magnon process prohibiting the condensate formation. We furthermore studied a modified Cherenkov process in order to see if this process could principally be responsible for the magnon thermalization. However, it turned out that the thermalization does not take place in a cascade of multiple scattering events, as observed in the experiments, and that the relaxation rate of the uniform mode drastically exceeds the measured rate in the Kasuya-LeCraw experiment. We subsequently discussed the case of continuous pumping, in which the characteristic overshoot of the pumped magnons, as observed in the experiment, is well reproduced by the kinetic model. We furthermore studied the stationary non-equilibrium states revealing the magnon distribution at low energies to be characterized by an effective temperature, exceeding the room temperature, which solely depends on the strength of the condensate damping. Based on this insight, we presented an alternative explanation for the recently observed upward jump of the condensate, which is caused by switching off the pumping at high pumping powers. By assuming a hypothetic strong condensate damping, which acts as long as the pumping is active, we showed that the timescales of dynamical processes governing the condensate as well as the gaseous magnon phase are in excellent agreement with the experiment. The condensate jump could be reproduced remarkably well, in contrast to the estimated effective temperature at low energies in the magnon spectrum, which significantly exceeds our theoretical result. Finally, we discussed the possibility of magnon BEC induced by an abrupt temperature decrease in the lattice, which affects the magnetic system via the magnon-phonon Cherenkov process. We showed that only a temperature decrease from initially $T_{\mathrm{ph}} = 500$ K to $T_{\mathrm{ph}} = 300$ K in the phonon system, which takes place within several nanoseconds, is sufficient to result in a moderate condensate in the magnetic system, initially being at $T_{\mathrm{m}} = 500$ K. Therefore, from the experimental point of view, we rule out the possibility of a phonon-mediated magnon BEC.

In conclusion, we have demonstrated that our kinetic model reveals the complex fundamental interaction processes, governing the dynamics in the magnetic system, and that it is capable of reproducing the experiments in the field of magnon BEC quantitatively. We however assumed a strong four-magnon process to be responsible for the thermalization process whose scattering amplitude has been modified artificially. The quantum mechanical correction term, appearing in the first Born approximation, indeed gives rise to a strong contribution to the four-magnon process in the low wave vector regime, which however vanishes in the t-matrix approach, as we have shown. Unfortunately, the microscopic origin of this strong four-magnon process could not be revealed conclusively, so that further research in this direction would indeed be promising.

A

Appendix

A.1 Magnon Coefficients

A.1.1 Bulk Case

The coefficients appearing in the bilinear part of the magnon Hamiltonian (2.10) read

$$\begin{aligned} A(\boldsymbol{q}) &= g\mu_\mathrm{B}\mu_0 H_0 + 2S\,[\,J(0) - J(\boldsymbol{q})\,] - S\,\frac{\mu_0\, g^2\mu_\mathrm{B}^2}{8\pi a_0^3}\,[\,D_1(\boldsymbol{q}) + 2D_1(0)\,] \\ &= \begin{cases} g\mu_\mathrm{B}\mu_0 H_0 + \frac{1}{2} g\mu_\mathrm{B}\mu_0 M_\mathrm{S}\,(1 - 3D_z) \\ g\mu_\mathrm{B}\mu_0 H_0 + 2S\,[\,J(0) - J(\boldsymbol{q})\,] + g\mu_\mathrm{B}\mu_0 M_\mathrm{S}\left(\frac{1}{2}\sin^2(\theta_{\boldsymbol{q}}) - D_z\right), \end{cases} \end{aligned} \tag{A.1a}$$

$$B(\boldsymbol{q}) = -\frac{3}{2} S\,\frac{\mu_0\, g^2\mu_\mathrm{B}^2}{8\pi a_0^3} D_2(\boldsymbol{q}) = \frac{1}{4} g\mu_\mathrm{B}\mu_0 M_\mathrm{S} \times \begin{cases} D_x - D_y \\ \sin^2(\theta_{\boldsymbol{q}}) \exp\left(-2i\phi_{\boldsymbol{q}}\right), \end{cases} \tag{A.1b}$$

where the upper terms in the brackets apply to $\boldsymbol{q} = 0$ and the lower terms apply to $\boldsymbol{q} \neq 0$ (cf. Ref. [64]). The functions D_1, D_2 and D_3 denote the three-dimensional dipole sums and are given and evaluated in Appendix A.2.1. In the above expressions, we have employed the original definition of the saturation magnetization $M_\mathrm{S} = g\mu_\mathrm{B} S/a_0^3$ [64].

The coefficients appearing in the interaction parts of the magnon Hamiltonian (2.25) and (2.31) read

$$V_3(\boldsymbol{q}) = 3\sqrt{2S}\,\frac{\mu_0\, g^2\mu_\mathrm{B}^2}{8\pi a_0^3}\,D_3(\boldsymbol{q}) = -\sqrt{2S}\,\frac{\mu_0\, g^2\mu_\mathrm{B}^2}{4 a_0^3}\,\sin(2\theta_{\boldsymbol{q}}) \exp\left(-i\phi_{\boldsymbol{q}}\right), \tag{A.2a}$$

$$V_4(\boldsymbol{q}) = 3\left(\frac{1}{4} + S_0\right)\frac{\mu_0\, g^2\mu_\mathrm{B}^2}{8\pi a_0^3}\,D_2(\boldsymbol{q}) = -\left(\frac{1}{4} + S_0\right)\frac{\mu_0\, g^2\mu_\mathrm{B}^2}{2 a_0^3}\,\sin^2(\theta_{\boldsymbol{q}}) \exp\left(-2i\phi_{\boldsymbol{q}}\right), \tag{A.2b}$$

$$D(\boldsymbol{q}) = \frac{\mu_0\, g^2\mu_\mathrm{B}^2}{8\pi a_0^3}\,D_1(\boldsymbol{q}) = \frac{\mu_0\, g^2\mu_\mathrm{B}^2}{a_0^3}\left(\frac{1}{3} - \frac{1}{2}\sin^2(\theta_{\boldsymbol{q}})\right), \tag{A.2c}$$

which are only given for the case $\boldsymbol{q} \neq 0$.

A.1.2 Thin Films

The coefficients appearing in the harmonic magnon Hamiltonian (2.21) read

$$A_{x_i,x_j}(\boldsymbol{q}) = \delta_{x_i,x_j}\, g\mu_\mathrm{B}\mu_0\left(H_0 - \frac{g\mu_\mathrm{B} S}{4\pi a_0^3}\sum_{x_k} D^{(1)}_{x_i,x_k}(0)\right) - S\,\frac{\mu_0\, g^2\mu_\mathrm{B}^2}{8\pi a_0^3} D^{(1)}_{x_i,x_j}(\boldsymbol{q}) + 2S J_{x_i,x_j}(\boldsymbol{q}), \tag{A.3a}$$

$$B_{x_i,x_j}(\boldsymbol{q}) = -\frac{3}{2} S\,\frac{\mu_0 g^2\mu_\mathrm{B}^2}{8\pi a_0^3} D^{(2)}_{x_i,x_j}(\boldsymbol{q}), \tag{A.3b}$$

with the exchange matrix [50]

$$J_{x_i,x_j}(\boldsymbol{q}) = J\Big[\delta_{x_i,x_j}\Big[6 - \delta_{x_i,0} - \delta_{x_i,N_x a_0} - 2\left(\cos(q_y\, a_0) + \cos(q_z\, a_0)\right)\Big] - \delta_{x_i,x_j+a_0} - \delta_{x_i,x_j-a_0}\Big]. \tag{A.3c}$$

The matrices $D^{(1)}_{x_i,x_j}$ and $D^{(2)}_{x_i,x_j}$ denote the two-dimensional dipole sums and are given in Appendix A.2.2 and converted for numerical implementation.

A.2 Dipole Sums

In this Appendix, we show how to treat the dipole sums arising in the magnon coefficients in Appendix A.1. In the bulk case, we are dealing with three-dimensional sums which can be evaluated by means of the corresponding integral representations, as we will show. In the case of thin films, two-dimensional dipole sums arise in the magnon coefficients, which we evaluate exactly. For this purpose, we first convert the slowly converging sums into rapidly converging sums by means of the Ewald summation technique for numerical implementation.

A.2.1 Evaluation of the 3d-Dipole Sums

The three-dimensional dipole sums appearing in the magnon coefficients in the bulk case, which are given in Appendix A.1.1, read

$$D_1(\boldsymbol{q}) = \frac{a_0^3}{N}\sum_{ij}\frac{1-3\hat{z}_{ij}^2}{|\boldsymbol{R}_{ij}|^3}\exp\left(i\boldsymbol{q}\cdot\boldsymbol{R}_{ij}\right), \tag{A.4a}$$

$$D_2(\boldsymbol{q}) = \frac{a_0^3}{N}\sum_{ij}\frac{\left(\hat{x}_{ij}-i\hat{y}_{ij}\right)^2}{|\boldsymbol{R}_{ij}|^3}\exp\left(i\boldsymbol{q}\cdot\boldsymbol{R}_{ij}\right), \tag{A.4b}$$

$$D_3(\boldsymbol{q}) = \frac{a_0^3}{N}\sum_{ij}\frac{\left(\hat{x}_{ij}-i\hat{y}_{ij}\right)\hat{z}_{ij}}{|\boldsymbol{R}_{ij}|^3}\exp\left(i\boldsymbol{q}\cdot\boldsymbol{R}_{ij}\right). \tag{A.4c}$$

The following derivations are based on Ref. [64]. Before we evaluate the dipole sums, we first introduce the demagnetization factors of a sample, which are defined as

$$D_z = \frac{1}{4\pi}\oint_S \frac{\boldsymbol{z}}{r^3}\cdot \mathrm{d}\boldsymbol{S}, \tag{A.5}$$

and analogously for D_x and D_y, where S denotes the surface of the sample. A useful relation between the demagnetization factors reads

$$D_x + D_y + D_z = \frac{1}{4\pi}\oint_S \frac{\boldsymbol{r}}{r^3}\cdot \mathrm{d}\boldsymbol{S} = -\frac{1}{4\pi}\oint_S\left(\boldsymbol{\nabla}\frac{1}{r}\right)\cdot \mathrm{d}\boldsymbol{S} = -\frac{1}{4\pi}\int \Delta\frac{1}{r}\,\mathrm{d}V = 1, \tag{A.6}$$

where we have employed Gauss's theorem. Turning again to the dipole sums (A.4a)-(A.4c), we approximate the sum over the whole sample by a sum within a small body which we assume to be symmetric with respect to the three spatial directions and by a volume integral over the rest of the sample

$$\sum_i^{\text{sample}} \to \sum_i^{\text{body}} + \frac{1}{a_0^3}\int \mathrm{d}V. \tag{A.7}$$

For small wave vectors $q\,d \ll 1$, where d denotes the size of the symmetric body, the sum over the body vanishes for the three dipole sums (A.4a)-(A.4c). This is true especially for the case $\boldsymbol{q} = 0$, for which the first dipole sum (A.4a) reads

$$D_1(0) = \int \frac{1}{r^3}\left(1 - 3\frac{z^2}{r^2}\right) \mathrm{d}V = \int \boldsymbol{\nabla}\cdot\left(\frac{\boldsymbol{z}}{r^3}\right) \mathrm{d}V = 4\pi\left(D_z - D_z^{\mathrm{body}}\right), \tag{A.8}$$

where we again employed Gauss's theorem. Due to the assumed symmetry of the body, the demagnetization factors read $D_x^{\mathrm{body}} = D_y^{\mathrm{body}} = D_z^{\mathrm{body}} = 1/3$, which follows from the relation (A.6). With this, the second dipole sum (A.4b) in the case $\boldsymbol{q} = 0$ reads

$$\begin{aligned} D_2(0) &= \int \frac{1}{r^3}\left(\frac{x^2}{r^2} - \frac{y^2}{r^2}\right) \mathrm{d}V = \frac{1}{3}\left(\int \frac{1}{r^3}\left(1 - 3\frac{y^2}{r^2}\right) \mathrm{d}V - \int \frac{1}{r^3}\left(1 - 3\frac{x^2}{r^2}\right) \mathrm{d}V\right) \\ &= \frac{4\pi}{3}\left(D_y - D_x\right), \end{aligned} \tag{A.9}$$

whereas $D_3(0) = 0$ due to the odd terms.

In the case $\boldsymbol{q} \neq 0$, the particular form of the sample is not relevant any more, because the magnetization rapidly alternates on the surface, averaging to zero. For convenience, we go over to spherical coordinates and choose a sphere with radius d being the small symmetric body. The dipole sums (A.4a)-(A.4c) then read

$$\begin{aligned} D_1(\boldsymbol{q}) &= \int_d^\infty \frac{\mathrm{d}R}{R} \int_0^\pi \mathrm{d}\theta\, \sin(\theta)\left(1 - 3\cos^2(\theta)\right) \int_0^{2\pi} \mathrm{d}\phi\, \exp\left(iqR\left[\cos(\phi - \phi_{\boldsymbol{q}})\, \sin(\theta)\, \sin(\theta_{\boldsymbol{q}})\right.\right. \\ &\qquad\qquad \left.\left. + \cos(\theta)\, \cos(\theta_{\boldsymbol{q}})\right]\right) \\ &= 2\pi \int_d^\infty \frac{\mathrm{d}R}{R} \int_0^\pi \mathrm{d}\theta\, \sin(\theta)\, \left(1 - 3\cos^2(\theta_{\boldsymbol{q}})\right) \mathrm{J}_0(qR\, \sin(\theta)\, \sin(\theta_{\boldsymbol{q}}))\, \exp\left(iqR\, \cos(\theta)\, \cos(\theta_{\boldsymbol{q}})\right) \\ &= \int_d^\infty \mathrm{d}R \left(12\pi\, \frac{(1 - 3\cos^2(\theta_{\boldsymbol{q}}))\, (qR\cos(qR) - \sin(qR)) + q^2R^2 \sin(qR)\, (1 - \cos^2(\theta_{\boldsymbol{q}}))}{q^3R^4}\right. \\ &\qquad\qquad \left. - 8\pi\, \frac{\sin(qR)}{qR^2}\right) \\ &\approx \frac{8\pi}{3} - 4\pi\sin^2(\theta_{\boldsymbol{q}}), \end{aligned} \tag{A.10a}$$

$$\begin{aligned} D_2(\boldsymbol{q}) &= \int_d^\infty \frac{\mathrm{d}R}{R} \int_0^\pi \mathrm{d}\theta\, \sin^3(\theta) \int_0^{2\pi} \mathrm{d}\phi\, \exp\left(-2i\phi\right) \exp\left(iqR\left[\cos(\phi - \phi_{\boldsymbol{q}})\, \sin(\theta)\, \sin(\theta_{\boldsymbol{q}})\right.\right. \\ &\qquad\qquad \left.\left. + \cos(\theta)\, \cos(\theta_{\boldsymbol{q}})\right]\right) \\ &= -2\pi\exp\left(-2i\phi_{\boldsymbol{q}}\right) \int_d^\infty \frac{\mathrm{d}R}{R} \int_0^\pi \mathrm{d}\theta\, \sin^3(\theta)\, \mathrm{J}_2(qR\, \sin(\theta)\, \sin(\theta_{\boldsymbol{q}}))\, \exp\left(iqR\, \cos(\theta)\, \cos(\theta_{\boldsymbol{q}})\right) \\ &= 4\pi\, \sin^2(\theta_{\boldsymbol{q}}) \exp\left(-2i\phi_{\boldsymbol{q}}\right) \int_d^\infty \mathrm{d}R\, \frac{3qR\cos(qR) + \sin(qR)\, (q^2R^2 - 3)}{q^3R^4} \\ &\approx -\frac{4\pi}{3}\, \sin^2(\theta_{\boldsymbol{q}}) \exp\left(-2i\phi_{\boldsymbol{q}}\right), \end{aligned} \tag{A.10b}$$

$$\begin{aligned}
D_3(\boldsymbol{q}) &= \int\limits_d^\infty \frac{\mathrm{d}R}{R} \int\limits_0^\pi \mathrm{d}\theta\, \sin^2(\theta)\, \cos(\theta) \int\limits_0^{2\pi} \mathrm{d}\phi\, \exp\left(-i\phi\right) \exp\big(iqR\big[\cos(\phi-\phi_{\boldsymbol{q}})\, \sin(\theta)\, \sin(\theta_{\boldsymbol{q}}) \\
&\qquad\qquad + \cos(\theta)\, \cos(\theta_{\boldsymbol{q}})\big]\big) \\
&= 2\pi i \exp\left(-i\phi_{\boldsymbol{q}}\right) \int\limits_d^\infty \frac{\mathrm{d}R}{R} \int\limits_0^\pi \mathrm{d}\theta\, \Big(\sin^2(\theta)\, \cos(\theta)\, \mathrm{J}_1(qR\, \sin(\theta)\, \sin(\theta_{\boldsymbol{q}})) \\
&\qquad\qquad \times \exp\left(iqR\, \cos(\theta)\, \cos(\theta_{\boldsymbol{q}})\right)\Big) \\
&= -2\pi\, \sin(2\theta_{\boldsymbol{q}}) \exp\left(-i\phi_{\boldsymbol{q}}\right) \int\limits_d^\infty \mathrm{d}R\, \sqrt{\frac{\pi}{2qR^3}}\, \mathrm{J}_{5/2}(qR) \\
&\approx -\frac{2\pi}{3}\, \sin(2\theta_{\boldsymbol{q}}) \exp\left(-i\phi_{\boldsymbol{q}}\right),
\end{aligned} \tag{A.10c}$$

where $J_\alpha(x)$ is the Bessel function of the first kind and the final results are valid for wave vectors $q\, d \ll 1$, respectively.

A.2.2 Converting of the 2d-Dipole Sums: Ewald Summation

The two-dimensional dipole sums appearing in the magnon coefficients in the case of thin films, which are given in Appendix A.1.2, read

$$D^{(1)}_{x_i,x_j}(\boldsymbol{q}) = \frac{a_0^3}{N_y N_z} \sum_{ij} \frac{1-3\hat{z}_{ij}^2}{\sqrt{x_{ij}^2+\boldsymbol{r}_{ij}^2}^{\,3}} \exp\left(i\boldsymbol{q}\cdot\boldsymbol{r}_{ij}\right), \tag{A.11a}$$

$$D^{(2)}_{x_i,x_j}(\boldsymbol{q}) = \frac{a_0^3}{N_y N_z} \sum_{ij} \frac{\left(\hat{x}_{ij}-i\hat{y}_{ij}\right)^2}{\sqrt{x_{ij}^2+\boldsymbol{r}_{ij}^2}^{\,3}} \exp\left(i\boldsymbol{q}\cdot\boldsymbol{r}_{ij}\right). \tag{A.11b}$$

In order to determine the magnon spectrum in thin films, we seek for exact solutions of the above dipole sums. Naively summing up these expressions would require a tremendous numerical effort, since the sums are slowly converging due to the $1/r^3$-power law. Therefore, we first convert these sums into rapidly converging sums for numerical implementation by means of the Ewald summation [87]. The following derivations are based on Refs. [50, 101].

We start by rewriting the two sums in a convenient form

$$D^{(1)}_x(\boldsymbol{k}) = \sum_{\boldsymbol{r}} \frac{x^2+y^2-2z^2}{\left(x^2+\boldsymbol{r}^2\right)^{5/2}} \exp\left(2\pi i\, \boldsymbol{k}\cdot\boldsymbol{r}\right), \tag{A.12a}$$

$$D^{(2)}_x(\boldsymbol{k}) = \sum_{\boldsymbol{r}} \frac{\left(x-iy\right)^2}{\left(x^2+\boldsymbol{r}^2\right)^{5/2}} \exp\left(2\pi i\, \boldsymbol{k}\cdot\boldsymbol{r}\right), \tag{A.12b}$$

where $(x,\boldsymbol{r}) = (x,y,z) \in \mathbb{Z}^3$ and $\boldsymbol{k} = (k_y,k_z) \in (-1/2,1/2)\times(-1/2,1/2)$. We then define the auxiliary function

$$C_x(\boldsymbol{k}) = \sum_{\boldsymbol{r}} \frac{\exp\left(2\pi i\, \boldsymbol{k}\cdot\boldsymbol{r}\right)}{\left(x^2+\boldsymbol{r}^2\right)^{5/2}}, \tag{A.13}$$

and we recognize that the two sums can also be expressed by derivatives of $C_x(\boldsymbol{k})$, which read

$$D_x^{(1)}(\boldsymbol{k}) = x^2\, C_x(\boldsymbol{k}) - \frac{1}{4\pi^2}\frac{\mathrm{d}^2}{\mathrm{d}k_y^2} C_x(\boldsymbol{k}) + \frac{1}{2\pi^2}\frac{\mathrm{d}^2}{\mathrm{d}k_z^2} C_x(\boldsymbol{k}), \tag{A.14a}$$

$$D_x^{(2)}(\boldsymbol{k}) = x^2\, C_x(\boldsymbol{k}) - \frac{x}{\pi}\frac{\mathrm{d}}{\mathrm{d}k_y} C_x(\boldsymbol{k}) + \frac{1}{4\pi^2}\frac{\mathrm{d}^2}{\mathrm{d}k_y^2} C_x(\boldsymbol{k}). \tag{A.14b}$$

Due to these relations, we only have to convert the sum $C_x(\boldsymbol{k})$. For this purpose, we use the relation

$$\Gamma(x) = \int\limits_0^\infty \mathrm{d}t\, t^{x-1} \exp(-t) = \lambda^x \int\limits_0^\infty \mathrm{d}t\, t^{x-1} \exp(-\lambda t), \tag{A.15}$$

and we set $\lambda = x^2 + \boldsymbol{r}^2$ and $x = 5/2$. Furthermore, we decompose the sum into two parts

$$C_x(\boldsymbol{k}) = C_x^{\mathrm{R}}(\boldsymbol{k}) + C_x^{\mathrm{D}}(\boldsymbol{k}), \tag{A.16}$$

where "D" refers to the direct lattice and "R" refers to the reciprocal lattice. The two parts read

$$C_x^{\mathrm{R}}(\boldsymbol{k}) = \frac{4}{3\sqrt{\pi}} \sum_{\boldsymbol{r}} \exp(2\pi i\, \boldsymbol{k}\cdot\boldsymbol{r}) \int\limits_0^{\beta^2} \mathrm{d}t\, t^{3/2} \exp\left(-\left(x^2+\boldsymbol{r}^2\right) t\right), \tag{A.17a}$$

$$C_x^{\mathrm{D}}(\boldsymbol{k}) = \frac{4}{3\sqrt{\pi}} \sum_{\boldsymbol{r}} \exp(2\pi i\, \boldsymbol{k}\cdot\boldsymbol{r}) \int\limits_{\beta^2}^{\infty} \mathrm{d}t\, t^{3/2} \exp\left(-\left(x^2+\boldsymbol{r}^2\right) t\right), \tag{A.17b}$$

where $\beta > 0$ is an arbitrary constant, and we used the relation $\Gamma(5/2) = 3\sqrt{\pi}/4$. In the second part (A.17b), we substitute t with s, where $s^2 = (x^2 + \boldsymbol{r}^2)\, t$, and get

$$\begin{aligned} C_x^{\mathrm{D}}(\boldsymbol{k}) &= \frac{8}{3\sqrt{\pi}} \sum_{\boldsymbol{r}} \frac{\exp(2\pi i\, \boldsymbol{k}\cdot\boldsymbol{r})}{(x^2+\boldsymbol{r}^2)^{5/2}} \int\limits_{\beta\sqrt{x^2+\boldsymbol{r}^2}}^{\infty} \mathrm{d}s\, s^4 \exp\left(-s^2\right) \\ &= \sum_{\boldsymbol{r}} \frac{\exp(2\pi i\, \boldsymbol{k}\cdot\boldsymbol{r})}{(x^2+\boldsymbol{r}^2)^{5/2}} \Bigg[\frac{2\beta}{3\sqrt{\pi}} \sqrt{x^2+\boldsymbol{r}^2} \exp\left(-\beta^2\left(x^2+\boldsymbol{r}^2\right)\right) \left(3 + 2\beta^2\left(x^2+\boldsymbol{r}^2\right)\right) \\ &\qquad + \operatorname{erfc}\left(\beta\sqrt{x^2+\boldsymbol{r}^2}\right) \Bigg], \end{aligned} \tag{A.18}$$

which we term *direct sum*, where $\operatorname{erfc}(x)$ is the complementary error function [102]. In the first part (A.17a), we use the Fourier transform of the Gaussian function

$$\exp\left(-w^2 t\right) = \sqrt{\frac{\pi}{t}} \int\limits_{-\infty}^{\infty} \mathrm{d}u \exp\left(-\frac{\pi^2 u^2}{t}\right) \exp(-2\pi i\, w u), \tag{A.19}$$

and thus obtain

$$C_x^{\mathrm{R}}(\boldsymbol{k}) = \frac{4\sqrt{\pi}}{3} \sum_{\boldsymbol{r}} \int\limits_0^{\beta^2} \mathrm{d}t\, \sqrt{t} \exp\left(-x^2 t\right) \iint_{\mathbb{R}^2} \mathrm{d}u^2 \exp\left(-\frac{\pi^2 \boldsymbol{u}^2}{t}\right) \exp\left(-2\pi i\, (\boldsymbol{u}-\boldsymbol{k})\cdot\boldsymbol{r}\right). \tag{A.20}$$

We now substitute the integration over the whole $\mathbb{R}^2$ by an integration over the reciprocal unit cell $V^* = (-1/2, 1/2) \times (-1/2, 1/2)$ and a summation over all reciprocal lattice vectors $\boldsymbol{n} \in \mathbb{Z}^2$

$$\iint_{\mathbb{R}^2} \mathrm{d}u^2 \to \sum_{\boldsymbol{n}} \iint_{V*+\boldsymbol{n}} \mathrm{d}v^2, \tag{A.21}$$

which results in

$$C_x^{\mathrm{R}}(\boldsymbol{k}) = \frac{4\sqrt{\pi}}{3} \sum_{\boldsymbol{r}\boldsymbol{n}} \int_0^{\beta^2} \mathrm{d}t\, \sqrt{t}\, \exp\left(-x^2 t\right) \iint_{V^*} \mathrm{d}v^2\, \exp\left(-\frac{\pi^2 \left(\boldsymbol{v}+\boldsymbol{n}\right)^2}{t}\right) \exp\left(-2\pi i\, \left(\boldsymbol{v}-\boldsymbol{k}\right) \cdot \boldsymbol{r}\right). \tag{A.22}$$

We now have to distinguish between two cases. For $x \neq 0$, the sum over $\boldsymbol{r}$ is equal to the sum over all Fourier coefficients, we therefore obtain

$$\begin{aligned} C_{x\neq 0}^{\mathrm{R}}(\boldsymbol{k}) &= \frac{4\sqrt{\pi}}{3} \sum_{\boldsymbol{n}} \int_0^{\beta^2} \mathrm{d}t\, \sqrt{t}\, \exp\left(-x^2 t\right) \exp\left(-\frac{\pi^2 \left(\boldsymbol{k}+\boldsymbol{n}\right)^2}{t}\right) \\ &= \sum_{\boldsymbol{n}} \left[-\frac{4\sqrt{\pi}\beta}{3x^2} \exp\left(-\beta^2 x^2 - \frac{\pi^2 \left(\boldsymbol{k}+\boldsymbol{n}\right)^2}{\beta^2}\right) + \frac{\pi}{3x^3} f_{x,\boldsymbol{k},\boldsymbol{n}}(2\pi x|\boldsymbol{k}+\boldsymbol{n}|)\right], \end{aligned} \tag{A.23a}$$

which we term *reciprocal sum*, where

$$\begin{aligned} f_{x,\boldsymbol{k},\boldsymbol{n}}(\alpha) = \exp\left(-2\pi x|\boldsymbol{k}+\boldsymbol{n}|\right)\left(1+\alpha\right) \operatorname{erfc}\left(\frac{\pi|\boldsymbol{k}+\boldsymbol{n}|}{\beta} - \beta x\right) \\ - \exp\left(2\pi x|\boldsymbol{k}+\boldsymbol{n}|\right)\left(1-\alpha\right) \operatorname{erfc}\left(\frac{\pi|\boldsymbol{k}+\boldsymbol{n}|}{\beta} + \beta x\right). \end{aligned} \tag{A.23b}$$

In the case $x = 0$, however, the index $\boldsymbol{r} = 0$ is excluded in the original sum. We therefore complement the sum with the index $\boldsymbol{r} = 0$, which we in turn correct by subtracting the corresponding self-energy (following from Eq. (A.17a)). We thus obtain

$$\begin{aligned} C_{x=0}^{\mathrm{R}}(\boldsymbol{k}) &= \frac{4\sqrt{\pi}}{3} \sum_{\boldsymbol{n}} \int_0^{\beta^2} \mathrm{d}t\, \sqrt{t}\, \exp\left(-\frac{\pi^2 \left(\boldsymbol{k}+\boldsymbol{n}\right)^2}{t}\right) - \frac{8\beta^5}{15\sqrt{\pi}} \\ &= \sum_{\boldsymbol{n}} \left[\frac{8\sqrt{\pi}\beta}{9} \exp\left(-\frac{\pi^2 \left(\boldsymbol{k}+\boldsymbol{n}\right)^2}{\beta^2}\right) \left(\beta^2 - 2\pi^2 \left(\boldsymbol{k}+\boldsymbol{n}\right)^2\right) + \frac{16\pi^4}{9} |\boldsymbol{k}+\boldsymbol{n}|^3 \right. \\ &\qquad \left. \times \operatorname{erfc}\left(\frac{\pi|\boldsymbol{k}+\boldsymbol{n}|}{\beta}\right)\right] - \frac{8\beta^5}{15\sqrt{\pi}}. \end{aligned} \tag{A.23c}$$

Except for the constant self-energy correction, which anyway vanishes by calculating the derivatives of $C_x(\boldsymbol{k})$, this expression coincides with the corresponding limit $x \to 0$ in Eq. (A.23a). Using the initial relations (A.14a) and (A.14b) together with the direct sum (A.18) and the reciprocal sum (A.23a), the converted dipole sums eventually read

$$\begin{aligned} D_x^{(1)}(\boldsymbol{k}) = \sum_{\boldsymbol{r}} \left(x^2 + y^2 - 2z^2\right) \frac{\exp\left(2\pi i\, \boldsymbol{k}\cdot\boldsymbol{r}\right)}{\left(x^2+\boldsymbol{r}^2\right)^{5/2}} \left[\frac{2\beta}{3\sqrt{\pi}} \sqrt{x^2+\boldsymbol{r}^2} \left(3 + 2\beta^2 \left(x^2+\boldsymbol{r}^2\right)\right) \right. \\ \left. \times \exp\left(-\beta^2 \left(x^2+\boldsymbol{r}^2\right)\right) + \operatorname{erfc}\left(\beta\sqrt{x^2+\boldsymbol{r}^2}\right)\right] \\ + \sum_{\boldsymbol{n}} \left[-\frac{4\sqrt{\pi}\beta}{3} \exp\left(-\beta^2 x^2 - \frac{\pi^2 \left(\boldsymbol{k}+\boldsymbol{n}\right)^2}{\beta^2}\right) + \frac{\pi}{3x}\left(f_{x,\boldsymbol{k},\boldsymbol{n}}(2\pi x|\boldsymbol{k}+\boldsymbol{n}|) \right.\right. \\ \left.\left. + f_{x,\boldsymbol{k},\boldsymbol{n}}(-2\pi x\frac{\left(k_y+n_y\right)^2}{|\boldsymbol{k}+\boldsymbol{n}|}) - 2 f_{x,\boldsymbol{k},\boldsymbol{n}}(-2\pi x\frac{\left(k_z+n_z\right)^2}{|\boldsymbol{k}+\boldsymbol{n}|})\right)\right], \end{aligned} \tag{A.24a}$$

$$\begin{aligned} D_x^{(2)}(\boldsymbol{k}) = \sum_{\boldsymbol{r}} (x - iy)^2 \, \frac{\exp\left(2\pi i \, \boldsymbol{k}\cdot\boldsymbol{r}\right)}{\left(x^2+\boldsymbol{r}^2\right)^{5/2}} \Big[\frac{2\beta}{3\sqrt{\pi}} \sqrt{x^2+\boldsymbol{r}^2} \, \left(3 + 2\beta^2 \left(x^2+\boldsymbol{r}^2\right)\right) & \\ \times \exp\left(-\beta^2 \left(x^2+\boldsymbol{r}^2\right)\right) + \operatorname{erfc}\left(\beta\sqrt{x^2+\boldsymbol{r}^2}\right) \Big] & \\ + \sum_{\boldsymbol{n}} \Big[- \frac{4\sqrt{\pi}\beta}{3} \, \exp\left(-\beta^2 x^2 - \frac{\pi^2 \left(\boldsymbol{k}+\boldsymbol{n}\right)^2}{\beta^2}\right) + \frac{4\pi^2}{3} \left(k_y + n_y\right) f_x(\boldsymbol{k},\boldsymbol{n},0) & \\ + \frac{\pi}{3x} \left(f_{x,\boldsymbol{k},\boldsymbol{n}}(2\pi x|\boldsymbol{k}+\boldsymbol{n}|) - f_{x,\boldsymbol{k},\boldsymbol{n}}(-2\pi x \frac{\left(k_y+n_y\right)^2}{|\boldsymbol{k}+\boldsymbol{n}|}) \right) \Big]. & \qquad \text{(A.24b)} \end{aligned}$$

Noteworthy, the final results do not depend on the arbitrary constant $\beta > 0$, which merely shifts the weighting between the direct sum ($\boldsymbol{r}$) and the reciprocal sum ($\boldsymbol{n}$). Throughout the numerical calculations, we set $\beta = 1$.

A.3 Bogoliubov Transformation

A.3.1 Bulk Case

In order to diagonalize the Hamiltonian (2.10), we first invert the Bogoliubov transformation (2.11a) and (2.11b) and obtain [18]

$$\hat{a}_{\boldsymbol{q}} = u^*(\boldsymbol{q}) \, \hat{c}_{\boldsymbol{q}} - v(\boldsymbol{q}) \, \hat{c}^\dagger_{-\boldsymbol{q}}, \qquad \text{(A.25a)}$$

$$\hat{a}^\dagger_{\boldsymbol{q}} = u(\boldsymbol{q}) \, \hat{c}^\dagger_{\boldsymbol{q}} - v^*(\boldsymbol{q}) \, \hat{c}_{-\boldsymbol{q}}, \qquad \text{(A.25b)}$$

where we have already assumed that $u(\boldsymbol{q}) = u(-\boldsymbol{q})$ and $v(\boldsymbol{q}) = v(-\boldsymbol{q})$, which follows from the symmetry properties of the coefficients $A(\boldsymbol{q}) = A(-\boldsymbol{q})$ and $B(\boldsymbol{q}) = B(-\boldsymbol{q})$. We then insert the transformation (A.25a) and (A.25b) into the Hamiltonian (2.10) which yields

$$\begin{aligned} \mathcal{H}_2 = & \sum_{\boldsymbol{q}} \left(A(\boldsymbol{q}) \, |v(\boldsymbol{q})|^2 - B(\boldsymbol{q}) \, u^*(\boldsymbol{q}) \, v(\boldsymbol{q}) - B^*(\boldsymbol{q}) \, u(\boldsymbol{q}) \, v^*(\boldsymbol{q}) \right) \\ & + \sum_{\boldsymbol{q}} \left(A(\boldsymbol{q}) \left(|u(\boldsymbol{q})|^2 + |v(\boldsymbol{q})|^2 \right) - 2B(\boldsymbol{q}) \, u^*(\boldsymbol{q}) \, v(\boldsymbol{q}) - 2B^*(\boldsymbol{q}) \, u(\boldsymbol{q}) \, v^*(\boldsymbol{q}) \right) \hat{c}^\dagger_{\boldsymbol{q}} \hat{c}_{\boldsymbol{q}} \\ & + \sum_{\boldsymbol{q}} \left(B(\boldsymbol{q}) \, u^*(\boldsymbol{q})^2 - A(\boldsymbol{q}) \, u^*(\boldsymbol{q}) \, v^*(\boldsymbol{q}) + B^*(\boldsymbol{q}) \, v^*(\boldsymbol{q})^2 \right) \hat{c}_{\boldsymbol{q}} \hat{c}_{-\boldsymbol{q}} \\ & + \sum_{\boldsymbol{q}} \left(B^*(\boldsymbol{q}) \, u(\boldsymbol{q})^2 - A(\boldsymbol{q}) \, u(\boldsymbol{q}) \, v(\boldsymbol{q}) + B(\boldsymbol{q}) \, v(\boldsymbol{q})^2 \right) \hat{c}^\dagger_{\boldsymbol{q}} \hat{c}^\dagger_{-\boldsymbol{q}}. \qquad \text{(A.26)} \end{aligned}$$

The transformed Hamiltonian will be diagonal if the anharmonic terms vanish, therefore we demand

$$B(\boldsymbol{q}) \, u^*(\boldsymbol{q})^2 - A(\boldsymbol{q}) \, u^*(\boldsymbol{q}) \, v^*(\boldsymbol{q}) + B^*(\boldsymbol{q}) \, v^*(\boldsymbol{q})^2 = 0. \qquad \text{(A.27)}$$

Completing the square brings us to the relation

$$u(\boldsymbol{q}) = v(\boldsymbol{q}) \, \frac{1}{2B^*(\boldsymbol{q})} \left(\sqrt{A^2(\boldsymbol{q}) - 4|B(\boldsymbol{q})|^2} + A(\boldsymbol{q}) \right), \qquad \text{(A.28)}$$

which shows that the phases of the Bogoliubov coefficients $u = |u| \exp(i\phi_u)$ and $v = |v| \exp(i\phi_v)$ have to obey $\phi_u = \phi_v + \phi_B$, where $B = |B| \exp(i\phi_B)$. We arbitrarily set $\phi_v = 0$. By multiplying Eq. (A.28) with the complex conjugate and using the relation (2.12a), we finally arrive at

$$u(\boldsymbol{q}) = \sqrt{\frac{1}{2}\left(\frac{A(\boldsymbol{q})}{\sqrt{A^2(\boldsymbol{q}) - 4|B(\boldsymbol{q})|^2}} + 1\right)} \exp(i\phi_B), \tag{A.29a}$$

$$v(\boldsymbol{q}) = \sqrt{\frac{1}{2}\left(\frac{A(\boldsymbol{q})}{\sqrt{A^2(\boldsymbol{q}) - 4|B(\boldsymbol{q})|^2}} - 1\right)}. \tag{A.29b}$$

With these coefficients, the transformed Hamiltonian (A.26) becomes

$$\hat{\mathcal{H}}_2 = G_{\mathrm{B}} + \sum_{\boldsymbol{q}} \hbar\omega(\boldsymbol{q})\, \hat{c}^\dagger_{\boldsymbol{q}} \hat{c}_{\boldsymbol{q}}, \tag{A.30}$$

where

$$G_{\mathrm{B}} = \frac{1}{2}\sum_{\boldsymbol{q}} \left(\hbar\omega(\boldsymbol{q}) - A(\boldsymbol{q})\right), \tag{A.31}$$

and

$$\hbar\omega(\boldsymbol{q}) = \sqrt{A^2(\boldsymbol{q}) - 4|B(\boldsymbol{q})|^2}. \tag{A.32}$$

Identical results have also been obtained by using a different approach [18].

A.3.2 Thin Films

In the case of thin films, we use a generalization of the approach given in Ref. [18] in order to diagonalize the Hamiltonian. The harmonic Hamiltonian (2.21) can be brought into the diagonal form (2.23) by means of the generalized Bogoliubov transformation (2.22a) and (2.22b), so that

$$\begin{aligned} \hat{\mathcal{H}}_2 &= G_{\mathrm{B}}^{\mathrm{film}} + \sum_j \sum_{\boldsymbol{q}} \hbar\omega_j(\boldsymbol{q})\, \hat{c}^\dagger_j(\boldsymbol{q})\hat{c}_j(\boldsymbol{q}) \\ &= \sum_{jk}\sum_{\boldsymbol{q}} \Big(A_{j,k}(\boldsymbol{q})\, \hat{a}^\dagger_j(\boldsymbol{q})\hat{a}_k(\boldsymbol{q}) + B_{j,k}(\boldsymbol{q})\, \hat{a}_j(\boldsymbol{q})\hat{a}_k(-\boldsymbol{q}) + B^*_{j,k}(\boldsymbol{q})\, \hat{a}^\dagger_j(\boldsymbol{q})\hat{a}^\dagger_k(-\boldsymbol{q})\Big). \end{aligned} \tag{A.33}$$

On the one hand, we evaluate the commutator

$$\Big[\hat{c}_i(\boldsymbol{q}), \hat{\mathcal{H}}_2\Big] = \hbar\omega_i(\boldsymbol{q})\, \hat{c}_i(\boldsymbol{q}) = \hbar\omega_i(\boldsymbol{q})\, \frac{1}{\sqrt{N_x}} \sum_k \Big(u_{i,k}(\boldsymbol{q})\, \hat{a}_k(\boldsymbol{q}) + v_{i,k}(\boldsymbol{q})\, \hat{a}^\dagger_k(-\boldsymbol{q})\Big), \tag{A.34}$$

which on the other hand also gives

$$\begin{aligned} \Big[\hat{c}_i(\boldsymbol{q}), \hat{\mathcal{H}}_2\Big] &= \frac{1}{\sqrt{N_x}} \sum_l \Big(u_{i,l}(\boldsymbol{q})\ \Big[\hat{a}_l(\boldsymbol{q}), \hat{\mathcal{H}}_2\Big] + v_{i,l}(\boldsymbol{q})\ \Big[\hat{a}^\dagger_l(-\boldsymbol{q}), \hat{\mathcal{H}}_2\Big]\Big) \\ &= \frac{1}{\sqrt{N_x}} \sum_{jk} \Big(u_{i,j}(\boldsymbol{q})\, A_{j,k}(\boldsymbol{q})\, \hat{a}_k(\boldsymbol{q}) + u_{i,j}(\boldsymbol{q})\ \Big(B^*_{j,k}(\boldsymbol{q}) + B^*_{k,j}(-\boldsymbol{q})\Big)\, \hat{a}^\dagger_k(-\boldsymbol{q}) \\ &\qquad - v_{i,j}(\boldsymbol{q})\, A_{k,j}(-\boldsymbol{q})\, \hat{a}^\dagger_k(-\boldsymbol{q}) - v_{i,j}(\boldsymbol{q})\ \left(B_{j,k}(-\boldsymbol{q}) + B_{k,j}(\boldsymbol{q})\right)\, \hat{a}_k(\boldsymbol{q})\Big). \end{aligned} \tag{A.35}$$

By comparing both results and by using the relations $A_{i,j}(\boldsymbol{q}) = A_{j,i}(-\boldsymbol{q})$, $B_{i,j}(\boldsymbol{q}) = B_{j,i}(-\boldsymbol{q})$ and $B_{i,j}(\boldsymbol{q}) = B^*_{i,j}(\boldsymbol{q})$, we obtain

$$\begin{aligned} &\sum_k \left(\sum_j u_{i,j}(\boldsymbol{q})\, [\,\hbar\omega_i(\boldsymbol{q})\, \delta_{j,k} - A_{j,k}(\boldsymbol{q})\,] + 2v_{i,j}(\boldsymbol{q})\, B_{j,k}(-\boldsymbol{q})\right) \hat{a}_k(\boldsymbol{q}) \\ &+ \sum_k \left(\sum_j -2u_{i,j}(\boldsymbol{q})\, B_{j,k}(\boldsymbol{q}) + v_{i,j}(\boldsymbol{q})\, [\,\hbar\omega_i(\boldsymbol{q})\, \delta_{j,k} + A_{j,k}(\boldsymbol{q})\,]\right) \hat{a}^\dagger_k(-\boldsymbol{q}) = 0. \end{aligned} \tag{A.36}$$

This equation can only be satisfied if the terms in the brackets vanish separately, which can be expressed as

$$\det\begin{pmatrix} \hbar\omega_i(\boldsymbol{q})\,\mathbb{1} - A(\boldsymbol{q}) & -2B(\boldsymbol{q}) \\ 2B(-\boldsymbol{q}) & \hbar\omega_i(\boldsymbol{q})\,\mathbb{1} + A(\boldsymbol{q}) \end{pmatrix} = 0, \tag{A.37}$$

with $\mathbb{1}$ being the $N_x \times N_x$ identity matrix. Solving this eigenvalue problem yields the magnon energies $\hbar\omega_i$.

A.4 Kinetic Equations in Energy Space

In this Appendix, we transform the kinetic equations, resulting from the three-magnon process (2.63) and from the Cherenkov process (2.66), from momentum space to energy space by means of the isotropic approximation introduced in Sec. 2.2. Furthermore, we present the isotropic version of the parallel pumping process (2.64).

Analogously to the case of the four-magnon kinetic equation, we first separate the integration over the angle-dependent parts in the respective equations, which read

$$F_3(q_0, q_1, q_2) = \frac{q_0 q_1 q_2}{4\pi} \iiint \mathrm{d}\Omega_0 \mathrm{d}\Omega_1 \mathrm{d}\Omega_2 \, |V_3(\boldsymbol{q}_1) + V_3(\boldsymbol{q}_2)|^2 \, \delta(\boldsymbol{q}_0 - \boldsymbol{q}_1 - \boldsymbol{q}_2), \tag{A.38a}$$

$$F_\sigma(q_0, q_1, q_2) = \frac{q_1 q_2}{4\pi a_0} \iiint \mathrm{d}\Omega_0 \mathrm{d}\Omega_1 \mathrm{d}\Omega_2 \, |V_\sigma(\boldsymbol{q}_1, \boldsymbol{q}_2)|^2 \, \delta(\boldsymbol{q}_0 - \boldsymbol{q}_1 - \boldsymbol{q}_2), \tag{A.38b}$$

and which are evaluated in Appendix A.5. Due to the anisotropy of the respective interaction potentials (cf. Eqs. (2.26) and (2.41)), we average the angle-dependent parts over the remaining angles $\phi_{\boldsymbol{q}_0}$ and $\theta_{\boldsymbol{q}_0}$ by means of an additional integration $\int \mathrm{d}\Omega_0/4\pi$. In the case of the parallel pumping process, which is strongly anisotropic, we thus also average over the polar angle and substitute

$$|V_{\mathrm{pump}}(\boldsymbol{q}_0)|^2 \to \frac{1}{4\pi} \int \mathrm{d}\Omega_0 \, |V_{\mathrm{pump}}(\boldsymbol{q}_0)|^2. \tag{A.39}$$

We now change from the momentum space to energy space by means of the substitutions

$$E_i = g\mu_{\mathrm{B}}\mu_0 H_0 + 2JS\,(q_i a_0)^2\,, \tag{A.40a}$$

$$E_{\mathrm{ph}} = \hbar v_\sigma q, \tag{A.40b}$$

$$\tilde{f}(E_i) = f(q_i), \tag{A.40c}$$

$$\tilde{F}_3(E_0, E_1, E_2) = F_3(q_0, q_1, q_2), \tag{A.40d}$$

$$\tilde{F}_\sigma(E_0, E_1, E_{\mathrm{ph}}) = F_\sigma(q_0, q_1, q_2). \tag{A.40e}$$

In the case of the Cherenkov process, the fixed phonon distribution (2.67) enters the kinetic equation. In order to remove the singularity at $q = 0$ in the Planck distribution emerging due to the linear phonon dispersion (2.78b), we define

$$\tilde{f}_\sigma(E_{\mathrm{ph}}) = q\, a_0\, f_\sigma(q). \tag{A.40f}$$

As a result, the kinetic equation resulting from the three-magnon process reads

$$
\begin{aligned}
\frac{\mathrm{d}}{\mathrm{d}t}\tilde{f}(E_0) = {} & \frac{1}{32\pi^2\hbar\,(2JS)^{3/2}}\,\Theta\left(E_0 - 2E_{\mathrm{min}}\right) \int\limits_{E_{\mathrm{min}}}^{E_0-E_{\mathrm{min}}} \mathrm{d}E_1 \left[\frac{\tilde{F}_3(E_0,E_1,E_0-E_1)}{\sqrt{E_0-E_{\mathrm{min}}}}\right. \\
& \left.\times\left(\tilde{f}(E_1)\tilde{f}(E_0-E_1)\left(1+\tilde{f}(E_0)\right) - \tilde{f}(E_0)\left(1+\tilde{f}(E_1)\right)\left(1+\tilde{f}(E_0-E_1)\right)\right)\right] \\
& + \frac{1}{16\pi^2\hbar\,(2JS)^{3/2}}\,\Theta\left(E_{\mathrm{cut}} - E_{\mathrm{min}} - E_0\right) \int\limits_{E_{\mathrm{min}}}^{E_{\mathrm{cut}}-E_0} \mathrm{d}E_1 \left[\frac{\tilde{F}_3(E_0+E_1,E_1,E_0)}{\sqrt{E_0-E_{\mathrm{min}}}}\right. \\
& \left.\times\left(\tilde{f}(E_0+E_1)\left(1+\tilde{f}(E_0)\right)\left(1+\tilde{f}(E_1)\right) - \tilde{f}(E_0)\tilde{f}(E_1)\left(1+\tilde{f}(E_0+E_1)\right)\right)\right],
\end{aligned}
\tag{A.41}
$$

where the first term describes the three-magnon splitting process and the second term describes the three-magnon confluence process with $\Theta(x)$ being the Heaviside step function. The kinetic equation resulting from the Cherenkov process reads

$$
\begin{aligned}
\frac{\mathrm{d}}{\mathrm{d}t}\tilde{f}(E_0) = {} & \frac{1}{16\pi^2\hbar JS}\sum_\sigma \frac{a_0}{\hbar v_\sigma} \int\limits_{\max\left(E_{\mathrm{min}},E_0-E^\sigma_{\mathrm{cut}}\right)}^{E_0} \mathrm{d}E_1 \left[\tilde{F}_\sigma(E_0,E_1,E_{\mathrm{ph}})\right. \\
& \left.\times\left(\tilde{f}(E_1)\tilde{f}_\sigma(E_{\mathrm{ph}})\left(1+\tilde{f}(E_0)\right) - \tilde{f}(E_0)\left(1+\tilde{f}(E_1)\right)\left(\frac{a_0}{\hbar v_\sigma}E_{\mathrm{ph}} + \tilde{f}_\sigma(E_{\mathrm{ph}})\right)\right)\right] \\
& + \frac{1}{16\pi^2\hbar JS}\sum_\sigma \frac{a_0}{\hbar v_\sigma} \int\limits_{E_0}^{\min(E_{\mathrm{cut}},E_0+E^\sigma_{\mathrm{cut}})} \mathrm{d}E_1 \left[\tilde{F}_\sigma(E_0,E_1,E_{\mathrm{ph}})\right. \\
& \left.\times\left(\tilde{f}(E_1)\left(1+\tilde{f}(E_0)\right)\left(\frac{a_0}{\hbar v_\sigma}E_{\mathrm{ph}} + \tilde{f}_\sigma(E_{\mathrm{ph}})\right) - \tilde{f}(E_0)\tilde{f}_\sigma(E_{\mathrm{ph}})\left(1+\tilde{f}(E_1)\right)\right)\right],
\end{aligned}
\tag{A.42}
$$

where $E_{\mathrm{ph}} = E_0 - E_1$ in the splitting process (first term in Eq. (A.42)) and $E_{\mathrm{ph}} = E_1 - E_0$ in the confluence process (second term in Eq. (A.42)), where we exploited the Hermitian property of the Cherenkov interaction potential $V_\sigma(\boldsymbol{q}_1,\boldsymbol{q}_2) = V^*_\sigma(\boldsymbol{q}_1+\boldsymbol{q}_2,-\boldsymbol{q}_2)$ (cf. Eq. (2.41)). Finally, the equation resulting from the parallel pumping process reads

$$
\frac{\mathrm{d}}{\mathrm{d}t}\tilde{f}(E_0) = \frac{\pi}{15}\frac{(g\mu_{\mathrm{B}}\mu_0)^4}{\hbar}\frac{h^2_{\mathrm{pump}}}{E_0^2}\,M_{\mathrm{S}}^2\,\delta(2E_0 - \hbar\omega_{\mathrm{pump}})\left(1+2\tilde{f}(E_0)\right), \tag{A.43}
$$

where we artificially broaden the delta distribution for numerical integration

$$
\delta(E) \to \frac{2}{\sqrt{\pi}\Delta E}\exp\left(-(2E/\Delta E)^2\right), \tag{A.44}
$$

and we choose $\Delta E = 0.5$ GHz.

A.5 Evaluation of Integrals in the Kinetic Equations

In this Appendix, we evaluate the integrals over the angle-dependent part (2.80) emerging in the four-magnon kinetic equation in Sec. 2.2 as well as the angle-dependent parts (A.38a) and (A.38b) emerging in the kinetic equations which result from the three-magnon process and from the Cherenkov process, given in Appendix A.4. Before we start, we already present the integrals required in the subsequent derivations, which read

$$I_1 = \iiint \mathrm{d}\Omega_1 \mathrm{d}\Omega_2 \mathrm{d}\Omega_3 \, \delta(\boldsymbol{q}_0 + \boldsymbol{q}_1 - \boldsymbol{q}_2 - \boldsymbol{q}_3) = \frac{8\pi^2}{q_0 q_1 q_2 q_3} \min(q_0, q_1, q_2, q_3), \tag{A.45a}$$

$$I_2 = q_0 q_1 \iiint \mathrm{d}\Omega_1 \mathrm{d}\Omega_2 \mathrm{d}\Omega_3 \, \cos\left(\theta_{\boldsymbol{q}_1}\right) \, \delta(\boldsymbol{q}_0 + \boldsymbol{q}_1 - \boldsymbol{q}_2 - \boldsymbol{q}_3) = -\frac{8\pi^2}{3\, q_0 q_1 q_2 q_3} \min(q_0, q_1, q_2, q_3)^3, \tag{A.45b}$$

$$\begin{aligned} I_3 &= q_0^2 q_1^2 \iiint \mathrm{d}\Omega_1 \mathrm{d}\Omega_2 \mathrm{d}\Omega_3 \, \cos^2\left(\theta_{\boldsymbol{q}_1}\right) \, \delta(\boldsymbol{q}_0 + \boldsymbol{q}_1 - \boldsymbol{q}_2 - \boldsymbol{q}_3) \\ &= \frac{8\pi^2}{15\, q_0 q_1 q_2 q_3} \left(2 \min(q_0, q_1, q_2, q_3)^2 + 5 \max(q_0, q_1, q_2, q_3)^2\right) \min(q_0, q_1, q_2, q_3)^3, \end{aligned} \tag{A.45c}$$

$$I_4 = \iiint \mathrm{d}\Omega_0 \mathrm{d}\Omega_1 \mathrm{d}\Omega_2 \, \sin^2(2\theta_{\boldsymbol{q}_1}) \, \delta(\boldsymbol{q}_0 - \boldsymbol{q}_1 - \boldsymbol{q}_2) = \frac{64\pi^2}{15 q_0 q_1 q_2} C_3(q_0, q_1, q_2), \tag{A.45d}$$

$$\begin{aligned} I_5 &= \iiint \mathrm{d}\Omega_0 \mathrm{d}\Omega_1 \mathrm{d}\Omega_2 \, \sin(2\theta_{\boldsymbol{q}_1}) \sin(2\theta_{\boldsymbol{q}_2}) \cos\left(\phi_{\boldsymbol{q}_1} - \phi_{\boldsymbol{q}_2}\right) \delta(\boldsymbol{q}_0 - \boldsymbol{q}_1 - \boldsymbol{q}_2) \\ &= \frac{8\pi^2}{15 q_0 q_1^3 q_2^3} C_3(q_0, q_1, q_2) \left(3\left(q_0^2 - q_1^2\right)^2 + 2q_2^2\left(q_1^2 - 3q_0^2\right) + 3q_2^4\right), \end{aligned} \tag{A.45e}$$

$$\begin{aligned} I_6 &= \iint \mathrm{d}\Omega_1 \mathrm{d}\Omega_2 \, \sin^2(2\theta_{\boldsymbol{q}_1}) \, \delta(\pm q_0 \, \boldsymbol{e}_z + \boldsymbol{q}_1 - \boldsymbol{q}_2) \\ &= -\frac{\pi}{2q_0^5 q_1^5 q_2} C_3(q_0, q_1, q_2) \left(q_0^2 + q_1^2 - q_2^2\right)^2 \left(q_0^4 + \left(q_1^2 - q_2^2\right)^2 - 2q_0^2\left(q_1^2 + q_2^2\right)\right), \end{aligned} \tag{A.45f}$$

where the first integral is evaluated explicitly in Appendix A.8 and the remaining integrals are evaluated similarly. Note that the integrals I_1, I_2 and I_3 are valid if in addition also $q_0^2 + q_1^2 = q_2^2 + q_3^2$ holds. This condition coincides with the energy conservation in the four-magnon scattering process in the case of the quadratic dispersion (2.78a). By default, this condition is always satisfied by the corresponding kinetic equation (2.83) due to the energy delta distribution. In the integrals I_4, I_5 and I_6, the function C_3 enters the right-hand side of the respective equations, which reads

$$C_3(q_0, q_1, q_2) = \begin{cases} 1 & \text{if } \ q_2 - q_1 < q_0 \\ 0 & \text{if } \ q_2 - q_1 > q_0, \end{cases} \tag{A.45g}$$

and which is valid without loss of generality for $q_2 > q_1 > q_0$. As it is apparent, this function originates from the momentum conservation in the three-magnon process.

A.5.1 Four-Magnon Process

In the case of the four-magnon scattering, we distinguish between two different cases. In the first case, which we refer to as *the modified process*, the quantum mechanical exchange interaction potential (2.30) is taken as a basis for the four-magnon scattering amplitude (2.58), which in the first Born approximation reads

$$A_4^{\mathrm{mod}}(\boldsymbol{q}_0, \boldsymbol{q}_1, \boldsymbol{q}_2, \boldsymbol{q}_3) = -2\, J\, a_0^2 \, (\boldsymbol{q}_0 \cdot \boldsymbol{q}_1 + \boldsymbol{q}_2 \cdot \boldsymbol{q}_3) + 4\, S_0\, J \left(24 - a_0^2 \left(\boldsymbol{q}_0^2 + \boldsymbol{q}_1^2 + \boldsymbol{q}_2^2 + \boldsymbol{q}_3^2\right)\right), \tag{A.46}$$

and which in the case of the quadratic dispersion (2.78a) reduces to

$$A_4^{\mathrm{mod}}(\boldsymbol{q}_0, \boldsymbol{q}_1) = -4\, J\, a_0^2 \, \boldsymbol{q}_0 \cdot \boldsymbol{q}_1 + 8\, S_0\, J \left(12 - a_0^2 \left(\boldsymbol{q}_0^2 + \boldsymbol{q}_1^2\right)\right). \tag{A.47}$$

The integral over the angle-dependent part (2.80) thus reads

$$\begin{aligned}F_4^{\mathrm{mod}}(q_0,q_1,q_2,q_3) =& \, q_1q_2q_3 \iiint \mathrm{d}\Omega_1\mathrm{d}\Omega_2\mathrm{d}\Omega_3 \, |A_4^{\mathrm{mod}}(\boldsymbol{q}_0,\boldsymbol{q}_1)|^2 \, \delta(\boldsymbol{q}_0+\boldsymbol{q}_1-\boldsymbol{q}_2-\boldsymbol{q}_3) \\ =& \, \frac{128\pi^2 J^2 \min(q_0,q_1,q_2,q_3)}{15q_0} \Bigg[a_0^4 \min(q_0,q_1,q_2,q_3)^2 \Big(2\min(q_0,q_1,q_2,q_3)^2 \\ & + 5\max(q_0,q_1,q_2,q_3)^2 \Big) + 20\, S_0\, a_0^2 \left(12 - a_0^2\left(q_0^2+q_1^2\right)\right) \\ & \times \min(q_0,q_1,q_2,q_3)^2 + 60\, S_0^2 \left(12 - a_0^2\left(q_0^2+q_1^2\right)\right)^2 \Bigg]. \end{aligned} \tag{A.48}$$

In the second case, which we refer to as *the common process*, we omit the correction term by setting $S_0 = 0$ in the exchange interaction potential (2.30). In turn, we add the dipolar contribution (2.32a) with $S_0 = 0$ to the classical exchange interaction potential and the resulting scattering amplitude thus reads

$$\begin{aligned}A_4^{\mathrm{com}}(\boldsymbol{q}_0,\boldsymbol{q}_1,\boldsymbol{q}_2,\boldsymbol{q}_3) =& -4\,J\,a_0^2\,\boldsymbol{q}_0\cdot\boldsymbol{q}_1 + \frac{\mu_0 g^2 \mu_\mathrm{B}^2}{a_0^3} \Big[2 - \sin^2(\theta_{\boldsymbol{q}_0-\boldsymbol{q}_2}) - \sin^2(\theta_{\boldsymbol{q}_0-\boldsymbol{q}_3}) \\ & - \frac{1}{4}\left(\sin^2(\theta_{\boldsymbol{q}_0}) + \sin^2(\theta_{\boldsymbol{q}_1}) + \sin^2(\theta_{\boldsymbol{q}_2}) + \sin^2(\theta_{\boldsymbol{q}_3})\right) \Big]. \end{aligned} \tag{A.49}$$

Due to the complex structure, we make an approximation and average the squared of A_4^{com} over all polar angles appearing in the dipolar part considering them as independent. We find

$$\overline{A_4^{\mathrm{com}}(\boldsymbol{q}_0,\boldsymbol{q}_1)^2} = \left(4\,J\,a_0^2\,\boldsymbol{q}_0\cdot\boldsymbol{q}_1\right)^2 + \frac{1}{5}\left(\frac{\mu_0 g^2\mu_\mathrm{B}^2}{a_0^3}\right)^2, \tag{A.50}$$

and the integral over the angle-dependent part (2.80) in this case reads

$$\begin{aligned}F_4^{\mathrm{com}}(q_0,q_1,q_2,q_3) =& \, q_1q_2q_3 \iiint \mathrm{d}\Omega_1\mathrm{d}\Omega_2\mathrm{d}\Omega_3 \, \overline{A_4^{\mathrm{com}}(\boldsymbol{q}_0,\boldsymbol{q}_1)^2} \, \delta(\boldsymbol{q}_0+\boldsymbol{q}_1-\boldsymbol{q}_2-\boldsymbol{q}_3) \\ =& \, \frac{\pi^2 \min(q_0,q_1,q_2,q_3)}{15q_0} \Bigg[128 J^2 a_0^4 \Big(2\min(q_0,q_1,q_2,q_3)^2 \\ & + 5\max(q_0,q_1,q_2,q_3)^2 \Big) \min(q_0,q_1,q_2,q_3)^2 + 24\left(\frac{\mu_0 g^2\mu_\mathrm{B}^2}{a_0^3}\right)^2 \Bigg]. \end{aligned} \tag{A.51}$$

A.5.2 Three-Magnon Process

The integral over the angle-dependent part (A.38a) in the case of the three-magnon process reads

$$\begin{aligned}F_3(q_0,q_1,q_2) =& \, \frac{1}{32\pi}\mu_0^2 M_\mathrm{S} \left(\frac{g\mu_\mathrm{B}}{a_0}\right)^3 q_0q_1q_2 \iiint \mathrm{d}\Omega_0\mathrm{d}\Omega_1\mathrm{d}\Omega_2 \Big[\delta(\boldsymbol{q}_0-\boldsymbol{q}_1-\boldsymbol{q}_2) \\ & \times |\sin(2\theta_{\boldsymbol{q}_1})\exp\left(-i\phi_{\boldsymbol{q}_1}\right) + \sin(2\theta_{\boldsymbol{q}_2})\exp\left(-i\phi_{\boldsymbol{q}_2}\right)|^2 \Big] \\ =& \, \frac{\pi}{30}\mu_0^2 M_\mathrm{S} \left(\frac{g\mu_\mathrm{B}}{a_0}\right)^3 C_3(q_0,q_1,q_2) \left(8 + \frac{3\left(q_0^2-q_1^2\right)^2 + 2q_2^2\left(q_1^2-3q_0^2\right) + 3q_2^4}{q_1^2q_2^2}\right). \end{aligned} \tag{A.52}$$

In the case of the phenomenological linear damping of the condensate introduced in Sec. 4.2, which results from a confluence process at the wave vector $\boldsymbol{q}_0 = \pm q_{\min}\boldsymbol{e}_z$, the integral over the angle-dependent part reads

$$\begin{aligned} F_3^c(q_{\min}, q_1, q_2) =& \, q_{\min} q_1 q_2 \iint \mathrm{d}\Omega_1 \mathrm{d}\Omega_2 \, |V_3(\pm q_{\min}\, \boldsymbol{e}_z) + V_3(\boldsymbol{q}_1)|^2 \, \delta(\pm q_{\min}\, \boldsymbol{e}_z + \boldsymbol{q}_1 - \boldsymbol{q}_2) \\ =& -\frac{\pi}{16}\mu_0^2 M_{\mathrm{S}} \left(\frac{g\mu_{\mathrm{B}}}{a_0}\right)^3 \frac{1}{q_{\min}^4 q_1^4} \left(q_{\min}^2 + q_1^2 - q_2^2\right)^2 \\ & \times \left(q_{\min}^4 + \left(q_1^2 - q_2^2\right)^2 - 2q_{\min}^2 \left(q_1^2 + q_2^2\right)\right), \end{aligned} \tag{A.53}$$

which is only valid if additionally the momentum conservation holds. Instead of the function C_3 defined in Eq. (A.45g), this condition can also be satisfied by the relation

$$E_1 \geq E_{\min} + \frac{E_{\min}^2}{8JS(q_{\min}a_0)^2}, \tag{A.54}$$

following from Eq. (3.12) in Sec. 3.1 in the case of the quadratic dispersion (2.78a). We finally make the transition to energy space by means of the substitution

$$\tilde{F}_3^c(E_0, E_1, E_2) = F_3^c(q_0, q_1, q_2). \tag{A.55}$$

A.5.3 Cherenkov Process

The integral over the angle-dependent part (A.38b) in the case of the Cherenkov process reads

$$\begin{aligned} F_\sigma(q_0, q_1, q_2) =& \frac{\hbar}{2\pi m v_\sigma} J^2 S^2 a_0^3 \, q_0^2 \, q_1^3 \, q_2^2 \iiint \mathrm{d}\Omega_0 \mathrm{d}\Omega_1 \mathrm{d}\Omega_2 \Big[\delta(\boldsymbol{q}_0 - \boldsymbol{q}_1 - \boldsymbol{q}_2) \\ & \times |\kappa \, \hat{\boldsymbol{e}}_\sigma(\boldsymbol{q}_2) \cdot \sum_{i=1}^{3} \hat{\boldsymbol{x}}_i \, (\hat{\boldsymbol{q}}_1 \cdot \hat{\boldsymbol{x}}_i) \, (\hat{\boldsymbol{q}}_2 \cdot \hat{\boldsymbol{x}}_i) \, (\hat{\boldsymbol{q}}_0 \cdot \hat{\boldsymbol{x}}_i) \, |^2\Big]. \end{aligned} \tag{A.56}$$

In order to simplify the integral, we neglect the last term including the dimensionless constant κ, which is of the order of unity for small wave vectors [62]. Hence, we get

$$F_\sigma(q_0, q_1, q_2) = \frac{4\pi\hbar}{m v_\sigma} J^2 S^2 a_0^3 \, q_0 \, q_1^2 \, q_2 \, C_3(q_0, q_1, q_2), \tag{A.57}$$

which follows by setting $q_1 \to 0$ in the general expression (A.97) in Appendix A.8.

A.6 The *t*-Matrix Approach

In this Appendix, we reveal important properties of the t-matrix, discussed in Sec. 2.2, by following the derivations made in Refs. [89,103]. We show that the t-matrix does not depend on the quantity S_0 and that it vanishes in the limit of zero wave vectors.

As we have shown in Sec. 2.2, the t-matrix is determined via the integral equation

$$\begin{aligned} t(\vec{\boldsymbol{q}}_0, \vec{\boldsymbol{q}}_1, \vec{\boldsymbol{q}}_2, \vec{\boldsymbol{q}}_3) =& \, V_4^{\mathrm{ex}}(\boldsymbol{q}_0, \boldsymbol{q}_1, \boldsymbol{q}_2, \boldsymbol{q}_3) + i\frac{\hbar a_0^3}{(2\pi)^4} \int \mathrm{d}^4 k \Big[V_4^{\mathrm{ex}}(\boldsymbol{q}_0, \boldsymbol{q}_1, \boldsymbol{k}, \boldsymbol{q}_0 + \boldsymbol{q}_1 - \boldsymbol{k}) \\ & \times G^{(0)}(\vec{\boldsymbol{k}}) \, G^{(0)}(\vec{\boldsymbol{q}}_0 + \vec{\boldsymbol{q}}_1 - \vec{\boldsymbol{k}}) \, t(\vec{\boldsymbol{k}}, \vec{\boldsymbol{q}}_0 + \vec{\boldsymbol{q}}_1 - \vec{\boldsymbol{k}}, \vec{\boldsymbol{q}}_2, \vec{\boldsymbol{q}}_3)\Big], \end{aligned} \tag{A.58}$$

where

$$V_4^{\mathrm{ex}}(\boldsymbol{q}_0,\boldsymbol{q}_1,\boldsymbol{q}_2,\boldsymbol{q}_3) = -\left[\,J(\boldsymbol{q}_0-\boldsymbol{q}_2)+J(\boldsymbol{q}_1-\boldsymbol{q}_2)\,\right]+\frac{1}{2}\,(1+4S_0) \times\left[\,J(\boldsymbol{q}_0)+J(\boldsymbol{q}_1)+J(\boldsymbol{q}_2)+J(\boldsymbol{q}_3)\,\right]. \tag{A.59}$$

The integral can be factorized by going over to total and relative coordinates

$$\vec{\boldsymbol{q}}_0+\vec{\boldsymbol{q}}_1=\vec{\boldsymbol{q}}_2+\vec{\boldsymbol{q}}_3=\vec{\boldsymbol{Q}}=(\boldsymbol{Q},\tilde{\omega}), \tag{A.60a}$$

$$\vec{\boldsymbol{q}}_0-\vec{\boldsymbol{q}}_1=2\vec{\boldsymbol{q}}, \tag{A.60b}$$

$$\vec{\boldsymbol{q}}_2-\vec{\boldsymbol{q}}_3=2\vec{\boldsymbol{q}}', \tag{A.60c}$$

$$\vec{\boldsymbol{k}}-\vec{\boldsymbol{Q}}/2=\vec{\boldsymbol{p}}=(\boldsymbol{p},\omega), \tag{A.60d}$$

and we define

$$t(\vec{\boldsymbol{q}}_0,\vec{\boldsymbol{q}}_1,\vec{\boldsymbol{q}}_2,\vec{\boldsymbol{q}}_3)\equiv t(\vec{\boldsymbol{q}},\vec{\boldsymbol{q}}',\vec{\boldsymbol{Q}}), \tag{A.61a}$$

$$V_4^{\mathrm{ex}}(\boldsymbol{q}_0,\boldsymbol{q}_1,\boldsymbol{q}_2,\boldsymbol{q}_3)\equiv V_4^{\mathrm{ex}}(\boldsymbol{q},\boldsymbol{q}',\boldsymbol{Q}). \tag{A.61b}$$

The integral equation (A.58) then reads

$$t(\boldsymbol{q},\boldsymbol{q}',\vec{\boldsymbol{Q}})=V_4^{\mathrm{ex}}(\boldsymbol{q},\boldsymbol{q}',\boldsymbol{Q})+i\frac{\hbar a_0^3}{(2\pi)^4}\int \mathrm{d}^4p\,\Big[V_4^{\mathrm{ex}}(\boldsymbol{q},\boldsymbol{p},\boldsymbol{Q})\,G^{(0)}(\vec{\boldsymbol{Q}}/2+\vec{\boldsymbol{p}}) \times G^{(0)}(\vec{\boldsymbol{Q}}/2-\vec{\boldsymbol{p}})\,t(\boldsymbol{p},\boldsymbol{q}',\vec{\boldsymbol{Q}})\Big], \tag{A.62}$$

where now $t(\boldsymbol{q},\boldsymbol{q}',\vec{\boldsymbol{Q}})$ only depends in its third argument on the fourth component as indicated. Therefore, the integral can be factorized and we first determine the integral

$$\int \mathrm{d}\omega\,G^{(0)}(\vec{\boldsymbol{Q}}/2+\vec{\boldsymbol{p}})\,G^{(0)}(\vec{\boldsymbol{Q}}/2-\vec{\boldsymbol{p}})=\int_{-\infty}^{\infty}\mathrm{d}\omega\left(\frac{1}{\hbar\tilde{\omega}/2+\hbar\omega-E(\boldsymbol{Q}/2+\boldsymbol{p})+i\delta}\times\frac{1}{\hbar\tilde{\omega}/2-\hbar\omega-E(\boldsymbol{Q}/2-\boldsymbol{p})+i\delta}\right)$$
$$=-\frac{2\pi i/\hbar}{\hbar\tilde{\omega}-E(\boldsymbol{Q}/2+\boldsymbol{p})-E(\boldsymbol{Q}/2-\boldsymbol{p})}, \tag{A.63}$$

where we have used the Dirac identity

$$\lim_{\delta\to 0}\frac{1}{x+i\delta}=P\frac{1}{x}-i\pi\delta(x), \tag{A.64}$$

where P denotes the principal value of the integral, which in our case vanishes. As we have shown in Sec. 2.1, the magnon dispersion for the simple cubic lattice without dipolar interaction reads

$$E(\boldsymbol{q})=g\mu_{\mathrm{B}}\mu_0H_0+2S\left[J(0)-J(\boldsymbol{q})\right], \tag{A.65}$$

and we set

$$\hbar\tilde{\omega}=E(\boldsymbol{q}_2)+E(\boldsymbol{q}_3)=E(\boldsymbol{Q}/2+\boldsymbol{q}')+E(\boldsymbol{Q}/2-\boldsymbol{q}'), \tag{A.66}$$

thus considering only the on-shell t-matrix relevant for the scattering process. Together with Eqs. (A.59), (A.63), (A.65) and (A.66) the integral equation (A.62) reads

$$\begin{aligned} t(\boldsymbol{q},\boldsymbol{q}',\vec{\boldsymbol{Q}}) &= -J(\boldsymbol{q}-\boldsymbol{q}') - J(\boldsymbol{q}+\boldsymbol{q}') + \frac{1}{2S}\frac{a_0^3}{(2\pi)^3} \\ &\times \int \mathrm{d}^3p \, \frac{[\, J(\boldsymbol{q}-\boldsymbol{p}) + J(\boldsymbol{q}+\boldsymbol{p})\,]\; t(\boldsymbol{p},\boldsymbol{q}',\vec{\boldsymbol{Q}})}{J(\boldsymbol{Q}/2+\boldsymbol{q}') + J(\boldsymbol{Q}/2-\boldsymbol{q}') - J(\boldsymbol{Q}/2+\boldsymbol{p}) - J(\boldsymbol{Q}/2-\boldsymbol{p})} \\ &+ \frac{1}{2}\,(1+4\,S_0)\,[\, J(\boldsymbol{Q}/2+\boldsymbol{q}) + J(\boldsymbol{Q}/2-\boldsymbol{q}) + J(\boldsymbol{Q}/2+\boldsymbol{q}') + J(\boldsymbol{Q}/2-\boldsymbol{q}')\,] \\ &\times \left(1 - \frac{1}{2S}\frac{a_0^3}{(2\pi)^3} \int \mathrm{d}^3p \, \frac{t(\boldsymbol{p},\boldsymbol{q}',\vec{\boldsymbol{Q}})}{J(\boldsymbol{Q}/2+\boldsymbol{q}') + J(\boldsymbol{Q}/2-\boldsymbol{q}') - J(\boldsymbol{Q}/2+\boldsymbol{p}) - J(\boldsymbol{Q}/2-\boldsymbol{p})}\right) \\ &+ \frac{1+4\,S_0}{4S}\frac{a_0^3}{(2\pi)^3} \int \mathrm{d}^3p \, t(\boldsymbol{p},\boldsymbol{q}',\vec{\boldsymbol{Q}}). \end{aligned} \tag{A.67}$$

Integration of both sides of Eq. (A.67) with respect to $\boldsymbol{q}$ and using the relation $\int \mathrm{d}^3q \, J(\boldsymbol{q}) = 0$ yields

$$\begin{aligned} \left(1 - \frac{1+4\,S_0}{4S}\right) \frac{a_0^3}{(2\pi)^3} \int \mathrm{d}^3p \, t(\boldsymbol{p},\boldsymbol{q}',\vec{\boldsymbol{Q}}) &= \frac{1}{2}\,(1+4\,S_0)\,[\, J(\boldsymbol{Q}/2+\boldsymbol{q}') + J(\boldsymbol{Q}/2-\boldsymbol{q}')\,] \\ \times \left(1 - \frac{1}{2S}\frac{a_0^3}{(2\pi)^3} \int \mathrm{d}^3p \, \frac{t(\boldsymbol{p},\boldsymbol{q}',\vec{\boldsymbol{Q}})}{J(\boldsymbol{Q}/2+\boldsymbol{q}') + J(\boldsymbol{Q}/2-\boldsymbol{q}') - J(\boldsymbol{Q}/2+\boldsymbol{p}) - J(\boldsymbol{Q}/2-\boldsymbol{p})}\right)&. \end{aligned} \tag{A.68}$$

By means of this relation we can bring Eq. (A.67) into the final form

$$\begin{aligned} t(\boldsymbol{q},\boldsymbol{q}',\vec{\boldsymbol{Q}}) &= -J(\boldsymbol{q}-\boldsymbol{q}') - J(\boldsymbol{q}+\boldsymbol{q}') + J(\boldsymbol{Q}/2+\boldsymbol{q}') + J(\boldsymbol{Q}/2-\boldsymbol{q}') \\ &+ \frac{1}{2S}\frac{a_0^3}{(2\pi)^3} \int \mathrm{d}^3p \, \frac{[\, J(\boldsymbol{q}-\boldsymbol{p}) + J(\boldsymbol{q}+\boldsymbol{p}) - J(\boldsymbol{Q}/2+\boldsymbol{p}) - J(\boldsymbol{Q}/2-\boldsymbol{p})\,]\; t(\boldsymbol{p},\boldsymbol{q}',\vec{\boldsymbol{Q}})}{J(\boldsymbol{Q}/2+\boldsymbol{q}') + J(\boldsymbol{Q}/2-\boldsymbol{q}') - J(\boldsymbol{Q}/2+\boldsymbol{p}) - J(\boldsymbol{Q}/2-\boldsymbol{p})} \\ &+ \Delta E(\boldsymbol{q},\boldsymbol{q}',\boldsymbol{Q})\, \frac{1}{2}\,(1+4\,S_0) \\ &\times \left(1 - \frac{1}{2S}\frac{a_0^3}{(2\pi)^3} \int \mathrm{d}^3p \, \frac{t(\boldsymbol{p},\boldsymbol{q}',\vec{\boldsymbol{Q}})}{J(\boldsymbol{Q}/2+\boldsymbol{q}') + J(\boldsymbol{Q}/2-\boldsymbol{q}') - J(\boldsymbol{Q}/2+\boldsymbol{p}) - J(\boldsymbol{Q}/2-\boldsymbol{p})}\right) \\ &+ f(S)\, \frac{a_0^3}{(2\pi)^3} \int \mathrm{d}^3p \, t(\boldsymbol{p},\boldsymbol{q}',\vec{\boldsymbol{Q}}), \end{aligned} \tag{A.69}$$

where

$$\Delta E(\boldsymbol{q},\boldsymbol{q}',\boldsymbol{Q}) = J(\boldsymbol{Q}/2+\boldsymbol{q}) + J(\boldsymbol{Q}/2-\boldsymbol{q}) - J(\boldsymbol{Q}/2+\boldsymbol{q}') - J(\boldsymbol{Q}/2-\boldsymbol{q}'), \tag{A.70}$$

and

$$f(S) = 2 - \frac{1+4S_0}{4S} - \frac{2}{1+4S_0}. \tag{A.71}$$

The quantity ΔE vanishes for on-shell scattering processes conserving the total energy. The spin factor $f(S)$ also just vanishes for the value S_0 defined in Eq. (2.7), so we can drop the last two addends in Eq. (A.69). We now see that the t-matrix does not depend on the factor S_0 any more and that it vanishes if only one of the ingoing wave vectors is zero, that is if $\boldsymbol{q} = \boldsymbol{Q}/2$ or $\boldsymbol{q} = -\boldsymbol{Q}/2$. Consequently, because of its Hermitian property, the t-matrix also vanishes if one of the outgoing wave vectors is zero.

A.7 Four-Magnon Relaxation Rate of the Uniform Mode

In this Appendix, we derive an analytic expression for the relaxation rate of the uniform mode caused by a four-magnon process. In order to keep the result general, we assume the scattering amplitude to be an arbitrary constant, which can be specified in the final expression.

We again start with relaxation rate resulting from the four-magnon process

$$\Gamma(\boldsymbol{q}_0) = \frac{2\pi}{\hbar}\frac{a_0^6}{(2\,\pi)^6}\frac{1}{2}\iiint \mathrm{d}^3q_1\mathrm{d}^3q_2\mathrm{d}^3q_3\Big[|A_4|^2\delta(\hbar\omega(\boldsymbol{q}_0)+\hbar\omega(\boldsymbol{q}_1)-\hbar\omega(\boldsymbol{q}_2)-\hbar\omega(\boldsymbol{q}_3)) \\ \times\,\delta(\boldsymbol{q}_0+\boldsymbol{q}_1-\boldsymbol{q}_2-\boldsymbol{q}_3)\Big(f(\boldsymbol{q}_1)\,(1+f(\boldsymbol{q}_2))\,(1+f(\boldsymbol{q}_3))-f(\boldsymbol{q}_2)f(\boldsymbol{q}_3)\,(1+f(\boldsymbol{q}_1))\Big)\Big], \tag{A.72}$$

where we extend the domain of integration to the full $\mathbb{R}^9$, which is well justified since the Bose-Einstein distributions in Eq. (A.72) quickly decline at large wave vectors. We further neglect the dipolar contribution to the magnon energy thus assuming an isotropic dispersion

$$\hbar\omega(q) = g\mu_\mathrm{B}\mu_0H_0 + 2JS\,(qa_0)^2, \tag{A.73}$$

which we derived in Sec. 2.1. We then go over to spherical coordinates and separate the integration over the angle-dependent part in Eq. (A.72) which reads

$$\iiint \mathrm{d}\Omega_1\mathrm{d}\Omega_2\mathrm{d}\Omega_3\,\delta(\boldsymbol{q}_0+\boldsymbol{q}_1-\boldsymbol{q}_2-\boldsymbol{q}_3) = \frac{8\pi^2}{q_0q_1q_2q_3}\,\min(q_0,q_1,q_2,q_3), \tag{A.74}$$

and which is proven in Appendix A.8. Inserting this relation into Eq. (A.72) yields

$$\Gamma(q_0) = \frac{a_0^6}{8\,\pi^3\hbar}\,|A_4|^2\iiint q_1\mathrm{d}q_1q_2\mathrm{d}q_2q_3\mathrm{d}q_3\left[\delta(E_0+E_1-E_2-E_3)\,\frac{\min(q_0,q_1,q_2,q_3)}{q_0} \\ \times\Big(f(q_1)\,(1+f(q_2))\,(1+f(q_3))-f(q_2)f(q_3)\,(1+f(q_1))\Big)\right]. \tag{A.75}$$

In this Appendix, we are only interested in the relaxation rate of the uniform mode which reads

$$\Gamma_0 = \frac{a_0^6}{8\,\pi^3\hbar}\,|A_4|^2\iiint q_1\mathrm{d}q_1q_2\mathrm{d}q_2q_3\mathrm{d}q_3\,\Big[\delta(E_\mathrm{min}+E_1-E_2-E_3) \\ \times\Big(f(q_1)\,(1+f(q_2))\,(1+f(q_3))-f(q_2)f(q_3)\,(1+f(q_1))\Big)\Big] \\ = \frac{|A_4|^2}{512\,\pi^3\hbar J^3S^3}\int\limits_{E_\mathrm{min}}^{\infty}\int\limits_{E_\mathrm{min}}^{\infty}\mathrm{d}E_2\mathrm{d}E_3\,\Big(\tilde{f}(E_2+E_3-E_\mathrm{min})\,\Big(1+\tilde{f}(E_2)\Big)\,\Big(1+\tilde{f}(E_3)\Big) \\ -\,\tilde{f}(E_2)\tilde{f}(E_3)\,\Big(1+\tilde{f}(E_2+E_3-E_\mathrm{min})\Big)\Big), \tag{A.76}$$

where $E_\mathrm{min} = g\mu_\mathrm{B}\mu_0H_0$. In equilibrium, the magnon occupation functions are Planck distributions

$$\tilde{f}(E_i) = \frac{1}{\exp\left(\frac{E_i}{k_\mathrm{B}T_\mathrm{m}}\right)-1} = g(x_i) = \frac{1}{\exp\left(\frac{g\mu_\mathrm{B}\mu_0H_0}{k_\mathrm{B}T_\mathrm{m}}+x_i\right)-1}, \tag{A.77}$$

where we have introduced the function $g(x)$ together with new dimensionless variables

$$x_i = \frac{E_i}{k_\mathrm{B}T_\mathrm{m}} - \frac{g\mu_\mathrm{B}\mu_0H_0}{k_\mathrm{B}T_\mathrm{m}}. \tag{A.78}$$

With this change of variables, Eq. (A.76) reads

$$\Gamma_0 = \frac{|A_4|^2(k_\mathrm{B}T_\mathrm{m})^2}{512\,\pi^3\hbar J^3S^3}\left[\int\limits_0^\infty\int\limits_0^\infty \mathrm{d}x_2\mathrm{d}x_3\, g(x_2+x_3)\left(g(x_2)+g(x_3)\right)\right.$$
$$\left. -\int\limits_0^\infty\int\limits_0^\infty \mathrm{d}x_2\mathrm{d}x_3\, g(x_2)g(x_3) + \int\limits_0^\infty\int\limits_0^\infty \mathrm{d}x_2\mathrm{d}x_3\, g(x_2+x_3)\right]. \tag{A.79}$$

At first, we consider only the first integral in Eq. (A.79)

$$I_1 = \int\limits_0^\infty\int\limits_0^\infty \mathrm{d}x_2\mathrm{d}x_3\, g(x_2+x_3)\left(g(x_2)+g(x_3)\right) = 2\int\limits_0^\infty\int\limits_0^\infty \mathrm{d}x_2\mathrm{d}x_3\, g(x_2+x_3)g(x_2), \tag{A.80}$$

and we make the substitutions

$$\tilde{x}_2 = x_2, \tag{A.81a}$$
$$\tilde{x}_3 = x_2 + x_3. \tag{A.81b}$$

Adapting the bounds of integration, we get

$$I_1 = 2\int\limits_0^\infty \mathrm{d}\tilde{x}_3\left[g(\tilde{x}_3)\int\limits_0^{\tilde{x}_3}\mathrm{d}\tilde{x}_2\, g(\tilde{x}_2)\right] = 2\int\limits_0^\infty \mathrm{d}\tilde{x}_3\, g(\tilde{x}_3)G(\tilde{x}_3) = 2\int\limits_0^\infty \mathrm{d}\tilde{x}_3\,\frac{1}{2}\frac{\mathrm{d}}{\mathrm{d}\tilde{x}_3}G(\tilde{x}_3)^2$$
$$= G(\tilde{x}_3\to\infty)^2 = \int\limits_0^\infty\int\limits_0^\infty \mathrm{d}x_2\mathrm{d}x_3\, g(x_2)g(x_3) = I_2, \tag{A.82}$$

which just compensates the second integral in Eq. (A.79). We therefore have to evaluate explicitly only the third integral

$$I_3 = \int\limits_0^\infty\int\limits_0^\infty \mathrm{d}x_2\mathrm{d}x_3\,\frac{1}{\exp\left(c+x_2+x_3\right)-1}, \qquad c = \frac{g\mu_\mathrm{B}\mu_0H_0}{k_\mathrm{B}T_\mathrm{m}}, \tag{A.83}$$

and we again use the substitutions (A.81a) and (A.81b) to obtain

$$I_3 = \int\limits_0^\infty \mathrm{d}\tilde{x}_3\,\frac{\tilde{x}_3}{\exp\left(c+\tilde{x}_3\right)-1} = -\int\limits_0^{\exp(-c)} \mathrm{d}x\,\frac{\ln(1-x)}{x} = D\Big(1-\exp(-c)\Big) \overset{c=0}{=} \frac{\pi^2}{6}, \tag{A.84}$$

with $D(x)$ being the dilogarithm also known as Spence's integral [102]. With this result, the relaxation rate of the uniform mode finally reads

$$\Gamma_0 = \frac{|A_4|^2(k_\mathrm{B}T_\mathrm{m})^2}{512\,\pi^3\hbar J^3S^3}\,D\left(1-\exp\left(-\frac{g\mu_\mathrm{B}\mu_0H_0}{k_\mathrm{B}T_\mathrm{m}}\right)\right) \approx \frac{|A_4|^2(k_\mathrm{B}T_\mathrm{m})^2}{3072\,\pi\hbar J^3S^3}. \tag{A.85}$$

A.8 Integration of the Delta Function over Solid Angles

In this Appendix, we proof the relation used in Appendixes A.5 and A.7

$$I = \iiint \mathrm{d}\Omega_1\mathrm{d}\Omega_2\mathrm{d}\Omega_3\,\delta(\boldsymbol{q}_0+\boldsymbol{q}_1-\boldsymbol{q}_2-\boldsymbol{q}_3) = \frac{8\pi^2}{q_0q_1q_2q_3}\,\min(q_0,q_1,q_2,q_3). \tag{A.86}$$

The starting point for the proof is given in Refs. [81,86] and consists of a Fourier transform of the delta distribution

$$\delta(\boldsymbol{q}_0+\boldsymbol{q}_1-\boldsymbol{q}_2-\boldsymbol{q}_3)=\frac{1}{(2\pi)^3}\int z^2\mathrm{d}z\int\mathrm{d}\Omega_z\exp(i\boldsymbol{z}\cdot(\boldsymbol{q}_0+\boldsymbol{q}_1-\boldsymbol{q}_2-\boldsymbol{q}_3)),\tag{A.87}$$

so we can factorize the integral

$$I=\frac{1}{(2\pi)^3}\int z^2\mathrm{d}z\Big[\int\mathrm{d}\Omega_z\exp(i\boldsymbol{z}\cdot\boldsymbol{q}_0)\int\mathrm{d}\Omega_1\exp(i\boldsymbol{z}\cdot\boldsymbol{q}_1)\int\mathrm{d}\Omega_2\exp(-i\boldsymbol{z}\cdot\boldsymbol{q}_2)\\ \times\int\mathrm{d}\Omega_3\exp(-i\boldsymbol{z}\cdot\boldsymbol{q}_3)\Big].\tag{A.88}$$

We evaluate the integrals over the solid angles individually by means of

$$\int\mathrm{d}\Omega_r\exp(i\boldsymbol{k}\cdot\boldsymbol{r})=4\pi\,\frac{\sin(kr)}{kr},\tag{A.89}$$

and we thus obtain

$$I=\frac{32\pi}{q_0q_1q_2q_3}\int_0^\infty\mathrm{d}z\frac{1}{z^2}\sin(zq_0)\,\sin(zq_1)\,\sin(zq_2)\,\sin(zq_3).\tag{A.90}$$

It is convenient to write the product of sine-functions into a sum of cosine-functions

$$\sin(zq_0)\,\sin(zq_1)\,\sin(zq_2)\,\sin(zq_3)=\frac{1}{8}\sum_{i=1}^{8}(-1)^i\cos(za_i),\tag{A.91}$$

$$\begin{aligned}\text{with}\quad a_1&=q_0+q_1+q_2-q_3,&a_2&=q_0+q_1+q_2+q_3,\\ a_3&=q_0+q_1-q_2+q_3,&a_4&=q_0+q_1-q_2-q_3,\\ a_5&=q_0-q_1+q_2+q_3,&a_6&=q_0-q_1+q_2-q_3,\\ a_7&=q_0-q_1-q_2-q_3,&a_8&=q_0-q_1-q_2+q_3,\end{aligned}$$

and to substitute

$$\frac{1}{z}=\int_0^\infty\mathrm{d}s\,\exp(-zs).\tag{A.92}$$

The integral I then reads

$$I=\frac{4\pi}{q_0q_1q_2q_3}\sum_{i=1}^{8}(-1)^i\int_0^\infty\mathrm{d}s\int_0^\infty\mathrm{d}s'\int_0^\infty\mathrm{d}z\,\cos(za_i)\,\exp(-z(s+s')),\tag{A.93}$$

and we see that the integration with respect to z is just the Fourier transform of a decaying exponential function which gives a Lorentzian function. Thus, we get

$$I=\frac{4\pi}{q_0q_1q_2q_3}\sum_{i=1}^{8}(-1)^i\int_0^\infty\mathrm{d}s\int_0^\infty\mathrm{d}s'\frac{s+s'}{a_i^2+(s+s')^2},\tag{A.94}$$

and we make the substitutions

$$x=s,\tag{A.95a}$$

$$y=s+s'.\tag{A.95b}$$

Adapting the bounds of integration, we arrive at

$$I = \frac{4\pi}{q_0 q_1 q_2 q_3} \sum_{i=1}^{8} (-1)^i \int_0^\infty \mathrm{d}y \left[\int_0^y \mathrm{d}x \, \frac{y}{a_i^2 + y^2} \right] = \frac{4\pi}{q_0 q_1 q_2 q_3} \int_0^\infty \mathrm{d}y \left(\underbrace{\sum_{i=1}^{8} (-1)^i}_{=0} - \sum_{i=1}^{8} (-1)^i \frac{a_i^2}{a_i^2 + y^2} \right)$$

$$= - \frac{2\pi^2}{q_0 q_1 q_2 q_3} \sum_{i=1}^{8} (-1)^i \, |a_i|. \tag{A.96}$$

Because I is invariant under pairwise exchange of two q_i, which are addends of the various a_i, we set $q_0 > q_3 > q_2 > q_1 > 0$ without loss of generality and obtain three different cases

$$I = \frac{4\pi^2}{q_0 q_1 q_2 q_3} \times \begin{cases} 2q_1 & \text{if} \quad q_0 - q_3 < q_2 - q_1 \\ q_1 + q_2 + q_3 - q_0 & \text{if} \quad q_1 + q_2 > q_0 - q_3 > q_2 - q_1 \\ 0 & \text{if} \quad q_0 - q_3 > q_1 + q_2. \end{cases} \tag{A.97}$$

We now show that in the four-magnon scattering process only the first case is relevant and that the other cases are forbidden by energy conservation. Assuming a quadratic dispersion

$$\hbar\omega(q) = g\mu_\mathrm{B}\mu_0 H_0 + 2JS\,(qa_0)^2, \tag{A.98}$$

the energy conservation law is only compatible with the relation $q_0 > q_3 > q_2 > q_1 > 0$ if the two ingoing magnons have wave vectors q_0 and q_1 and the two outgoing magnons have wave vectors q_2 and q_3 or vice versa. The energy conservation in this case reads

$$q_0^2 + q_1^2 = q_2^2 + q_3^2, \tag{A.99}$$

which can also be expressed as

$$(q_0 - q_3)\,(q_0 + q_3) = (q_2 - q_1)\,(q_2 + q_1). \tag{A.100}$$

Assuming now that $q_0 - q_3 > q_2 - q_1$ which is an implication of the second and third case in Eq. (A.97), the energy conservation (A.100) requires that

$$q_0 + q_3 < q_2 + q_1, \tag{A.101}$$

which contradicts the relation $q_0 > q_3 > q_2 > q_1 > 0$. Therefore, only the first case in Eq. (A.97) is compatible with the energy conservation and can in general be written as

$$I = \frac{8\pi^2}{q_0 q_1 q_2 q_3} \, \min(q_0, q_1, q_2, q_3). \tag{A.102}$$

Bibliography

[1] S. N. Bose. *Plancks Gesetz und Lichtquantenhypothese.* Z. Phys. **26** 178 (1924)

[2] A. Einstein. *Quantentheorie des einatomigen idealen Gases.* Sber. Preuss. Akad. Wiss. **22** 261 (1924)

[3] A. Einstein. *Quantentheorie des einatomigen idealen Gases. Zweite Abhandlung.* Sber. Preuss. Akad. Wiss. **1** 3 (1925)

[4] L. Pitaevskii, S. Stringari. *Bose-Einstein Condensation.* Clarendon Press Oxford (2003)

[5] I. Duck, E. C. G. Sudarshan. *Pauli and the Spin-Statistics Theorem.* World Scientific (1997)

[6] M. H. Anderson, J. R. Ensher, M. R. Matthews, C. E. Wieman, E. A. Cornell. *Observation of Bose-Einstein Condensation in a Dilute Atomic Vapor.* Science **269** 198 (1995)

[7] K. B. Davis, M.-O. Mewes, M. R. Andrews, N. J. van Druten, D. S. Durfee, D. M. Kurn, W. Ketterle. *Bose-Einstein Condensation in a Gas of Sodium Atoms.* Phys. Rev. Lett. **75** 3969 (1995)

[8] T. Fukuzawa, E. E. Mendez, J. M. Hong. *Phase transition of an exciton system in GaAs coupled quantum wells.* Phys. Rev. Lett. **64** 3066 (1990)

[9] L. V. Butov, C. W. Lai, A. L. Ivanov, A. C. Gossard, D. S. Chemla. *Towards Bose–Einstein condensation of excitons in potential traps.* Nature **417** 47 (2002)

[10] J. P. Eisenstein, A. H. MacDonald. *Bose–Einstein condensation of excitons in bilayer electron systems.* Nature **432** 691 (2004)

[11] H. Deng, G. Weihs, C. Santori, J. Bloch, Y. Yamamoto. *Condensation of Semiconductor Microcavity Exciton Polaritons.* Science **298** 199 (2002)

[12] J. Kasprzak, M. Richard, S. Kundermann, A. Baas, P. Jeambrun, J. M. J. Keeling, F. M. Marchetti, M. H. Szymańska, R. André, J. L. Staehli, V. Savona, P. B. Littlewood, B. Deveaud, Le Si Dang. *Bose–Einstein condensation of exciton polaritons.* Nature **443** 409 (2006)

[13] R. Balili, V. Hartwell, D. Snoke, L. Pfeiffer, K. West. *Bose-Einstein Condensation of Microcavity Polaritons in a Trap.* Science **316** 1007 (2007)

[14] J. Klaers, J. Schmitt, F. Vewinger, M. Weitz. *Bose–Einstein condensation of photons in an optical microcavity.* Nature **468** 545 (2010)

[15] T. Nikuni, M. Oshikawa, A. Oosawa, H. Tanaka. *Bose-Einstein Condensation of Dilute Magnons in* $TlCuCl_3$. Phys. Rev. Lett. **84** 5868 (2000)

[16] C. Rüegg, N. Cavadini, A. Furrer, H.-U. Güdel, K. Krämer, H. Mutka, A. Wildes, K. Habicht, P. Vorderwisch. *Bose–Einstein condensation of the triplet states in the magnetic insulator* $TlCuCl_3$. Nature **423** 62 (2003)

[17] F. Bloch. *Zur Theorie des Ferromagnetismus.* Z. Phys. **61** 206 (1930)

[18] W. Nolting, A. Ramakanth. *Quantum Theory of Magnetism.* Springer (2009)

[19] S. O. Demokritov, V. E. Demidov, O. Dzyapko, G. A. Melkov, A. A. Serga, B. Hillebrands, A. N. Slavin. *Bose–Einstein condensation of quasi-equilibrium magnons at room temperature under pumping.* Nature **443** 430 (2006)

[20] A. G. Gurevich, G. A. Melkov. *Magnetization Oscillations and Waves.* CRC Press, Boca Raton (1996)

[21] V. S. L'vov. *Wave Turbulence under Parametric Excitation.* Springer (1992)

[22] S. O. Demokritov, B. Hillebrands, A. N. Slavin. *Brillouin light scattering studies of confined spin waves: linear and nonlinear confinement.* Phys. Rep. **348** 441 (2001)

[23] O. Dzyapko, V. E. Demidov, S. O. Demokritov, G. A. Melkov, A. N. Slavin. *Direct observation of Bose–Einstein condensation in a parametrically driven gas of magnons.* New J. Phys. **9** 64 (2007)

[24] S. O. Demokritov, V. E. Demidov, O. Dzyapko, G. A. Melkov, A. N. Slavin. *Quantum coherence due to Bose–Einstein condensation of parametrically driven magnons.* New J. Phys. **10** 045029 (2008)

[25] V. E. Demidov, O. Dzyapko, S. O. Demokritov, G. A. Melkov, A. N. Slavin. *Observation of Spontaneous Coherence in Bose-Einstein Condensate of Magnons.* Phys. Rev. Lett. **100** 047205 (2008)

[26] O. Dzyapko, V. E. Demidov, M. Buchmeier, T. Stockhoff, G. Schmitz, G. A. Melkov, S. O. Demokritov. *Excitation of two spatially separated Bose-Einstein condensates of magnons.* Phys. Rev. B (Rapid Communications) **80** 060401 (2009)

[27] A. V. Chumak, G. A. Melkov, V. E. Demidov, O. Dzyapko, V. L. Safonov, S. O. Demokritov. *Bose-Einstein Condensation of Magnons under Incoherent Pumping.* Phys. Rev. Lett. **102** 187205 (2009)

[28] V. E. Demidov, O. Dzyapko, S. O. Demokritov, G. A. Melkov, A. N. Slavin. *Thermalization of a Parametrically Driven Magnon Gas Leading to Bose-Einstein Condensation.* Phys. Rev. Lett. **99** 037205 (2007)

[29] V. E. Demidov, O. Dzyapko, M. Buchmeier, T. Stockhoff, G. Schmitz, G. A. Melkov, S. O. Demokritov. *Magnon Kinetics and Bose-Einstein Condensation Studied in Phase Space.* Phys. Rev. Lett. **101** 257201 (2008)

[30] O. Dzyapko, V. E. Demidov, S. O. Demokritov, G. A. Melkov, V. L. Safonov. *Monochromatic microwave radiation from the system of strongly excited magnons.* Appl. Phys. Lett. **92** 162510 (2008)

[31] P. Nowik-Boltyk, O. Dzyapko, V. E. Demidov, N. G. Berloff, S. O. Demokritov. *Spatially non-uniform ground state and quantized vortices in a two-component Bose-Einstein condensate of magnons.* Sci. Rep. **2** 482 (2012)

[32] A. A. Serga, V. S. Tiberkevich, C. W. Sandweg, V. I. Vasyuchka, D. A. Bozhko, A. V. Chumak, T. Neumann, B. Obry, G. A. Melkov, A. N. Slavin, B. Hillebrands. *Bose–Einstein condensation in an ultra-hot gas of pumped magnons.* Nat. Commun. **5** 3452 (2014)

[33] P. Clausen, D. A. Bozhko, V. I. Vasyuchka, B. Hillebrands, G. A. Melkov, A. A. Serga. *Stimulated thermalization of a parametrically driven magnon gas as a prerequisite for Bose-Einstein magnon condensation.* Phys. Rev. B (Rapid Communications) **91** 220402 (2015)

[34] S. M. Rezende. *Theory of Bose–Einstein condensation in a microwave-driven interacting magnon gas.* J. Phys. Condens. Matter **22** 164211 (2010)

[35] S. M. Rezende. *Theory of microwave superradiance from a Bose-Einstein condensate of magnons.* Phys. Rev. B (Rapid Communications) **79** 060410 (2009)

[36] S. M. Rezende. *Theory of coherence in Bose-Einstein condensation phenomena in a microwave-driven interacting magnon gas.* Phys. Rev. B **79** 174411 (2009)

[37] S. M. Rezende. *Crossover behavior in the phase transition of the Bose-Einstein condensation in a microwave-driven magnon gas.* Phys. Rev. B **80** 092409 (2009)

[38] B. A. Malomed, O. Dzyapko, V. E. Demidov, S. O. Demokritov. *Ginzburg-Landau model of Bose-Einstein condensation of magnons.* Phys. Rev. B **81** 024418 (2010)

[39] F. S. Vannucchi, Á. R. Vasconcellos, R. Luzzi. *Nonequilibrium Bose-Einstein condensation of hot magnons.* Phys. Rev. B (Rapid Communications) **82** 140404 (2010)

[40] F. S. Vannucchi, Á. R. Vasconcellos, R. Luzzi. *Dynamics of a Bose-Einstein condensate of excited magnons.* Eur. Phys. J. B **86** 463 (2013)

[41] S. N. Andrianov, V. V. Bochkarev, S. Moiseev. *Kinetics of pulse-induced magnon Bose-Einstein condensate.* Eur. Phys. J. B **87** 128 (2014)

[42] Rakesh Kar, Anirban Misra, N. H. March, D. J. Klein. *Bose–Einstein condensation of magnons in ferromagnetic thin films.* Phase Transitions **85** 831 (2012)

[43] J. Hick, T. Kloss, P. Kopietz. *Thermalization of magnons in yttrium-iron garnet: Nonequilibrium functional renormalization group approach.* Phys. Rev. B **86** 184417 (2012)

[44] A. Rückriegel, P. Kopietz, D. A. Bozhko, A. A. Serga, B. Hillebrands. *Magnetoelastic modes and lifetime of magnons in thin yttrium iron garnet films.* Phys. Rev. B **89** 184413 (2014)

[45] A. Rückriegel, P. Kopietz. *Rayleigh-Jeans Condensation of Pumped Magnons in Thin-Film Ferromagnets.* Phys. Rev. Lett. **115** 157203 (2015)

[46] V. Cherepanov, I. Kolokolov, V. L'Vov. *The saga of YIG: Spectra, thermodynamics, interaction and relaxation of magnons in a complex magnet.* Phys. Rep. **229** 81 (1993)

[47] R. C. LeCraw, E. G. Spencer, C. S. Porter. *Ferromagnetic Resonance Line Width in Yttrium Iron Garnet Single Crystals.* Phys. Rev. **110** 1311 (1958)

[48] T. Kasuya, R. C. LeCraw. *Relaxation Mechanisms in Ferromagnetic Resonance.* Phys. Rev. Lett. **6** 223 (1961)

[49] I. S. Tupitsyn, P. C. E. Stamp, A. L. Burin. *Stability of Bose-Einstein Condensates of Hot Magnons in Yttrium Iron Garnet Films.* Phys. Rev. Lett. **100** 257202 (2008)

[50] A. Kreisel, F. Sauli, L. Bartosch, P. Kopietz. *Microscopic spin-wave theory for yttrium-iron garnet films.* Eur. Phys. J. B **71** 59 (2009)

[51] M. Wu, A. Hoffmann. *Recent Advances in Magnetic Insulators - From Spintronics to Microwave Applications.* Academic Press (2013)

[52] B. R. Tittmann. *Possible identification of magnetostatic surface spin wave modes in ferromagnetic resonance on epitaxial yttrium—iron—garnet films.* Solid State Commun. **13** 463 (1973)

[53] T. Holstein, H. Primakoff. *Field Dependence of the Intrinsic Domain Magnetization of a Ferromagnet.* Phys. Rev. **58** 1098 (1940)

[54] H. Benson, D. L. Mills. *Spin Waves in Thin Films; Dipolar Effects.* Phys. Rev. **178** 839 (1969)

[55] R. P. Erickson, D. L. Mills. *Microscopic theory of spin arrangements and spin waves in very thin ferromagnetic films.* Phys. Rev. B **43** 10715 (1991)

[56] R. P. Erickson, D. L. Mills. *Thermodynamics of thin ferromagnetic films in the presence of anisotropy and dipolar coupling.* Phys. Rev. B **44** 11825 (1991)

[57] R. N. Costa Filho, M. G. Cottam, G. A. Farias. *Microscopic theory of dipole-exchange spin waves in ferromagnetic films: Linear and nonlinear processes.* Phys. Rev. B **62** 6545 (2000)

[58] H. T. Nguyen, M. G. Cottam. *The effect of lattice structure on dipole–exchange spin waves in ultrathin ferromagnetic films.* J. Phys. Condens. Matter **23** 126004 (2011)

[59] E. Meloche, J. I. Mercer, J. P. Whitehead, T. M. Nguyen, M. L. Plumer. *Dipole-exchange spin waves in magnetic thin films at zero and finite temperature: Theory and simulations.* Phys. Rev. B **83** 174425 (2011)

[60] T. Kloss, A. Kreisel, P. Kopietz. *Parametric pumping and kinetics of magnons in dipolar ferromagnets.* Phys. Rev. B **81** 104308 (2010)

[61] J. Hick, F. Sauli, A. Kreisel, P. Kopietz. *Bose-Einstein condensation at finite momentum and magnon condensation in thin film ferromagnets.* Eur. Phys. J. B **78** 429 (2010)

[62] A. I. Akhiezer, V. G. Bar'yakhtar, S. V. Peletminskii. *Spin Waves.* North-Holland, Amsterdam (1968)

[63] M. Sparks. *Ferromagnetic-Relaxation Theory.* McGraw-Hill, New York (1964)

[64] R. M. White. *Quantum Theory of Magnetism.* Springer-Verlag (1983)

[65] P. Krivosik, C. E. Patton. *Hamiltonian formulation of nonlinear spin-wave dynamics: Theory and applications.* Phys. Rev. B **82** 184428 (2010)

[66] C. Kittel. *On the Theory of Ferromagnetic Resonance Absorption.* Phys. Rev. **73** 155 (1948)

[67] B. A. Kalinikos, A. N. Slavin. *Theory of dipole-exchange spin wave spectrum for ferromagnetic films with mixed exchange boundary conditions.* J. Phys. C: Solid State Phys. **19** 7013 (1986)

[68] M. Sparks, R. Loudon, C. Kittel. *Ferromagnetic Relaxation. I. Theory of the Relaxation of the Uniform Precession and the Degenerate Spectrum in Insulators at Low Temperatures.* Phys. Rev. **122** 791 (1961)

[69] G. T. Rado, H. Suhl. *Magnetism: Vol. I.* Academic Press (1963)

[70] E. Schlömann. *Ferromagnetic Relaxation Caused by Interaction with Thermally Excited Magnons.* Phys. Rev. **121** 1312 (1961)

[71] A. Kreisel. *Spin-wave calculations for Heisenberg magnets with reduced symmetry.* Ph.D. thesis, Johann Wolfgang Goethe-Universität, Frankfurt am Main (2011)

[72] N. Majlis. *The Quantum Theory of Magnetism.* World Scientific (2007)

[73] T.-M. Cheng, L. Li. *Magnon–phonon coupling in two-dimensional Heisenberg ferromagnetic system.* J. Magn. Magn. Mater. **320** 1 (2008)

[74] R. Balescu. *Equilibrium and Nonequilibrium Statistical Mechanics.* John Wiley & Sons (1975)

[75] C. M. Van Vliet. *Equilibrium and Non-equilibrium Statistical Mechanics.* World Scientific (2008)

[76] D. Zubarev, V. Morozov, G. Röpke. *Statistical Mechanics of Nonequilibrium Processes 1.* Akad. Verl. (1996)

[77] J. J. Sakurai. *Modern Quantum Mechanics.* Addison-Wesley (1994)

[78] A. Messiah. *Quantum Mechanics Vol. II.* North-Holland, Amsterdam (1966)

[79] D. W. Snoke. *Solid State Physics: Essential Concepts.* Pearson/Addison-Wesley, San Francisco (2009)

[80] U. Weiss. *Quantum Dissipative Systems.* World Scientific (1999)

[81] M. Escobedo, S. Mischler, M. A. Valle. *Homogeneous Boltzmann equation in quantum relativistic kinetic theory.* Electron. J. Diff. Eqns. **4** 1 (2003)

[82] P. A. Markowich, L. Pareschi. *Fast conservative and entropic numerical methods for the Boson Boltzmann equation.* Numer. Math. **99** 509 (2005)

[83] L. Bányai, P. Gartner, O. M. Schmitt, H. Haug. *Condensation kinetics for bosonic excitons interacting with a thermal phonon bath.* Phys. Rev. B **61** 8823 (2000)

[84] D. W. Snoke, J. P. Wolfe. *Population dynamics of a Bose gas near saturation.* Phys. Rev. B **39** 4030 (1989)

[85] D. V. Semikoz, I. I. Tkachev. *Kinetics of Bose Condensation.* Phys. Rev. Lett. **74** 3093 (1995)

[86] D. V. Semikoz, I. I. Tkachev. *Condensation of bosons in the kinetic regime.* Phys. Rev. D **55** 489 (1997)

[87] J. M. Ziman. *Principles of the Theory of Solids.* Cambridge University Press (1972)

[88] C. Josserand, Y. Pomeau. *Nonlinear aspects of the theory of Bose–Einstein condensates.* Nonlinearity **14** R25 (2001)

[89] A. A. Abrikosov, L. P. Gorkov, I. E. Dzyaloshinski. *Methods of Quantum Field Theory in Statistical Physics.* Prentice-Hall, Inc., Englewood Cliffs, N. J. (1963)

[90] R. D. Mattuck. *A Guide to Feynman Diagrams in the Many-Body Problem.* Dover Publications, Inc., Mineola, N. Y. (1992)

[91] F. J. Dyson. *General Theory of Spin-Wave Interactions.* Phys. Rev. **102** 1217 (1956)

[92] F. J. Dyson. *Thermodynamic Behavior of an Ideal Ferromagnet.* Phys. Rev. **102** 1230 (1956)

[93] S. V. Maleev. *Scattering of slow neutrons in ferromagnets.* Sov. Phys. JETP **6** 776 (1958)

[94] A. Klein, E. R. Marshalek. *Boson realizations of Lie algebras with applications to nuclear physics.* Rev. Mod. Phys. **63** 375 (1991)

[95] T. Oguchi. *Theory of Spin-Wave Interactions in Ferro- and Antiferromagnetism.* Phys. Rev. **117** 117 (1960)

[96] P. D. Loly, S. Doniach. *Removal of an Apparent Discrepancy between Calculations of Dyson and of Oguchi for the Heisenberg Ferromagnet.* Phys. Rev. **144** 319 (1966)

[97] F. Bertaut, F. Forrat. *Structure of ferrimagnetic ferrites of rare earths.* Compt. rend. **242** 382 (1956)

[98] S. Geller, M. A. Gilleo. *Structure and ferrimagnetism of yttrium and rare-earth-iron garnets.* Acta Cryst. **10** 239 (1957)

[99] M. Sparks, C. Kittel. *Ferromagnetic Relaxation Mechanism for M_z in Yttrium Iron Garnet.* Phys. Rev. Lett. **4** 232 (1960)

[100] L. D. Landau, E. M. Lifshitz. *Course of Theoretical Physics, Vol. 8, Electrodynamics of Continuous Media.* Pergamon Press, Oxford (1984)

[101] G. Gao. *Large Scale Molecular Simulations with Application to Polymers and Nanoscale Materials.* Ph.D. thesis, California Institute of Technology, Pasadena, California (1998)

[102] M. Abramowitz, I. A. Stegun. *Handbook of Mathematical Functions.* Dover Publications, Inc., New York (1972)

[103] M. I. Kaganov, A. V. Chubukov. *Interacting magnons.* Sov. Phys. Usp. **30** 1015 (1987)

List of Publications

J. Hüser and T. Kuhn. *A kinetic approach to Bose-Einstein condensation of magnons in yttrium iron garnet.* To be submitted to Physical Review B.

Conference Contributions etc.

National Conferences

18/03/2015, DPG Spring Meeting, Berlin. Talk: *Ferromagnetic relaxation in yttrium iron garnet at small wave vectors*

03/04/2014, DPG Spring Meeting, Dresden. Talk: *Thermalization and Bose-Einstein condensation of magnons*

15/03/2013, DPG Spring Meeting, Regensburg. Talk: *Effects of the lattice discreteness on the Damon-Eshbach mode*

28/03/2012, DPG Spring Meeting, Berlin. Talk: *Quantum mechanical contribution to the magnon dispersion in the Heisenberg model*

18/03/2011, DPG Spring Meeting, Dresden. Poster: *Higher-order corrections to the magnon dispersion in the Heisenberg model*

International Conferences

29/04/2014, ICSM, Antalya (Turkey). Poster: *Nonequilibrium Dynamics and Bose-Einstein Condensation of Magnons*

05/08/2013, Magnonics III, Varberg (Sweden). Contributed Talk: *Dynamics and thermalization of hot magnons in yttrium-iron garnet*

Seminars & Workshops

12/02/2015, SE-MS Conference, Münster. Talk: *Bose-Einstein condensation of magnons: A theoretical study of magnon-magnon and magnon-phonon interactions*

28/07/2014, AG Hillebrands, Kaiserslautern. Invited Seminar Talk: *Bose-Einstein condensation of magnons: A theoretical study of magnon-magnon and magnon-phonon interactions*

15/05/2014, AG Demokritov, Münster. Talk: *Bose-Einstein condensation of magnons: A theoretical study of magnon-magnon and magnon-phonon interactions*

28/11/2012, Group of Prof. Krawczyk, Poznań (Poland). Talk: *Effects of the lattice discreteness on the spin wave dispersion in ferromagnetic thin films*

27/11/2012, Group of Prof. Machnikowski, Wrocław (Poland). Talk: *Effects of the lattice discreteness on the spin wave dispersion in ferromagnetic thin films*

03/09/2012, Magnonics (Summer School), Santa Margherita Ligure (Italy). Poster: *Quantum mechanical contribution to the magnon dispersion in the Heisenberg model*

14/03/2012, 2nd Polish-German Workshop, Münster. Poster: *Quantum mechanical contribution to the magnon dispersion in the Heisenberg model*

15/02/2011, 1st Polish-German Workshop, Wrocław (Poland). Poster: *Higher-order corrections to the magnon dispersion in the Heisenberg model*

Lebenslauf

Der Lebenslauf ist in dieser digital publizierten Version nicht enthalten.

Danksagung

An dieser Stelle möchte ich mich bei allen Personen bedanken, die zum Gelingen dieser Arbeit beigetragen haben.

Als erstes bedanke ich mich bei Prof. Dr. Tilmann Kuhn, der mich vor sechs Jahren sehr freundlich in seine Arbeitsgruppe aufgenommen hat. Für die Möglichkeit über das spannende Thema der Bose-Einstein Kondensation von Magnonen zu promovieren, bin ich ihm sehr dankbar. Ich danke ihm ebenfalls für sein stetes Interesse an meiner Arbeit, für die vielen, oft langen fachlichen Diskussionen und Denkanstöße, sowie das Vertrauen, das er mir entgegengebracht hat, weitgehend selbstständig wissenschaftlich arbeiten zu können.

Danken möchte ich auch Prof. Dr. Peter Krüger für die Übernahme der Zweitgutachterschaft sowie Prof. Dr. Sergej Demokritov für die Übernahme der Drittprüferschaft.

Als nächstes bedanke ich mich bei Thomas Kendziorczyk für die vielen privaten und fachlichen Gespräche, sowie die schönen Kaffeepausen nach dem Mittagessen. Immer in Erinnerung bleiben für mich die tollen Erfahrungen, die wir auf Konferenzen gemacht haben, sowie die Menschen, die wir zusammen dort kennengelernt haben. Und nicht zuletzt danke ich ihm für das Korrekturlesen meiner Arbeit. Vier Augen sehen wirklich mehr als zwei!

Als nächstes bedanke ich mich bei Dr. habil. Oleksandr Serha, der mich freundlicherweise in die AG Hillebrands nach Kaiserslautern eingeladen hat um über meine Forschung zu referieren. Ich danke ihm auch für seine experimentellen Daten, die er mir für diese Arbeit zur Verfügung gestellt hat.

Bei der gesamten Arbeitsgruppe möchte ich mich natürlich auch für die schöne Zeit und die gute Arbeitsatmosphäre bedanken. Ich freue mich schon auf den traditionellen Mad Dog mit euch!

Bedanken möchte ich mich auch bei meinen Eltern, die mir das Studium erst ermöglicht haben, und die mich in jeglicher Hinsicht in jedem Vorhaben unterstützen.

Ganz besonders möchte ich mich bei Judith und Karl für ihre Geduld bedanken, sowie die Freude, die sie in mein Leben gebracht haben.